Comprehensive Cancer Center München

Klinikum rechts der Isar

Technische Universität München

Direktor: Prof. Dr. Hana Algül

Entzündung-assoziierte Transkriptionsfaktoren als Targets im Pankreaskarzinom

Zusammenstellung wissenschaftlicher Veröffentlichungen zur Erlangung

der Lehrbefähigung für das Fach Experimentelle Medizin

an der

Medizinischen Fakultät der Technischen Universität München

vorgelegt von

Dr. rer. nat. Marina Lesina

2023

Mit Genehmigung der Medizinischen Fakultät

der Technischen Universität München

Fachmentorat:	Prof. Dr. med. Hana Algül (Vorsitzender)
	Prof. Dr. med. Wilko Weichert
	Prof. Dr. Olaf Groß
Dekan:	Prof. Dr. med. S. E. Combs

Inhaltsverzeichnis

1 Einleitung

Das duktale Adenokarzinom der Bauchspeicheldrüse (PDAC) ist die vierthäufigste Ursache für krebsbedingte Todesfälle in der westlichen Welt mit einer im Laufe der Zeit steigenden Inzidenz. Prognostischen Berechnungen zufolge wird die Krebs-assoziierte Letalität zum Jahr 2030 die des Brust- und Dickdarmkarzinoms übertreffen und an zweiter Stelle rangieren. Trotz der Fortschritte in den Bereichen Chirurgie, Chemotherapie und Strahlentherapie ist die 5-Jahres-Überlebensrate bei PDAC immer noch alarmierend (1, 2). Hierfür ist neben der verspäteten Diagnose und der frühen Metastasierung die ausgesprochene Strahlen- und Chemoresistenz verantwortlich.

1.1 Molekulargenetik des Pankreaskarzinoms

Viele publizierte Untersuchungen in den letzten Jahren erbrachten wesentliche Fortschritte im Verständnis zur Pathophysiologie dieser Erkrankung und der genetischen Alterationen in der pankreatischen Karzinogenese (3-5). Die häufigsten molekulargenetischen Veränderungen sind neben der Verkürzung von Telomeren, Mutationen im *Kras* Gen, Verlust von *INK4A* (*Cyclin-Dependent Kinase 4 Inhibitor A*) (frühe Ereignisse) sowie Verlust der Funktion von *TP53* (*Tumor Protein p53*), *Smad4* (*Mothers Against Decapentaplegic Homolog 4*) und *BRCA2* (*Breast Cancer Type 2*) (späte Veränderungen) (6-10). Die meisten duktalen Pankreaskarzinome sind mäßig bis hoch differenziert und führen zu einer deutlichen desmoplastischen Stromareaktion. Ähnlich der Dysplasie-Karzinom-Sequenz des Kolonkarzinoms wurde auch für das duktale Pankreaskarzinom ein Progressionsmodell definiert und im Jahr 2000 ein allgemeines Nomenklatursystem für Vorläuferläsionen des invasiven Pankreaskarzinoms, so genannten intraepithelialen Neoplasien des Pankreas (PanIN) eingeführt (7). Die Tumorprogression wird sowohl von den Tumorzellen als auch vom Tumormicroenvironment verursacht, das aus verschiedenen nicht-malignen Zellen (Fibroblasten, fibroblast-ähnlichen Stromazellen und Immunzellen), extrazellulärer Matrix und löslichen Molekülen besteht (11). Dysregulation der Signalkaskaden, die die maligne Transformation regulieren, in Krebszellen führt zur Freisetzung von Faktoren, die das Tumormicroenvironment aktiv modulieren. Das Verständnis der molekularen Signalwege, die die Zellproliferation und das Zellüberleben während der pankreatischen Karzinogenese regulieren, ist wichtig für die Identifizierung neuer therapeutischer Ansätze für diese Krankheit.

1.2 STAT/JAK Signalweg

Es konnte die Schlüsselrolle des STAT/JAK Signalwegs bei der Entstehung und dem Fortschreiten maligner Neoplasien nachgewiesen werden. Bei STAT-Proteinen (*Signal Transducers and Activators of Transcription*) handelt es sich um Transkriptionsfaktoren, die durch eine Phosphorylierung an Tyrosinen aus dem inaktiven in den aktiven Zustand versetzt werden. Ihre Aktivierung wird durch mehr als 20 verschiedene Zytokine, aber auch Wachstumsfaktoren wie z.B. EGF (*Epidermal Growth Factor*), PDGF (*Platelet-Derived Growth Factor*), HGF (*Hepatocyte Growth/Scatter Factor*) oder VEGF (*Vascular Endothelial Growth Factor*) vermittelt (12-14). Diese Faktoren aktivieren eine übergeordnete Kinase, die *Janus Kinase 2* (JAK2), die wiederum den Transkriptionsfaktor STAT3 unter anderem am Tyrosin 705 phosphoryliert. Die auf diese Weise Tyrosin-phosphorylierten STATs können über eine sogenannte reziproke Phosphotyrosine-SH2-Interaktion (*SRC Homology 2*) dimerisieren, in den Kern translozieren, sich an spezifische Promotorregionen binden und auf diese Weise die Transkription bestimmter Gene regulieren.

Eine gezielte Kontrolle der STAT-Aktivierung erfolgt unter verschiedene Mechanismen. Hierzu gehören zum einen die klassischen Degradierungsprozesse nach Ubiquitinylierung (15, 16), zum anderen die Dephosphorylierung über nukleäre Phosphatasen (17, 18). Auch durch die Inaktivierung von Zytokinrezeptoren und Januskinasen durch Phosphatasen, wie SHP1 (*Src Homology Region 2 Domain-Containing Phosphatase-1*), SHP2 (*Src Homology Region 2 Domain-Containing Phosphatase-2*) oder CD45 (*Protein Tyrosine Phosphatase, Receptor Type, C*) wird die Aktivität der STAT-Familie moduliert (19). SHP2 ist eine ubiquitär exprimierte Nicht-Rezeptor Protein-Tyrosinphosphatase, welche die Signaltransduktion verschiedener Wachstumsfaktoren durch die kontext- und zelltypabhängige Modulierung des JAK-STAT Signalweges regulieren kann. Des Weiteren existieren hemmende Mechanismen im Sinne eines negativen Feedbacks, wobei STAT-Proteine spezifische Inhibitoren wie z.B. *Suppressors of Cytokine Signalling* (SOCS) Proteine, *Protein Inhibitor of Ativated STAT* (PIAS) und Protein Tyrosin Phosphatasen (PTPasen) aktivieren. Diese verhindern eine überschießende und andauernde STAT-Aktivierung (20).

Da der STAT/JAK Signalweg in der Regulation wichtiger biologischer Prozesse wie Zellzyklus-Progression, Apoptose, Tumorangiogenese und Immunresistenz involviert ist, ist es nicht überraschend, dass dieser Signalweg in einer Reihe von Tumoren konstitutiv aktiv ist (21). Dabei scheinen verschiedene STAT-Proteine in unterschiedlichen Tumorerkrankungen beteiligt zu sein. Während hämato/lymphoblastische Tumore eine konstitutive Phosphorylierung von STAT1, STAT3 und STAT5 aufweisen, zeigen solide Tumore und

daraus gewonnene Zelllinien eine dauerhafte Phosphorylierung des STAT3 am Tyrosin 705 (22).

Für die Beteiligung des STAT3 im Pankreaskarzinom des Menschen liegen mittlerweile viele Daten vor. In Resektaten von humanem Bauchspeicheldrüsenkrebs konnte man an Tyrosin 705 phosphoryliertes STAT3 in duktalen Karzinomen nachweisen. In sämtlichen humanen Pankreaskarzinomzelllinien ist STAT3 an Tyrosin 705 phosphoryliert (23). *In vitro* Experimente konnten zeigen, dass die pharmakologische Hemmung von pSTAT3 die G1/S-Phase-Progression in Karzinomzelllinien deutlich verlangsamt und das Metastasierungs- wie auch das Invasionspotential abschwächt (24-26). *In vivo* Untersuchungen an Mausmodellen zeigten, dass die Onkogen-induzierte pankreatische Karzinogenese von der Mikroumgebung abhängt, in der myeloide Zellen IL-6 (*Interleukin 6*) sezernieren. Das freigesetzte IL-6 führt zur Stat3-Aktivierung über das IL-6 Transsignalling und beschleunigt dadurch die Progression von präneoplastischen Läsionen (PanIN) zum duktalen Pankreaskarzinom (11). Darüber hinaus konnte gezeigt werden, dass eine anhaltende Stat3-Aktivierung für die Tumorentwicklung und -progression entscheidend ist, während eine vorübergehende Stat3-Aktivierung an der PanIN-Progression beteiligt ist (27).

Damit erscheint dieser Signalweg auf der Grundlage der bisher verfügbaren Erkenntnisse ein wichtiges Zielelement für die pankreatische Onkogenese zu sein.

1.3 NF-κB/Rel Signalweg

Untersuchungen der letzten Jahre zeigten, dass die Aktivierung des NF-κB (*Nuclear Factor kappa B*) Signalwegs eine wichtige Rolle bei der Progression des Pankreaskarzinoms spielt. In der Tat belegen zahlreiche Studien den Nachweis der Aktivierung dieses Signalwegs im Pankreaskarzinom und Karzinomzelllinien.

NF-κB/Rel umfasst eine Familie von Transkriptionsfaktoren, der fünf verschiedene Mitglieder angehören. Ihr gemeinsames Kennzeichen ist eine 300 Aminosäuren umfassende hochkonservierte Domäne, die so genannte Rel-Homologie-Domäne (RHD) (28). Diese vermittelt die DNA-Bindung, Dimerisierung der NF-κB/Rel-Proteine, die nukleäre Translokation, sowie die Interaktion mit inhibitorischen IκB-Proteinen (*Inhibitor of Nuclear Factor kappa B*). In nicht stimulierten Zellen werden NF-κB-Transkriptionsfaktoren durch die Assoziation mit den IκB-Proteinen im Zytoplasma in ihrer inaktiven Form gehalten. Diese Interaktion führt dazu, dass das für die nukleäre Translokation notwendige *Nuclear Localization Site* (NLS)-Signal durch IκBs maskiert wird (29-32). Auf diese Weise wird eine

unkontrollierte nukleäre Translokation von Hetero-dimeren verhindert. Die Mitglieder der IκB-Proteinfamilie enthalten im C-Terminus die so genannten Ankyrin-Repeat-Sequenzen, die mit der RHD der NF-κB-Proteine interagieren. NF-κB-Proteine können durch eine Vielzahl extra- und intrazellulärer Stimuli aktiviert werden. Die NF-κB aktivierenden Stimuli führen zur Phosphorylierung, Polyubiquitinierung und zu einem proteasomalem Abbau der IκB-Proteine, wodurch die NF-κB-Dimere freigesetzt werden und in den Kern translozieren. Die nukleäre Translokation von NF-kB-Proteinen kann über den Signalweg erfolgen, der durch den IκB-Kinase-Komplex vermittelt wird. Der gesamte Komplex besteht aus drei Untereinheiten: IKKα, IKKβ und IKKγ (33). Der klassische Weg der NF-κB-Aktivierung wird hauptsächlich durch verschiedene Stimuli ausgelöst. Es kommt zur Phosphorylierung von IκBα. Das dabei freigesetzte Heterodimer, meist bestehend aus RelA/p65 und NF-κB1/p50, kann über die unmaskierte NLS in den Zellkern translozieren, wo es die Transkription seiner Zielgene reguliert. Dazu gehört auch IκBα, welches nach einer Neusynthese in den Kern wandert, NF-κB von der DNA ablöst und zurück ins Zytoplasma transportiert. Durch diese negative Rückkopplung reguliert NF-κB seine eigene Aktivität (34).

Zu den Zielgenen des Heterodimers RelA/p65 gehören solche, die in Immunantwort, Stress- und entzündlichen Reaktionen involviert sind (35). Die Mitglieder des NF-κB Signalweges können die Proliferation der Zellen durch die Regulation der Transkription von Cyclin D1, Cyclin E, CDK2 (*Cyclin-Dependent Kinase 2*) und c-Myc steuern (36, 37). Des Weiteren spielt der NF-κB Signalweg bei der Regulation der Apoptose eine wesentliche Rolle (38). Der Transkriptionsfaktor kann sowohl pro- als auch anti-apoptotische Prozesse regulieren. Darüber hinaus scheint NF-κB/Rel für die Ras-vermittelte Transformation in verschiedenen Zelllinien unabdingbar zu sein (39, 40). Weitere Untersuchungen haben gezeigt, dass RelA/p65 die Karzinomentwicklung im Pankreas über einen zweistufigen Mechanismus beeinflusst. In den frühen Stadien hemmt RelA/p65 die PanIN-Progression durch die Regulation von CXCL1/KC (*Chemokine (C-X-C motif) Ligand 1*) und die Induktion von Onkogen-induzierter Seneszenz über den CXCR2 Rezeptor (*Interleukin 8 Receptor, beta*). In den späteren Stadien, wenn Onkogen-induzierte Seneszenz überwunden wird, wirkt die Aktivierung von RelA tumorfördernd. Dies legt daher die zentrale Bedeutung des Transkriptionsfaktors (als Tumorsuppressor oder Tumorpromoter) in der Entwicklung von Tumoren nahe.

Wenngleich die Bedeutung des NF-κB/Rel Signalweges in zahlreichen Untersuchungen an Tumorzelllinien, aber auch an murinen Tumormodellen (41-48) gezeigt wurde, sind noch viele

Fragen zu Mechanismen, über die der NF-κB/Rel Signalweg die pankreatische Karzinogenese beeinflusst, offen.

1.4 Autophagie

Die Autophagie hat sich als wichtiger Prozess in physiologischen und pathologischen Szenarien herausgestellt. Studien an Tiermodellen sowie Untersuchungen und genetische Analysen bei Patienten weisen eindeutig darauf hin, dass die Autophagie bei zahlreichen Krankheiten eine Rolle spielt, darunter Krebs, neurodegenerative und Muskelerkrankungen, Lebererkrankungen, Herzversagen, Infektions- und Entzündungskrankheiten, Diabetes und Fettleibigkeit (49, 50).

Die Autophagie - ein evolutionär hochkonservierter Mechanismus - übernimmt eine Vielzahl von Aufgaben, darunter die Aufrechterhaltung der zellulären Homöostase. Im Rahmen der Autophagie werden Aminosäuren, Glukose und Lipide für den Stoffwechsel bereitgestellt. Die Autophagie dient auch der Beseitigung beschädigter Proteine und Organellen innerhalb der Zelle und trägt zu einer Reihe von physiologischen und pathologischen Prozessen bei.

Ein zentraler Mechanismus der Autophagie besteht in der Bildung von Autophagosomen, welche durch Fusion mit Lysosomen das abzubauende Material degradieren und die dadurch gewonnenen Baustoffe dem zellulären Recyclingsystem wieder zuführen (51). Zudem spielt die Autophagie eine wichtige Rolle bei der Zellantwort auf Stress und ist mit der Zellentwicklung, der Tumorsuppression, Resistenzen gegenüber Pathogenen und der Verlängerung der Lebensspanne assoziiert (52). Eine Schlüsselrolle bei der Bildung von Autophagosomen spielen *Autophagie-Related Genes* (Atg). Atg5 bindet an Atg12-Atg16 und vermittelt die Konjugation von LC3 I (*Microtubule-associated proteins 1A/1B light chain 3A*) an Phosphatidylethanolamin, wodurch LC3 II entsteht. LC3 II wird an die autophagosomale Membran gebunden und interagiert mit mehreren Adaptorproteinen, z. B. Sqstm1/p62 (*Ubiquitin-Binding Protein p62*), die Frachtmoleküle zu den Autophagosomen transportieren. Atg5 ist für die Bildung von LC3 II-positiven Autophagosomen und die Aufrechterhaltung des autophagischen Flusses erforderlich.

Die Hemmung der Autophagie durch eine Deletion von Atg5 im Zusammenhang mit der Aktivierung von Onkogenen bzw. der Hemmung von Tumorsuppressorgenen wurde in verschiedenen Gewebetypen durchgeführt, um die Rolle der Autophagie in verschiedenen Stadien der Karzinogenese zu untersuchen (53). Überraschenderweise hat sich gezeigt, dass eine Deletion von Atg5 in der Bauchspeicheldrüse (54, 55) und der Lunge (56) die Tumorentstehung verstärkt, aber die Tumorprogression verringert, was auf eine vom

Tumorstadium abhängige Wirkung der Autophagie hinweist. Als zugrundeliegende Ursachen für diese Phänotypen wurden erhöhte DNA-Schäden, Zellstress, Apoptose und Stoffwechseldefizite vermutet.

Mit Hilfe etablierter *in vitro* und *in vivo* Modelle konnte gezeigt werden, dass die Stadien der Pankreaskarzinogenese vom Atg5-Spiegel abhängen (52). Der vollständige Verlust von Atg5 in der Bauchspeicheldrüse während der Embryogenese beschleunigt die Tumorentstehung, blockiert aber die Tumorprogression, während der monoallelische Verlust die Tumorinzidenz und die Metastasierungsrate signifikant erhöht. Die Deletion eines Atg5-Allels und die Verringerung der Atg5-Proteinkonzentration die Aggressivität von PDAC durch zellautonome und nicht-zellautonome Effekte erhöht, was insgesamt die Tumoraggressivität fördert. Die Ausschaltung von Atg5 mittels Small-Hairpin-RNA (shRNA) zeigte außerdem, dass der genaue Zusammenhang zwischen dem Atg5-Spiegel und dem PDAC-Phänotyp einem nicht-linearen Muster folgt. Diese Ergebnisse liefern somit neue Erkenntnisse über die Rolle der Autophagie bei der Entstehung und dem Fortschreiten von PDAC.

2 Ergebnisse und Diskussion eigener Arbeiten

2.1 Einfluss der Stat3/Socs3-Aktivierung im Fortschreiten der pankreatischen Karzinogenese

Stat3/Socs3 Activation by IL-6 Transsignaling Promotes Progression of Pancreatic Intraepithelial Neoplasia and Development of Pancreatic Cancer
Lesina M., … Algül H. (2011). Cancer Cell 19, 456-469.

In der vorliegenden Studie haben wir die Rolle des IL-6-abhängigen Stat3-Signalwegs in der pankreatischen Karzinogenese anhand von gentechnisch-veränderten Mausmodellen untersucht.

2.1.1 Nicht-zellautonome Aktivierung von Stat3^{Y705} bei der pankreatischen Karzinogenese

Für diese Studie verwendeten wir die *Kras^{G12D}* Mauslinie, die eine konstitutiv aktive Form des mutierten *Kras* in der Bauchspeicheldrüse exprimiert und damit das gesamte Spektrum der Bauchspeicheldrüsenkrebsentstehung rekapituliert, das beim Menschen beobachtet wird (57). Zahlreiche Studien belegen eine Aktivierung von Stat3^{Y705} in humanen Pankreaskarzinomen (PDAC). Diese Beobachtung konnten wir im *Kras^{G12D}* Modell reproduzieren. Obwohl sich in Vorläuferläsionen und Karzinomen sowie Metastasen Stat3-Aktivität biochemisch und immunhistochemisch *in vivo* nachweisen ließ, zeigten die aus primären Tumoren und Metastasen isolierten Zelllinien *in vitro* keine konstitutive Stat3-Phosphorylierung.

Diese Ergebnisse lieferten Hinweise für einen möglichen parakrinen Mechanismus, der bei der Stat3-Phosphorylierung *in vivo* eine Rolle spielen kann. Da die Aktivierung der JAK/Stat3 Kaskade von gp130 (*Glycoprotein 130*) - Liganden (IL-6, LIF (*Leukemia Inhibitory Factor*), OSM (*Oncostatin M*), CNTF (*Ciliary Neurotrophic Factor*), IL-11 (*Interleukin 11*)) abhängig ist, wurde als nächstes ihre Expression im Pankreas der *Kras^{G12D}* Mäuse zu verschiedenen Zeitpunkten untersucht. Dabei konnte anhand von der qRT-PCR Analyse gezeigt werden, dass nur IL-6 zeitabhängig und signifikant induziert wird, während LIF, OSM, CNTF sowie IL-11 geringgradig oder unverändert bleiben. Des Weiteren zeigte sich, dass Pankreaskarzinomzellen, die aus dem primären Tumor einer repräsentativen *Kras^{G12D}* Maus isoliert wurden, nach IL-6-Stimulation mit der Stat3-Phosphorylierung reagieren. Die Auswirkung der Zytokin-Stimulation auf die Aktivierung von Stat3 in Karzinomzellen wurde an dieser Stelle exemplarisch beschrieben und ist in den weiteren Zelllinien ähnlich.

Zur weiteren Charakterisierung dieser Beobachtung wurden Pankreata 9 Wochen alter *Kras^{G12D}* Mäuse analysiert, um die zelluläre Quelle von IL-6 zu bestimmen. Das

Pankreasgewebe in *Kras*^{G12D} Mäusen ist zu diesem Zeitpunkt heterogen und enthält neben den azinären Zellen und murinen pankreatischen intraepithelialen Neoplasien (mPanIN) auch Bindegewebe und Entzündungszellen, die in ihrer Gesamtheit das Microenvironment bilden. Bei immunhistochemischen Analysen konnte eine starke IL-6-Expression in infiltrierenden Immunzellen und nur eine geringfügige Positivität in azinären Zellen nachgewiesen werden. Weitere Analysen zeigten, dass infiltrierende F4/80-positive Makrophagen einen wesentlichen Bestandteil des Microenvironment ausmachen, während die Anzahl der CD3-positiven Lymphozyten eher in geringer Anzahl vertreten sind. Diese Ergebnisse suggerierten eine nicht-zellautonome Aktivierung von Stat3^{Y705} *in vivo*, die möglicherweise von F4/80-positiven Makrophagen im Pankreaskarzinom abhängig ist**.**

2.1.2 IL-6 Transsignaling beschleunigt mPanIN-Progression in Kras^{G12D} *Mäusen.*

In weiteren Schritten wurde der Frage nachgegangen, ob die Stat3-Aktivierung im Pankreas von myeloiden Zellen, die den gp130-Liganden IL-6 sezernieren, beeinflusst wird. Dazu etablierten wir ein Ko-Kultursystem, um zu untersuchen, ob Tumor-assoziierte Makrophagen (TAM) die Aktivierung von Stat3 in *Kras*^{G12D}-positiven azinären Zellen bewirken. Die Ko-Kultivierung von Makrophagen aus Pankreata 18 Wochen alter *Kras*^{G12D} Mäuse mit *Kras*^{G12D} Azinuszellen reichte nicht aus, um Stat3 verstärkt zu phosphorylieren. Selbst nach einer Vorstimulation der Makrophagen mit IL-6 konnte keine robuste Stat3-Aktivierung in *Kras*^{G12D} Azinuszellen beobachtet werden.

Diese Daten belegen, dass *Kras*^{G12D}-exprimierende azinäre Zellen auf das Zytokin IL-6 jedoch nicht direkt (klassisches IL-6 Signaling) reagieren. Aufgrund dessen haben wir in weiteren Untersuchungen überprüft, ob das IL-6 über die Komplexierung mit dem löslichen IL-6 Rezeptor ein sogenanntes Hyper-IL-6 (IL-6 + löslicher IL-6 Rezeptor) formt und dieser Faktor den ubiquitär vorkommenden gp130 Rezeptor in azinären Zellen bindet, um Stat3 zu aktivieren (IL-6 Transsignaling). Dafür wurden *Kras*^{G12D}-exprimierende azinäre Zellen mit IL-6 und Hyper-IL-6 inkubiert und auf Stat3-Phosphorylierung getestet. Diese Analyse zeigte eindeutig, dass Stat3-Phosphorylierung *in vitro* das IL-6 Transsignaling und nicht das klassische IL-6 Signaling erfordert.

Um den Einfluss des IL-6 Transsignaling auf die Aktivierung des IL-6-abhängigen Stat3-Signalwegs während der pankreatischen Onkogenese *in vivo* zu überprüfen, haben wir zwei weitere genetisch-modifizierte Mauslinien etabliert. Die *Kras*^{G12D} Mauslinie wurde zum einen mit der *sgp130*^{tg} Mauslinie (*Kras*^{G12D};*sgp130*^{tg}) und zum anderen mit der *Il-6*$^{-/-}$ Mauslinie (*Kras*^{G12D};*Il-6*$^{-/-}$*)* gekreuzt. Die *sgp130*^{tg} Mauslinie exprimiert den löslichen gp130 Rezeptor

(sgp130Fc) unter Kontrolle des hepatischen PEPCK-Promotors (58). Beim sgp130Fc handelt es sich um ein Fusionsprotein aus dem extrazellulären Anteil des Glycoproteins gp130 und des Fc-Anteils des IgG1. Dieses rekombinant hergestellte Protein bindet den IL-6/IL-6-Rezeptor-Komplex und hemmt seine Bindung an membranständiges gp130. So wird durch das Abfangen von IL-6/IL-6-Rezeptor-Komplexen das IL-6 Transsignaling spezifisch *in vivo* gehemmt, während die IL-6 Bindung an den membrangebundenen IL-6-Rezeptor (klassisches IL-6 Signaling) nicht tangiert wird. Genetische Deletion von IL-6 in *Il-6*$^{-/-}$Mauslinie verhindert hingegen klassisches IL-6 Signaling und IL-6 Transsignaling *in vivo*.

Diese Mauslinien wurden 18 Wochen lang beobachtet. Histologisch gesehen entwickelten *Kras*^{G12D}*;Il-6*$^{-/-}$ Mäuse nach 18 Wochen weniger und überwiegend niedrig-gradige mPanINs im Vergleich zu *Kras*^{G12D} Mäusen mit zahlreichen niedrig- und hoch-gradigen mPanINs. Bemerkenswerterweise hatte die postnatale Inaktivierung des IL-6 Signaling bei *Kras*^{G12D}*;sgp130*^{tg} Mäusen eine ähnliche Wirkung auf die mPanIN-Progression. Die verminderte mPanIN-Progression korrelierte mit dem Level von p-Stat3^{Y705} im Pankreas; immunhistologische und Western Blot Analysen zeigten eine attenuierte Phosphorylierung von Stat3^{Y705} in *Kras*^{G12D}*;Il-6*$^{-/-}$ und *Kras*^{G12D}*;sgp130*^{tg} Pankreata im Vergleich zu *Kras*^{G12D} Pankreas.

Diese Ergebnisse legen naher, dass die Stat3-Phosphorylierung im Pankreas *in vivo* überwiegend das IL-6 Transsignaling und zu einem geringeren Anteil das klassische IL-6 Signaling erfordert.

Um diese Beobachtungen der IL-6-abhängigen mPanIN-Progression weiter zu untermauern, haben wir ein Knochenmarktransplantationsmodell entwickelt. Dieses Experiment soll dazu beitragen, die Rolle von Makrophagen in der IL-6-vermittelten Stat3-Phosphorylierung zu untersuchen. Knochenmarkzellen von *Il-6*$^{+/+}$ (*BM-Il-6*$^{+/+}$) als auch von *Il-6*$^{-/-}$ (*BM-Il-6*$^{-/-}$) Maus-Spender wurden in bestrahlte *Kras*^{G12D} Mäuse transplantiert. Auf diese Weise entstanden Mauschimäre, die eine Differenzierung zwischen myeloidem und nicht-myeloidem IL-6 zulassen. *Kras*^{G12D} Mäuse entwickeln nach der Transplantation von *Il-6*$^{+/+}$ kompetenten Knochenmarkzellen (*BM-Il-6*$^{+/+}$ *Kras*^{G12}) hoch-gradige mPanIN-3-Läsionen, was in *BM-Il-6*$^{-/-}$ *Kras*^{G12D} Mäusen nicht zu beobachten ist. Die Stat3-Phosphorylierung in *BM-Il-6*$^{-/-}$ *Kras*^{G12D} Mäusen war deutlich attenuiert.

Zusammengefasst implizieren diese Daten, dass myeloide Zellen die mPanIN-Progression eher durch das IL-6 Transsignaling als durch das klassische IL-6 Signaling fördern. Der *downstream effector* Stat3 scheint mit der Entwicklung von mPanIN-Läsionen in Verbindung zu stehen.

2.1.3 Inaktivierung des Stat3-Signalwegs verzögert die mPanIN-Progression und Pankreaskarzinomentwicklung.

Da Stat3 als der wichtigste pro-tumorigene Effektor von IL-6 gilt, sollte in weiteren Experimenten der Einfluss einer Stat3-Aktivierung auf die mPanIN-Progression zum Karzinom untersucht werden. Immunfluoreszenzanalysen belegen eine frühzeitige Aktivierung von Stat3^{Y705} im Pankreas sowie in infiltrierenden Makrophagen 13 Wochen alter *Kras^{G12D}* Mäuse. Um die Auswirkungen der Stat3-Aktivierung im exokrinen Pankreas während der Onkogenese zu untersuchen, wurde eine Mauslinie unter Anwendung der Cre/loxP-basierten Technologie generiert, in der neben der Expression des mutierten *Kras^{G12D}* Onkogens zusätzlich Stat3 Pankreas-spezifisch inaktiviert wurde (*Kras^{G12D};Stat3$^{\Delta panc}$*) (59-61). Dabei wurde Exon 21 des *Stat3* Gens deletiert. Exon 21 codiert für die Proteindomäne des Stat3 Proteins, in der das für die Dimerisierung und damit nukleäre Translokation des Transkriptionsfaktors notwendige Tyrosin 705 enthalten ist. Zur Überprüfung der mPanIN-Progression analysierten wir *Kras*^{G12D} und *Kras^{G12D};Stat3$^{\Delta panc}$* Mauslinien zum Zeitpunkt von 18 Wochen. *Kras^{G12D}* Mäuse entwickelten die typischen mPanIN-1, mPanIN-2 und die ersten mPanIN-3-Läsionen zu diesem Zeitpunkt. Hingegen ging die Progression der präneoplastischen Läsionen in *Kras^{G12D};Stat3$^{\Delta panc}$* Mäusen nicht über das mPanIN-1 Stadium hinaus, was darauf hindeutet, dass die Stat3-Inaktivierung in der Bauchspeicheldrüse das Fortschreiten von mPanIN verhindert, nicht aber dessen Entstehung. In einem weiteren Schritt wurden zwei Mauskohorten (*Kras*^{G12D} und *Kras^{G12D};Stat3$^{\Delta panc}$*) über einen längeren Zeitraum beobachtet. Während 55% (11 von 20) der *Kras*^{G12D} Mäuse ein Pankreaskarzinom entwickelten, lag die Tumorinzidenz in der *Kras^{G12D};Stat3$^{\Delta panc}$* Gruppe hingegen nur bei 24,5% (10 von 41) der Fälle. Wir beobachteten im Folgenden auch, dass Stat3-defiziente Karzinome eine deutlich niedrigere Proliferationsrate aufwiesen. Histopathologische Analysen zeigten, dass weder *Kras^{G12D};Stat3$^{\Delta panc}$* primäre Tumore noch Metastasen p-Stat3^{Y705} exprimieren. Eine Stimulation von *Kras^{G12D};Stat3$^{\Delta panc}$* Karzinomzelllinien mit IL-6 führt zu keiner Stat3-Phosphorylierung.

Insgesamt deuten diese Daten darauf hin, dass epitheliales Stat3 für die Übertragung der tumorfördernden Signale von IL-6 erforderlich ist, insbesondere während der mPanIN-Progression zum Karzinom.

2.1.4 Homozygote Deletion von Socs3 beschleunigt die mPanIN-Progression und fördert die Entwicklung von PDAC.

In einem weiteren Teil unserer Untersuchungen ging es um die Frage, wie Stat3 die PanIN-Progression reguliert. Die Stat3-Aktivierung wird durch den endogenen

Rückkopplungsinhibitor Socs3, der die Stat3-Signalübertragung durch Bindung an gp130 hemmt, streng reguliert. *Kras*^{G12D} Mäuse exprimierten hohe Mengen an Socs3 mRNA. Socs3 war in Azinuszellen und mPanIN-Läsionen von *Kras*^{G12D} Mäusen nachweisbar. Um eine frühzeitige und anhaltende Aktivierung von p-Stat3^{Y705} im *Kras*^{G12D} Pankreas zu induzieren, haben wir eine mutierte Mauslinie generiert, der Socs3 spezifisch im Pankreas fehlte (62). Die homozygote Deletion von Socs3 in *Kras*^{G12D} Mäusen (*Kras*^{G12D}*;Socs3*$^{\Delta panc}$) führte bereits im Alter von vier Wochen zu einer verstärkten Phosphorylierung von Stat3^{Y705} im Pankreas. In diesem Alter entwickelten *Kras*^{G12D}*;Socs3*$^{\Delta panc}$ Mäuse große Bereiche reaktiver Gänge sowie niedrig- und hoch-gradige mPanINs im gesamten Pankreas. Um festzustellen, ob die Deletion von Socs3 und eine anhaltende Aktivierung von Stat3 die Entwicklung von PDAC beeinflusst, haben wir 41 *Kras*^{G12D}*;Socs3*$^{\Delta panc}$ Mäuse fast ein Jahr lang beobachtet. Die Kombination aus aktiviertem *Kras*^{G12D} und der Deletion von Socs3 führte zu einer deutlichen Abnahme des Mauskörper- und Pankreasgewichts. Des Weiteren war das mediane Gesamtüberleben dieser Tiere signifikant kürzer als das von regulären *Kras*^{G12D} Mäusen ($p < 0{,}0001$ für die *Kras*^{G12D}*;Socs3*$^{\Delta panc}$ Kohorte im Vergleich zur *Kras*^{G12D} Gruppe). 37,5 % (12/32) der *Kras*^{G12D}*;Socs3*$^{\Delta panc}$ Mäuse entwickelten PDAC.

Zusammenfassend legen diese Daten nahe, dass der Phosphorylierungsgrad von Stat3 die Progression von mPanIN-Läsionen zum PDAC bestimmt.

2.1.5 Evidenz für die Existenz der IL-6/Stat3 Kaskade in humanen Pankreaskarzinomen

Um die Relevanz der IL-6/Stat3 Kaskade für den Menschen zu überprüfen, haben wir humane Pankreaskarzinome auf die Phosphorylierung von Stat3 getestet. Karzinomstrukturen, tumornahe azinäre Zellen und humane PanIN-Läsionen (hPanIN) wiesen phosphoryliertes Stat3^{Y705} auf. Mit Hilfe weiterer immunhistochemischer Analyse konnten wir feststellen, dass ein essentieller Bestandteil des Microenvironment in humanen Pankreaskarzinomen und in tumornahen Arealen infiltrierende CD68-positive Makrophagen sind, während die Anzahl der CD3-positiven Lymphozyten eher gering war. Eine Immunfluoreszenzfärbung belegte überdies, dass CD68-positive Makrophagen die Hauptquelle für die IL-6-Produktion im Pankreaskarzinom ausmachen.

Unsere Analysen an humanen Proben zeigten, dass die IL-6/Stat3 Achse zwischen Makrophagen und präneoplastischen Läsionen im Pankreas auch bei Menschen besteht und möglicherweise einen Mechanismus der pankreatischen Onkogenese definiert (Abbildung 1).

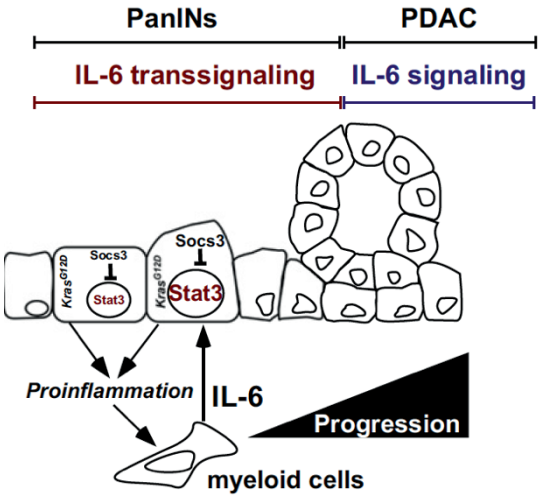

Abbildung 1: Schema der zentralen Rolle von Stat3 bei der PanIN-Progression und der Entwicklung von PDAC.

2.1.6 Zusammenfassung

In der vorliegenden Studie haben wir einen wichtigen Mechanismus identifiziert, der bei der Entstehung und Progression des Pankreaskarzinoms essenziell ist. Die *Kras*^{G12D}-induzierte pankreatische Onkogenese hängt von der Mikroumgebung ab, in der myeloide Zellen IL-6 sezernieren. Das freigesetzte IL-6 führt zur Stat3-Aktivierung über das IL-6 Transsignalling und beschleunigt die Progression von präneoplastischen Läsionen zum duktalen Pankreaskarzinom. Anhand von Patientendaten und menschlichen PDAC-Proben konnten wir zeigen, dass diese Verbindung auch bei der menschlichen Erkrankung besteht.

2.2 Rolle von RelA/p65 in der Karzinomentwicklung des Pankreas

RelA regulates CXCL1/CXCR2-dependent oncogene-induced senescence in murine Kras-driven pancreatic carcinogenesis
Lesina M., … Algül H. (2016). *The Journal of clinical investigation* 126, 2919-2932.

Dieses Projekt hat wesentlich dazu beigetragen, das Verständnis der Funktion des NF-κB/Rel Signalwegs in der pankreatischen Onkogenese zu vertiefen. Unsere Ergebnisse belegen eine wichtige Funktion des RelA in der Regulation von „Seneszenz-assoziiertem sekretorischem Phänotyp“ (SASP) während der Progression von präneoplastischen Läsionen zum Karzinom. Das RelA scheint für eine Induktion von onkogen-induzierter Seneszenz (OIS) essentiell zu sein. In den frühen Stadien der pankreatischen Karzinogenese hemmt RelA die PanIN-Progression durch die Regulation von SASP und die Induktion von OIS über den CXCR2 Rezeptor. In den späteren Stadien, wenn OIS überwunden wird, wirkt die Aktivierung von RelA tumorfördernd. Zusammengenommen demonstrieren unsere Daten, dass RelA eine duale Rolle in der pankreatischen Karzinomentwicklung spielt.

2.2.1 Die Pankreas-spezifische Inaktivierung von RelA beschleunigt die Pankreaskarzinomentwicklung.

Grundlage für unsere Untersuchungen war das *Kras*^{G12D}-induzierte Mausmodell der pankreatischen Karzinogenese. In unseren Vorarbeiten konnten wir die NF-κB Aktivierung in mPanINs und in benachbarten Azini im Pankreas nachweisen. Ausgehend von dieser Beobachtung haben wir genetisch basierte Analysen zur Funktion des klassischen NF-κB Signalwegs durchgeführt. Dazu haben wir eine Mauslinie generiert, in der neben der Expression des mutierten *Kras*^{G12D} Onkogens zusätzlich die aktive Untereinheit RelA Pankreas-spezifisch deletiert wurde (*Kras;RelA*).

Zur Überprüfung des Einflusses des RelA auf die Pankreaskarzinomentwicklung wurden zwei Gruppen (*Kras* und *Kras;RelA*) über die Zeitachse genauer beobachtet. Entgegen den bisherigen Erwartungen war das mediane Überleben der *Kras;RelA* Mäuse signifikant verkürzt und lag bei 378 Tagen im Vergleich zu 459 Tagen in der *Kras* Mauslinie. *Kras;RelA* Mäuse entwickelten dabei Pankreaskarzinome deutlich früher (350 Tage vs. 443 Tage). Die Tumorinzidenz in der *Kras;RelA* Gruppe lag bei 87,9%, in der *Kras* Linie hingegen bei 56,5% der Fälle. Bei 92% der Mäuse in der *Kras* Mauslinie und bei 93% in der *Kras;RelA* Mauslinie wurden gut bis mäßig differenzierte duktale Adenokarzinome dokumentiert. Es konnte kein Unterschied in der Metastasierungsrate zwischen den beiden Mausgruppen beobachtet werden. Die Tumore in der *Kras;RelA* Mauslinie waren histologisch von denen in der *Kras*

Mauslinie nicht zu unterscheiden. Erstaunlicherweise zeigte die Proliferationsanalyse, dass die Proliferation sowohl in den etablierten *Kras;RelA* Pankreaskarzinomen als auch in den aus primären Tumoren isolierten Karzinomzelllinien signifikant niedriger ist, als in der *Kras* Kohorte.

Mit diesen Daten konnte gezeigt werden, dass die Pankreas-spezifische Inaktivierung von des RelA entgegen den bisherigen Erwartungen die Pankreaskarzinomentstehung beschleunigt, obwohl die Proliferation von RelA-defizienten Karzinomzellen signifikant niedriger ist.

2.2.2 Die Pankreas-spezifische Inaktivierung von RelA beschleunigt die mPanIN-Progression – RelA als Tumorsuppressor.

Um den Einfluss der gewebespezifischen Deletion von RelA auf die Progression der mPanIN-Läsionen und das Überleben zu untersuchen, wurden *Kras* und *Kras;RelA* Mauslinien zu verschiedenen Zeitpunkten analysiert. Interessanterweise entwickelten dabei *Kras;RelA* Mäuse bereits nach 13 Wochen ein deutlich vergrößertes fibrotisches Pankreas. Weitere morphologische Analysen zeigten zudem eine rapide Progression der mPanIN-Läsionen. Während die 13 Wochen alten *Kras* Mäuse neben reaktiven Gängen einzelne mPanIN-1-Läsionen entwickelt haben, zeigte die *Kras;RelA* Mauslinie bereits zu diesem Zeitpunkt fortgeschrittene mPanIN-2 und sogar mPanIN-3-Läsionen in einem zunehmend fibrotisch-umgebauten Pankreas. Erstaunlicherweise entwickelten *Kras;RelA* Mäuse bereits nach 18 Wochen fokale Pankreaskarzinome. Bemerkenswert ist, dass die Signalwege, die für die azinär-duktale Metaplasie (ADM) und die mPanIN-Progression relevant sind (Phosphorylierung von ERK1/2 (*Extracellular Signal-Regulated Kinases*), STAT3 und c-Jun (*Transcription Factor Jun*)), in *Kras;RelA* mPanIN-Läsionen hochreguliert waren.

Diese Daten zeigen, dass die Inaktivierung von RelA in *Kras* Mäusen die pankreatische Karzinogenese beschleunigt. Der klassische NF-κB/RelA-Signalweg scheint die ADM und die mPanIN-Progression zu hemmen und möglicherweise eine spezifische Tumorsuppressor-Funktion in der Frühphase auszuüben.

2.2.3 Genomweite Analysen von Pankreata RelA-defizienter Kras Mauslinie

Im nächsten Schritt haben wir genomweite Analysen in 7 Tagen alten *Kras* und *Kras;RelA* Mäusen vorgenommen, um die Mechanismen, die die pankreatische Karzinogenese in *Kras;RelA* Mäusen fördern, weiter aufzuklären. 35 Gensets in *Kras;RelA* Pankreata waren im Vergleich zu *Kras* Pankreata hochreguliert. ***G**ene-**S**et-**E**nrichment-**A**nalysis* (GSEA) der

mRNA-Expressionsprofile muriner Pankreata zeigte eine signifikante Anreicherung NF-κB kontrollierter Gene in *Kras* Gewebe, die in den RelA-defizienten *Kras* Mäusen nicht erkennbar sind. Interessanterweise zeigten GSEA-Analysen einen wesentlichen Unterschied in einer sogenannten SASP-Signatur. Unter dem Begriff „Seneszenz-assoziierter sekretorischer Phänotyp“ (SASP) versteht man eine Ansammlung zahlreicher Chemokine und Zytokine, die von seneszenten Zellen sezerniert werden. Diese SASP-Faktoren sind in ihrer Gesamtheit für die Induktion und Aufrechterhaltung der onkogen-induzierten Seneszenz (OIS) wichtig. Die Arrayanalysen zeigen, dass die SASP-Aktivierung offensichtlich mit der nukleären Lokalisation von RelA zusammenhängt. In der Tat sind einige der Faktoren vom NF-κB Signalweg abhängig. Darüber hinaus enthalten signifikant hochregulierten Gengruppen in *Kras;RelA* Pankreas Gene, die für die Zellstress und Zelldifferenzierung relevant sind.

Um den Einfluss der gewebespezifischen Inaktivierung des RelA auf die Transdifferenzierung in Pankreas genauer analysieren zu können, wurde die azinär-duktale Umwandlung *in vitro* rekapituliert. Im Rahmen dieser Arbeit wurden die Techniken der Isolation pankreatischer azinärer Zellen und der Kultivierung dieser Zellen in einer Kollagenmatrix etabliert. Azinäre Zellen wurden von 5 Wochen alten gefloxten RelA ($RelA^{wt}$) und RelA-defizienten ($RelA^{\Delta}$) Mäusen isoliert. Frisch isolierte Azini wurden in Kollagenmatrix mit 50ng/ml rhTGFα 5 Tage behandelt. Als Kontrolle dienten unbehandelte Azini von beiden Mauslinien. Um die metaplastischen Strukturen charakterisieren zu können, wurde eine Immunfluoreszenzdoppelfärbung mit den azinus-spezifischen α-Amylase und duktal-spezifischen CK-19 Markern durchgeführt. Bei der Quantifizierung der duktalen Strukturen nach einer 5-tägigen Behandlung mit rhTGFα wurde deutlich, dass beide Zelllinien metaplastische Veränderungen aufwiesen, aber die Anzahl der duktalen Strukturen in $RelA^{\Delta}$ (40,9 % ± 3,7 %) ist höher als im $RelA^{wt}$ (24,2 % ± 7,2 %). Um die azinär-duktale Umwandlung in $RelA^{wt}$ und $RelA^{\Delta}$ Azinuszellen in einem onkogenen Kras-Hintergrund zu analysieren, isolierten wir Azinuszellen aus *Kras* und *Kras;RelA* Pankreata zu einem frühen Zeitpunkt, um eine maximale Menge an exokrinem Gewebe zu erhalten. Nach 5-tägiger Behandlung mit rhTGFα wurde bei 59,02 % ± 0,14 % der $RelA^{\Delta}$ Azinusexplantate eine duktale Morphologie beobachtet. Im Gegensatz dazu transdifferenzierten nur 30,26 % ± 0,09 % der Azinusexplantate aus *Kras* Pankreas.

Diese Ergebnisse zeigen eine protektive Wirkung von RelA beim Zellstress und im Prozess der Transdifferenzierung. Darüber hinaus suggerieren diese Ergebnisse einen Zusammenhang der Onkogen-induzierten Seneszenz mit der Aktivierung von RelA.

2.2.4 Die Onkogen-induzierte Seneszenz erfordert die Aktivierung von RelA.

Da die Progression der *Kras*-induzierten Onkogenese durch die Onkogen-induzierte Seneszenz (OIS) kontrolliert wird (63), gingen wir der Frage nach, welchen Einfluss die Aktivierung von RelA auf die Induktion von OIS tatsächlich besitzt. Typischerweise exprimieren seneszente Zellen lysosomale β-Galactosidase (64). Unsere Analysen zeigen, dass die Anzahl der SA-β-Gal (zuverlässiger Marker für seneszente Zellen) positiven mPanIN-Zellen signifikant niedriger in den *Kras;RelA* Pankreata war im Vergleich zu *Kras* Gewebe. Darüber hinaus haben immunhistochemische, proteinbiochemische, sowie transkriptionelle Analysen gezeigt, dass eine Reihe von Seneszenz-assoziierten Markern (DCR2 (*Decoy Receptor 2*), Dec1 (*Deleted in Esophageal Cancer 1*), p16, p19, p21, p53) in *Kras;RelA* Pankreata runterreguliert sind.

Diese Ergebnisse legen eine Assoziation der onkogen-induzierten Seneszenz mit der Aktivierung von RelA in der pankreatischen Karzinogenese nahe.

2.2.5 Die Aktivierung des RelA induziert OIS über CXCL1/KC.

Unsere Analysen haben gezeigt, dass die niedrig-gradigen mPanIN-Läsionen *in vivo* SA-β-Gal Aktivität aufweisen. Es ist jedoch unklar, ob dies RelA einen zellautonomen oder nicht-zellautonomen Effekt reguliert. Deswegen haben wir $Kras^{G12D}$-exprimierende duktale Zellen (PDEC *Kras*) aus dem Pankreas der *Kras* Mäuse isoliert und auf Kollagen-Gel kultiviert. Die Behandlung dieser PDEC *Kras* mit einem spezifischen NF-κB Inhibitor (JSH-23), der eine nukleäre Translokation vom RelA blockiert (65), führte zu einer deutlichen Reduktion der SA-β-Gal Aktivität. Um zu untersuchen, welche Rolle das RelA in der Sekretion von SASP-Faktoren bei PDEC *Kras* spielt. Dazu wurde das Medium von PDEC *Kras* und PDEC *Kras*/JSH-23 gesammelt und mittels *Cytokine Array* analysiert. Diese Analyse zeigte eine signifikant-reduzierte Sezernierung von G-CSF (*Granulocyte Colony-Stimulating Factor*), GM-CSF (*Granulocyte-macrophage colony-stimulating factor*), sICAM-1 (*Soluble Intercellular Adhesion Molecule 1*), CCL-5 (*Chemokine (C-C motif) Ligand 5*), TIMP-1 (*Tissue Inhibitor of Metalloproteinases 1*) und TNF-α (*Tumor Necrosis Factor alpha*) in PDEC *Kras*/JSH-23 Proben. Unter 40 getesteten Botenstoffen ist die Sekretion von CXCL1/KC in PDEC *Kras*/JSH-23 Proben am stärksten reduziert. Die Inkubation der PDEC *Kras* mit CXCL1/KC (100ng/ml) führte zu einer deutlichen Induktion der SA-β-Gal Aktivität.

Unsere Daten belegen, dass CXCL1/KC RelA-abhängig produziert wird und in $Kras^{G12D}$-exprimierenden duktalen Zellen OIS *in vitro* induzieren kann.

2.2.6 Einfluss der Hemmung der CXCL1/KC/CXCR2 Achse auf OIS und mPanIN-Progression

CXCL1/KC vermittelt seine Funktionen über den G-Protein-gekoppelten Chemokinrezeptor CXCR2, der in mPanIN-Läsionen exprimiert wird. Im Folgenden wurde der Frage nachgegangen, ob die CXCL1/KC/CXCR2 Achse in der OIS und mPanIN-Progression eine Rolle spielt. Hierfür haben wir eine pharmakologische und genetische Inaktivierung von CXCR2 im *Kras* Modell durchgeführt. 5 Wochen alte *Kras* Mäuse wurden mit dem CXCR2 Inhibitor SB225002 behandelt. Diese Analyse zeigte, dass die pharmakologische Inhibition von CXCR2 zu einer signifikanten Reduktion der Anzahl der SA-β-Gal-positiven mPanIN-Zellen in *Kras* Mäusen führt. Darüber hinaus konnten wir die zunehmende Anzahl und Progression der mPanIN-Läsionen in behandelten *Kras* Mäusen registrieren. Für eine genetische Inaktivierung von CXCR2 wurde eine *LSL-Kras^{G12D};Pdx1-Cre* Mauslinie mit einer gefloxten CXCR2 Mauslinie gekreuzt (**Kras CXCR2*). In diesen Mäusen konnte eine signifikante Reduktion der Anzahl der SA-β-Gal-positiven mPanIN-Zellen und die zunehmende Anzahl und Progression der mPanIN-Läsionen in **Kras CXCR2* Pankreata beobachtet werden.

Zusammenfassend legen diese Daten nahe, dass sowohl die pharmakologische als auch genetisch vermittelte CXCR2-Inaktivierung OIS und mPanIN-Progression beeinflusst.

2.2.7 Rolle von RelA in der pankreatischen Karzinogenese im Kontext von p53 und p16

Nach den bisherigen Erkenntnissen wird OIS vornehmlich durch den Tumorsuppressor p53, aber auch p16, nicht nur induziert, sondern auch erhalten (66, 67). Da durch ein Funktionsverlust von p53 oder p16 OIS überwunden werden kann, haben wir den Einfluss von RelA auf die pankreatische Karzinogenese in diesem Kontext untersucht. Daher generierten wir weitere Mauslinien: 1. mit Pankreas-spezifischer Deletion von *Trp53* in *Kras* (*Kras;Trp53*) und in *Kras;RelA* (*Kras;RelA;Trp53*) Mäusen; 2. mit Pankreas-spezifischer Deletion von *p16* in *Kras* (*Kras;p16*) und in *Kras;RelA* (*Kras;RelA;p16*) Mäusen.

Wir beobachteten Maus-Kohorten über einen längeren Zeitraum und registrierten das Überleben dieser Mäuse. Erstaunlicherweise zeigten diese Überlebensanalysen, dass die RelA-defizienten *Kras;RelA;Trp53* und *Kras;RelA;p16* Mäuse deutlich länger leben als die entsprechenden Vergleichsgruppen *Kras;Trp53* und *Kras;p16*. Diese Analysen suggerieren im Gegensatz zu den Ergebnissen aus dem *Kras* Modell eine tumorfördernde Wirkung von RelA.

2.2.8 Zusammenfassung

Zusammengenommen demonstrieren unsere Daten, dass das RelA die Karzinomentwicklung im Pankreas über einen zweistufigen Mechanismus beeinflusst. In den frühen Stadien der pankreatischen Karzinogenese hemmt das RelA die PanIN-Progression durch die Regulation von SASP und die Induktion von OIS über den CXCR2 Rezeptor. In den späteren Stadien, wenn OIS überwunden wird, wirkt die Aktivierung vom RelA tumorfördernd (Abbildung 2).

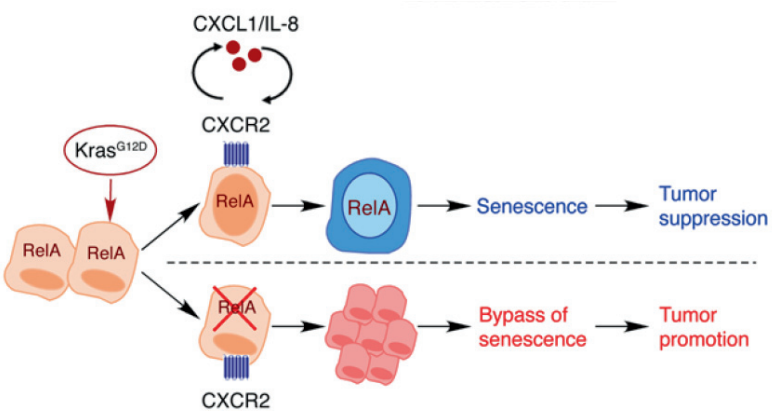

Abbildung 2: RelA beeinflusst die Karzinomentwicklung im Pankreas über einen zweistufigen Mechanismus.

2.3 Rolle der Autophagie bei der Entstehung und Progression von PDAC

Levels of the Autophagy-Related 5 Protein Affect Progression and Metastasis of Pancreatic Tumors in Mice
Görgülü K., Diakopoulos K. N., …. **Lesina M.***, and Algül H.* (2019). Gastroenterology *156*, 203-217 e220.
* Equally contributed

In der vorliegenden Studie beschreiben wir die gegensätzlichen Funktionen, die unterschiedliche Atg5-Spiegel während der Pankreaskarzinogenese haben. Mit Hilfe etablierter *in vitro* und *in vivo* Modelle für die Pankreaskarzinogenese konnte gezeigt werden, dass die Stadien der Pankreaskarzinogenese entscheidend von den Atg5-Spiegeln abhängen.

2.3.1 Monoallelischer Atg5-Verlust beeinflusst die Metastasierungsrate.

Der Autophagie-Prozess kann in der Bauchspeicheldrüse anhand von GFP (*Green Fluorescent Protein*) - LC3-positiven Autophagosomen unter Zuhilfenahme *GFP-LC3*-transgener Mäuse visualisiert werden. Im normalen Pankreas können Autophagosomen vereinzelt nachgewiesen werden, diese nehmen jedoch im Zuge der pankreatischen Karzinogenese zu. Dabei sind Autophagosomen in azinär-duktalen Metaplasien (ADM), in präneoplastischen Läsionen (PanIN) sowie in Pankreastumoren und Lebermetastasen von *GFP-LC3;Kras*-Mäusen nachweisbar. Darüber hinaus sind Zellen, die aus Pankreastumoren und ihren Metastasen isoliert wurden, positiv für GFP-LC3-Autophagosomen. Interessanterweise fehlen GFP-LC3-positive Puncta in PanIN-angrenzenden normalen Azinuszellen, obwohl sie die onkogene $Kras^{G12D}$-Mutation tragen. Bei vollständigem Verlust von Atg5 ist jedoch nur eine diffuse Färbung sichtbar. Damit konnten wir zeigen, dass die Autophagie in jedem Stadium der pankreatischen Karzinogenese und Metastasierung vorhanden ist.

Um die Rolle der Autophagie während der pankreatischen Karzinogenese aufzuklären, generierten wir Mäuse mit homozygoter (*A5;Kras*) und heterozygoter (*A5+/–;Kras*) Deletion von *Atg5* und verglichen diese mit Autophagie-kompetenten *Kras*-Mäusen. Während *A5;Kras*-Mäuse erst im Alter von 9 Wochen nur niedrig-gradige PanIN-1-Läsionen entwickeln, aber keine Karzinome, führte überraschenderweise der monoallelische Verlust von *Atg5* zu einer signifikanten Erhöhung der Tumor- und Metastasierungsinzidenz.

Diese überraschende Beobachtung *in vivo* legte nahe, dass anders als der biallelische Verlust, die monoallelische Deletion des Autophagie-relevanten Gens Atg5 das Metastasierungspotential des Pankreaskarzinoms beeinflusst.

2.3.2 Die Autophagie ist nach monoallelischem Verlust von Atg5 konstitutiv aktiv und beeinflusst das Überleben in vitro.

Im nächsten Schritt haben wir untersucht, wie der monoallelische Atg5-Verlust den Autophagie-Prozess beeinflusst. Da der Autophagiefluss *in vitro* leicht analysiert werden kann, isolierten wir primäre Pankreaskarzinomzellen aus *Kras*- und *A5+/-;Kras*-Mäusen. Obwohl kein Unterschied im Autophagiefluss (gemessen an der Expression der Proteine p62 und LC3 I/II) *in vitro* und *in vivo* zwischen *Kras* und *A5+/-;Kras* festgestellt werden konnte, wurde die Autophagie-Regulation in Karzinomzellen nach Behandlung mit Autophagie-Aktivatoren oder -Inhibitoren beeinflusst. Nach der Behandlung mit HBSS, einem bekannten Auslöser der Autophagie, reduziert sich die Koloniezahl in *Kras*-Zellen deutlich. Die Koloniebildung in *A5+/-;Kras*-Zellen war hingegen nicht beeinträchtigt. Die Behandlung unter Hungerbedingungen (kein FCS im Medium) mit Chloroquin, einem Hemmer des Prozesses der Autophagie, führte zu einer deutlichen Akkumulation von LC3-II in *Kras*-Zellen im Vergleich zu *A5+/-;Kras*-Zellen. Die Hemmung des Autophagieflusses wurde durch erhöhte p62-Level in beiden Zelllinien bestätigt. Darüber hinaus beeinträchtigte eine Behandlung mit Chloroquin die Koloniebildung nur in *Kras*-Zellen signifikant. Schließlich zeigte die Quantifizierung von Autophagosomen unter Hungerbedingungen nur in *Kras*-Zellen einen Anstieg. Bemerkenswert ist, dass kein Unterschied in der Koloniebildungsfähigkeit von *Kras*- und *A5+/-;Kras*-Zellen nach der Behandlung mit verschiedenen Stoffwechselregulatoren (10 % FCS, 6-AA, Rotenon, Galaktose/Glutamin, hohe Glukose) festgestellt werden konnte.

Diese Ergebnisse legen nahe, dass der monoallelische Verlust von Atg5 und reduzierte Atg5-Proteinslevel aufgrund von spezifischen Veränderungen in der Autophagie-Regulierung zu einer Resistenz von *A5+/-;Kras*-Zelllinien gegenüber Standard-Autophagie-Stimulation und -Inhibition führen.

2.3.3 Monoallelischer Verlust von Atg5 erhöht die metastatischen Eigenschaften von Krebszellen in vitro und in vivo.

Da *A5+/-;Kras*-Mäuse eine höhere Tumor- und Metastasierungsinzidenz aufwiesen, sollten in weiteren Experimenten die Auswirkungen des Atg5-monoallelischen Verlusts auf die Tumor- und Metastasierungsbildung genauer analysiert werden. *In vitro* Experimente mit *Kras*- und

A5+/-;Kras-Zellen ergaben eine signifikant erhöhte Resistenz gegenüber Anoikis-Bildung, eine erhöhte Migration, Invasion und Zellausbreitung in *A5+/-;Kras*-Zellen, die in ihrer Gesamtheit die Metastasierungsfähigkeit von Tumorzellen beeinflussen. Die Bildung von Filopodien, Indikatoren für die Zellausbreitung, war ebenfalls in *A5+/–;Kras*-Zellen deutlich nachweisbar, während *Kras*-Zellen nur kleine Ausstülpungen aufwiesen.

Nach orthotoper Transplantation konnte kein Unterschied in der Tumorbildung bei Kras- und *A5+/-;Kras*-Zelllinien festgestellt werden. Die Metastasierungshäufigkeit und -ausdehnung (Lymphknoten, Leber, Lunge und Milz) war jedoch in *A5+/-;Kras*-Zellen signifikant erhöht. Auch in einem zweiten Modell bildeten sich nach der Injektion von *A5+/-;Kras*-Zellen in die Schwanzvene von Wildtyp-Mäusen signifikant mehr Lungentumore als bei *Kras*-Zellen. Das Körpergewicht der Mäuse als Indikator für Kachexie und Tumoraggressivität war nach der Injektion von *A5+/-;Kras*-Zellen ebenfalls reduziert. Zusätzlich zur Bildung von Lungentumoren wiesen einige Mäuse Leber- und Milzmetastasen auf, was auf eine höhere Aggressivität der Pankreastumorzellen nach monoallelischem Verlust von Atg5 hindeutet. Die Proliferation von Lungentumoren sowie die *in vitro* Proliferation von *A5+/-;Kras*-Zelllinien nach Re-Isolierung aus Lungentumoren war ebenfalls erhöht.

Um den Zusammenhang zwischen der Atg5-Expression und PDAC-Malignität aufzuklären, haben wir Atg5 in *Kras*-Zelllinien unter Verwendung von shRNAs mit verschiedener Knockdown-Effizienz (54%, 58%, 81%, 86% und 94%) ausgeschaltet. Da der 58% Atg5-Knock-down der Situation nach monoallelischem Verlust von Atg5 am nächsten kommt, haben wir weitere Analysen mit diesen Zellen durchgeführt. Als interne Kontrolle wurden 94% Atg5-Knockdown-Zellen verwendet. Wichtig ist, dass der Knock-down von Atg5 sowohl um 58% als auch um 94% die Migration und Invasion *in vitro* sowie die Lungenmetastasierung *in vivo* signifikant erhöhte.

Daher deuten die Daten darauf hin, dass der monoallelische Verlust von Atg5 bzw. die shRNA-vermittelte Atg5-Dosisreduktion die Metastasierungskapazität und die Aggressivität von Zellen *in vitro* und *in vivo* erhöhen.

2.3.4 Monoallelischer Verlust von Atg5 reduziert die mitochondriale Funktionalität.

Um weitere Erkenntnisse über die Auswirkungen des monoallelischen Atg5-Verlusts auf den Stoffwechsel zu erhalten, führten wir eine Reihe von Experimenten im Zusammenhang mit mitochondrialer Funktionalität und Zellstress durch. Elektronenmikroskopische Analysen zeigten Veränderungen in der Morphologie der Mitochondrien, insbesondere im Bereich der

„mitochondrial fission“ und „cristae stacking“. Proteinexpressionsanalysen (COX II/IV (*Cytochrome C Oxidase Complex*), ATP Core 2, SOD2 (*Superoxide Dismutase 2*), BiP (*Binding Immunoglobulin Protein 1*)) deuten auf Veränderungen in der zellulären Homöostase und insbesondere in den Mitochondrien hin. Die mitochondriale Funktion wurde durch einen detaillierten Vergleich zur oxidativen und glykolytischen Kapazitäten in *Kras*- und *A5+/-;Kras*-Zelllinien weiter untersucht. Die oxidativen Fähigkeiten der Zelle waren gemessen an der zellulären, mitochondrialen Respirationsrate sowie der maximalen Substratoxidation zu Lasten der ATP-Produktion in Mitochondrien reduziert. Außerdem zeigten *A5+/-;Kras*-Zellen eine reduzierte Glykolyse, die sich an der verringerten Zellversauerungsrate, der maximalen glykolytischen Kapazität und Basislinien-Ansäuerungsrate dargestellt hat. Die mitochondriale Kopplungseffizienz wies keine signifikante Veränderung zwischen *Kras*- und *A5+/-;Kras*-Zellen auf.

Interessanterweise zeigten Zellfraktionierungsexperimente gemessen an der Glutamat-Dehydrogenase-Aktivität eine Verlagerung der mitochondrialen Fraktion. Dabei scheinen Mitochondrien in autophagosomalen Fraktionen zu akkumulieren, was auf eine Beeinträchtigung der Mitochondrien hinweist. Entsprechend war die mRNA-Expression von Nrf1 (*Nuclear Respiratory Factor 1***)** und mitochondrialem Sod2 erhöht, was einen erhöhten mitochondrialen Stress bestätigte; Nrf2 (*Nuclear Respiratory Factor 2***)** und zytosolisches Sod1 (*Superoxide Dismutase 1*), blieben unverändert.

Zusammenfassend lässt sich sagen, dass der monoallelische Verlust von Atg5 die zelluläre Homöostase durch eine Beeinträchtigung der mitochondrialen Morphologie und Funktion beeinflusst.

2.3.5 Der Atg5-Spiegel beeinflusst den intrazellulären Ca^{2+}-Fluss und die extrazelluläre Cathepsin-Aktivität.

Mitochondrien spielen eine wichtige Rolle in der Regulation des intrazellulären Ca^{2+}-Spiegels und sind daher eng mit Ca^{2+}-Fluktuationen assoziiert. Der Ca^{2+}-Spiegel ist in der Regulation verschiedener Prozesse involviert, wie z.B. bei der mitochondrialen Funktion/Morphologie, der Genregulation, dem Vesikeltransport, der Zellmigration und der Bildung von Lamellipodien an der Migrationsfront (68-71). Daher untersuchten wir die zelluläre Ca^{2+}-Antwort. *A5+/-;Kras*-Zellen zeigten dabei unter verschiedenen Bedingungen (0,01 % oder 0.05 % FCS) signifikant höhere Ca^{2+}-Amplituden als *Kras*-Zellen. Auch die Expression des S100a4, eines Ca2+-bindenden Proteins, das mit einer erhöhten Metastasierungsfähigkeit in Verbindung gebracht

wird, war sowohl in *A5+/-;Kras* Tumoren als auch in höhergradigen PanIN-Läsionen stark erhöht.

Das „Trafficking“ von Lysosomen und deren Exozytose werden auch durch intrazelluläre Ca2+-Fluktuationen reguliert (72). Daher untersuchten wir im nächsten Schritt die Lysosomenaktivität im Zellkulturüberstand. Eine signifikant höhere Aktivität von Cathepsin L und Cathepsin D konnte in *A5+/-;Kras*-Zellen nachgewiesen werden; Cathepsin B war nicht betroffen. Darüber hinaus haben wir die Rolle der extrazellulären Cathepsin-Aktivität in der Zellausbreitung und -invasion untersucht. Dazu behandelten wir *Kras*- und *A5+/-;Kras*-Zellen mit dem Cathepsin-Inhibitor E64d und quantifizierten die Anzahl der Filopodien sowie die Zellinvasion. Während sich die Anzahl der von *Kras*- und *A5+/-;Kras*-Zellen gebildeten Kolonien nach der E64d-Behandlung nicht veränderte, waren die Invasionsfähigkeiten der *A5+/-;Kras*-Zellen deutlich reduziert. Bemerkenswert ist, dass E64d keinen Einfluss auf die Filopodienbildung und die Invasionsfähigkeit von *Kras*-Zellen hatte.

Zusammenfassend führt die monoallelische Atg5-Deletion zu einer verstärkten extrazellulären lysosomalen Aktivität, die mit der gesteigerten Invasivität der Krebszellen assoziiert ist. Dies ist vermutlich eine weitere Erklärung für die höhere Metastasierungsinzidenz, die in *A5+/;Kras*-Mäusen beobachtet wurde.

2.3.6 Die ATG5-Expression korreliert mit der Aggressivität des menschlichen Bauchspeicheldrüsenkrebses.

Um die Relevanz unserer Erkenntnisse aus den Mausmodellen für die Erkrankung bei Menschen zu analysieren, untersuchten wir die Expression von ATG5-Protein in 3 unabhängigen Patientenkohorten. Die ATG5-ATG12-Proteinexpression in Lysaten von Pankreastumorpatienten (Kohorte 1) unterschied sich innerhalb der Proben. Die Einteilung der Patienten in eine Gruppe mit hoher ATG5-Expression und eine Gruppe mit niedriger bis moderater ATG5-Expression zeigte einen Trend zu einem reduzierten Überleben in der Gruppe mit niedriger bis moderater ATG5-Expression. Aufgrund der Unterschiede in der Tumorzellularität und der Limitationen eines Western Blots führten wir eine ATG5-Immunhistochemie durch (Kohorten 2 und 3). Wie erwartet und bereits beschrieben (ProteinAtlas), wird ATG5 nicht nur in den epithelialen Tumorstrukturen des Pankreas, sondern auch in anderen Zelltypen (z.B. Endothel- und Inselzellen) im Gewebe exprimiert. Nach Festlegung eines ATG5-Expressions-Scores (Score 1, Score 2 und Score 3), unterteilten wir die Patienten in folgende Gruppen: Patienten mit geringer (Score 1, Score 2) und hoher (Score 3) ATG5-Expression. Die Anwendung dieser Analyse auf eine kleine Kohorte von Patienten

mit Fernmetastasen (Kohorte 2) zeigte eine höhere Metastasierungsinzidenz bei den Patienten mit geringer ATG5-Expression. Darüber hinaus konnten wir in einer größeren Kohorte von Patienten, die sich einer Pankreaskarzinomresektion unterzogen (Kohorte 3), eine signifikante Korrelation zwischen einem reduzierten Überleben und einer geringeren ATG5-Expression feststellen.

Da Lymphknoten- und Resektionsstatus zwischen den Gruppen nicht unterschiedlich waren und wichtige Störfaktoren ausgeschlossen werden konnten, spiegeln diese Analysen mit hoher Wahrscheinlichkeit das Wiederauftreten von Metastasen und damit die Aggressivität der Tumoren wider. Schließlich identifizierte die Analyse aus dem Cancer Genome Atlas eine Verringerung der ATG5-Kopienzahlen zwischen humanen Bauchspeicheldrüsenkrebsproben und normaler Bauchspeicheldrüse.

Somit stehen niedrigere ATG5-Spiegel stehen also im Zusammenhang mit einer erhöhten Metastasierung von Bauchspeicheldrüsenkrebs und einem längeren Überleben der Patienten.

2.3.7 Zusammenfassung

Der vollständige Verlust von Atg5 in der Bauchspeicheldrüse während der Embryogenese beschleunigt die Tumorentstehung, blockiert aber die Tumorprogression, während der monoallelische Verlust die Tumorinzidenz und die Metastasierungsrate signifikant erhöht. Wichtig ist, dass die Deletion eines Atg5-Allels und die Verringerung der Atg5-Proteinkonzentration die Aggressivität von PDAC durch zellautonome und nicht-zellautonome Effekte erhöht, was insgesamt die Tumoraggressivität fördert. Unsere Ergebnisse liefern also nicht nur neue Erkenntnisse über die Rolle der Autophagie bei der Entstehung und Progression von PDAC, sondern zeigen auch, wie wichtig es ist, bei der Blockierung der Autophagie in der pankreatischen Karzinogenese Vorsicht walten zu lassen.

2.4 Wirksamkeit der Therapiekombination aus SHP2-Inhibitor und ERK-Inhibitor in PDAC-Mausmodellen

Extensive preclinical validation of combined RMC-4550 and LY3214996 supports clinical investigation for KRAS mutant pancreatic cancer
Frank KJ, Mulero-Sanchez A, Berninger A, Ruiz-Canas L, Bosma A, Gorgulu K, … **Lesina M*** and Mainardi S* *Cell Rep Med*. 2022 Nov 15;3(11):100815.
* Equally contributed

In einer früheren Studie konnten wir vielversprechende *in vitro* und *in vivo* Ergebnisse zeigen, die eine Hemmung der ubiquitär exprimierten Tyrosin-Phosphatase SHP2 (*Src Homology-2 Domain-Containing Protein Tyrosine Phosphatase-2*) in Kombination mit MEK (*Mitogen-Activated Extracellular Signal-Regulated Kinase*) als therapeutische Option beim Bauchspeicheldrüsenkrebs unterstützen (73, 74). Die häufig beobachteten Nebenwirkungen und die hohe Resistenzrate bei MEK-Inhibitoren wie Trametinib (75-77) haben uns jedoch dazu geführt, nach weiteren Optionen zu suchen. Da die Aktivierung von ERK (*Extracellular Signal-Regulated Kinase*) ein wichtiger Mechanismus ist, der die Wirksamkeit von MEK-Inhibitoren (MEKi) hemmt (75, 78, 79), stellten wir die Hypothese auf, dass die direkte ERK-Inhibition eine weitere Option sein könnte. Die Verwendung von ERK-Inhibitoren hat zwei Vorteile gegenüber den MEK-Inhibitoren. ERK-Inhibition ist besser verträglich und zeigte auch Wirkung in Kras-mutierten Tumoren, welche unter MEK-Inhibition refraktär waren (80). Der neu entwickelte ERK-Inhibitor LY3214996 (80) erwies sich als selektiver, wirksamer und reversibler A(80)TP-kompetitiver Inhibitor der ERK1/2-Aktivität in KRAS- und BRAF-mutierten Zelllinien. Parallel dazu wurde ein selektiver allosterischer SHP2-Inhibitor (RMC-4550) entwickelt, dessen Wirkungsweise mit der von SHP099 von Novartis vergleichbar ist, der jedoch eine etwas höhere Effektivität aufweist (81).
In der vorliegenden Studie validierten wir eine Strategie, indem die Inhibition des MEK-Downstream-Effektors ERK (LY3214996) mit der Hemmung von SHP2 (RMC-4550) *in vitro* und in mehreren *in vivo* PDAC-Modellen kombiniert wurde.

2.4.1 Kombinierte Behandlung von murinen und humanen KRAS-mutierten Pankreaskrebs-Zelllinien mit RMC-4550 (SHP2i) und LY3214996 (ERKi)

Unsere *in vitro* Analysen an murinen und humanen KRAS-mutierten PDAC-Zelllinien deuteten auf eine synergistische Wirkung von SHP2i und ERKi hin. Dabei wurden sowohl die Zellproliferation und die MAPK-Signalübertragung gehemmt als auch die Apoptose signifikant

induziert, was uns dazu veranlasste, die kombinierte Behandlung mit SHP2i und ERKi *in vivo* zu testen.

2.4.2 Bestimmung der maximal verträglichen Dosis (MTD) in vivo

Da eine Verwendung von SHP2i und ERKi in Kombination *in vivo* noch nicht untersucht wurde, führten wir eine Verträglichkeitsstudie an nicht tumortragenden Wildtyp- (*Kras*$^{LSL\text{-}G12D}$*;Trp53*$^{flox/flox}$ - kein Cre) und NOD-scid gamma (NSG)-Mäusen durch, um die maximal verträgliche Dosis (MTD) beider Inhibitoren in Kombination zu bestimmen. Die Inhibitoren wurden einmal täglich an 14 aufeinanderfolgenden Tagen den Versuchstieren per oral verabreicht. In Anlehnung an die Dosierungsempfehlungen von Eli Lilly und Revolution Medicines haben wir 9 verschiedene Dosen mit der Bezeichnung d1 (niedrigste) bis d9 (höchste) festgelegt und ein modifiziertes "3 + 3"-Studiendesign (82, 83) angewandt, das auf Kohorten von drei Tieren pro Dosis basiert. Die Dosis wurde bei jeder nachfolgenden Kohorte angehoben, bis eine vorgegebene Anzahl der Mäuse an einer dosislimitierenden Toxizität (DLT - Nebenwirkungen, die so schwer sind, dass die Dosis nicht weiter gesteigert werden kann) gelitten hat. Die Kriterien, die als Indikatoren für DLT verwendet wurden, waren Gewichtsverlust von mehr als 20 %, klinische Symptome wie abnormales Verhalten, Anzeichen von körperlichem Unwohlsein und Tod. Bei dieser Studie wurde eine Dosis (d8 = 10 mg/kg SHP2i + 100 mg/kg ERKi) ermittelt, die sowohl bei Wildtyp- als auch bei NSG-Mäusen gut verträglich war.

2.4.3 In vivo Untersuchung therapeutischer Wirksamkeit bei kombinierter Behandlung mit SHP2i und ERKi in einem orthotopen PDAC-Modell

Als nächstes untersuchten wir die potenzielle Anti-Tumor-Wirksamkeit der Behandlung mit der SHP2i + ERKi-Kombination *in vivo*. Zunächst haben wir ein PDAC-Modell mit orthotop transplantierten *Kras*^{G12D}*;Trp53*$^{R172H/+}$*;Pdx-1Cre*-Tumoren in immunkompetenten C57BL/6J-Mäusen (KCPmut) entwickelt. Nach der postoperativen Tumorexpansion über 2 Wochen wurden die Mäuse randomisiert und entweder der Kontrollkohorte (Vehikel), SHP2i-mono, ERKi-mono oder der SHP2i + ERKi - Kombination zugeordnet. Die Kontrollmäuse wurden vor der Therapie untersucht, um das Vorhandensein gut integrierter Tumoren zu bestätigen. Alle anderen Mäuse wurden 14 Tage lang täglich per oral behandelt. Eine signifikante Hemmung des Tumorwachstums, die makroskopisch zu erkennen war und sich im verringerten Tumorgewicht widerspiegelte, wurde sowohl in beiden Monotherapiegruppen als auch in der Kombinationsgruppe im Vergleich zur Kontrollkohorte beobachtet. Die Kombinationstherapie

war am wirksamsten und bewirkte eine signifikant stärkere Verringerung des Tumorvolumens als die SHP2i- oder ERKi-Monotherapien.

2.4.4 In vivo Analyse des optimalen Behandlungsregime im endogenen murinen PDAC-Modell und im präklinischen humanen PDX-Modell

Im Hinblick auf die künftige klinische Anwendung wollten wir das optimale Behandlungsregime bestimmen, das eine maximale Anti-Tumor-Wirkung bei minimaler Toxizität zeigt. Für diese Untersuchung wurden folgende Therapieregimen angesetzt: kontinuierliche tägliche Applikation beider Medikamente in Kombination sowie drei verschiedene nicht-kontinuierliche Applikationsregime. Wir testeten diese Schemata im endogenen (*Kras*$^{LSL\text{-}G12D}$*;Trp53*$^{flox/flox}$*;Ptf1a-Cre*^{ex1}) (KCP) Mausmodell mit spontaner Tumorentwicklung und im aus Patientenmaterial abgeleiteten Xenograft-Modell (PDX - „*patient-derived xenograft*“). Keines der getesteten Schemata war mit dosis- oder schema-limitierender Toxizität verbunden. Das endogene KCP-Modell zeigte, dass die Kombinationsbehandlung in der Lage war, das Tumorwachstum deutlich zu hemmen und sogar eine Verringerung des Pankreasvolumens zu bewirken. Bemerkenswert ist, dass die kontinuierliche Behandlung das Volumen der Bauchspeicheldrüse um mehr als 30 % reduzieren konnte, wenn die Maus früh genug behandelt wurde. Dies zeigte sich in der morphologischen Analyse, dem relativen Gewicht der Bauchspeicheldrüse und der Anzahl intakter Azini im Vergleich zur Kontrollgruppe.
Im PDX-Modell konnte bestätigt werden, dass alle getesteten Kombinationstherapien in der Lage waren, das Tumorwachstum deutlich zu reduzieren und sogar eine Verringerung des Tumorvolumens zu bewirken. Obwohl es keinen statistisch signifikanten Unterschied zwischen den drei Behandlungsarmen gab, zeigten die Daten einen Vorteil der kontinuierlichen Behandlung im Vergleich zu den intermittierenden Schemata. Interessanterweise wiesen alle Tumore von Mäusen, die die Kombinationsbehandlungen erhielten, lytische nekrotische Tumorbereiche auf, was darauf hindeutet, dass die Tumorzellen zusätzlich zu den beobachteten zytostatischen Wirkungen eliminiert wurden.

2.4.5 Untersuchung des Ansprechens auf die Behandlung in einem subkutanen Tumormausmodell

Nachdem wir die therapeutische Wirksamkeit in verschiedenen KRAS-mutierten PDAC-Modellen zeigen konnten, ist es nun unser Ziel, eine Anwendung für diese neue Therapie in der Klinik zu finden. Es ist nach wie vor unerlässlich, festzustellen, ob Patienten auf die Therapie ansprechen, vorzugsweise mit minimalinvasiven Methoden. Interessanterweise beschrieben Ying et al. (84), dass das onkogene *KRAS*^{G12D} für die Aufrechterhaltung des

PDAC-Tumors erforderlich ist und den PDAC-Stoffwechsel umprogrammiert, indem es die Glukoseaufnahme und die Glykolyse stimuliert, während Bryant et al. feststellten, dass sowohl die KRAS-Suppression als auch die ERK-Hemmung die Glukoseaufnahme bei PDAC verringerten (85). Auf der Grundlage dieser Berichte untersuchten wir die Möglichkeit, die mittels PET (*Positron Emission Tomography*)-Scan gemessene 18F-FDG (Fluordesoxyglucose)-Aufnahme als Marker für ein frühes Ansprechen zu verwenden.

Zu diesem Zweck behandelten wir Mäuse, die subkutane KCP-Tumore trugen, 7 Tage lang täglich entweder mit Vehikel oder mit der Kombination aus SHP2i + ERKi. PET-Scans wurden an den Tagen 0 (vor der Behandlung), 3 und 7 durchgeführt. Unsere Ergebnisse zeigen, dass die 18F-FDG-Aufnahme durch PET-CT-Scans von subkutan implantierten KCP-Tumoren nachweisbar ist und dass die Abnahme des PET-Signals einer Verringerung des Tumorvolumens vorausgeht und damit verbunden ist. Diese Daten eröffnen die Möglichkeit, die FDG-Aufnahme in der Klinik zur Überwachung des frühen Ansprechens auf diese neuartige Kombinationstherapie für PDAC-Patienten einzusetzen.

2.4.6 Zusammenfassung

Wir konnten eine gute Verträglichkeit und Wirksamkeit der Kombination aus SHP2-Inhibitor und ERK-Inhibitor mit einer signifikanten Rückbildung des Tumors in mehreren PDAC-Mausmodellen nachweisen. Darüber hinaus zeigten wir, dass mittels PET-Scan gemessene 18F-FDG (Fluordesoxyglucose)-Aufnahme zur Beurteilung des frühen Ansprechens auf die Therapie in Tiermodellen verwendet werden kann. Auf der Grundlage dieser Ergebnisse werden wir diese Therapiekombination in der klinischen Studie SHERPA (SHP2- und ERK-Inhibition bei Bauchspeicheldrüsenkrebs, NCT04916236) untersuchen, in die Patienten mit KRAS-mutiertem PDAC aufgenommen werden.

3 Zusammenfassung

Das duktale Adenokarzinom der Bauchspeicheldrüse (PDAC) ist einer der aggressivsten humanen malignen Tumoren. PDAC stellt die vierthäufigste Ursache für krebsbedingte Todesfälle in der westlichen Welt dar und nur ca. 9 Prozent der Patienten überleben die ersten fünf Jahre nach ihrer Diagnose. Aufgrund fehlender oder auch oft uncharakteristischer Symptome wie beispielsweise Abdominal- oder Rückenschmerzen, Gewichtsverlust oder eine neu entwickelte Diabeteserkrankung wird PDAC häufig erst in einem fortgeschrittenen, bereits metastasierten Stadium diagnostiziert. Durch die begrenzten diagnostischen Möglichkeiten und die wenigen wirksamen Medikamente ist die Behandlung nur in seltenen Fällen erfolgreich. Daher ist es wichtig, spezifische und für die pankreatische Onkogenese relevante Signalwege zu identifizieren, die den aggressiven Krankheitsverlauf verursachen und somit die Grundlage für eine gerichtete und effektive Therapie darstellen. Im Rahmen dieser Arbeit wurden unter Anwendung genetisch-basierter Modelle die Mechanismen der pathologischen Aktivierung von Signalwegen aufgeklärt, die das Zellwachstum und Zellüberleben während der Tumorentstehung in der Bauchspeicheldrüse regulieren.

Diverse Studien aus den letzten Jahren und Jahrzehnten weisen auf eine Aktivierung des Transkriptionsfaktors STAT3 in humanen Malignomen hin und schreiben damit dem JAK/STAT-Signalweg und insbesondere STAT3 eine zentrale Rolle im Prozess der Karzinogenese zu. In unseren experimentellen Untersuchungen konnten wir wichtige Funktionen der IL-6/STAT3 Kaskade und ihre Bedeutung für verschiedene Aspekte der pankreatischen Onkogenese beschreiben und eine Interaktion zwischen Pankreaskarzinomzellen und Mikroumgebung identifizieren. Das von myeloiden Zellen freigesetzte IL-6 führt zur vorübergehenden Stat3-Aktivierung über das IL-6 Transsignalling und beschleunigt die Progression von präneoplastischen Läsionen zum duktalen Pankreaskarzinom. In einer weiteren Studie konnten wir zeigen, dass die p53-abhängige anhaltende Stat3-Aktivierung an der Tumorprogression beteiligt ist und als wichtiger Regulator der Modulierung des Tumorstaromas gilt (27). Klinische Daten bestätigen, dass der Phosphorylierungsgrad von STAT3 und *„loss of function“* von p53 mit einem kürzeren Gesamtüberleben bei PDAC-Patienten korreliert. Zusammenfassend lässt sich sagen, dass unsere Ergebnisse neue Möglichkeiten für eine gezielte und individualisierte Therapie eröffnen. Eine Therapie des PDAC mit Medikamenten mit JAK2/STAT3-abhängiger Wirkung könnte das Tumorstroma modulieren und damit die Therapieresistenz überwinden.

Als negativer Regulator des JAK/STAT Signalwegs spielt SHP2, eine ubiquitär exprimierte Nicht-Rezeptor Protein-Tyrosinphosphatase, eine wesentliche Rolle während der KRAS-

getriebenen Karzinogenese. Da SHP2 die Signaltransduktion verschiedener Wachstumsfaktoren, Zytokine und Integrin-Rezeptoren durch die kontext- und zelltypabhängige Modulierung des JAK/STAT Signalwegs regulieren kann, wurde SHP2 als eine attraktive Zielstruktur in der Krebstherapie identifiziert. Kürzlich wurde ein allosterischer SHP2-Inhibitor als Therapieoption für Tyrosinkinase-getriebene Tumore vorgestellt, der sich jedoch bei KRAS-mutierten Tumorzelllinien *in vitro* als unwirksam erwies (86). Wir setzten uns deshalb in unserer Arbeit das Ziel, eine Medikamentenkombination zu finden, die für die aggressiven KRAS-getriebenen Pankreastumore wirksam sein kann. In der vorliegenden Studie haben wir eine Strategie validiert, in der die Hemmung von SHP2 (RMC-4550) mit der Inhibition des MEK-Downstream-Effektors ERK (LY3214996) kombiniert wurde. Unsere Daten konnten eine gute Verträglichkeit und Wirksamkeit der Kombination aus SHP2-Inhibitor und ERK-Inhibitor mit einer signifikanten Rückbildung des Tumors in mehreren *in vitro* und *in vivo* Modellen des murinen und menschlichen PDAC nachweisen. Diese Therapiekombination wird in der klinischen Studie SHERPA (NCT04916236) untersucht, in die Patienten mit KRAS-mutiertem PDAC aufgenommen werden.

Eine weitere Signalkaskade, deren Aktivierung eine wichtige Rolle für die Progression des Pankreaskarzinoms spielt, ist der NF-κB Signalweg. Mit Hilfe des $Kras^{G12D}$ Modells konnte eine duale Funktion der NF-κB-Untereinheit RelA in PDAC gezeigt werden. Die tumorsuppressive oder tumorfördernde Funktion von RelA ist kontextspezifisch und hängt vom Stadium der malignen Transformation ab. Die Progression der *Kras*-induzierten Onkogenese wird im Wesentlichen durch das Phänomen der Onkogen-induzierten Seneszenz (OIS) kontrolliert. OIS führt in einer Zelle zu einem Proliferationsarrest, obwohl diese Zellen einen aktiven Metabolismus betreiben. Seneszente Zellen sezernieren verschiedene Zytokine, Chemokine, Proteasen und Wachstumsfaktoren, um ein Netzwerk mit den benachbarten Zellen zu bilden, nämlich den Seneszenz-assoziierten sekretorischen Phänotyp (SASP). Das murine Cxcl1 (und sein humanes funktionelles Homolog IL-8) wurde als eine wichtige SASP-Komponente identifiziert. Cxcl1 wird RelA-abhängig produziert und vermittelt seine Funktionen über den G-Protein-gekoppelten Chemokinrezeptor CXCR2. In den frühen Stadien der pankreatischen Karzinogenese hemmt RelA die PanIN-Progression durch die Regulation von SASP und die Induktion von OIS über den CXCR2 Rezeptor. In den späteren Stadien, wenn OIS überwunden wird, wirkt die Aktivierung von RelA tumorfördernd. Somit zeigen unsere Ergebnisse Mechanismen, die die Komplexität des NF-κB-Signalwegs während der pankreatischen Karzinogenese verdeutlichen, und auf einige neue Aspekte hinweisen, die berücksichtigt werden müssen, insbesondere bei dem Therapieeinsatz spezifischer NF-κB- und CXCR2-Inhibitoren.

Eines der Probleme in der Entwicklung zielgerichteter Krebstherapien ist, dass der Stoffwechsel in Tumorzellen, im Vergleich zu normal wachsenden Zellen, stark verändert ist. Dieser veränderte Stoffwechsel dient den Tumorzellen zur Bereitstellung molekularer Bausteine, zur Förderung ihrer abnormen Proliferation und zur Deckung ihres hohen Energiebedarfs. Daher ist die Entwicklung neuer Krebsmedikamente, die den Stoffwechsel von Tumorzellen modulieren, in den Mittelpunkt des Interesses gerückt. Dabei hängt der Erfolg im Wesentlichen vom Verständnis bestimmter Stoffwechselwege und deren Bedeutung für die Tumorzellen ab. Die Autophagie, ein wesentlicher Mechanismus im Stoffwechsel, hat sich als wichtiger Regulator von mehreren Aspekten der Krebsbiologie herausgestellt. Atg5 als Teil des Atg-Konjugationsystems wird für die Aufrechterhaltung des autophagischen Flusses benötigt. Es vermittelt die Formation von Autophagosomen und ist für den anschließenden lysosomalen Abbau und Recycling von Membrankomponenten notwendig. Der Verlust von Atg5 im Pankreas führt zur Akkumulation von nicht abbaubaren Autophagosomen in der Azinuszelle. In diesem Zusammenhang konnten wir zeigen, dass der Pankreas-spezifische vollständige Verlust von Atg5 im *Kras*^{G12D} Modell während der Embryogenese ausreicht, um transkriptionelle und metabolische Veränderungen zu induzieren. Dabei wird die Initiation präneoplastischer Läsionen im Atg5-defizienten *Kras*^{G12D} Mausmodell beschleunigt, die Tumorprogression aber blockiert. Darüber hinaus sind wir anders als in bisher konzipierten Studien der Rolle eines monoallelischen Verlustes von Atg5 nachgegangen. Dabei konnten wir zum ersten Mal zeigen, dass der Verlust eines Atg5-Allels nicht nur die Tumorinzidenz erhöht, sondern auch die Metastasierungsrate. Interessanterweise führt der monoallelische Verlust von Atg5 zu einer Beeinträchtigung des Autophagie-Prozesses, die in der Konsequenz eine Resistenz gegen Chloroquin vermittelt und schließlich zu einer Selektion von resistenten und aggressiv wachsenden Krebszellklonen führt. Auch klinische Daten bestätigen eine Korrelation zwischen der ATG5-Proteinexpression und der Metastasierung und dem Überleben in 3 unabhängigen humanen Pankreaskarzinom-Kohorten. Damit stellen unsere Ergebnisse klar, dass die Hemmung des Autophagie-Prozesses einem komplexeren Regulierungsmechanismus unterliegt und vielseitige Effekte ausübt. Das soll bei der Anwendung von Autophagie-Blockern in klinischen Studien bei Patienten mit Pankreaskarzinom berücksichtigt werden.

4 Literaturverzeichnis

1. Hidalgo M. Pancreatic cancer. *N Engl J Med.* 2010;362(17):1605-17.
2. Siegel RL, Miller KD, and Jemal A. Cancer statistics, 2019. *CA Cancer J Clin.* 2019;69(1):7-34.
3. Makohon-Moore A, Brosnan JA, and Iacobuzio-Donahue CA. Pancreatic cancer genomics: insights and opportunities for clinical translation. *Genome Med.* 2013;5(3):26.
4. Pishvaian MJ, Bender RJ, Halverson D, Rahib L, Hendifar AE, Mikhail S, et al. Molecular Profiling of Patients with Pancreatic Cancer: Initial Results from the Know Your Tumor Initiative. *Clin Cancer Res.* 2018;24(20):5018-27.
5. Pishvaian MJ, Blais EM, Brody JR, Lyons E, DeArbeloa P, Hendifar A, et al. Overall survival in patients with pancreatic cancer receiving matched therapies following molecular profiling: a retrospective analysis of the Know Your Tumor registry trial. *Lancet Oncol.* 2020;21(4):508-18.
6. Heinmoller E, Dietmaier W, Zirngibl H, Heinmoller P, Scaringe W, Jauch KW, et al. Molecular analysis of microdissected tumors and preneoplastic intraductal lesions in pancreatic carcinoma. *Am J Pathol.* 2000;157(1):83-92.
7. Hruban RH, Goggins M, Parsons J, and Kern SE. Progression model for pancreatic cancer. *Clin Cancer Res.* 2000;6(8):2969-72.
8. Hustinx SR, Hruban RH, Leoni LM, Iacobuzio-Donahue C, Cameron JL, Yeo CJ, et al. Homozygous deletion of the MTAP gene in invasive adenocarcinoma of the pancreas and in periampullary cancer: a potential new target for therapy. *Cancer Biol Ther.* 2005;4(1):83-6.
9. Maitra A, Adsay NV, Argani P, Iacobuzio-Donahue C, De Marzo A, Cameron JL, et al. Multicomponent analysis of the pancreatic adenocarcinoma progression model using a pancreatic intraepithelial neoplasia tissue microarray. *Mod Pathol.* 2003;16(9):902-12.
10. Vincent A, Herman J, Schulick R, Hruban RH, and Goggins M. Pancreatic cancer. *Lancet.* 2011;378(9791):607-20.
11. Lesina M, Kurkowski MU, Ludes K, Rose-John S, Treiber M, Kloppel G, et al. Stat3/Socs3 activation by IL-6 transsignaling promotes progression of pancreatic intraepithelial neoplasia and development of pancreatic cancer. *Cancer Cell.* 2011;19(4):456-69.
12. Leaman DW, Pisharody S, Flickinger TW, Commane MA, Schlessinger J, Kerr IM, et al. Roles of JAKs in activation of STATs and stimulation of c-fos gene expression by epidermal growth factor. *Mol Cell Biol.* 1996;16(1):369-75.
13. Schaper F, Siewert E, Gomez-Lechon MJ, Gatsios P, Sachs M, Birchmeier W, et al. Hepatocyte growth factor/scatter factor (HGF/SF) signals via the STAT3/APRF transcription factor in human hepatoma cells and hepatocytes. *FEBS Lett.* 1997;405(1):99-103.
14. Vignais ML, Sadowski HB, Watling D, Rogers NC, and Gilman M. Platelet-derived growth factor induces phosphorylation of multiple JAK family kinases and STAT proteins. *Mol Cell Biol.* 1996;16(4):1759-69.
15. Hoey T, and Schindler U. STAT structure and function in signaling. *Curr Opin Genet Dev.* 1998;8(5):582-7.
16. Yasukawa H, Sasaki A, and Yoshimura A. Negative regulation of cytokine signaling pathways. *Annu Rev Immunol.* 2000;18:143-64.
17. ten Hoeve J, de Jesus Ibarra-Sanchez M, Fu Y, Zhu W, Tremblay M, David M, et al. Identification of a nuclear Stat1 protein tyrosine phosphatase. *Mol Cell Biol.* 2002;22(16):5662-8.
18. Yamamoto T, Matsuda T, Junicho A, Kishi H, Saatcioglu F, and Muraguchi A. Cross-talk between signal transducer and activator of transcription 3 and estrogen receptor signaling. *FEBS Lett.* 2000;486(2):143-8.

19. Irie-Sasaki J, Sasaki T, Matsumoto W, Opavsky A, Cheng M, Welstead G, et al. CD45 is a JAK phosphatase and negatively regulates cytokine receptor signalling. *Nature.* 2001;409(6818):349-54.
20. Hirano T, Ishihara K, and Hibi M. Roles of STAT3 in mediating the cell growth, differentiation and survival signals relayed through the IL-6 family of cytokine receptors. *Oncogene.* 2000;19(21):2548-56.
21. Grivennikov S, and Karin M. Autocrine IL-6 signaling: a key event in tumorigenesis? *Cancer Cell.* 2008;13(1):7-9.
22. Yu H, Pardoll D, and Jove R. STATs in cancer inflammation and immunity: a leading role for STAT3. *Nat Rev Cancer.* 2009;9(11):798-809.
23. Scholz A, Heinze S, Detjen KM, Peters M, Welzel M, Hauff P, et al. Activated signal transducer and activator of transcription 3 (STAT3) supports the malignant phenotype of human pancreatic cancer. *Gastroenterology.* 2003;125(3):891-905.
24. Huang C, Cao J, Huang KJ, Zhang F, Jiang T, Zhu L, et al. Inhibition of STAT3 activity with AG490 decreases the invasion of human pancreatic cancer cells in vitro. *Cancer Sci.* 2006;97(12):1417-23.
25. Lewis HD, Winter A, Murphy TF, Tripathi S, Pandey VN, and Barton BE. STAT3 inhibition in prostate and pancreatic cancer lines by STAT3 binding sequence oligonucleotides: differential activity between 5' and 3' ends. *Mol Cancer Ther.* 2008;7(6):1543-50.
26. Zhao S, Venkatasubbarao K, Lazor JW, Sperry J, Jin C, Cao L, et al. Inhibition of STAT3 Tyr705 phosphorylation by Smad4 suppresses transforming growth factor beta-mediated invasion and metastasis in pancreatic cancer cells. *Cancer Res.* 2008;68(11):4221-8.
27. Wörmann SM, Song L, Ai J, Diakopoulos KN, Gorgulu K, Ruess D, et al. Loss of P53 Function Activates JAK2-STAT3 Signaling to Promote Pancreatic Tumor Growth, Stroma Modification, and Gemcitabine Resistance in Mice and is Associated With Patient Survival. *Gastroenterology.* 2016.
28. Gilmore TD. Introduction to NF-kappaB: players, pathways, perspectives. *Oncogene.* 2006;25(51):6680-4.
29. Baeuerle PA, and Baltimore D. Activation of DNA-binding activity in an apparently cytoplasmic precursor of the NF-kappa B transcription factor. *Cell.* 1988;53(2):211-7.
30. Baeuerle PA, and Baltimore D. I kappa B: a specific inhibitor of the NF-kappa B transcription factor. *Science.* 1988;242(4878):540-6.
31. Haskill S, Beg AA, Tompkins SM, Morris JS, Yurochko AD, Sampson-Johannes A, et al. Characterization of an immediate-early gene induced in adherent monocytes that encodes I kappa B-like activity. *Cell.* 1991;65(7):1281-9.
32. Link E, Kerr LD, Schreck R, Zabel U, Verma I, and Baeuerle PA. Purified I kappa B-beta is inactivated upon dephosphorylation. *J Biol Chem.* 1992;267(1):239-46.
33. Karin M, and Delhase M. The I kappa B kinase (IKK) and NF-kappa B: key elements of proinflammatory signalling. *Semin Immunol.* 2000;12(1):85-98.
34. Hoffmann A, Natoli G, and Ghosh G. Transcriptional regulation via the NF-kappaB signaling module. *Oncogene.* 2006;25(51):6706-16.
35. Luo JL, Kamata H, and Karin M. IKK/NF-kappaB signaling: balancing life and death--a new approach to cancer therapy. *J Clin Invest.* 2005;115(10):2625-32.
36. Karin M, Cao Y, Greten FR, and Li ZW. NF-kappaB in cancer: from innocent bystander to major culprit. *Nat Rev Cancer.* 2002;2(4):301-10.
37. Kim HJ, Hawke N, and Baldwin AS. NF-kappaB and IKK as therapeutic targets in cancer. *Cell Death Differ.* 2006;13(5):738-47.
38. Baldwin AS. Control of oncogenesis and cancer therapy resistance by the transcription factor NF-kappaB. *J Clin Invest.* 2001;107(3):241-6.
39. Dajee M, Lazarov M, Zhang JY, Cai T, Green CL, Russell AJ, et al. NF-kappaB blockade and oncogenic Ras trigger invasive human epidermal neoplasia. *Nature.* 2003;421(6923):639-43.

40. Hanson JL, Hawke NA, Kashatus D, and Baldwin AS. The nuclear factor kappaB subunits RelA/p65 and c-Rel potentiate but are not required for Ras-induced cellular transformation. *Cancer Res.* 2004;64(20):7248-55.
41. Basseres DS, Ebbs A, Levantini E, and Baldwin AS. Requirement of the NF-kappaB subunit p65/RelA for K-Ras-induced lung tumorigenesis. *Cancer Res.* 2010;70(9):3537-46.
42. Daniluk J, Liu Y, Deng D, Chu J, Huang H, Gaiser S, et al. An NF-kappaB pathway-mediated positive feedback loop amplifies Ras activity to pathological levels in mice. *J Clin Invest.* 2012;122(4):1519-28.
43. Greten FR, Eckmann L, Greten TF, Park JM, Li ZW, Egan LJ, et al. IKKbeta links inflammation and tumorigenesis in a mouse model of colitis-associated cancer. *Cell.* 2004;118(3):285-96.
44. Lesina M, Wormann SM, Morton J, Diakopoulos KN, Korneeva O, Wimmer M, et al. RelA regulates CXCL1/CXCR2-dependent oncogene-induced senescence in murine Kras-driven pancreatic carcinogenesis. *The Journal of clinical investigation.* 2016;126(8):2919-32.
45. Ling J, Kang Y, Zhao R, Xia Q, Lee DF, Chang Z, et al. KrasG12D-induced IKK2/beta/NF-kappaB activation by IL-1alpha and p62 feedforward loops is required for development of pancreatic ductal adenocarcinoma. *Cancer Cell.* 2012;21(1):105-20.
46. Luedde T, Beraza N, Kotsikoris V, van Loo G, Nenci A, De Vos R, et al. Deletion of NEMO/IKKgamma in liver parenchymal cells causes steatohepatitis and hepatocellular carcinoma. *Cancer Cell.* 2007;11(2):119-32.
47. Maniati E, Bossard M, Cook N, Candido JB, Emami-Shahri N, Nedospasov SA, et al. Crosstalk between the canonical NF-kappaB and Notch signaling pathways inhibits Ppargamma expression and promotes pancreatic cancer progression in mice. *J Clin Invest.* 2011;121(12):4685-99.
48. Meylan E, Dooley AL, Feldser DM, Shen L, Turk E, Ouyang C, et al. Requirement for NF-kappaB signalling in a mouse model of lung adenocarcinoma. *Nature.* 2009;462(7269):104-7.
49. Levine B, and Kroemer G. Autophagy in the pathogenesis of disease. *Cell.* 2008;132(1):27-42.
50. Mizushima N, Levine B, Cuervo AM, and Klionsky DJ. Autophagy fights disease through cellular self-digestion. *Nature.* 2008;451(7182):1069-75.
51. Klionsky DJ. The molecular machinery of autophagy: unanswered questions. *J Cell Sci.* 2005;118(Pt 1):7-18.
52. Gorgulu K, Diakopoulos KN, Kaya-Aksoy E, Ciecielski KJ, Ai J, Lesina M, et al. The Role of Autophagy in Pancreatic Cancer: From Bench to the Dark Bedside. *Cells.* 2020;9(4).
53. Santana-Codina N, Mancias JD, and Kimmelman AC. The Role of Autophagy in Cancer. *Annu Rev Cancer Biol.* 2017;1:19-39.
54. Rosenfeldt MT, O'Prey J, Morton JP, Nixon C, MacKay G, Mrowinska A, et al. p53 status determines the role of autophagy in pancreatic tumour development. *Nature.* 2013;504(7479):296-300.
55. Yang A, Rajeshkumar NV, Wang X, Yabuuchi S, Alexander BM, Chu GC, et al. Autophagy is critical for pancreatic tumor growth and progression in tumors with p53 alterations. *Cancer Discov.* 2014;4(8):905-13.
56. Rao S, Tortola L, Perlot T, Wirnsberger G, Novatchkova M, Nitsch R, et al. A dual role for autophagy in a murine model of lung cancer. *Nat Commun.* 2014;5:3056.
57. Hingorani SR, Petricoin EF, Maitra A, Rajapakse V, King C, Jacobetz MA, et al. Preinvasive and invasive ductal pancreatic cancer and its early detection in the mouse. *Cancer Cell.* 2003;4(6):437-50.
58. Rabe B, Chalaris A, May U, Waetzig GH, Seegert D, Williams AS, et al. Transgenic blockade of interleukin 6 transsignaling abrogates inflammation. *Blood.* 2008;111(3):1021-8.

59. Algül H, Treiber M, Lesina M, Nakhai H, Saur D, Geisler F, et al. Pancreas-specific RelA/p65 truncation increases susceptibility of acini to inflammation-associated cell death following cerulein pancreatitis. *The Journal of clinical investigation.* 2007;117(6):1490-501.
60. Nakhai H, Sel S, Favor J, Mendoza-Torres L, Paulsen F, Duncker GI, et al. Ptf1a is essential for the differentiation of GABAergic and glycinergic amacrine cells and horizontal cells in the mouse retina. *Development.* 2007;134(6):1151-60.
61. Sano S, Itami S, Takeda K, Tarutani M, Yamaguchi Y, Miura H, et al. Keratinocyte-specific ablation of Stat3 exhibits impaired skin remodeling, but does not affect skin morphogenesis. *EMBO J.* 1999;18(17):4657-68.
62. Nakaya M, Hashimoto M, Nakagawa R, Wakabayashi Y, Ishizaki T, Takada I, et al. SOCS3 in T and NKT cells negatively regulates cytokine production and ameliorates ConA-induced hepatitis. *J Immunol.* 2009;183(11):7047-53.
63. Guerra C, Collado M, Navas C, Schuhmacher AJ, Hernandez-Porras I, Canamero M, et al. Pancreatitis-induced inflammation contributes to pancreatic cancer by inhibiting oncogene-induced senescence. *Cancer Cell.* 2011;19(6):728-39.
64. Caldwell ME, DeNicola GM, Martins CP, Jacobetz MA, Maitra A, Hruban RH, et al. Cellular features of senescence during the evolution of human and murine ductal pancreatic cancer. *Oncogene.* 2012;31(12):1599-608.
65. Hu C, Sun L, Hu Y, Lu D, Wang H, and Tang S. Functional characterization of the NF-kappaB binding site in the human NOD2 promoter. *Cell Mol Immunol.* 2010;7(4):288-95.
66. Campisi J. Aging, cellular senescence, and cancer. *Annu Rev Physiol.* 2013;75:685-705.
67. Tchkonia T, Zhu Y, van Deursen J, Campisi J, and Kirkland JL. Cellular senescence and the senescent secretory phenotype: therapeutic opportunities. *J Clin Invest.* 2013;123(3):966-72.
68. Boland ML, Chourasia AH, and Macleod KF. Mitochondrial dysfunction in cancer. *Front Oncol.* 2013;3:292.
69. Gomes LC, and Scorrano L. Mitochondrial morphology in mitophagy and macroautophagy. *Biochim Biophys Acta.* 2013;1833(1):205-12.
70. Gunter TE, Yule DI, Gunter KK, Eliseev RA, and Salter JD. Calcium and mitochondria. *FEBS Lett.* 2004;567(1):96-102.
71. Tsai FC, and Meyer T. Ca2+ pulses control local cycles of lamellipodia retraction and adhesion along the front of migrating cells. *Curr Biol.* 2012;22(9):837-42.
72. Settembre C, Fraldi A, Medina DL, and Ballabio A. Signals from the lysosome: a control centre for cellular clearance and energy metabolism. *Nat Rev Mol Cell Biol.* 2013;14(5):283-96.
73. Mainardi S, Mulero-Sanchez A, Prahallad A, Germano G, Bosma A, Krimpenfort P, et al. SHP2 is required for growth of KRAS-mutant non-small-cell lung cancer in vivo. *Nat Med.* 2018;24(7):961-7.
74. Ruess DA, Heynen GJ, Ciecielski KJ, Ai J, Berninger A, Kabacaoglu D, et al. Mutant KRAS-driven cancers depend on PTPN11/SHP2 phosphatase. *Nat Med.* 2018;24(7):954-60.
75. Hayes TK, Neel NF, Hu C, Gautam P, Chenard M, Long B, et al. Long-Term ERK Inhibition in KRAS-Mutant Pancreatic Cancer Is Associated with MYC Degradation and Senescence-like Growth Suppression. *Cancer cell.* 2016;29(1):75-89.
76. Welsh SJ, and Corrie PG. Management of BRAF and MEK inhibitor toxicities in patients with metastatic melanoma. *Ther Adv Med Oncol.* 2015;7(2):122-36.
77. Yang JC-H, Lin C-C, and Chu C-Y. In: Pass HI, Ball D, and Scagliotti GV eds. *IASLC Thoracic Oncology (Second Edition)*. Philadelphia: Elsevier; 2018:490-500.e3.
78. Drosten M, and Barbacid M. Targeting the MAPK Pathway in KRAS-Driven Tumors. *Cancer Cell.* 2020;37(4):543-50.
79. Ryan MB, Der CJ, Wang-Gillam A, and Cox AD. Targeting RAS-mutant cancers: is ERK the key? *Trends Cancer.* 2015;1(3):183-98.

80. Bhagwat SV, McMillen WT, Cai S, Zhao B, Whitesell M, Shen W, et al. ERK Inhibitor LY3214996 Targets ERK Pathway-Driven Cancers: A Therapeutic Approach Toward Precision Medicine. *Mol Cancer Ther.* 2020;19(2):325-36.
81. Nichols RJ, Haderk F, Stahlhut C, Schulze CJ, Hemmati G, Wildes D, et al. RAS nucleotide cycling underlies the SHP2 phosphatase dependence of mutant BRAF-, NF1- and RAS-driven cancers. *Nat Cell Biol.* 2018;20(9):1064-73.
82. Huang X, Biswas S, Oki Y, Issa JP, and Berry DA. A parallel phase I/II clinical trial design for combination therapies. *Biometrics.* 2007;63(2):429-36.
83. Le Tourneau C, Lee JJ, and Siu LL. Dose escalation methods in phase I cancer clinical trials. *J Natl Cancer Inst.* 2009;101(10):708-20.
84. Ying H, Kimmelman AC, Lyssiotis CA, Hua S, Chu GC, Fletcher-Sananikone E, et al. Oncogenic Kras maintains pancreatic tumors through regulation of anabolic glucose metabolism. *Cell.* 2012;149(3):656-70.
85. Bryant KL, Stalnecker CA, Zeitouni D, Klomp JE, Peng S, Tikunov AP, et al. Combination of ERK and autophagy inhibition as a treatment approach for pancreatic cancer. *Nat Med.* 2019;25(4):628-40.
86. Chen YN, LaMarche MJ, Chan HM, Fekkes P, Garcia-Fortanet J, Acker MG, et al. Allosteric inhibition of SHP2 phosphatase inhibits cancers driven by receptor tyrosine kinases. *Nature.* 2016;535(7610):148-52.

5 Verzeichnis eigener Schriften

5.1 Originalarbeiten

1. Frank KJ, Mulero-Sanchez A, Berninger A, Ruiz-Canas L, Bosma A, Gorgulu K, … **Lesina M**, …, et al. Extensive preclinical validation of combined RMC-4550 and LY3214996 supports clinical investigation for KRAS mutant pancreatic cancer. *Cell Rep Med.* 2022;3(11):100815.
2. Kabacaoglu D, Ruess DA, Gorgulu K, Steiger K, **Lesina M**, and Algul H. A Pancreas-Specific Ptf1a-Driven Cre Mouse Line Causes Paternally Transmitted Germline Recombination. *Gastroenterology.* 2021;161(5):1695-7 e4.
3. Erener S, Ellis CE, Ramzy A, Glavas MM, O'Dwyer S, Pereira S, … **Lesina M**, …, et al. Deletion of pancreas-specific miR-216a reduces beta-cell mass and inhibits pancreatic cancer progression in mice. *Cell Rep Med.* 2021;2(11):100434.
4. Masamune A, Kotani H, Sorgel FL, Chen JM, Hamada S, Sakaguchi R, … **Lesina M**, …, et al. Variants That Affect Function of Calcium Channel TRPV6 Are Associated With Early-Onset Chronic Pancreatitis. *Gastroenterology.* 2020;158(6):1626-41 e8.
5. Hidalgo-Sastre A, Desztics J, Dantes Z, Schulte K, Ensarioglu HK, Bassey-Archibong B, … **Lesina M**, …, et al. Loss of Wasl improves pancreatic cancer outcome. *JCI Insight.* 2020;5(10).
6. Hedegger K, Stumpf F, Blum H, Graf A, Schmid RM, **Lesina M**, et al. The protective effect of betacellulin against acute pancreatitis is ERBB4 dependent. *J Gastroenterol.* 2020;55(3):317-29.
7. Hedegger K, Algul H, **Lesina M**, Blutke A, Schmid RM, Schneider MR, et al. Unraveling ERBB network dynamics upon betacellulin signaling in pancreatic ductal adenocarcinoma in mice. *Mol Oncol.* 2020;14(8):1653-69.
8. Gorgulu K, Diakopoulos KN, Ai J, Schoeps B, Kabacaoglu D, Karpathaki AF, … **Lesina M**, …, et al. Levels of the Autophagy-Related 5 Protein Affect Progression and Metastasis of Pancreatic Tumors in Mice. *Gastroenterology.* 2019;156(1):203-17 e20.
9. Demir IE, Heinrich T, Carty DG, Saricaoglu OC, Klauss S, Teller S, … **Lesina M**, …, et al. Targeting nNOS ameliorates the severe neuropathic pain due to chronic pancreatitis. *EBioMedicine.* 2019;46:431-43.
10. Ruess DA, Heynen GJ, Ciecielski KJ, Ai J, Berninger A, Kabacaoglu D, … **Lesina M**, …, et al. Mutant KRAS-driven cancers depend on PTPN11/SHP2 phosphatase. *Nat Med.* 2018;24(7):954-60.
11. Poplutz M, Levikova M, Luscher-Firzlaff J, **Lesina M**, Algul H, Luscher B, et al. Endotoxin tolerance in mast cells, its consequences for IgE-mediated signalling, and the effects of BCL3 deficiency. *Sci Rep.* 2017;7(1):4534.
12. Perkhofer L, Schmitt A, Romero Carrasco MC, Ihle M, Hampp S, Ruess DA, … **Lesina M**, …, et al. ATM Deficiency Generating Genomic Instability Sensitizes Pancreatic Ductal Adenocarcinoma Cells to Therapy-Induced DNA Damage. *Cancer Res.* 2017;77(20):5576-90.
13. Demir IE, Kujundzic K, Pfitzinger PL, Saricaoglu OC, Teller S, Kehl T, … **Lesina M**, …, et al. Early pancreatic cancer lesions suppress pain through CXCL12-mediated chemoattraction of Schwann cells. *Proc Natl Acad Sci U S A.* 2017;114(1):E85-E94.
14. Wörmann SM, Song L, Ai J, Diakopoulos KN, Gorgulu K, Ruess D, … **Lesina M**, …, et al. Loss of P53 Function Activates JAK2-STAT3 Signaling to Promote Pancreatic Tumor Growth, Stroma Modification, and Gemcitabine Resistance in Mice and is Associated With Patient Survival. *Gastroenterology.* 2016.
15. Steiner JM, Schwamberger S, Pantchev N, Balzer HJ, Vrhovec MG, **Lesina M**, et al. Use of Ronidazole and Limited Culling To Eliminate Tritrichomonas muris from Laboratory Mice. *J Am Assoc Lab Anim Sci.* 2016;55(4):480-3.

16. Song L, Wormann S, Ai J, Neuhofer P, **Lesina M**, Diakopoulos KN, et al. BCL3 Reduces the Sterile Inflammatory Response in Pancreatic and Biliary Tissues. *Gastroenterology.* 2016;150(2):499-512 e20.
17. **Lesina M**, Wormann SM, Morton J, Diakopoulos KN, Korneeva O, Wimmer M, et al. RelA regulates CXCL1/CXCR2-dependent oncogene-induced senescence in murine Kras-driven pancreatic carcinogenesis. *J Clin Invest.* 2016;126(8):2919-32.
18. Diakopoulos KN, **Lesina M**, Wormann S, Song L, Aichler M, Schild L, et al. Impaired autophagy induces chronic atrophic pancreatitis in mice via sex- and nutrition-dependent processes. *Gastroenterology.* 2015;148(3):626-38 e17.
19. Demir IE, Boldis A, Pfitzinger PL, Teller S, Brunner E, Klose N, … **Lesina M**, …, et al. Investigation of Schwann cells at neoplastic cell sites before the onset of cancer invasion. *Journal of the National Cancer Institute.* 2014;106(8).
20. Zhang H, Neuhofer P, Song L, Rabe B, **Lesina M**, Kurkowski MU, et al. IL-6 trans-signaling promotes pancreatitis-associated lung injury and lethality. *The Journal of clinical investigation.* 2013;123(3):1019-31.
21. Neuhofer P, Liang S, Einwachter H, Schwerdtfeger C, Wartmann T, Treiber M, … **Lesina M**, …, et al. Deletion of IkappaBalpha activates RelA to reduce acute pancreatitis in mice through up-regulation of Spi2A. *Gastroenterology.* 2013;144(1):192-201.
22. Conradt L, Henrich A, Wirth M, Reichert M, **Lesina M**, Algul H, et al. Mdm2 inhibitors synergize with topoisomerase II inhibitors to induce p53-independent pancreatic cancer cell death. *International journal of cancer.* 2013;132(10):2248-57.
23. Hamidi T, Algul H, Cano CE, Sandi MJ, Molejon MI, Riemann M, … **Lesina M**, …, et al. Nuclear protein 1 promotes pancreatic cancer development and protects cells from stress by inhibiting apoptosis. *The Journal of clinical investigation.* 2012;122(6):2092-103.
24. Treiber M, Neuhofer P, Anetsberger E, Einwachter H, **Lesina M**, Rickmann M, et al. Myeloid, but not pancreatic, RelA/p65 is required for fibrosis in a mouse model of chronic pancreatitis. *Gastroenterology.* 2011;141(4):1473-85, 85 e1-7.
25. **Lesina M**, Kurkowski MU, Ludes K, Rose-John S, Treiber M, Kloppel G, et al. Stat3/Socs3 activation by IL-6 transsignaling promotes progression of pancreatic intraepithelial neoplasia and development of pancreatic cancer. *Cancer Cell.* 2011;19(4):456-69.
26. Heid I, Lubeseder-Martellato C, Sipos B, Mazur PK, **Lesina M**, Schmid RM, et al. Early requirement of Rac1 in a mouse model of pancreatic cancer. *Gastroenterology.* 2011;141(2):719-30, 30 e1-7.
27. Dahlhoff M, Algul H, Siveke JT, **Lesina M**, Wanke R, Wartmann T, et al. Betacellulin protects from pancreatitis by activating stress-activated protein kinase. *Gastroenterology.* 2010;138(4):1585-94, 94 e1-3.
28. Algul H, Wagner M, **Lesina M**, and Schmid RM. Overexpression of ErbB2 in the exocrine pancreas induces an inflammatory response but not increased proliferation. *International journal of cancer.* 2007;121(7):1410-6.
29. Algül H, Treiber M, **Lesina M**, Nakhai H, Saur D, Geisler F, et al. Pancreas-specific RelA/p65 truncation increases susceptibility of acini to inflammation-associated cell death following cerulein pancreatitis. *J Clin Invest.* 2007;117(6):1490-501.

5.2 Reviews

1. Gorgulu K, **Lesina M**, and Algul H. Combating pancreatic cancer during its Rip Van Winkle sleep. *Cell Res.* 2020;30(8):637-8.
2. Gorgulu K, Diakopoulos KN, Kaya-Aksoy E, Ciecielski KJ, Ai J, **Lesina M**, et al. The Role of Autophagy in Pancreatic Cancer: From Bench to the Dark Bedside. *Cells.* 2020;9(4).
3. Fan Y, **Lesina M**, and Algul H. Subtypes of pancreatic stellate cells and distant metastasis of pancreatic ductal adenocarcinoma. *Ann Transl Med.* 2020;8(11):671.
4. Wormann SM, Diakopoulos KN, **Lesina M**, and Algul H. The immune network in pancreatic cancer development and progression. *Oncogene.* 2014;33(23):2956-67.
5. **Lesina M**, Wormann SM, Neuhofer P, Song L, and Algul H. Interleukin-6 in inflammatory and malignant diseases of the pancreas. *Seminars in immunology.* 2014;26(1):80-7.
6. Algul H, Treiber M, **Lesina M**, and Schmid RM. Mechanisms of disease: chronic inflammation and cancer in the pancreas--a potential role for pancreatic stellate cells? *Nature clinical practice Gastroenterology & hepatology.* 2007;4(8):454-62.

6 Danksagung

An dieser Stelle möchte ich ganz herzlich all denen danken, die zum Gelingen dieser Arbeit beigetragen haben.

Zu allererst möchte ich mich bei meiner Familie bedanken. Meine Mutter und mein Vater weckten mein Interesse für die Wissenschaft und standen mir während meines Studiums immerzu unterstützend und liebevoll zur Seite. Ganz besonders danke ich meinen beiden Töchtern, Olga und Maria, die mich inspirieren und mir jeden Tag Kraft und Mut geben. Ihnen allen sei die vorliegende Arbeit gewidmet.

Großer Dank gilt Herrn Prof. Dr. Schmid, welcher mich in der von ihm geleiteten Abteilung während meiner ersten wissenschaftlichen Schritte in der Tumorbiologie begleitete und unterstützte.

Weiterhin danke ich allen Mitarbeitern unserer Arbeitsgruppe für die herzliche und sehr produktive Arbeitsatmosphäre, die praktische Hilfe im Laboralltag und auch für den wissenschaftlichen Gedankenaustausch.

Unermesslichen Dank möchte ich Herrn Prof. Dr. med. Hana Algül aussprechen, der nicht nur die Betreuung meiner Forschungsprojekte übernahm, sondern auch meine wissenschaftliche Karriere förderte. Ich danke ihm zutiefst für die motivierende und professionelle Anleitung, unsere produktiven Gespräche, für sein Vertrauen, das er mir entgegenbrachte, sowie für seine offene Art, Lebensfreude und Kampfgeist, auch in schwierigen Situationen. Ohne ihn wäre diese Arbeit nicht zustande gekommen.

Nicht zuletzt gebührt großer Dank auch meinem Partner Peter Karle und meinen engen Freunden und Freundinnen für ihre Geduld, bedingungslose Unterstützung und den Rückhalt, den sie mir in allen Lebenssituationen gaben und geben.

Cancer Cell
Article

Stat3/Socs3 Activation by IL-6 Transsignaling Promotes Progression of Pancreatic Intraepithelial Neoplasia and Development of Pancreatic Cancer

Marina Lesina,[1] Magdalena U. Kurkowski,[1] Katharina Ludes,[1] Stefan Rose-John,[2] Matthias Treiber,[1] Günter Klöppel,[3] Akihiko Yoshimura,[4] Wolfgang Reindl,[1] Bence Sipos,[5] Shizuo Akira,[6] Roland M. Schmid,[1,*] and Hana Algül[1,*]
[1]II. Medizinische Klinik, Klinikum rechts der Isar, Technische Universität München, 81675 Munich, Germany
[2]Institute of Biochemistry, Christian-Albrechts-University of Kiel, 24098 Kiel, Germany
[3]Institute of Pathology, Technische Universität München, 81675 Munich, Germany
[4]Department of Microbiology and Immunology, Keio University School of Tokyo, and Japan Science and Technology Agency (JST), CREST, Chiyoda-ku, 102-0075 Tokyo, Japan
[5]Department of Pathology, Universitätsklinikum Tübingen, 72076 Tübingen, Germany
[6]Laboratory of Host Defense, WPI Immunology Frontier Research Center, Osaka University, 565-0871 Osaka, Japan
*Correspondence: hana.alguel@lrz.tum.de (H.A.), roland.schmid@lrz.tum.de (R.M.S.)
DOI 10.1016/j.ccr.2011.03.009

SUMMARY

Physiological levels of *Kras*^{G12D} are sufficient to induce pancreatic intraepithelial neoplasias (PanINs); the mechanisms that drive PanIN progression are unknown. Here, we establish that, in addition to oncogenic *Kras*^{G12D}, IL-6 transsignaling-dependent activation of Stat3/Socs3 is required to promote PanIN progression and pancreatic ductal adenocarcinoma (PDAC). Myeloid compartment induces Stat3 activation by secreting IL-6; consequently, IL-6 transsignaling activates Stat3 in the pancreas. Using genetic tools, we show that inactivation of IL-6 transsignaling or Stat3 inhibits PanIN progression and reduces the development of PDAC. Aberrant activation of Stat3 through homozygous deletion of *Socs3* in the pancreas accelerates PanIN progression and PDAC development. Our data describe the involvement of IL-6 transsignaling/Stat3/Socs3 in PanIN progression and PDAC development.

INTRODUCTION

Despite the considerable efforts that have been made in basic and clinical research, pancreatic ductal adenocarcinoma (PDAC) affects 230,000 patients in the Western Hemisphere annually. PDAC is notable for its high mortality, constituting the fourth leading cause of death due to cancer (Hidalgo, 2010).

Recent efforts have helped identify the molecular genetic determinants of PDAC. Activating *KRAS* mutations have been detected in 30% of pancreatic intraepithelial neoplasias (PanINs), which are precursor lesions, increasing to 100% in advanced PDACs. Inactivation of *INK4A* and *TRP53* occurs later during PanIN progression and PDAC formation (Hruban et al., 2006).

These findings have been mirrored in mouse models. Pancreas-specific expression of mutations (*Kras*^{G12D}, *Kras*^{G12V}, *Kras*^{G12D}, *Trp53*^{R172H}) or deletion of tumor suppressor genes (*Trp53*, *Ink4A/Arf*) in genetically engineered mice (GEM) recapitulates PanIN initiation and progression to pancreatic cancer (PC), similar to the clinical pathology (Aguirre et al., 2003; Guerra et al., 2007; Hingorani et al., 2003, 2005; Kelly et al., 2008). Although it has been studied in GEM for pancreatic cancer, the role of concomitant stromal reactions (stromal desmoplasia) in PanIN progression and cancer development has not been addressed; most existing concepts have merely been inferred.

The presence of stromal desmoplasia is a hallmark of PDAC (Algul et al., 2007b), forming a unique microenvironment that comprises many cell types, including proliferating fibroblasts and pancreatic stellate cells that produce and deposit fibronectin and collagen, and inflammatory cells and macrophages that release chemokines and cytokines. In particular, the function of concomitant inflammation in PDAC has garnered recent interest, because proinflammatory markers in the serum, such

Significance

Despite the availability of current multimodal therapies, treatment outcomes in pancreatic ductal adenocarcinoma (PDAC) are poor, generating overall survival rates of less than 5%. Late diagnosis, early metastasis, and the lack of a specific therapy contribute to this dismal prognosis. Although genetic studies have observed that activating *Kras* mutations are the initial, frequently occurring genetic alterations, signaling pathways that drive PanIN progression have not been described. In this study, we implicate the IL-6 transsignaling/Stat3/Socs3 pathway as an important mediator of PanIN progression and PDAC development.

as interleukin (IL)-1β and IL-6, are associated with outcomes in PDAC (Ebrahimi et al., 2004; Sawai et al., 2003). Additionally, chronic pancreatitis is a risk factor for PDAC, supporting the involvement of concomitant inflammation in pancreatic oncogenesis (Lowenfels et al., 1993).

Dysregulated activation of **s**ignal **t**ransducer and **a**ctivator of **t**ranscription (Stat) family members occurs often in many human malignancies. Of the seven Stat proteins, activation of Stat3 in cancer is related to tumor growth directly through tumor-autonomous mechanisms and indirectly by modulating tumor-associated stroma and the immune system. Activation depends on the phosphorylation of a conserved tyrosine residue (Y705) by upstream kinases, such as Janus kinase 2 (Jak2). Jak2 activation requires activation of the ubiquitously expressed gp130 receptor by specific ligands (IL-6, leukemia inhibitor factor [LIF], IL-11, oncostatin M [OSM], ciliary neurotrophic factor [CNTF], IL-27).

Of these ligands, IL-6 has the unique capacity to activate Stat3 using two modes. The first mode entails classical signaling mechanisms, characterized by the binding of IL-6 to the IL-6 receptor (IL-6R) and gp130 on specific target cells. However, a few subsets of cells, such as monocytes/macrophages and hepatocytes, express the membrane-bound IL-6R, whereas gp130 is ubiquitously expressed. Alternatively, IL-6 binds to a naturally occurring soluble form of IL-6R (sIL-6R), forming a complex that induces IL-6-specific signaling in cells that lack membrane-bound IL-6R, a process that is called IL-6 transsignaling. In humans, sIL-6R is generated either by alternative splicing or by proteolytic release of the ectodomain of the membrane-bound IL-6R, whereas in the mouse, sIL-6R is exclusively generated by proteolysis (Rose-John and Heinrich, 1994). All of these events result in the dimerization of phosphorylated Stat3 monomers via Src homology-2 (SH2) domains, shifting them into a transcriptionally active conformation. Stat3 regulates its own endogenous inhibitor, Socs3, to form a negative feedback loop (Yu et al., 2009).

Stat3 activation in PDAC has been documented in human tissues and pancreatic cancer cell lines, although the mechanism of Stat3 activation in the absence of *JAK2* mutations and its function in pancreatic oncogenesis has not been examined (Kocher et al., 2007; Scholz et al., 2003).

In the present study, we aim to identify the role of the IL-6 dependent Stat3 signaling pathway in pancreatic cancer using genetically engineered mouse models.

RESULTS

Non-Cell-Autonomous Activation of Stat3^{Y705} in Pancreatic Cancer

Although Stat3 activation occurs in human PanIN, PC, and pancreatic cancer cell lines, its function in pancreatic carcinogenesis has not been examined (Scholz et al., 2003). First, we determined whether this finding could be repeated in *Kras*^{G12D} mice. *Kras*^{G12D} mouse lines express a constitutively active form of mutated K-Ras in the pancreas, thereby recapitulating the entire spectrum of pancreatic carcinogenesis that is observed in humans (Hingorani et al., 2003).

Phosphorylation of Stat3^{Y705} was analyzed in four PDACs (ID 14128, 9907, 17027, 16069) (see Table S1 available online) derived from *Kras*^{G12D} mice by immunohistochemistry (IHC) and immunoblot (IB). By IB, p-Stat3^{Y705} levels were highest in PDAC (ID 9907, 16069, 17027) compared with 18 week old non-tumor *Kras*^{G12D} mice, which harbor numerous low-grade PanIN lesions. Normal pancreas (LSL-*Kras*^{G12D}) was negative for p-Stat3^{Y705} (Figure 1A).

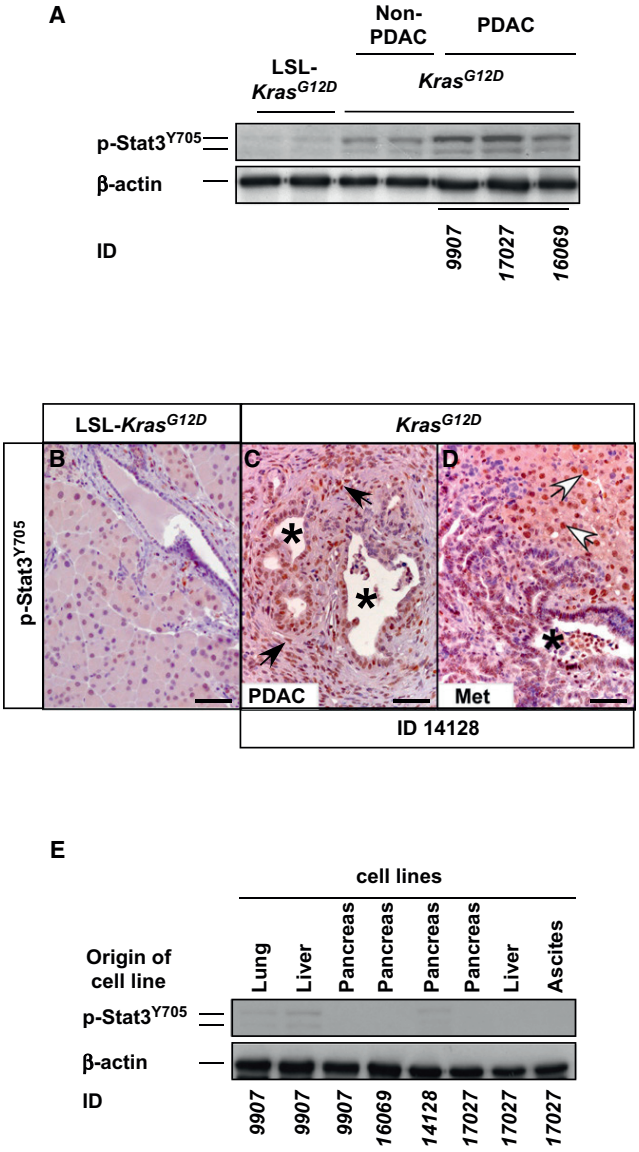

Figure 1. Non-Cell-Autonomous Activation of Stat3^{Y705} in Pancreatic Cancer

(A) Western blot analysis of p-Stat3^{Y705} in normal pancreas (LSL-*Kras*^{G12D}) and 18 week old noncancer-bearing *Kras*^{G12D} (non-PDAC) and cancer-bearing *Kras*^{G12D} (PDAC) (ID 9907, 16069, 17027) mice.

(B–D) Immunohistochemical analysis of p-Stat3^{Y705} in LSL-*Kras*^{G12D} pancreas (B), pancreatic cancer (C), and liver metastases (D) from *Kras*^{G12D} mice (representative PDAC, ID 14128). Black arrows indicate p-Stat3^{Y705} in infiltrating cells (C); white arrows indicate hepatocytes (D). Black stars indicate malignant cells.

(E) Various cell lines from primary tumors and metastases were examined for constitutive phosphorylation of Stat3. β-actin served as the control. Scale bars equal 50 μM.

See also Table S1.

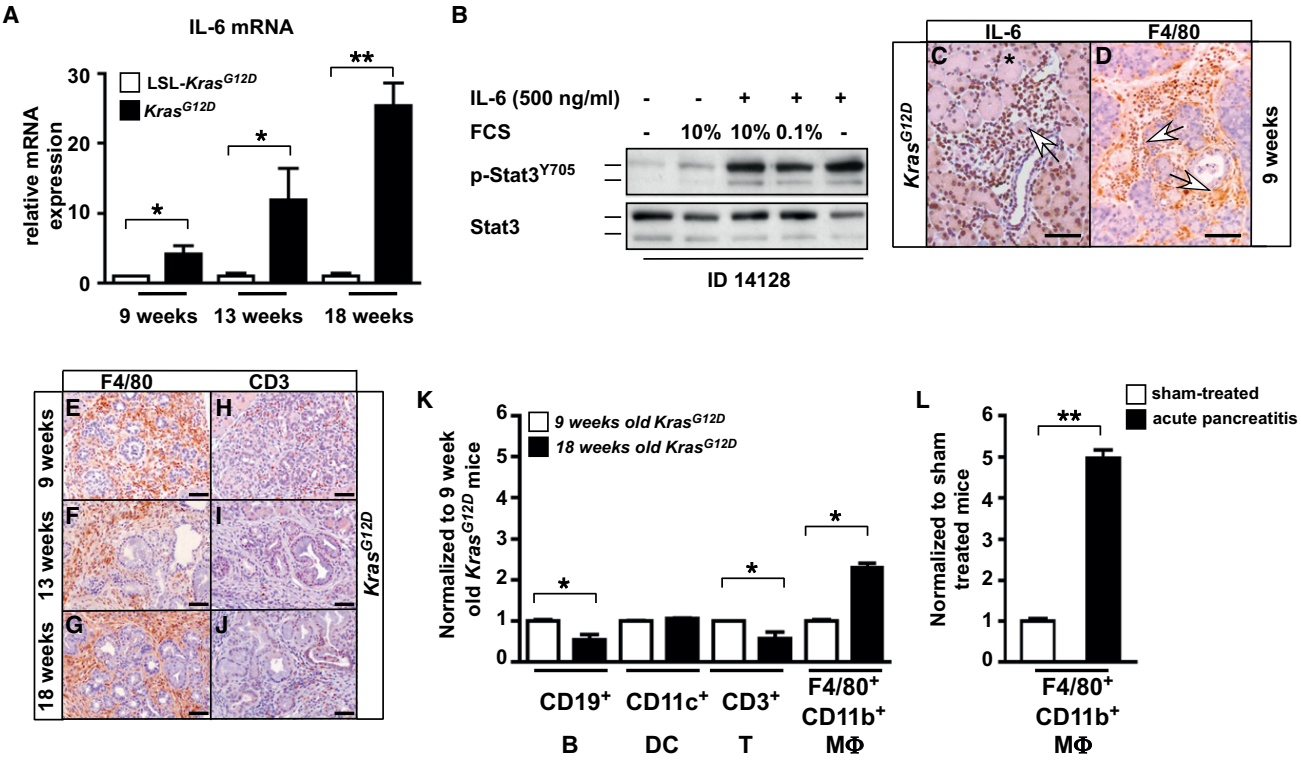

Figure 2. Myeloid Cells are the Cellular Source of IL-6

(A) Relative expression of IL-6 mRNA in whole pancreas in 9, 13, and 18 week old $Kras^{G12D}$ mice. Data are expressed as fold increase compared with controls (LSL- $Kras^{G12D}$ mice). Means ± SD ($n \geq 5$). *$p < 0.05$. **$p < 0.005$.

(B) IL-6-dependent activation of p-Stat3^{Y705} in one representative PDAC cell line (ID 14128).

(C and D) Immunohistochemical localization of F/80 and IL-6 in the pancreas of 9 week old $Kras^{G12D}$ mice. White arrows indicate infiltrating cells; black star indicates acini.

(E–J) Immunohistochemical staining of F4/80 and CD3 in the pancreas of 9, 13, and 18 week old $Kras^{G12D}$ mice.

(K) Pancreata from three mice were pooled and analyzed for macrophages ($CD45^+$ $F4/80^+CD11b^+CD11c^-$), dendritic cell ($CD45^+CD11c^+CD11b^+F4/80^-$), T cell ($CD45^+CD3^+$), and B cell ($CD45^+CD19^+$) content by fluorescence-activated cell sorting (FACS). The percentages of these cells were determined and normalized to 9 week old mice. Means ± SD (n = 3), *$p < 0.05$.

(L) Percentages of macrophages ($CD45^+F4/80^+CD11b^+CD11c^-$) in the pancreas during acute pancreatitis. Acute pancreatitis was induced by repetitive hourly injections of cerulein. Pancreata from three C57BL/6 mice were pooled and analyzed by FACS. Means ± SD (n = 3), **$p < 0.005$. Scale bars equal 50 μM.

See also Figure S1.

By IHC of PDAC (ID 14128) in $Kras^{G12D}$ mice, we observed strong phosphorylation of Stat3 at tyrosine residue 705 in primary cancers (Figure 1C) and their metastases (Figure 1D) in contrast to normal pancreas (LSL-$Kras^{G12D}$) (Figure 1B), similar to findings in humans. Notably, p-Stat3^{Y705} was restricted to malignant cells (Figure 1B, black stars) and infiltrating cells (Figure 1B, black arrows) or hepatocytes (Figure 1B, white arrows) that surrounded the metastasis. These data suggest that the level of Stat3 activation correlates with the progression of PanINs to PDAC. Moreover, Stat3^{Y705} phosphorylation is restricted to malignant cells and cells in the microenvironment.

To examine the mechanism of Stat3 activation in vitro, we generated cell lines from primary (pancreas) and metastatic (liver, lung, ascites) tumors (ID 9907, 16069, 17027; see Table S1). In contrast to their primary tumors or metastases, the isolated cancer cell lines showed low-level Stat3 activation in vitro or none at all (Figure 1E; for ID numbers, see Table S1). This observation is consistent with non-cell-autonomous phosphorylation of Stat3. Likely, Stat3 phosphorylation depends on the microenvironment of the PDAC.

To determine the mechanisms and factors through which Stat3 is phosphorylated in vivo, we measured the expression of gp130 ligands (IL-6, LIF, OSM, CNTF, IL-11) in the pancreas of $Kras^{G12D}$ mice, because these ligands activate the Stat3 cascade. Only IL-6 mRNA levels increased robustly and time dependently (Figure 2A); the levels of LIF, OSM, CNTF, and IL-11 remained unchanged or rose slightly (Figure S1A). The primary cancer cell lines that were derived from $Kras^{G12D}$ mice (ID 14128) responded to IL-6, experiencing strong phosphorylation of Stat3 (Figure 2B).

Due to its high expression in nontumor $Kras^{G12D}$ mice and its abilty to activate the Stat3 cascade in PDAC cell lines, we determined the cellular source of IL-6. By IHC, IL-6 was expressed predominantly by infiltrating immune cells (Figure 2C, white arrow); acinar cells expressed low levels (Figure 2C, black star). These pancreatic infiltrates in $Kras^{G12D}$ mice comprised

primarily F4/80-positive macrophages (Figures 2D and 2E–2G) and rare CD3-positive (Figures 2H–2J) cells. The inflammatory response in $Kras^{G12D}$ mice was accompanied by the elevated expression of MCP-1, MIP-2, KC, MIP-1α, IL-1β, and ICAM-1 mRNA (Figure S1B).

To characterize the cellular composition of these infiltrates, we digested the pancreas to immunophenotype the inflammatory cells. By flow cytometry, among CD45-positive cells in $Kras^{G12D}$ mice, the fraction of $F4/80^+CD11b^+$ (macrophages, $CD45^+F4/80^+CD11b^+CD11c^-$) cells increased, as did $CD11c^+$ cells (dendritic cells, $CD45^+CD11c^+CD11b^+F4/80^-$) to a lesser extent (Figure 2K). However, the accumulation of $F4/80^+CD11b^+$ cells (macrophages) was less compared with that in acute pancreatitis (AP) (Figure 2L). Consistent with the immunohistochemistry findings, the cellular proportion of lymphocytes did not increase.

In summary, our data demonstrate the time-dependent recruitment of inflammatory cells to the pancreas in $Kras^{G12D}$ mice. We identified macrophages ($CD45^+F4/80^+CD11b^+CD11c^-$) as the chief component of the cellular infiltrate and the source of IL-6 during pancreatic oncogenesis.

IL-6 Transsignaling Promotes PanIN Progression

Based on these findings, we hypothesized that Stat3 activation in pancreatic oncogenesis depends on the microenvironment, particularly on myeloid cells that secrete the gp130 ligand IL-6. To examine the interaction between macrophages and acinar cells that harbor $Kras^{G12D}$, we developed a coculture system in which macrophages were isolated from the pancreas of 18 week old $Kras^{G12D}$ mice and incubated with acinar cells derived from $Kras^{G12D}$ mice. Even prestimulation of the macrophages with IL-6 was insufficent to induce robust Stat3 activation in $Kras^{G12D}$ acinar cells. These data suggest that factors other than IL-6 are required to activate Stat3 in acinar cells from $Kras^{G12D}$ mice (Figure S2A).

IL-6 signals are transmitted via gp130 through IL-6 engagement of IL-6R or formation of a complex with soluble IL-6R, that latter of which is called IL-6 transsignaling. To determine the effects of IL-6 on the pancreas, we extended our in vitro analysis in acinar cells that were isolated from $Kras^{G12D}$ mice.

As shown in Figure 3A, only the IL-6R/IL-6 complex (termed as Hyper-IL-6) induced robust phosphorylation of Stat3 in acinar cells; IL-6 resulted only in slight phosphorylation. These data suggest that acinar cells require IL-6 transsignaling, rather than classical IL-6 signaling, to activate Stat3 in response to IL-6.

To characterize the impact of classical and IL-6 transsignaling on PanIN progression in vivo, $Kras^{G12D}$ mice were interbred with $Il\text{-}6^{-/-}$ and $sgp130^{tg}$ mice to obtain $Kras^{G12D};Il\text{-}6^{-/-}$ and $Kras^{G12D};sgp130^{tg}$ mice. Transgenic $sgp130^{tg}$ mice postnatally overexpress circulating sgp130Fc postnatally under control of the hepatic PEPCK promoter, thereby specifically inhibiting IL-6 transsignaling (Rabe et al., 2008). The genetic deletion of IL-6 in $Il\text{-}6^{-/-}$ mice occurs in the germ line and affects classical and IL-6 transsignaling. These strains were observed for 18 weeks.

By histology, $Kras^{G12D}$ mice developed numerous MUC5-positive (Figure 3D), low- and high-grade PanINs (Figures 3B and 3C, black arrow and black star) at 18 weeks, while $Kras^{G12D};Il\text{-}6^{-/-}$ mice had fewer and predominantly low-grade PanINs (Figures 3E–3G). Notably, postnatal inactivation of IL-6 transsignaling in $Kras^{G12D};sgp130^{tg}$ mice had a similar effect on PanIN formation: PanIN-1 and PanIN-2 lesion numbers fell significantly in these mice (Figures 3H–3K). Impaired PanIN progression correlated with phosphorylated Stat3 levels in the pancreas; IHC and IB analysis demonstrated less phosphorylated Stat3 on tyrosine 705 in $Kras^{G12D};Il\text{-}6^{-/-}$ and $Kras^{G12D};sgp130^{tg}$ mice compared with $Kras^{G12D}$ mice (Figures 3L–3O).

Similar results were observed in reciprocal bone marrow chimeras. Bone marrow from wild-type (WT) ($Il\text{-}6^{+/+}$) or $Il\text{-}6^{-/-}$ mice was introduced into irradiated $Kras^{G12D}$, according to the schedule in Figure S2B. As shown in Figure S2C, reconstitution of $Kras^{G12D}$ mice with IL-6-competent ($Il\text{-}6^{+/+}$) bone marrow ($BM\text{-}Il\text{-}6^{+/+}Kras^{G12D}$) induced PanIN progression, as evidenced by PanIN-3 lesions throughout the entire pancreas in three of the four transplanted mice. None of the $BM\text{-}Il\text{-}6^{-/-}Kras^{G12D}$ mice developed high-grade PanIN lesions (Figures S2D–S2G). Accordingly, Stat3 phosphorylation in PanIN lesions was attenuated in $BM\text{-}Il\text{-}6^{-/-}Kras^{G12D}$ mice (Figures S2H–S2I).

Collectively, these data suggest that myeloid cells use IL-6 transsignaling rather than classical IL-6 signaling to promote PanIN progression. The downstream effector Stat3 appears to be associated with the development of PanIN lesions.

Stat3 Constitutes a Central Node that Mediates PanIN Progression and PDAC Development

Because Stat3 is considered the major protumorigenic effector of IL-6, we determined the contribution of pancreatic Stat3 to PanIN progression and PC development. By immunofluorescence, we observed early phosphorylation of Stat3 at tyrosine residue 705 in the pancreas of 13-week-old $Kras^{G12D}$ mice (Figures 4A–4C, white star) and in infiltrating macrophages (Figures 4A–4C, white arrows). In parallel, the expression of *bona fide Stat3* target genes increased in the pancreas of these mice (data not shown). The widespread phosphorylation of Stat3 in the pancreas clearly suggested paracrine/autocrine stimulation rather than a cell-autonomous effect.

To examine the effect of Stat3 activation in the exocrine pancreas during oncogenesis, we generated compound mutant $Kras^{G12D}$ mice that lacked phosphorylatable $Stat3^{Y705}$ specifically in the exocrine pancreas and parts of the endocrine compartment using the $Ptf1a\text{-}cre^{ex1}$ mouse line ($Kras^{G12D};Stat3^{\Delta panc}$) (Algul et al., 2007a; Nakhai et al. 2007; Sano et al., 1999). *Stat3* inactivation had no effect on pancreatic development in adult mice, and basal proliferation rate and apoptotic index were indistinguishable between $Stat3^{\Delta panc}$ and $Stat3^{F/F}$ under steady-state conditions (to be published elsewhere).

Inactivation of the Stat3 pathway was confirmed by IB analysis. Whereas $Kras^{G12D}$ mice experienced strong Stat3 phosphorylation at tyrosine residue 705 at 9 and 13 weeks, *Stat3*-deficient $Kras^{G12D}$ mice failed to express p-$Stat3^{Y705}$. In contrast, Stat1 phosphorylation did not differ between genotypes (Figure 4D). Consistent with the $Kras^{G12D}$ expression in both mouse lines, total protein lysates from the pancreata of compound mutant mice expressed increased levels of activated and GTP-bound Ras (not significant between lines), concomitant with the induction of the downstream targets ERK1 and ERK2 (Figure 4E).

Notably, the typical macroscopic appearance (enlarged pancreas and focally nodular parenchyma) of $Kras^{G12D}$ mice was absent in $Kras^{G12D};Stat3^{\Delta panc}$ mice 13 weeks postpartum (p.p.); the $Kras^{G12D};Stat3^{\Delta panc}$ pancreas was similar to that in

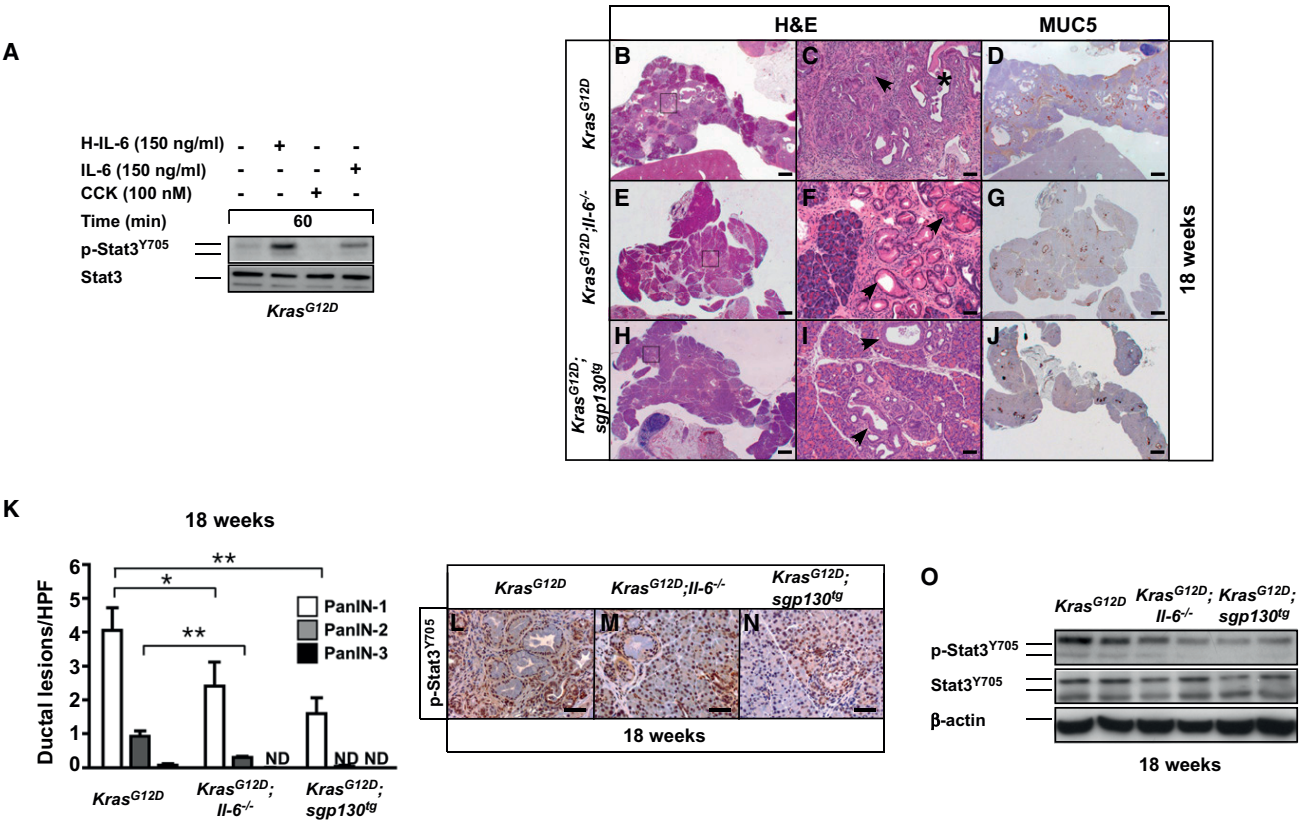

Figure 3. IL-6 Transsignaling Promotes PanIN Progression

(A) Stimulation of isolated acinar cells derived from *Kras*^{G12D} mice. Acinar cells were incubated with CCK (100 nM), IL-6 (150 ng/ml), or Hyper-IL-6 (H-IL-6 150 ng/ml) or were untreated. Lysates were analyzed for p-Stat3^{Y705}. Stat3 served as the positive control.

(B–J) Representative H&E-stained pancreatic sections from 18 week old *Kras*^{G12D} (B and C), *Kras*^{G12D};*Il-6*$^{-/-}$ (E and F), and *Kras*^{G12D};*sgp130*^{tg} mice (H and I). Black star indicates PanIN-3 lesions; black arrows indicate PanIN-1 lesions. Immunohistochemical analysis of MUC5 in the pancreas of 18 week old *Kras*^{G12D} (D) *Kras*^{G12D};*Il-6*$^{-/-}$ (G) and *Kras*^{G12D};*sgp130*^{tg} (J) mice.

(K) Number of PanINs was counted per 200x field. Means ± SD (n = 6), *p < 0.05 and **p < 0.005; ND, (not detectable).

(L–N) Immunohistochemical detection of p-Stat3^{Y705} in 18 week old mice of the indicated genotypes.

(O) Immunoblot analysis of p-Stat3^{Y705} and Stat3 in lysates from *Kras*^{G12D}, *Kras*^{G12D};*Il-6*$^{-/-}$, and *Kras*^{G12D};*sgp130*^{tg} mice.

Scale bars equal 500 μM (B, E, H, D, G, and J) and 50 μM (C, F, I, L, M, and N). See also Figure S2.

LSL-*Kras*^{G12D} mice (Figure 4F). Histologically, *Kras*^{G12D} mice developed progressive PanIN lesions (Figures 4G–4L, black arrow), which was not observed in *Kras*^{G12D};*Stat3*$^{\Delta panc}$ mice (Figures 4M–4R). Only rare reactive ducts (Figure 4P, white arrow) and low-grade PanIN lesions (PanIN-1) (Figure 4R, black arrow) were detectable in 13 and 18 week old mice, suggesting that *Stat3* inactivation in the pancreas prevents PanIN progression but not its initiation (Figure 4S).

To determine whether Stat3 inactivation influences PDAC development, we followed two cohorts, 20 *Kras*^{G12D} and 41 *Kras*^{G12D};*Stat3*$^{\Delta panc}$ mice, for nearly two years (Table 1; Table S1). The mice were sacrificed when they became moribund, particularly if they presented with weight loss, ascites, jaundice, a palpable abdominal mass, or any other compromising disease.

Only 24.5% (10/41) of the *Kras*^{G12D};*Stat3*$^{\Delta panc}$ mice developed PC, and 55% (11/20) of *Kras*^{G12D} mice succumbed to PC (Figure 4T). Tumor proliferation index was significantly lower in Stat3-deficient *Kras*^{G12D} mice compared with *Kras*^{G12D} animals (Figure 4U). Tumors from *Kras*^{G12D};*Stat3*$^{\Delta panc}$ mice did not express nuclear Stat3 in the primary cancer or its metastasis (Figures S3A and S3B); in adjacent tissues, p-Stat3^{Y705} expression was restricted to inflammatory cells (Figure S3C). Accordingly, cell lines from *Kras*^{G12D};*Stat3*$^{\Delta panc}$ mice did not respond to IL-6 (Figure S3D) because they failed to phosphorylate Stat3.

Consequently, proliferation was delayed after incubation with various concentrations of FCS (Figure S3E) and IL-6 (Figures S3F). Similar results were obtained when these cell lines were incubated with Hyper-IL-6 (data not shown). These cell lines expressed a slightly smaller version of Stat3, termed as Stat3$^{\Delta panc}$.

Collectively, our data suggest that epithelial Stat3 is required for the transduction of tumor-promoting signals of IL-6, particularly during the progression of PanIN to PDAC, but not in the initiation of PanIN.

Stat3 Regulates Cell-Autnomous Effects during Pancreatic Oncogenesis in *Kras*^{G12D} Mice

Apoptosis is a rare event in early and late PanIN lesions, while proliferation is detectable and predominant throughout progression (Luttges et al., 2003). Thus, we analyzed these aspects to determine the molecular mechanisms by which Stat3 confers

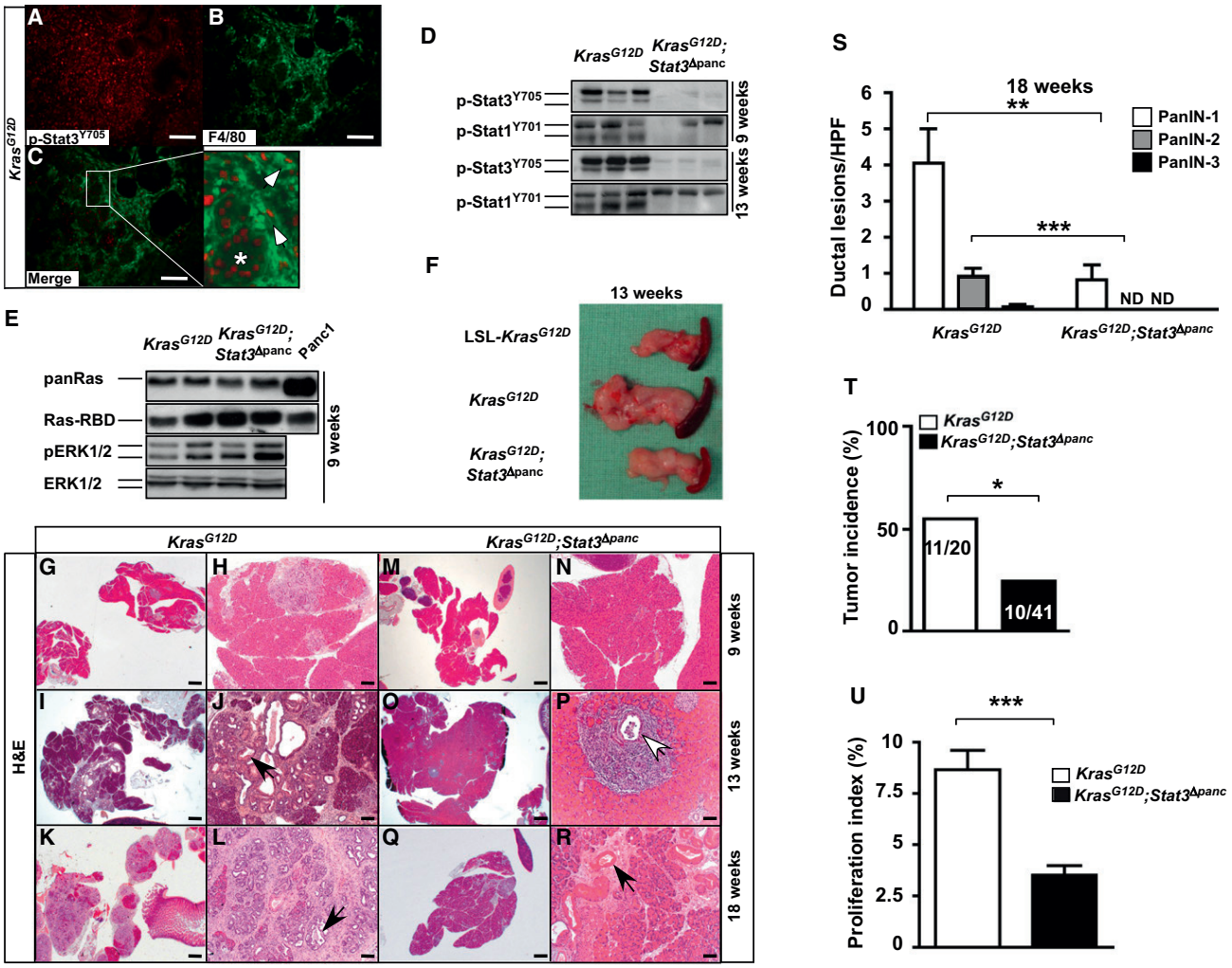

Figure 4. Stat3 Is Essential for PanIN Progression

(A–C) Immunofluorescence analysis of p-Stat3^{Y705} and F4/80 in pancreata of 13 week old LSL-*Kras*^{G12D} mice. White arrows indicate F4/80-positive macrophages, white star acini (see magnification).

(D) Immunoblot analysis of p-Stat3^{Y705} and p-Stat1^{Y701} in lysates from *Kras*^{G12D} and *Kras*^{G12D};*Stat3*$^{\Delta panc}$ mice.

(E) Immunoprecipitation of activated Ras with Raf-1 RBD agarose. Immunoblot analysis with anti-Ras and p-ERK1/2 and ERK1/2. Panc-1 lysates were positive controls.

(F) Macroscopic view of pancreas from LSL-*Kras*^{G12D}, *Kras*^{G12D}, and *Kras*^{G12D};*Stat3*$^{\Delta panc}$ mice.

(G–R) Representative H&E-stained sections from mice of the indicated genotypes. Black arrows indicate PanIN lesions; white arrow is reactive ducts.

(S) Number of PanINs was counted per 200x field. Means ± SD (n = 6), **p < 0.005, ***p < 0.0005. ND, not detectable.

(T) Determination of tumor incidence in both mouse cohorts, *p < 0.05.

(U) Proliferation index was measured in BrdU-stained PC sections from *Kras*^{G12D} (n = 9) and *Kras*^{G12D};*Stat3*$^{\Delta panc}$ mice. Means ± SD (n = 5), ***p < 0.0005. Scale bars equal 50 μM (A, B, C, H, J, L, N, P, and R) and 500 μM (G, I, K, M, O, and Q). See also Figure S3.

its tumorigenic properties. To examine whether pancreas-specific inactivation of the Stat3 cascade renders acinar/ductal cells more susceptible to apoptosis, we measured caspase-3 cleavage in 13 week old mice by IHC.

Many acinar and ductal cells in the pancreas of *Kras*^{G12D};*Stat3*$^{\Delta panc}$ mice were positive for cleaved caspase-3 (Figure 5A, magnified box), which was absent in *Kras*^{G12D} mice (Figure 5B, magnified box); this finding was confirmed by quantification (Figure 5C) and immunoblot analysis (data not shown). By immunoblot, Bcl-X_L, Survivin, and Mcl-1 were upregulated in *Kras*^{G12D} mice but absent in *Kras*^{G12D};*Stat3*$^{\Delta panc}$ mice, consistent with findings that *bcl-x*, *survivin,* and *mcl-1* are transcriptionally induced by Stat3 (Figure S4A) (Yu et al., 2009).

To determine whether Stat3 regulates proliferation in the pancreas of *Kras*^{G12D} mice, we injected mice with 5-bromo-2-deoxyuridine (BrdU), which incorporates into newly synthesized DNA, and sacrificed the animals two hours later. By anti-BrdU staining, we observed the time-dependent incorporation of BrdU into acinar and ductal cells (data not shown), but mice that were deficient for phosphorylable Stat3^{Y705} expressed fewer BrdU-positive cells in the pancreas, even after 13 weeks of age (Figure 5D). Consistent with this result, proliferating cell

Table 1. Clinical Spectrum of Diseases in *Kras^{G12D};Stat3$^{\Delta panc}$* Mice

ID	Age (days)	PDAC	Histology	Liver	Lung	Diaphragm	Ascites	Other
302	369	Y	G	Y^M	Y^M	N	N	BO, pLN
303	240	N		N	N	N	N	A
317	480	N		N	N	N	N	A
320	426	N		N	N	N	N	A
321	484	Y	U	Y^M	N	N	N	P
322	537	N		N	N	N	N	A
352	445	Y	U	Y^M	Y^M	Y^M	N	pLN
362	329	Y	G	Y^M	Y^M	N	N	BO
365	381	Y	G	N	N	N	Y	
370	314	N		N	N	N	N	SD
371	213	N		N	N	N	N	
407	361	Y	U	N	N	N	N	P
408	396	N		N	N	N	N	A
419	445	Y	U	N	N	N	N	
2163	413	Y	U	Y^M	N	N	Y	pLN, BO
2206	113	N		N	N	N	N	SD
2755	331	N		N	N	N	N	A, SD
2756	239	N		N	N	N	N	
2827	213	N		N	N	N	N	P
2865	489	N		N	N	N	N	A
2950	573	N		N	N	N	N	A
2951	438	N		N	N	N	N	A
2959	306	N		N	N	N	N	A
2969	386	N		N	N	N	N	A, SD
2992	136	Y	G	N	N	N	N	
3038	707	N		N	N	N	N	A, SD
3045	447	N		N	N	N	N	P
3050	699	N		N	N	N	N	A
3098	166	N		N	N	N	N	A
3103	426	N		N	N	N	N	A
3140	683	N		N	N	N	N	A
3141	418	N		N	N	N	N	A
3142	510	N		N	N	N	N	A
3144	320	N		N	N	N	N	A, P
5101	609	N		N	N	N	N	
5105	609	N		N	N	N	N	
5110	277	N		N	N	N	N	A, SD
5185	191	Y	G	N	N	N	N	SD
5277	341	N		N	N	N	N	A, SD
5311	233	N		N	N	N	N	A
5530	452	N		N	N	N	N	A
Totals		10/41		5/41	3/41	1/41	2/41	

pLN, peripancreatic lymph node; M, metastasis; pC, pancreatic cyst; U, undifferentiated; G, glandular; A, atrophy; SD, skin disease; BO, biliary obstruction; P, paralysis.

nuclear antigen (PCNA) expression was generally higher in *Kras^{G12D}* mice (Figure 5E).

Next, we identified proteins that were expressed during proliferation by generating pancreatic protein lysates from 9 and 13 week old *Kras^{G12D}* and *Kras^{G12D};Stat3$^{\Delta panc}$* mice and performing immunoblot analysis of cell cycle regulators. The time-dependent induction of Cyclin D1 and c-myc was attenuated in *Kras^{G12D};Stat3$^{\Delta panc}$* mice, suggesting that Stat3^{Y705} phosphorylation regulates proliferation during *Kras^{G12D}*-driven PanIN progression (Figure 5E).

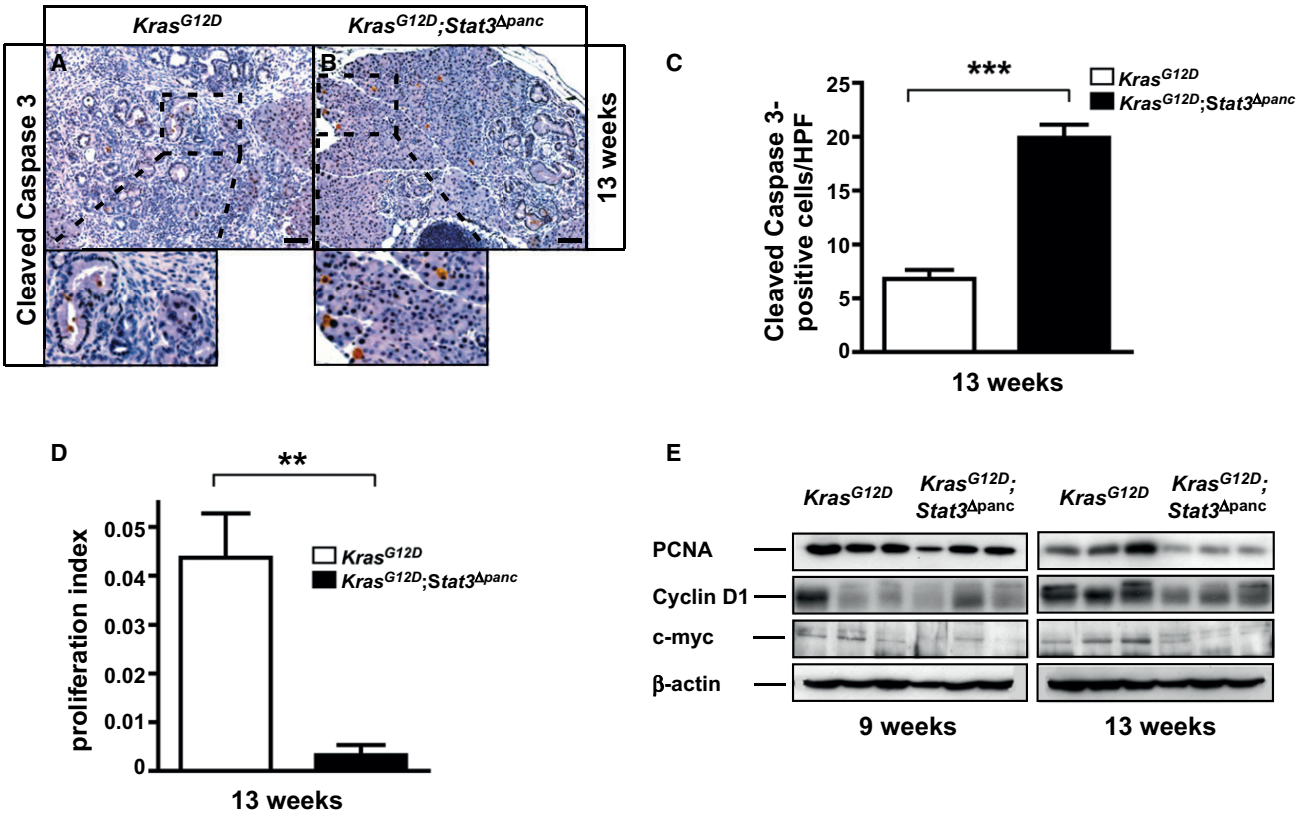

Figure 5. Stat3 Regulates Apoptosis and Influences Cell Cycle Progression during PanIN Progression

(A and B) Immunohistochemical analysis of cleaved caspase-3 in pancreata of $Kras^{G12D}$ and $Kras^{G12D};Stat3^{\Delta panc}$ mice.

(C) Apoptosis (cleaved caspase-3) index in pancreas of $Kras^{G12D}$ (n = 6 mice, 20 fields per mouse) and $Kras^{G12D};Stat3^{\Delta panc}$ mice (n = 7 mice, 20 fields per mouse). Means ± SD, ***$p < 0.0005$.

(D) BrdU proliferation index of pancreas in $Kras^{G12D}$ (n = 6 mice, 20 fields per mouse) and $Kras^{G12D};Stat3^{\Delta panc}$ mice (n = 7 mice, 20 fields per mouse). Means ± SD ($n \geq 5$), **$p < 0.005$.

(E) Immunoblot analysis of the indicated proteins in lysates from both genotypes. Scale bars equal 200 μM.

See also Figure S4.

Further, Stat3 seems to be involved in concomitant inflammation in the pancreas, as the accumulation of F4/80-positive macrophages declined in Stat3-proficient mice (Figures S4B and S4C). In addition, the Stat3-dependent and proinflammatory enzyme Cox-2 was not expressed in $Kras^{G12D};Stat3^{\Delta panc}$ mice compared with $Kras^{G12D}$ animals (Figure S4D). Cox-2 was detectable in acinar cells and in ductal lesions (Figures S4E and S4F).

Based on our data, we conclude that Stat3 activation regulates $Kras^{G12D}$-dependent effects on apoptosis, proliferation, and inflammation.

Homozygous Deletion of *Socs3* Accelerates PanIN Progression and Promotes PDAC Development

Although Stat3 regulates PanIN progression, it is unknown whether Stat3 alone is sufficient to mediate these effects. Stat3 activation is tightly regulated by the endogenous feedback inhibitor Socs3, which inhibits Stat3 signaling by binding to gp130.

$Kras^{G12D}$ mice expressed high levels of *Socs3* mRNA (Figure 6A). Socs3 was detectable in acinar cells (Figure 6B, black arrows) and PanIN lesions (Figure 6B, white arrows) of $Kras^{G12D}$ mice.

To induce early and prolonged activation of p-Stat3^{Y705} in the pancreas of these mice, we generated a mutant mouse line that lacked *Socs3* specifically in the pancreas (Nakaya et al., 2009). Hetero- or homozygous deletion of *Socs3* did not affect pancreatic morphology or cellular homeostasis (data not shown). Homozygous deletion of *Socs3* in $Kras^{G12D}$ mice ($Kras^{G12D};Socs3^{\Delta panc}$), however, induced early and high phosphorylation levels of Stat3^{Y705} in the pancreas as early as four weeks of age (Figure 6C).

At this age, $Kras^{G12D};Socs3^{\Delta panc}$ mice developed large areas of reactive ducts (Figure 6K) and low- (Figure 6H) and high-grade (Figure 6E) PanINs throughout the pancreas (Figure 6D). The nuclei of ductal lesions and acinar cells were positive for phosphorylated Stat3^{Y705} (Figures 6F–6L) and Cyclin D1 (Figures 6G–6M). By quantification of ductal lesions, we observed rapid progression of PanINs in these mice (Figure 6N).

To determine whether the deletion of Socs3 and the subsequent early and robust activation of Stat3 influences PDAC development, we monitored 41 $Kras^{G12D};Socs3^{\Delta panc}$ mice for

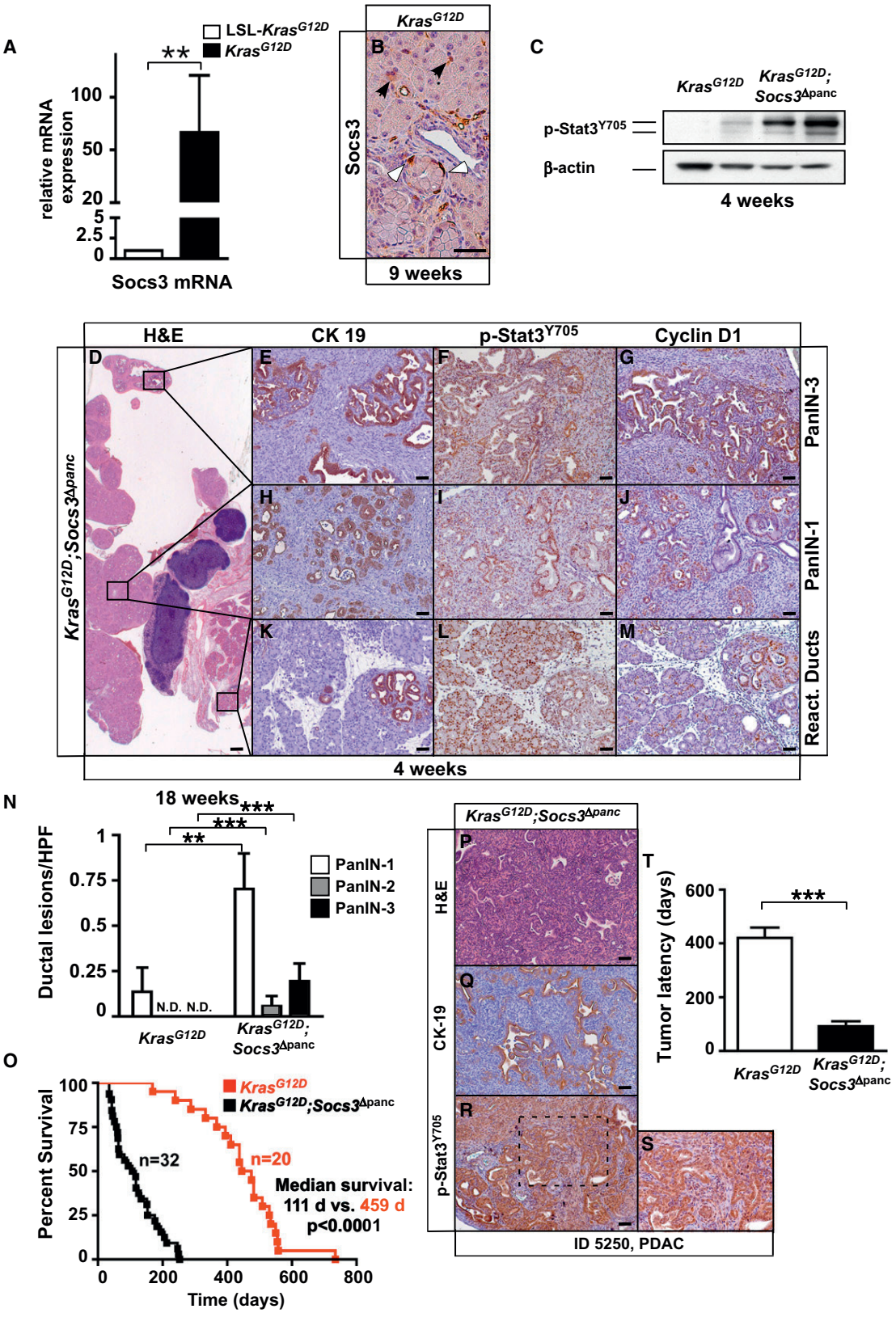
A
LSL-Kras^G12D
Kras^G12D
**
relative mRNA expression
100
50
20
5
2.5
0
Socs3 mRNA
Kras^G12D
B
Socs3
9 weeks
C
Kras^G12D
Kras^G12D; Socs3^Δpanc
p-Stat3^Y705
β-actin
4 weeks
H&E
CK 19
p-Stat3^Y705
Cyclin D1
D
E
F
G
H
I
J
K
L
M
Kras^G12D;Socs3^Δpanc
PanIN-3
PanIN-1
React. Ducts
4 weeks
N
18 weeks
***
***
**
Ductal lesions/HPF
1
0.75
0.5
0.25
0
PanIN-1
PanIN-2
PanIN-3
N.D. N.D.
Kras^G12D
Kras^G12D; Socs3^Δpanc
O
Percent Survival
100
75
50
25
0
Kras^G12D
Kras^G12D;Socs3^Δpanc
n=32
n=20
Median survival:
111 d vs. 459 d
p<0.0001
0
200
400
600
800
Time (days)
Kras^G12D;Socs3^Δpanc
H&E
CK-19
p-Stat3^Y705
P
Q
R
S
ID 5250, PDAC
T
Tumor latency (days)
600
400
200
0
***
Kras^G12D
Kras^G12D; Socs3^Δpanc

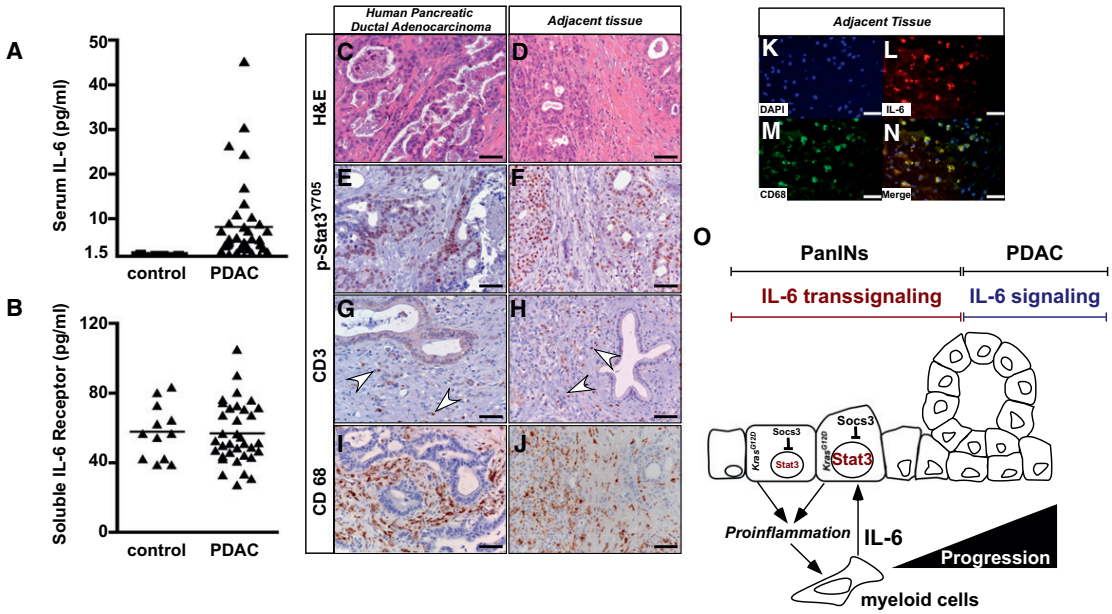

Figure 7. Evidence of IL-6/Stat3 Cascade in Human PDAC

(A and B) Analysis of IL-6 and soluble IL-6R in patients with PDAC.

(C–J) H&E staining and detection of p-Stat3^{Y705}, CD3, and CD68 in human PDAC (B–E) and in adjacent nonmalignant tissue (F–I). White arrows indicate infiltrating cells.

(K–N) Immunofluorescence analysis of human specimens. Nuclei were visualized with DAPI. Anti-IL-6 and anti-CD68 were used to label IL-6 and macrophages. Signals were merged to identify the site of IL-6 production.

(O) Scheme of the central role of Stat3 in PanIN progression and PDAC development. Scale bars equal 50 μM.

nearly one year (Table S2). The combination of activated *Kras*^{G12D} and Socs3 deficiency led to significant decreases in body and pancreatic weight (data not shown). As shown in Figure 6O, these mice reached terminal morbidity between 6 and 31 weeks of age and had a median survival of 111 days ($p < 0.0001$ for *Kras*^{G12D};*Socs3*$^{\Delta panc}$ colony compared with *Kras*^{G12D} cohort). Within the observation period, 37.5% (12/32) of *Kras*^{G12D};*Socs3*$^{\Delta panc}$ mice developed pancreatic cancer (Table S2). These ductal adenocarcinomas (Figure 6P) were positive for CK-19 (Figure 6Q) and p-Stat3^{Y705} (Figure 6R). Phosphorylated Stat3^{Y705} was restricted primarily to the nuclei of cancer cells (Figure 6S). Tumor latency in these mice was lower compared with *Kras*^{G12D} mice (93 vs 428 days, Figure 6T).

Collectively, these results suggest that levels of Stat3 phosphorylation determine the progression of PanIN lesions to pancreatic cancer.

Evidence for the IL-6/Stat3 Cascade in Human PDAC

To determine the relevance of the observed link between myeloid IL-6 and p-Stat3^{Y705} in PDAC, we measured IL-6 and soluble IL-6-receptor (sIL-6R) levels in patients with PDAC. Serum IL-6 levels in 39 patients were significantly higher than in healthy control groups (Figure 7A), and sIL-6R levels did not differ (Figure 7B).

Based on the the significantly high systemic levels of IL-6 and the presence of sIL-6R in patients, we examined whether the IL-6/Stat3 cascade was detectable locally in human specimens (Figures 7C and 7D) by performing the IHC of p-Stat3^{Y705} and IL-6 in human specimens of PDAC. Notably, Stat3 was activated in PDAC (Figure 7E) and in the acinar cells or early PanIN lesions in tumor-adjacent tissues, similar to the observations in our mouse models (Figure 7F). Most infiltrating cells were macrophages by anti-CD68 staining (Figure 7E), and CD3-positive

Figure 6. Homozygous Deletion of *Socs3* Enhances Stat3 Activation, Promotes PDAC Development, and Reduces Survival in Kras^{G12D} Mice

(A) Relative expression of Socs3 mRNA in pancreas from 9 week old *Kras*^{G12D} mice. Means ± SD ($n \geq 5$), **$p < 0.005$.

(B) Immunohistochemical localization of Socs3 in the pancreas of 9 week old *Kras*^{G12D} mice. Black arrows indicate positivity within acini, white arrows positivity within PanIN lesions.

(C) Immunoblot analysis of p-Stat3^{Y705} and β-actin in lysates from 4 week old *Kras*^{G12D} and *Kras*^{G12D};*Socs3*$^{\Delta panc}$ mice.

(D–M) Representative H&E staining and detection of CK-19, p-Stat3^{Y705}, and Cyclin D1 in pancreas from 4 week old *Kras*^{G12D};*Socs3*$^{\Delta panc}$ mice.

(N) Number of PanINs was counted per 200x field. Means ± SD ($n = 5$), **$p < 0.005$, and ***$p < 0.0005$. ND, (not detectable).

(O) Kaplan-Meier curves show a median survival in *Kras*^{G12D};*Socs3*$^{\Delta panc}$ mice of 111 days, significantly less (459 days) than *Kras*^{G12D} mice ($p < 0.0001$, log-rank test, for pairwise combination).

(P–S) Ductal adenocarcinoma (P) from an approximately 2 month old mouse (ID 5250), demonstrating CK-19 (Q) expression and abundant nuclear localization of p-Stat3^{Y705} (R, see magnification in S).

(T) Tumor latency in *Kras*^{G12D} ($n = 11$) and *Kras*^{G12D};*Socs3*$^{\Delta panc}$ ($n = 12$) cohorts. Means ± SD, ***$p < 0.0005$.

Scale bars equal 500 μM (D) and 50 μM (B, E–M, and P–R). See also Table S2.

lymphocytes were scattered around cancer cell clusters and preneoplastic lesions (Figures 7G and 7H). In tumor-adjacent tissues, macrophages were observed between nontransformed acini (Figure 7I). By immunofluorescence, macrophages were determined to be the principal source of IL-6 (Figures 7K–7N).

Collectively, these data suggest that the basis for classical IL-6 and IL-6 transsignaling, linking myeloid IL-6 to p-Stat3^{Y705} in preneoplastic or neoplastic cells, exists in human PDAC and potentially define a mechanism of pancreatic oncogenesis.

DISCUSSION

Aberrant activation of Stat3 in the absence of Jak2 mutations is a recurring theme in human PDAC; however, its implication in pancreatic oncogenesis in vivo has remained undetermined (Glienke et al., 2010; Hutzen et al., 2009; Lin et al., 2010b; Scholz et al., 2003). Using genetic and pharmacological tools, we identified important functions of IL-6 and Stat3 and their implications for multiple aspects of pancreatic oncogenesis.

Also, we detailed a signaling network between stromal and preneoplastic pancreatic cells and identified Stat3 as the critical node in this interplay. Our study provides evidence that myeloid cells release IL-6 to induce Stat3 activation in the pancreas via IL-6 transsignaling, thus potentiating a feed-forward response in the tumor microenvironment to promote PanIN progression and, ultimately, PDAC development in vivo. Genetic inactivation of classical IL-6 signaling, IL-6 transsignaling, and the Stat3 effector pathway impaired PanIN progression and PDAC development (Figure 7O).

By identifying the underlying mechanisms, we have explained the implications of IL-6 and myeloid cells in human PDAC mechanistically. Many studies have observed a robust and consistent assocation of IL-6 with patient outcomes (Ebrahimi et al., 2004; Talar-Wojnarowska et al., 2009), and a specific polymorphism of IL-6 has been reported to be overrepresented in such patients (Talar-Wojnarowska et al., 2009). The density of inflammatory cells in pancreatic carcinoma, especially of macrophages, has predictive value for patient prognoses (Kurahara et al., 2009).

In this study, we found that pancreatic myeloid cells mediate tumor promotion substantially by releasing IL-6 into the stroma. Consistent with this observation, enhanced pancreatic inflammation in *Kras*^{G12D} mice through repetitive application of the hormone cerulein accelerates PanIN progression and PDAC development, underscoring the significance of inflammatory cells in these settings (Guerra et al., 2007). Because cerulein fails to induce phosphorylation of Stat3 in acinar cells derived from *Kras*^{G12D} mice in vitro, we assume that inflammatory cells release IL-6 to induce p-Stat3 in the pancreas, thus promoting oncogenesis in this inflammation-associated model of PDAC.

The paracrine effects of IL-6, however, are not restricted to preneoplastic and cancer cells in the pancreas. We observed Stat3 activation in infiltrating macrophages and normal hepatocytes that surrounded metastatic lesions, suggesting a general effect of IL-6 on the various cells that constitute the microenvironment; whether this activation in nontransformed cells impacts oncogenesis or the formation of metastatic lesions is unknown.

The IL-6/Stat3 cascade appears to be ubiquitous—not restricted solely to the pancreas. In a model of inflammation-associated colorectal carcinogenesis, for example, myeloid IL-6 activates Stat3 to promote the formation of adenoma and tumors (Bollrath et al., 2009; Grivennikov et al., 2009). Our data do not exclude the involvement of other cytokines, because transgenic overexpression of *Il-1beta* in the pancreas has been shown to be sufficent to induce proliferation, robust desmoplasia, and rare acinar-ductal metaplasia (Marrache et al., 2008). Notably, IL-1β failed to acitvate Stat3 in pancreatic cancer cells, suggesting that other signaling pathways transmit its signals in the pancreas.

Although the involvement of IL-6 in cancer-promoting inflammation in various organs is well established, no study has implicated IL-6 or IL-6 transsignaling in spontaneous tumor formation. Using the *Kras*^{G12D} model in the pancreas, we defined a central function for IL-6 during oncogenesis.

Two distinct processes control IL-6 responses in vivo. IL-6 signals are transmitted via gp130 through IL-6 engagement of IL-6R or formation of a complex with soluble IL-6R (i.e., IL-6 transsignaling). Because IL-6R is sparsely expressed, IL-6 transsignaling increases the number of potential IL-6 target cells (Rose-John et al., 2006). Nontransformed acinar cells that express oncogenic *Kras*^{G12D} require IL-6 transsignaling to induce robust phosphorylation of Stat3. IL-6 itself is predominantly secreted by inflammatory cells, most likely in an NF-κB-dependent manner. Similarily, recruitment of these cells to the pancreas also involves induction of NF-κB, potentially as a consequence of *Kras*^{G12D} dependent activation (Finco et al., 1997). Beyond its capacity to secret IL-6, immune cells have also been shown to participate in the process of IL-6R shedding (Chalaris et al., 2007), a process that also involves the metalloproteinases ADAM17 (**a** **d**esintegrin **a**nd **m**etalloproteinase), and to a lesser extent ADAM10 (Matthews et al., 2003). In addition to its function as an important regulator of proinflammatory chemokines and cytokines, NF-κB might therefore be implicated in establishing IL-6 transsginaling during pancreatic oncogenesis (Algul et al., 2007c; Guerra et al., 2007). Whether the metallproteinases ADAM17 and ADAM10 has a role to play, and what role it plays, during pancreatic oncogenesis remains to be elucidated in further studies. Using genetic tools, we herein found that IL-6 transsignaling, not classical IL-6 signaling, entails Stat3 activation to promote PanIN progression in vivo. Thereby, our data extend previous findings implicating immune cells to include myeloid-derived suppressor cells, tumor-associated macrophages, and Treg in PDAC development (Clark et al., 2007).

The major protumorigenic IL-6 effector is Stat3, the ablation or prolonged activation in the pancreas of which influences PanIN progression but not PanIN initiation. Stat3 has been implicated in apoptosis and cell cycle progression during oncogenic (*Kras*^{G12D}) stress. We identified Stat3 activation as the chief mediator of programmed cell death. Stat3 upregulated the antiapoptotic proteins Bcl-X_L, Mcl-1, and Survivin, which were recently demonstrated to be Stat3 target genes (Yu et al., 2009). Their activity during apoptosis in pancreatic cancer has also been observed.

Inhibition of Stat3 in human pancreatic cancer cells facilitates apoptosis and inhibits chemoresistance (Lin et al. 2010a). Persistent Stat3 activation during PanIN progression also mediates the proliferation of preneoplastic lesions in the pancreas.

Similarily, deletion of IKK in hepatocytes effects chronic Stat3 activation, inducing proliferation and promoting hepatocellular carcinoma on exposure to diethylnitrosamine (He et al., 2010). Consistent with this observation, Stat3 inactivation mitigates the incorporation of BrdU in the pancreas, paralleled by impaired induction of Cyclin D1 (Masuda et al., 2002) and c-myc (Barre et al., 2005), which are regulated by nuclear Stat3 and overexpressed in human specimens of PDAC (Kawesha et al., 2000). These factors are central in driving cancer cells from G0/G1 to S phase, propelling cell cycle progression. Similarly, isolated pancreatic cancer cell lines from Stat3-deficient $Kras^{G12D}$ mice proliferated less in response to FCS, IL-6, and Hyper-IL-6.

Intracellular regulation of Stat3 activation is tightly controlled by the concomitant expression of its endogenous inhibitor, Socs3 (Yu et al., 2009). In $Kras^{G12D}$ mice, we noted high pancreatic levels of Socs3, suggesting that the activation and inhibition of Stat3 are balanced during PanIN progression. Deleting both alleles of *Socs3* in $Kras^{G12D}$ tipped this balance toward robust phosphorylation of Stat3, which accelerated the progression of PanIN lesions and the development of PC. Survival and tumor latency were curtailed in Socs3-deficient $Kras^{G12D}$ mice. Thus, we propose that the Stat3/Socs3 pathway assumes a central role during pancreatic oncogenesis.

The most notable observations pertained to tumor cells from PDAC in $Kras^{G12D}$ mice. All cancer cell lines that we examined failed to exhibit constitutive phosphorlyation of Stat3, which formed the basis for our hypothesis that Stat3 activation during pancreatic oncogenesis depends on the microenvironment. These findings contrast other studies that have observed constitutive phosphorylation of Stat3 in nearly all human pancreatic cancer cell lines (Glienke et al. 2010; Greten et al., 2002; Hutzen et al., 2009; Kim et al. 2010; Lin et al. 2010a; Scholz et al., 2003; Trevino et al., 2006).

One explanation for this discrepancy proposes that additional mutations in p53 in human cancer cell lines mediate constitutive phosphorylation of Stat3, as seen in other tumor cells (Lin et al., 2002). Wild-type p53 regulates Stat3 phosphorylation in ovarian cancer cell lines (Caov-3 and MDAH2774) by controlling Jak2 through p53-dependent upregulation of protein tyrosine phosphatase 1-B (PTP-1B), which inactivates Jak2 (Reid et al., 2004). The balance between PTP-1B and Jak2 is likely to be dysregulated in human pancreatic cancer cell lines, because nearly all established human PDAC cell lines harbour p53 mutations (Sipos et al., 2003). In contrast, such mutations were absent in the cell lines that were derived from $Kras^{G12D}$ mice (data not shown).

We have identified an important mechanism that determines the progression and development of PanIN to PDAC. $Kras^{G12D}$-induced pancreatic oncogenesis depends on the microenvironment, wherein myeloid cells in the pancreas accelerate PanIN progression and PDAC development by releasing IL-6. In examining the routes of IL-6 dependent activation of Stat3, we have demonstrated a relevant function of IL-6 transsignalling in pancreatic oncogenesis. Through IL-6 transsignaling and Stat3, IL-6 promotes tumor development in the pancreas. Genetic manipulation of IL-6 transsignaling and Stat3 activation impairs PanIN formation and significantly impedes PDAC development. Using patient data and human PDAC specimens, we have demonstrated that this crosslink also exists in the human disease.

EXPERIMENTAL PROCEDURES

Mice

The LSL-$Kras^{G12D}$ knockin (Jackson et al., 2001), $Ptf1a\text{-}cre^{ex1}$ (Nakhai et al., 2007), $Stat3^{F/F}$ (Sano et al., 1999), $sgp130^{tg}$ (Rabe et al., 2008), and $Socs3^{F/F}$ (Nakaya et al., 2009) strains were interbred to obtain compound mutant LSL-$Kras^{G12D}$;$Stat3^{F/F}$;$Ptf1a\text{-}cre^{ex1}$ (termed $Kras^{G12D}$;$Stat3^{\Delta panc}$), LSL-$Kras^{G12D}$;$Ptf1a\text{-}cre^{ex1}$;$sgp130tg$ (termed $Kras^{G12D}$;$sgp130^{tg}$), or LSL-$Kras^{G12D}$;$Socs3^{\Delta/\Delta}$;$Ptf1a\text{-}cre^{ex1}$ (termed $Kras^{G12D}$;$Socs3^{\Delta panc}$) mice. LSL-$Kras^{G12D}$ (the negative control) and mutant LSL-$Kras^{G12D}$;$Ptf1a\text{-}cre^{ex1}$ (termed $Kras^{G12D}$, the positive control) mice were used as control animals.

$Il\text{-}6^{-/-}$ (C57BL/6 background) mice were obtained from The Jackson Laboratory, Maine. LSL-$Kras^{G12D}$ knockin and $Il\text{-}6^{-/-}$ mice were interbred to generate LSL-$Kras^{G12D}$;$Il6^{-/-}$;$Ptf1a\text{-}cre^{ex1}$ mice (termed $Kras^{G12D}$;$Il6^{-/-}$). All procedures conformed to the regulatory standards and were approved by the Regierung von Oberbayern.

Human Serum IL-6 Measurements

Serum samples were obtained from 38 patients with histologically or cytologically confirmed PDCA from whom pretreatment serum samples were available. The analysis group consisted of 15 females (median age 67 years, range 41–81 years) and 23 males (median age 68 years, range 50–80 years). Whole blood was collected prior to administration of chemotherapy. Serological analysis was performed at the Institute for Clinical Chemistry, Technical University, Munich. Control sera were obtained from healthy probands. The Local Ethics Committee approved the analysis, and written informed consent was obtained from all patients and controls.

Quantification of Proliferation, Apoptosis, and Inflammation

Mice were injected intraperitoneally with 50 mg/kg BrdU (Sigma) 2 hr prior to sacrifice, and paraffin sections were stained with anti-BrdU. Apoptosis was measured by immunohistochemistry of cleaved caspase-3. Inflammation was assessed using macrophage markers (F4/80). For each analysis, positive cells were scored in the pancreata from several animals of each genotype.

Flow Cytometry

Pancreata were injected with 1.2 mg/ml collagenase P (Roche) and minced. Single-cell suspensions of pancreatic cells were immunolabeled with fluorochrome-conjugated antibodies in PBS that was supplemented with 2% heat-inactivated FBS (Gibco-Invitrogen) and 5 mM EDTA (Sigma). All antibodies were purchased from eBioscience: eFluor 450-conjugated anti-CD45, fluorescein isothiocyanate-conjugated anit-CD19, PE-conjugated anti-F4/80, allophycocyanin-conjugated anti-CD11c, APC-eFluor 780-conjugated anti-CD11b, and Alexa Fluor 700-conjugated anti-CD3. Cells were stained with propidium iodide (BD Biosciences) to assess viability. Flow cytometry analysis was performed on a Gallios flow cytometer (Beckman Coulter) after gating and excluding dead cells. Data were analyzed using FlowJo software.

Statistical Analyses

Data are presented as averages ± standard deviaions (SD) and were analyzed by built-in t test using Microsoft Excel. $p < 0.05$ was considered significant. For the overall survival analysis, Kaplan-Meier curves were analyzed by log rank test. Tumor incidence was analyzed using Fisher's exact test. In all cases, we chose a group size that produced statistically unambiguous results.

SUPPLEMENTAL INFORMATION

Supplemental Information includes two table, four figures, and Supplemental Experimental Procedures and can be found with this article online at doi:10.1016/j.ccr.2011.03.009.

ACKNOWLEDGMENTS

We thank Karen Dlubatz for excellent technical assistance. M.U.K. is an MD/PhD candidate at the Technische Universität München. Y.A. received grants from the Ministry of Education, Culture, Sports, Science, and Technology of Japan, and the Program for Promotion of Fundamental Studies in Health Sciences of the National Institute of Biomedical Innovation. S.R.-J.

was supported by the Deutsche Forschungsgemeinschaft (SFB 877, TP A 1) and by the Cluster of Excellence "Inflammation at Interfaces." H.A. and R.M.S. were supported by the Deutsche Forschungsgemeinschaft (SFB 576, TP A 10 to H.A. and R.M.S), Deutsche Krebshilfe (Grant 10994 to H.A.), Else-Kröner-Fresenius-Stiftung (Grant 2010_A144 to H.A.), and by promotional programs of the Technische Universität München (KKF-C to H.A. and KKF-A to R.M.S). S.R.-J. is inventor on patents describing the function of sgp130Fc and is a shareholder of the CONARIS Research Institute (Kiel, Germany).

Received: June 23, 2010
Revised: December 1, 2010
Accepted: March 7, 2011
Published: April 11, 2011

REFERENCES

Aguirre, A.J., Bardeesy, N., Sinha, M., Lopez, L., Tuveson, D.A., Horner, J., Redston, M.S., and DePinho, R.A. (2003). Activated Kras and Ink4a/Arf deficiency cooperate to produce metastatic pancreatic ductal adenocarcinoma. Genes Dev. *17*, 3112–3126.

Algul, H., Treiber, M., Lesina, M., Nakhai, H., Saur, D., Geisler, F., Pfeifer, A., Paxian, S., and Schmid, R.M. (2007a). Pancreas-specific RelA/p65 truncation increases susceptibility of acini to inflammation-associated cell death following cerulein pancreatitis. J. Clin. Invest. *117*, 1490–1501.

Algul, H., Treiber, M., Lesina, M., and Schmid, R.M. (2007b). Mechanisms of disease: chronic inflammation and cancer in the pancreas–a potential role for pancreatic stellate cells? Nat. Clin. Pract. Gastroenterol. Hepatol. *4*, 454–462.

Algul, H., Wagner, M., Lesina, M., and Schmid, R.M. (2007c). Overexpression of ErbB2 in the exocrine pancreas induces an inflammatory response but not increased proliferation. Int. J. Cancer *121*, 1410–1416.

Barre, B., Vigneron, A., and Coqueret, O. (2005). The STAT3 transcription factor is a target for the Myc and riboblastoma proteins on the Cdc25A promoter. J. Biol. Chem. *280*, 15673–15681.

Bollrath, J., Phesse, T.J., von Burstin, V.A., Putoczki, T., Bennecke, M., Bateman, T., Nebelsiek, T., Lundgren-May, T., Canli, O., Schwitalla, S., et al. (2009). gp130-mediated Stat3 activation in enterocytes regulates cell survival and cell-cycle progression during colitis-associated tumorigenesis. Cancer Cell *15*, 91–102.

Chalaris, A., Rabe, B., Paliga, K., Lange, H., Laskay, T., Fielding, C.A., Jones, S.A., Rose-John, S., and Scheller, J. (2007). Apoptosis is a natural stimulus of IL6R shedding and contributes to the proinflammatory trans-signaling function of neutrophils. Blood *110*, 1748–1755.

Clark, C.E., Hingorani, S.R., Mick, R., Combs, C., Tuveson, D.A., and Vonderheide, R.H. (2007). Dynamics of the immune reaction to pancreatic cancer from inception to invasion. Cancer Res. *67*, 9518–9527.

Ebrahimi, B., Tucker, S.L., Li, D., Abbruzzese, J.L., and Kurzrock, R. (2004). Cytokines in pancreatic carcinoma: correlation with phenotypic characteristics and prognosis. Cancer *101*, 2727–2736.

Finco, T.S., Westwick, J.K., Norris, J.L., Beg, A.A., Der, C.J., and Baldwin, A.S., Jr. (1997). Oncogenic Ha-Ras-induced signaling activates NF-kappaB transcriptional activity, which is required for cellular transformation. J. Biol. Chem. *272*, 24113–24116.

Glienke, W., Maute, L., Wicht, J., and Bergmann, L. (2010). Curcumin inhibits constitutive STAT3 phosphorylation in human pancreatic cancer cell lines and downregulation of survivin/BIRC5 gene expression. Cancer Invest. *28*, 166–171.

Greten, F.R., Weber, C.K., Greten, T.F., Schneider, G., Wagner, M., Adler, G., and Schmid, R.M. (2002). Stat3 and NF-kappaB activation prevents apoptosis in pancreatic carcinogenesis. Gastroenterology *123*, 2052–2063.

Grivennikov, S., Karin, E., Terzic, J., Mucida, D., Yu, G.Y., Vallabhapurapu, S., Scheller, J., Rose-John, S., Cheroutre, H., Eckmann, L., and Karin, M. (2009). IL-6 and Stat3 are required for survival of intestinal epithelial cells and development of colitis-associated cancer. Cancer Cell *15*, 103–113.

Guerra, C., Schuhmacher, A.J., Canamero, M., Grippo, P.J., Verdaguer, L., Perez-Gallego, L., Dubus, P., Sandgren, E.P., and Barbacid, M. (2007). Chronic pancreatitis is essential for induction of pancreatic ductal adenocarcinoma by K-Ras oncogenes in adult mice. Cancer Cell *11*, 291–302.

He, G., Yu, G.Y., Temkin, V., Ogata, H., Kuntzen, C., Sakurai, T., Sieghart, W., Peck-Radosavljevic, M., Leffert, H.L., and Karin, M. (2010). Hepatocyte IKKbeta/NF-kappaB inhibits tumor promotion and progression by preventing oxidative stress-driven STAT3 activation. Cancer Cell *17*, 286–297.

Hidalgo, M. (2010). Pancreatic cancer. N. Engl. J. Med. *362*, 1605–1617.

Hingorani, S.R., Petricoin, E.F., Maitra, A., Rajapakse, V., King, C., Jacobetz, M.A., Ross, S., Conrads, T.P., Veenstra, T.D., Hitt, B.A., et al. (2003). Preinvasive and invasive ductal pancreatic cancer and its early detection in the mouse. Cancer Cell *4*, 437–450.

Hingorani, S.R., Wang, L., Multani, A.S., Combs, C., Deramaudt, T.B., Hruban, R.H., Rustgi, A.K., Chang, S., and Tuveson, D.A. (2005). Trp53R172H and KrasG12D cooperate to promote chromosomal instability and widely metastatic pancreatic ductal adenocarcinoma in mice. Cancer Cell *7*, 469–483.

Hruban, R.H., Adsay, N.V., Albores-Saavedra, J., Anver, M.R., Biankin, A.V., Boivin, G.P., Furth, E.E., Furukawa, T., Klein, A., Klimstra, D.S., et al. (2006). Pathology of genetically engineered mouse models of pancreatic exocrine cancer: consensus report and recommendations. Cancer Res. *66*, 95–106.

Hutzen, B., Friedman, L., Sobo, M., Lin, L., Cen, L., De Angelis, S., Yamakoshi, H., Shibata, H., Iwabuchi, Y., and Lin, J. (2009). Curcumin analogue GO-Y030 inhibits STAT3 activity and cell growth in breast and pancreatic carcinomas. Int. J. Oncol. *35*, 867–872.

Jackson, E.L., Willis, N., Mercer, K., Bronson, R.T., Crowley, D., Montoya, R., Jacks, T., and Tuveson, D.A. (2001). Analysis of lung tumor initiation and progression using conditional expression of oncogenic K-ras. Genes Dev. *15*, 3243–3248.

Kawesha, A., Ghaneh, P., Andren-Sandberg, A., Ograed, D., Skar, R., Dawiskiba, S., Evans, J.D., Campbell, F., Lemoine, N., and Neoptolemos, J.P. (2000). K-ras oncogene subtype mutations are associated with survival but not expression of p53, p16(INK4A), p21(WAF-1), cyclin D1, erbB-2 and erbB-3 in resected pancreatic ductal adenocarcinoma. Int. J. Cancer *89*, 469–474.

Kelly, K.A., Bardeesy, N., Anbazhagan, R., Gurumurthy, S., Berger, J., Alencar, H., Depinho, R.A., Mahmood, U., and Weissleder, R. (2008). Targeted nanoparticles for imaging incipient pancreatic ductal adenocarcinoma. PLoS Med. *5*, e85.

Kim, D., Sun, M., He, L., Zhou, Q.H., Chen, J., Sun, X.M., Bepler, G., Sebti, S.M., and Cheng, J.Q. (2010). A small molecule inhibits Akt through direct binding to Akt and preventing Akt membrane translocation. J. Biol. Chem. *285*, 8383–8394.

Kocher, H.M., Mears, L., Lea, N.C., Raj, K., and Mufti, G.J. (2007). JAK V617F missense mutation is absent in pancreatic cancer. Gut *56*, 1174–1175.

Kurahara, H., Shinchi, H., Mataki, Y., Maemura, K., Noma, H., Kubo, F., Sakoda, M., Ueno, S., Natsugoe, S., and Takao, S. (2009). Significance of M2-polarized tumor-associated macrophage in pancreatic cancer. J. Surg. Res., in press. Published online June 16, 2009. 10.1016/j.jss2009.05.026.

Lin, J., Jin, X., Rothman, K., Lin, H.J., Tang, H., and Burke, W. (2002). Modulation of signal transducer and activator of transcription 3 activities by p53 tumor suppressor in breast cancer cells. Cancer Res. *62*, 376–380.

Lin, L., Hutzen, B., Li, P.K., Ball, S., Zuo, M., DeAngelis, S., Foust, E., Sobo, M., Friedman, L., Bhasin, D., et al. (2010a). A novel small molecule, LLL12, inhibits STAT3 phosphorylation and activities and exhibits potent growth-suppressive activity in human cancer cells. Neoplasia *12*, 39–50.

Lin, L., Hutzen, B., Zuo, M., Ball, S., Deangelis, S., Foust, E., Pandit, B., Ihnat, M.A., Shenoy, S.S., Kulp, S., et al. (2010b). Novel STAT3 phosphorylation inhibitors exhibit potent growth-suppressive activity in pancreatic and breast cancer cells. Cancer Res. *70*, 2445–2454.

Lowenfels, A.B., Maisonneuve, P., Cavallini, G., Ammann, R.W., Lankisch, P.G., Andersen, J.R., Dimagno, E.P., Andren-Sandberg, A., and Domellof, L. (1993). Pancreatitis and the risk of pancreatic cancer. International Pancreatitis Study Group. N. Engl. J. Med. *328*, 1433–1437.

Luttges, J., Neumann, S., Jesnowski, R., Borries, V., Lohr, M., and Kloppel, G. (2003). Lack of apoptosis in PanIN-1 and PanIN-2 lesions associated with pancreatic ductal adenocarcinoma is not dependent on K-ras status. Pancreas *27*, e57–e62.

Marrache, F., Tu, S.P., Bhagat, G., Pendyala, S., Osterreicher, C.H., Gordon, S., Ramanathan, V., Penz-Osterreicher, M., Betz, K.S., Song, Z., and Wang, T.C. (2008). Overexpression of interleukin-1beta in the murine pancreas results in chronic pancreatitis. Gastroenterology *135*, 1277–1287.

Masuda, M., Suzui, M., Yasumatu, R., Nakashima, T., Kuratomi, Y., Azuma, K., Tomita, K., Komiyama, S., and Weinstein, I.B. (2002). Constitutive activation of signal transducers and activators of transcription 3 correlates with cyclin D1 overexpression and may provide a novel prognostic marker in head and neck squamous cell carcinoma. Cancer Res. *62*, 3351–3355.

Matthews, V., Schuster, B., Schutze, S., Bussmeyer, I., Ludwig, A., Hundhausen, C., Sadowski, T., Saftig, P., Hartmann, D., Kallen, K.J., and Rose-John, S. (2003). Cellular cholesterol depletion triggers shedding of the human interleukin-6 receptor by ADAM10 and ADAM17 (TACE). J. Biol. Chem. *278*, 38829–38839.

Nakaya, M., Hashimoto, M., Nakagawa, R., Wakabayashi, Y., Ishizaki, T., Takada, I., Komai, K., Yoshida, H., and Yoshimura, A. (2009). SOCS3 in T and NKT cells negatively regulates cytokine production and ameliorates ConA-induced hepatitis. J. Immunol. *183*, 7047–7053.

Nakhai, H., Sel, S., Favor, J., Mendoza-Torres, L., Paulsen, F., Duncker, G.I., and Schmid, R.M. (2007). Ptf1a is essential for the differentiation of GABAergic and glycinergic amacrine cells and horizontal cells in the mouse retina. Development *134*, 1151–1160.

Rabe, B., Chalaris, A., May, U., Waetzig, G.H., Seegert, D., Williams, A.S., Jones, S.A., Rose-John, S., and Scheller, J. (2008). Transgenic blockade of interleukin 6 transsignaling abrogates inflammation. Blood *111*, 1021–1028.

Reid, T., Jin, X., Song, H., Tang, H.J., Reynolds, R.K., and Lin, J. (2004). Modulation of Janus kinase 2 by p53 in ovarian cancer cells. Biochem. Biophys. Res. Commun. *321*, 441–447.

Rose-John, S., and Heinrich, P.C. (1994). Soluble receptors for cytokines and growth factors: generation and biological function. Biochem. J. *300*, 281–290.

Rose-John, S., Scheller, J., Elson, G., and Jones, S.A. (2006). Interleukin-6 biology is coordinated by membrane-bound and soluble receptors: role in inflammation and cancer. J. Leukoc. Biol. *80*, 227–236.

Sano, S., Itami, S., Takeda, K., Tarutani, M., Yamaguchi, Y., Miura, H., Yoshikawa, K., Akira, S., and Takeda, J. (1999). Keratinocyte-specific ablation of Stat3 exhibits impaired skin remodeling, but does not affect skin morphogenesis. EMBO J. *18*, 4657–4668.

Sawai, H., Funahashi, H., Matsuo, Y., Yamamoto, M., Okada, Y., Hayakawa, T., and Manabe, T. (2003). Expression and prognostic roles of integrins and interleukin-1 receptor type I in patients with ductal adenocarcinoma of the pancreas. Dig. Dis. Sci. *48*, 1241–1250.

Scholz, A., Heinze, S., Detjen, K.M., Peters, M., Welzel, M., Hauff, P., Schirner, M., Wiedenmann, B., and Rosewicz, S. (2003). Activated signal transducer and activator of transcription 3 (STAT3) supports the malignant phenotype of human pancreatic cancer. Gastroenterology *125*, 891–905.

Sipos, B., Moser, S., Kalthoff, H., Torok, V., Lohr, M., and Kloppel, G. (2003). A comprehensive characterization of pancreatic ductal carcinoma cell lines: towards the establishment of an in vitro research platform. Virchows Arch. *442*, 444–452.

Talar-Wojnarowska, R., Gasiorowska, A., Smolarz, B., Romanowicz-Makowska, H., Kulig, A., and Malecka-Panas, E. (2009). Clinical significance of interleukin-6 (IL-6) gene polymorphism and IL-6 serum level in pancreatic adenocarcinoma and chronic pancreatitis. Dig. Dis. Sci. *54*, 683–689.

Trevino, J.G., Gray, M.J., Nawrocki, S.T., Summy, J.M., Lesslie, D.P., Evans, D.B., Sawyer, T.K., Shakespeare, W.C., Watowich, S.S., Chiao, P.J., et al. (2006). Src activation of Stat3 is an independent requirement from NF-kappaB activation for constitutive IL-8 expression in human pancreatic adenocarcinoma cells. Angiogenesis *9*, 101–110.

Yu, H., Pardoll, D., and Jove, R. (2009). STATs in cancer inflammation and immunity: a leading role for STAT3. Nat. Rev. Cancer *9*, 798–809.

RelA regulates CXCL1/CXCR2-dependent oncogene-induced senescence in murine *Kras*-driven pancreatic carcinogenesis

Marina Lesina,[1] Sonja Maria Wörmann,[1] Jennifer Morton,[2] Kalliope Nina Diakopoulos,[1] Olga Korneeva,[1] Margit Wimmer,[1] Henrik Einwächter,[1] Jan Sperveslage,[3] Ihsan Ekin Demir,[4] Timo Kehl,[5] Dieter Saur,[1] Bence Sipos,[6] Mathias Heikenwälder,[7,8] Jörg Manfred Steiner,[1,9] Timothy Cragin Wang,[10] Owen J. Sansom,[2] Roland Michael Schmid,[1] and Hana Algül[1]

[1]II. Medizinische Klinik, Klinikum rechts der Isar, Technische Universität München, Munich, Germany. [2]Cancer Research UK Beatson Institute, Department of Pathology, Glasgow, United Kingdom. [3]Universitätsklinikum Münster, Münster, Germany. [4]Department of Surgery, Klinikum rechts der Isar, Technische Universität München, Munich, Germany. [5]German Cancer Research Center (DKFZ), Heidelberg, Germany. [6]Universitätsklinikum Tübingen, Tübingen, Germany. [7]Institute of Virology, Technische Universität München, Helmholtz Zentrum München, Munich, Germany. [8]Division of Chronic Inflammation and Cancer, German Cancer Research Center (DKFZ), Heidelberg, Germany. [9]Department of Small Animal Clinical Sciences, Texas A&M University, College Station, Texas, USA. [10]Division of Digestive and Liver Diseases, Department of Medicine, Irving Cancer Research Center, Columbia University, New York, New York, USA.

Tumor suppression that is mediated by oncogene-induced senescence (OIS) is considered to function as a safeguard during development of pancreatic ductal adenocarcinoma (PDAC). However, the mechanisms that regulate OIS in PDAC are poorly understood. Here, we have determined that nuclear RelA reinforces OIS to inhibit carcinogenesis in the *Kras* mouse model of PDAC. Inactivation of RelA accelerated pancreatic lesion formation in *Kras* mice by abrogating the senescence-associated secretory phenotype (SASP) gene transcription signature. Using genetic and pharmacological tools, we determined that RelA activation promotes OIS via elevation of the SASP factor CXCL1 (also known as KC), which activates CXCR2, during pancreatic carcinogenesis. In *Kras* mice, pancreas-specific inactivation of CXCR2 prevented OIS and was correlated with increased tumor proliferation and decreased survival. Moreover, reductions in CXCR2 levels were associated with advanced neoplastic lesions in tissue from human pancreatic specimens. Genetically disabling OIS in *Kras* mice caused RelA to promote tumor proliferation, suggesting a dual role for RelA signaling in pancreatic carcinogenesis. Taken together, our data suggest a pivotal role for RelA in regulating OIS in preneoplastic lesions and implicate the RelA/CXCL1/CXCR2 axis as an essential mechanism of tumor surveillance in PDAC.

Introduction

Pancreatic ductal adenocarcinoma (PDAC) is the fourth leading cause of cancer-associated death in Western populations. Morphologically, PDAC is characterized by the presence of pancreatic intraepithelial neoplasia (PanIN) with an activating *KRAS* mutation occurring in 30% of precursor lesions and in 100% of advanced PDAC lesions. Mouse models with pancreas-specific activation of oncogenic *Kras* recapitulate the features of human PDAC.

As a ubiquitously expressed transcription factor, NF-κB can regulate the growth and malignancy of many solid tumors, including pancreatic cancer, via the regulation of expression of proinflammatory and prosurvival genes. However, despite extensive characterization of NF-κB signaling, the specific functional roles of different members of the NF-κB family in tumor development are not completely understood. Recently, the role of the kinase IKK2 in PDAC has been explored, demonstrating that IKK exerts its tumor-promoting effects through cross-talk with either Notch1 or p62 protein (1–3). NF-κB inhibition in lung epithelial cells by genetic deletion of the NF-κB subunit RelA or IKK2 reduced lung tumorigenesis in a *Kras*-induced mouse model of lung adenocarcinoma (4, 5). In keeping with those reports, overexpression of IκBα super-repressor (IκBαSR) also resulted in a significantly diminished lung tumor growth, supporting a protumorigenic role of NF-κB in epithelial cells (6). Although a number of reports display a tumor-promoting role of NF-κB signaling, it has also been reported to exhibit tumor-suppressing functions in different tumor models. Hepatocyte-specific knockout of IKKβ resulted in increased tumor development in a chemical-driven model of hepatic carcinogenesis (7). Another study of hepatic carcinogenesis showed that NEMO/IKKγ-mediated NF-κB activation in hepatocytes prevented the spontaneous development of hepatic steatosis and hepatocellular carcinoma (8, 9), suggesting that components of the NF-κB pathway play highly pleiotropic roles (10). NF-κB signaling, when activated, can act as both a tumor promoter and a tumor suppressor. However, the pathogenetic mechanisms by which NF-κB induces these opposite effects during tumor development remains unclear.

One possibility is the involvement of NF-κB in the regulation of factors, including CXCL chemokines, IL-6, GM-CSF, and MCP-1, -2, and -3, that are subsumed under the term "senescence-associated secretory phenotype" (SASP) (11). It is now clear that SASP components actively participate in the cellular senescence

▶ Related Commentary: p. 2799

Conflict of interest: The authors have declared that no conflict of interest exists.
Submitted: January 13, 2016; **Accepted:** May 13, 2016.
Reference information: *J Clin Invest.* 2016;126(8):2919–2932. doi:10.1172/JCI86477.

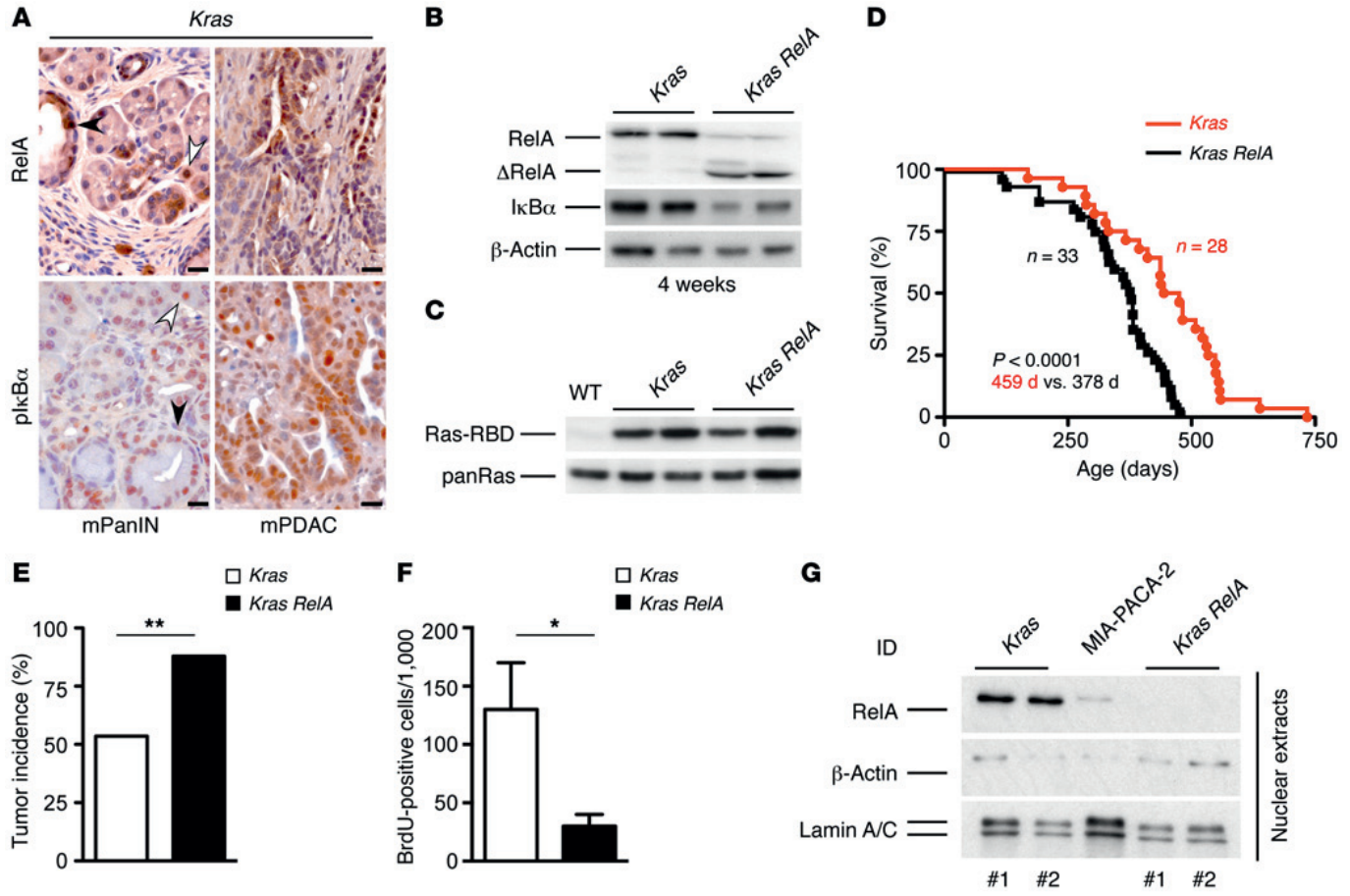

Figure 1. RelA deficiency promotes pancreatic carcinogenesis. (**A**) IHC analysis of RelA and phosphorylated IκBα (pIκBα) in pancreata from *Kras* mice. Representative images show that RelA and pIκBα expression is intense in ductal lesions (black arrowhead), acinar cells (white arrowhead), and PDAC lesions from *Kras* mice. Scale bars: 20 μm. (**B**) Immunoblot analysis of RelA, truncated RelA (ΔRelA), and IκBα in lysates from 4-week-old *Kras* and *Kras RelA* mice. β-Actin was used as the loading control. (**C**) Immunoprecipitation of activated Ras (Ras-RBD) in pancreata from mice with the indicated genotypes. Lysate from a WT (LSL-$Kras^{G12D}$) mouse served as the negative control. (**D**) RelA deficiency cooperates with oncogenic $Kras^{G12D}$ to influence survival. Kaplan-Meier analysis shows a median survival of 378 days in *Kras RelA* mice ($n = 33$; black line) versus 459 days in *Kras* mice ($n = 28$; red line). $P < 0.0001$ by Mantel-Cox log rank test; *n*, number of mice. (**E**) Tumor incidence was significantly lower in *Kras* (53.6%) than in *Kras RelA* (87.9%) cohorts. $^{**}P = 0.0041$ by Fisher's exact test. (**F**) Proliferation index of pancreatic tumors from mice with the indicated genotypes. The number of BrdU-positive cells was counted in 10 fields per mouse. Mean ± SD; $n = 3$; $^{*}P < 0.05$ by unpaired *t* test; *n*, number of mice. (**G**) Immunoblot analysis of nuclear extracts from *Kras* and *Kras RelA* primary pancreatic cancer cell lines displays nuclear RelA in tumor cells isolated from *Kras* but not RelA-deficient *Kras* mice. MIA-PACA-2 cell line extract served as the positive control. β-Actin and lamin A/C served as loading controls.

process. Oncogene-induced senescence (OIS) has only recently been shown to govern the carcinogenesis of PDAC (12–16). More specifically, OIS in oncogenic $Kras^{G12D}$ mice establishes an incomplete tumor-suppressive program that prevents the expansion of cells that harbor mutant *Kras* (17, 18). Despite the potential significance of SASP in senescence, little is known about its regulation. Importantly, the impact of SASP on pancreatic carcinogenesis has not been examined directly.

In this study, we aimed to determine the function of RelA in pancreatic cancer in vivo. Surprisingly, our results show that, unlike IKK2 or NEMO, RelA has a tumor-suppressive role. RelA controls the development of pancreatic cancer, because of its function in mediating OIS and immune surveillance. The tumor-promoting functions of RelA are unmasked upon disabling OIS, thus revealing a dual stage function of RelA in the carcinogenesis of PDAC. These findings might prove to be of relevance for future clinical applications.

Results

Inactivation of RelA increases pancreatic cancer incidence and decreases survival in Kras mice, although tumor proliferation is reduced. Although nuclear RelA is typically detectable in human pancreatic cancer, its functional relevance for this disease is unknown. To determine the function of RelA in pancreatic carcinogenesis, we used the LSL-$Kras^{G12D}$ $Ptf1a\text{-}Cre^{ex1}$ (hereafter referred to as *Kras*) mouse model of pancreatic cancer. Nuclear RelA and phosphorylated IκBα were detectable in *Kras* mice starting in preneoplastic lesions and adjacent acinar cells and remained visible in established PDAC lesions (Figure 1A). To elucidate the role of canonical NF-κB signaling in the *Kras* model, we deleted *Rela* using a conditional *Rela* allele (LSL-$Kras^{G12D}$ $Rela^{fl/fl}$ $Ptf1a\text{-}Cre^{ex1}$ mice, hereafter referred to as *Kras RelA*) (19). Inactivation of RelA in the pancreas had no impact on Ras activity, while less expression of the target gene IκBα was detectable (Figure 1, B and C, and Supplemental Figure 1, A and B; supple-

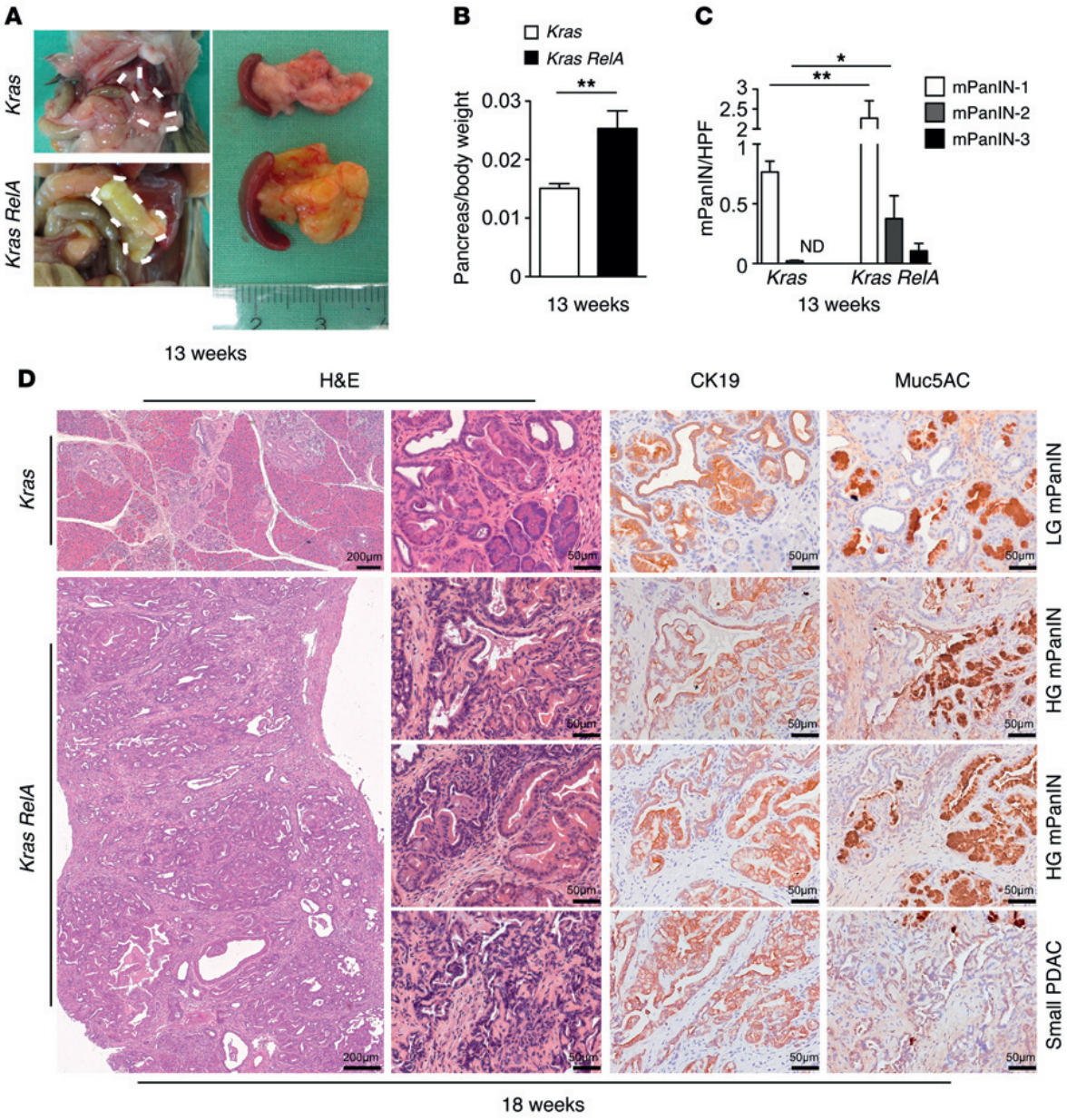

Figure 2. Ablation of RelA accelerates progression of mPanIN lesions. (**A**) Representative macroscopic appearance of pancreata from 13-week-old *Kras* and *Kras RelA* mice. (**B**) Pancreas–to–body weight ratio in 13-week-old *Kras* (n = 15) and *Kras RelA* (n = 12) mice. Mean ± SEM; $^{**}P$ = 0.0015 by unpaired t test; n, number of mice. (**C**) Number of mPanIN lesions in 13-week-old *Kras* (n = 3) and *Kras RelA* (n = 3) mice was counted per ×200 optical field (high-power field, HPF). Mean ± SD; $^{*}P < 0.05$, $^{**}P < 0.005$ by unpaired t test; n, number of mice; N.D., none detectable. (**D**) Representative H&E staining and expression of CK19 and Muc5AC in pancreata from 18-week-old *Kras* and *Kras RelA* mice. Positive immunostaining for cytokeratin-19 confirms the ductal phenotype of mPanIN lesions. Muc5AC staining can be seen in low-grade lesions (LG mPanIN) but not in high-grade lesions (HG mPanIN) or small PDACs. Scale bars: 200 μm and 50 μm.

mental material available online with this article; doi:10.1172/JCI86477DS1). Cohorts of *Kras* and *Kras RelA* mice were monitored for survival. Unexpectedly, overall survival of analyzed *Kras RelA* mice was significantly shorter than that of *Kras* mice (Figure 1D). *Kras RelA* mice reached terminal morbidity between 117 and 484 days and had a median survival of 378 days ($P < 0.0001$ for *Kras RelA* compared with *Kras*). In addition, *Kras RelA* mice developed PDAC significantly earlier (350 days in *Kras RelA* vs. 443 days in *Kras* cohort) and showed 1.6-fold increased tumor incidence compared to *Kras* mice (Figure 1E). Tumor type (i.e., ductal vs. mixed) and rate of metastasis did not differ between the cohorts (Supplemental Figure 1, C–E). Surprisingly, proliferation of tumors in established PDAC was 77% lower in *Kras* mice lacking RelA in the pancreas (Figure 1F and Supplemental Figure 1F). Notably, the deletion of *Rela* exons 7–10 is maintained in *Kras RelA* primary tumors and metastases, as tumor-derived cell lines displayed truncated RelA and therefore lacked nuclear RelA. On the other hand, RelA-proficient murine and human pancreatic cell lines displayed RelA in the nuclear fraction, suggestive of canonical NF-κB activation (Figure 1G and Supplemental Figure 1G). Moreover, isolated tumor cell lines from *Kras RelA* mice proliferate significantly less than tumor cells derived from *Kras* mice

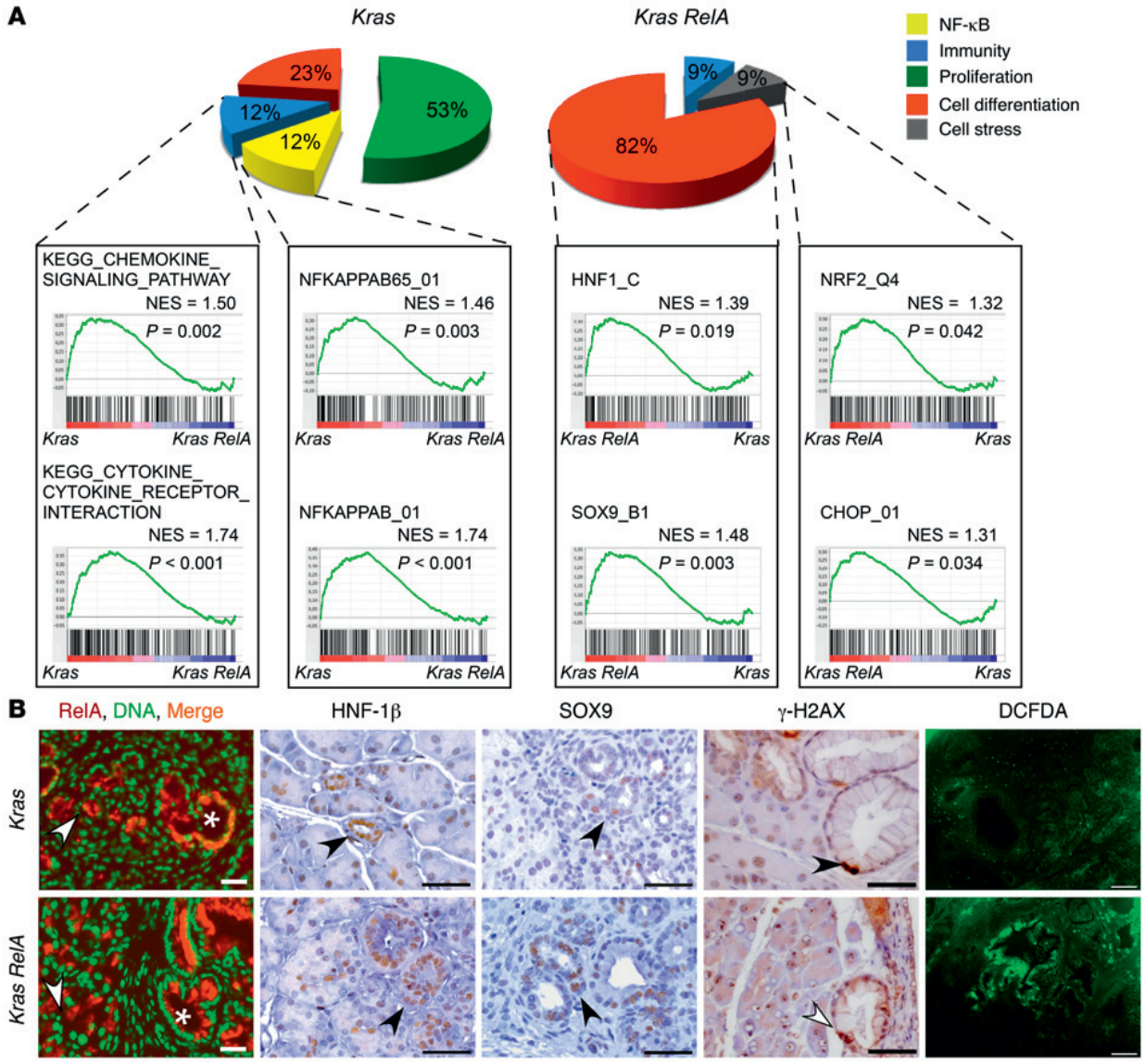

Figure 3. Transcriptomic analysis of *Kras RelA* pancreata reveals increased cell differentiation and cell stress signaling. (**A**, top) Classification of upregulated gene sets (NES ≥1.2; nominal *P* value < 0.05) in pancreata from *Kras* and *Kras RelA* mice, based on KEGG and the transcription factor pathway analyses. (**A**, bottom and boxed) GSEA illustrating enriched gene sets. KEGG analyses illustrating highly enriched gene sets for "chemokine signaling pathways" and "cytokine–cytokine receptor interaction pathways." (**B**) Immunofluorescent staining of RelA in *Kras* and *Kras RelA* mice. White stars indicate ductal lesions, white arrowheads indicate acinar cells. Scale bars: 20 μm. IHC detection of HNF-1β, SOX9, and γ-H2AX in *Kras* and *Kras RelA* mice. Scale bars: 50 μm. 2′,7′-Dichlorofluorescein diacetate (DCFDA) staining. Scale bars: 50 μm. All representative images are shown.

(Supplemental Figure 1H). These results indicate that functional inactivation of RelA accelerates pancreatic cancer development, although proliferation of RelA-deficient tumor cells in established PDAC was significantly reduced.

Taken together, our data suggest an opposite function of RelA compared with IKK2 and NEMO in pancreatic carcinogenesis. RelA seems to play a dual stage-dependent role during tumor development.

Functional inactivation of RelA accelerates progression of murine PanIN (mPanIN) lesions. PDAC is preceded by the evolution of PanIN precursor lesions. Under certain conditions, acinar-to-ductal metaplasia (ADM) might be critical for the development of PanIN lesions. Because functional inactivation of RelA increased tumor incidence while reducing tumor cell proliferation, it seemed very likely that RelA affects mPanIN initiation and progression. Therefore, we evaluated pancreatic carcinogenesis in RelA-deficient *Kras* mice in more detail. Macroscopically, pancreata of 13-week-old *Kras RelA* mice appeared enlarged, indurated, and fibrotic when compared with age-matched pancreata of *Kras* mice (Figure 2, A and B). Histologically, mPanIN progression in *Kras RelA* mice was significantly accelerated. Indeed, mPanIN-2 and mPanIN-3 lesions were present in *Kras RelA* mice as early as 13 weeks of age (Figure 2C). IHC examination of *Kras RelA* pancreata at 18 weeks of age revealed clusters of high-grade mPanIN lesions alongside small PDACs (Figure 2D). At these time points neither high-grade mPanIN lesions nor focal cancers could be detected in *Kras* mice (Figure 2D). In addition, pathways that are known to be relevant for ADM formation and mPanIN progression were upregulated in *Kras*

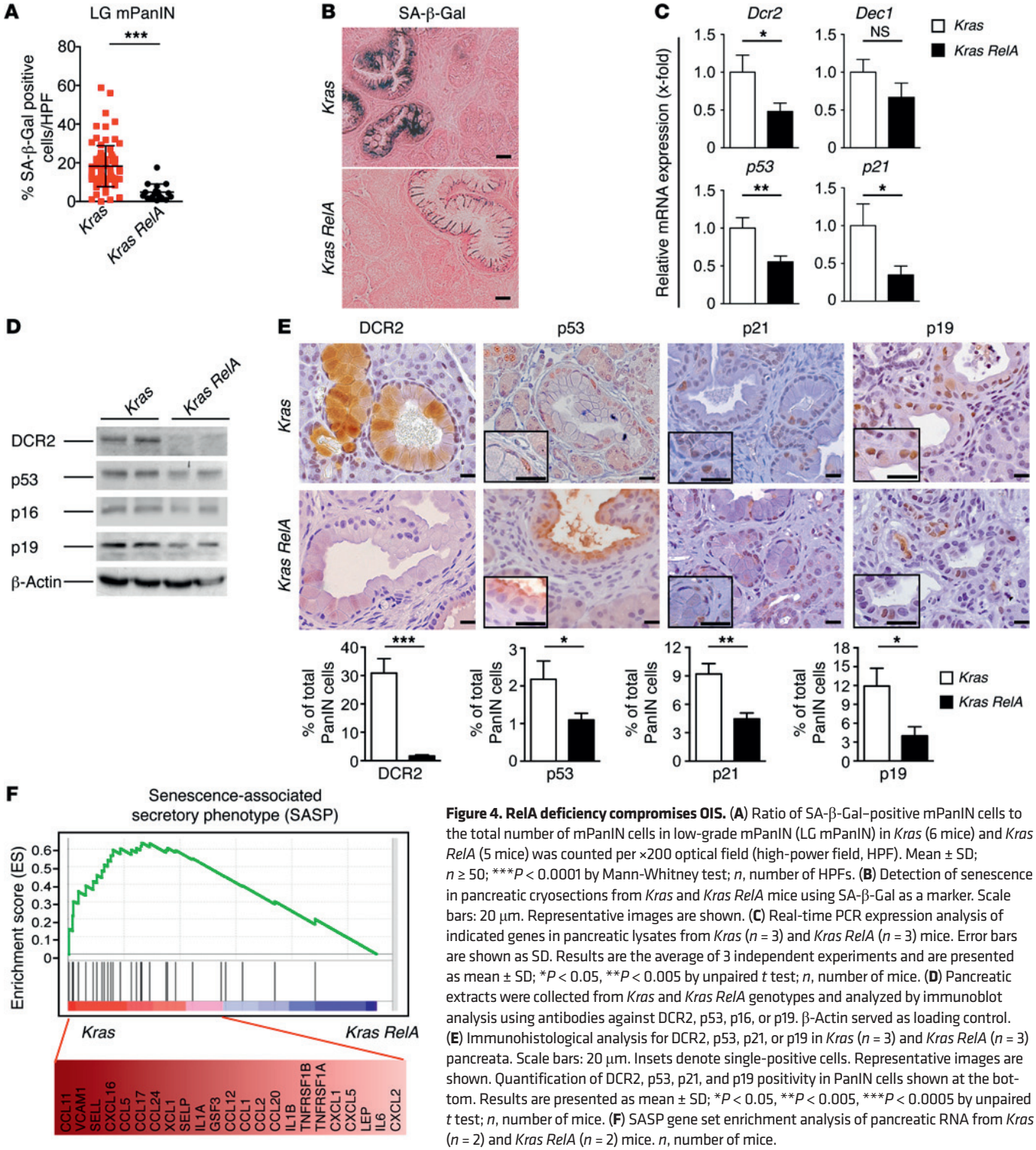

Figure 4. RelA deficiency compromises OIS. (**A**) Ratio of SA-β-Gal–positive mPanIN cells to the total number of mPanIN cells in low-grade mPanIN (LG mPanIN) in *Kras* (6 mice) and *Kras RelA* (5 mice) was counted per ×200 optical field (high-power field, HPF). Mean ± SD; $n \geq 50$; $^{***}P < 0.0001$ by Mann-Whitney test; *n*, number of HPFs. (**B**) Detection of senescence in pancreatic cryosections from *Kras* and *Kras RelA* mice using SA-β-Gal as a marker. Scale bars: 20 μm. Representative images are shown. (**C**) Real-time PCR expression analysis of indicated genes in pancreatic lysates from *Kras* ($n = 3$) and *Kras RelA* ($n = 3$) mice. Error bars are shown as SD. Results are the average of 3 independent experiments and are presented as mean ± SD; $^{*}P < 0.05$, $^{**}P < 0.005$ by unpaired *t* test; *n*, number of mice. (**D**) Pancreatic extracts were collected from *Kras* and *Kras RelA* genotypes and analyzed by immunoblot analysis using antibodies against DCR2, p53, p16, or p19. β-Actin served as loading control. (**E**) Immunohistological analysis for DCR2, p53, p21, or p19 in *Kras* ($n = 3$) and *Kras RelA* ($n = 3$) pancreata. Scale bars: 20 μm. Insets denote single-positive cells. Representative images are shown. Quantification of DCR2, p53, p21, and p19 positivity in PanIN cells shown at the bottom. Results are presented as mean ± SD; $^{*}P < 0.05$, $^{**}P < 0.005$, $^{***}P < 0.0005$ by unpaired *t* test; *n*, number of mice. (**F**) SASP gene set enrichment analysis of pancreatic RNA from *Kras* ($n = 2$) and *Kras RelA* ($n = 2$) mice. *n*, number of mice.

RelA mPanIN lesions. These pathways included phosphorylation of ERK1/2, STAT3, and c-Jun (Supplemental Figure 2).

These data reveal that inactivation of RelA in *Kras* mice accelerates pancreatic carcinogenesis. Classical NF-κB/RelA signaling seems to inhibit ADM and progression of mPanIN lesions, exerting a specific tumor suppressor function in pancreatic carcinogenesis.

Loss of functional RelA abrogates NF-κB signatures, but increases signatures of cell stress and ADM. To further elucidate the mechanisms that promote pancreatic carcinogenesis in *Kras RelA* mice, we performed microarray analysis with RNA from RelA-proficient and -deficient *Kras* total pancreata. In order to ensure homogeneous sampling, we used mice younger than 4 weeks of age, as pancreata in both groups did not reveal relevant morphological differences at this time point (Supplemental Figure 3A). For all the transcriptional analysis we compared *Kras RelA* to *Kras* pancreas or vice versa. Thus the control for *Kras RelA* was *Kras* pancreas with RelA proficiency.

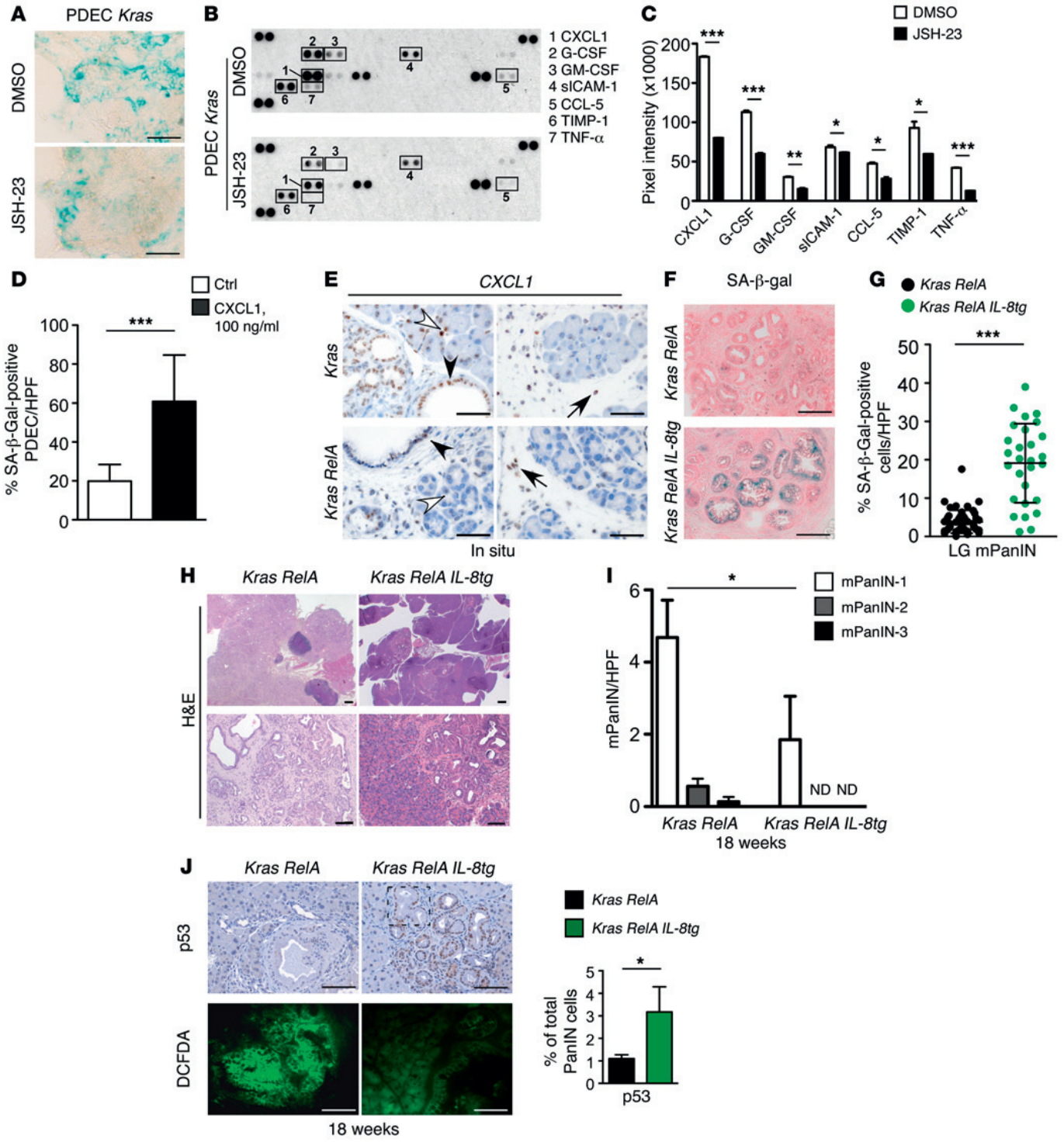

Figure 5. Regulation of OIS by RelA is mediated by CXCL1. (**A**) *Kras* PDECs treated with vehicle control (DMSO) or an NF-κB inhibitor (JSH-23) were plated for the senescence assay. Scale bars: 100 μm. Representative images are shown. (**B**) Conditioned media were collected from PDECs treated with DMSO or JSH-23 for cytokine array analysis. The boxed regions on the representative blot indicate the differentially secreted cytokines. (**C**) Quantitative analysis of **B**, representing the average of the pixel intensity of 2 independent experiments. Mean ± SD; $^{*}P < 0.05$, $^{**}P < 0.005$, $^{***}P < 0.0005$ by unpaired *t* test. (**D**) Quantification of SA-β-Gal staining in *Kras* PDECs treated with DMSO or 100 ng/ml CXCL1. Ratio of SA-β-Gal–positive *Kras* PDEC cultures to the total number of *Kras* PDECs was counted per ×100 optical high-power field (HPF). Mean ± SD; $^{***}P < 0.0005$ by unpaired *t* test. (**E**) Representative photomicrographs showing in situ *Cxcl1* mRNA in ductal lesions (black arrowhead), in acinar cells (white arrowhead), and in immune cells (black arrow). Scale bars: 50 μm. (**F**) Representative SA-β-Gal staining. Scale bars: 100 μm. (**G**) Ratio of SA-β-Gal–positive cells to the total number of mPanIN cells in 18-week-old *Kras RelA* (5 mice) and *Kras RelA IL-8tg* (4 mice) was counted per ×200 optical field (HPF). Mean ± SD; $n \geq 28$; $^{***}P < 0.0001$ by Mann-Whitney test; *n*, number of HPF. (**H**) Representative H&E staining. Scale bars: 100 μm. (**I**) Numbers of mPanINs were counted per ×200 optical HPF. Mean ± SD; $n \geq 3$; $^{*}P < 0.05$ by unpaired *t* test; N.D., not detectable; *n*, number of mice. (**J**) Representative immunohistological analysis for p53 and 2′,7′-dichlorofluorescein diacetate (DCFDA) from *Kras RelA* ($n = 3$) and *Kras RelA IL-8tg* ($n = 3$) mice. Scale bars: 50 μm. Quantification of p53 positivity shown at the right. Mean ± SD; $^{*}P < 0.05$ by unpaired *t* test; *n*, number of mice.

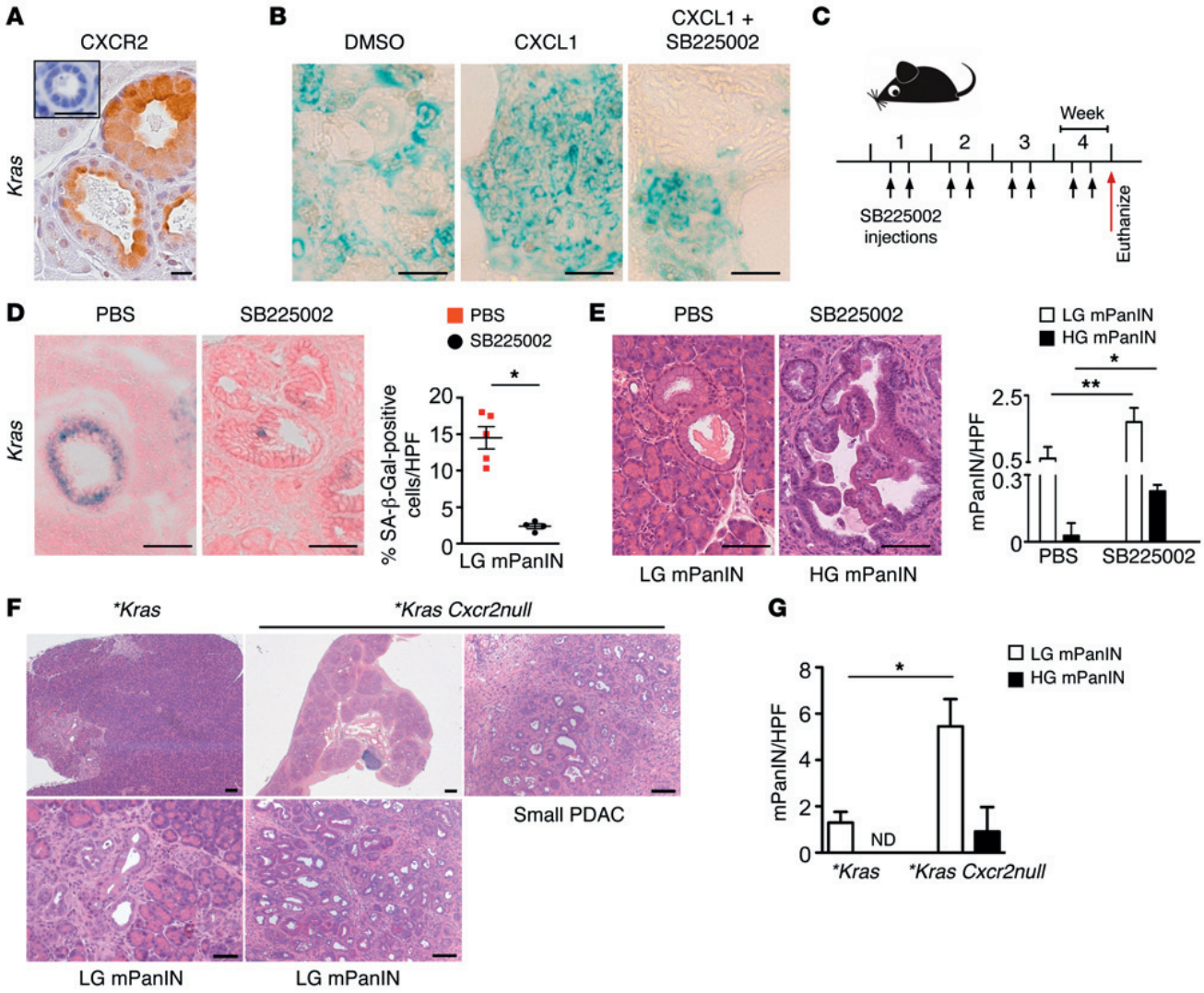

Figure 6. Reinforcement of OIS depends on CXCL1/CXCR2 axis. (**A**) Representative immunohistological staining for CXCR2 in mPanIN lesions from *Kras* pancreatic tissue and in normal ductal epithelium (inset). Scale bar: 20 μm. (**B**) *Kras* PDECs treated with vehicle control (DMSO), CXCL1, or a combination of CXCL1 and a CXCR2 inhibitor (SB225002) were plated for the senescence assay. Scale bar: 100 μm. (**C**) Injection protocol: Each injection contained 0.5 mg CXCR2 inhibitor (SB225002) per kilogram body weight. Mice were treated 2 times a week over 4 weeks. One injection was administrated at each injection day. Animals were euthanized and dissected 4 days after the last injection. (**D**) Detection of senescence in pancreatic cryosections from 9-week-old *Kras* mice treated with PBS as vehicle or CXCR2 inhibitor (SB225002), using SA-β-Gal as a marker. Scale bar: 50 μm. Ratio of SA-β-Gal–positive mPanIN cells to the total number of mPanIN cells in low-grade mPanIN (LG mPanIN) in 9-week-old *Kras* mice treated with PBS as vehicle or CXCR2 inhibitor (SB225002) was counted per ×200 optical high-power field (HPF). Mean ± SEM; $n \geq 4$; $^*P < 0.05$ by Mann-Whitney test; *n*, number of mice. (**E**) Representative H&E staining of pancreata from 9-week-old *Kras* mice after treatment with SB225002 or PBS. Scale bar: 50 μm. Number of low-grade (LG) or high-grade (HG) mPanIN in 9-week-old *Kras* mice treated with SB225002 or PBS per ×200 optical field. Mean ± SD; $n \geq 4$; $^*P < 0.05$, $^{**}P < 0.005$ by unpaired *t* test; *n*, number of mice. (**F**) Representative H&E staining of pancreata from 18-week-old **Kras* and **Kras CXCR2null* mice. Scale bars: 500 μm, 100 μm. (**G**) Numbers of low-grade (LG) and high-grade (HG) mPanIN in 18-week-old **Kras* ($n = 2$) and **Kras Cxcr2null* ($n = 3$) mice were counted per ×200 optical field (HPF). Mean ± SD; $^*P < 0.05$ by unpaired *t* test; N.D., not detectable; *n*, number of mice.

A total of 390 gene sets were shown to be upregulated, 35 of which were significantly induced in *Kras RelA* compared with *Kras* pancreata (Supplemental Figure 3B; gene set enrichment analysis). Furthermore, NF-κB–mediated transcriptional pathways were highly enriched in *Kras* but not in *Kras RelA* pancreata (12% in *Kras* vs. none in *Kras RelA*) (Figure 3A). Similarly, immunofluorescence staining revealed nuclear RelA in early mPanIN lesions and a few adjacent acinar cells of 4-week-old *Kras* mice, while *Kras RelA* pancreata were negative for nuclear RelA (Figure 3B). Moreover, "chemokine signaling pathways" (normalized enrichment score[NES] 1.5; $P = 0.002$) and "cytokine–cytokine receptor interaction pathways" (NES = 1.74; $P < 0.001$) were highly enriched in *Kras* but not in *Kras RelA* pancreata (Figure 3A). The largest group of upregulated transcription factor signatures in *Kras* mice was associated with proliferation, while signatures belonging to cell differentiation were highest in the *Kras RelA* group (Figure 3A). Positive gene set enrichment analysis (GSEA) signatures of HNF1_C (NES = 1.39; $P = 0.019$) and SOX9_B1 (NES = 1.48; $P = 0.003$) in *Kras RelA* mice indicate the possibility for increased ADM formation (Figure 3A). Furthermore, cell stress–associated transcription factor signatures were significantly increased upon loss of functional RelA

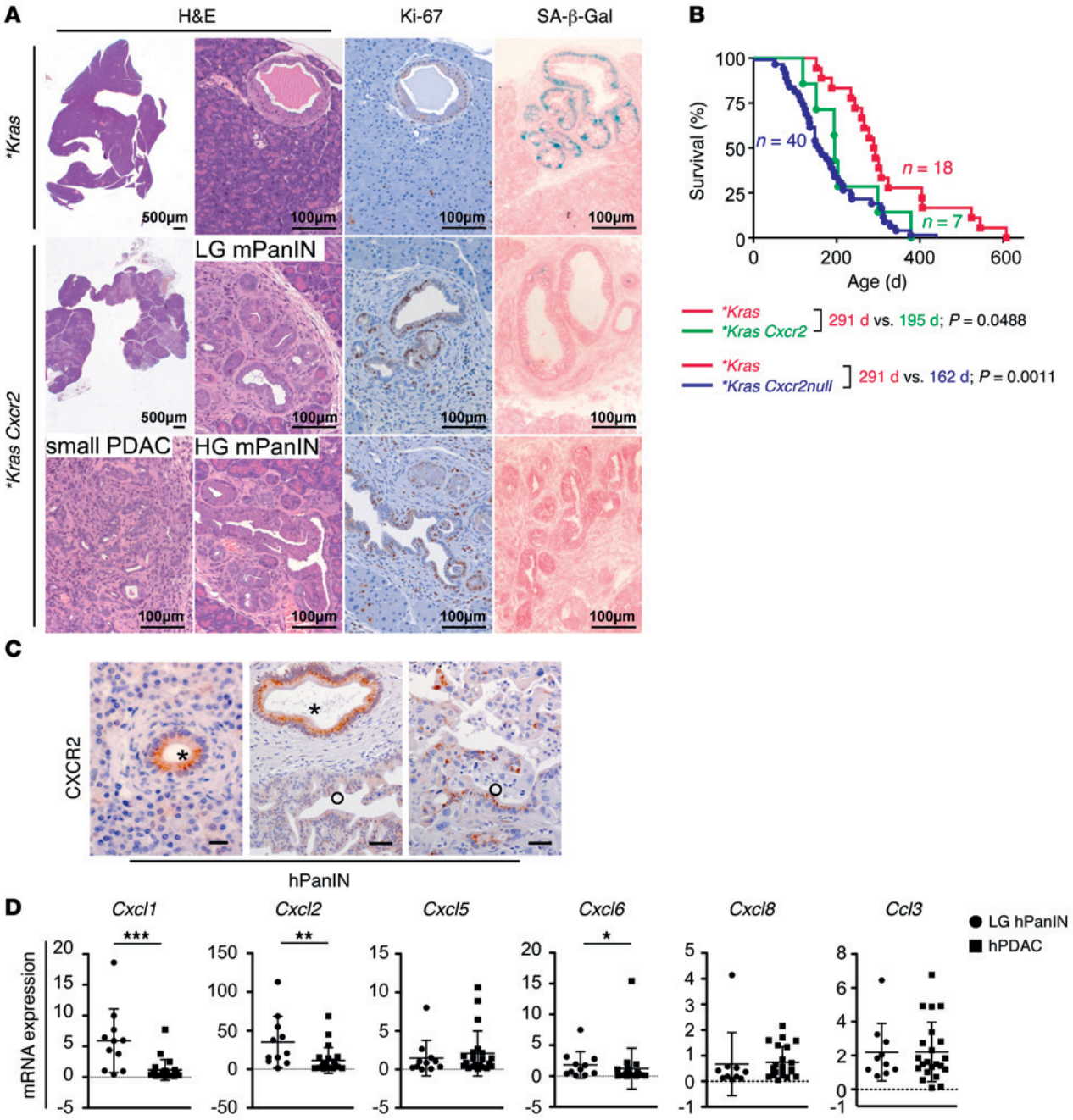

Figure 7. Pancreas-specific inactivation of CXCR2 is sufficient to bypass OIS. (**A**) H&E staining, expression of Ki-67, and SA-β-Gal activity in pancreata from 18-week-old **Kras* and **Kras Cxcr2* mice. Scale bars: 500 μm, 100 μm. Representative images are shown. (**B**) Kaplan-Meier curves documenting a median survival of 195 days in **Kras Cxcr2* mice (n = 7; green line) and of 162 days in **Kras CXCR2null* mice (n = 40; blue line) versus 291 days in **Kras* mice (n = 18; magenta line); P = 0.0488 and P = 0.0011 by Mantel-Cox log rank test. n, number of mice. (**C**) IHC analysis of human pancreatic cancer and tumor-adjacent tissue illustrates positive staining for CXCR2 in low-grade hPanIN (asterisk) and weak staining in high-grade hPanIN (circle) lesions. Scale bars: 20 μm. Representative images are shown. (**D**) Real-time PCR expression analysis of mRNA from microdissected human (h) low-grade (LG) PanIN cells and tumor ductal cells (hPDAC) for *Cxcl1*, *Cxcl2*, *Cxcl5*, *Cxcl6*, *Cxcl8*, and *Ccl3*. Mean ± SD; $n \geq 11$; *$P < 0.05$, **$P < 0.005$, ***$P < 0.0005$ by Mann-Whitney test; n, number of samples.

(Figure 3A). Indeed, IHC confirmed pronounced expression of SOX9, HNF1β, and γ-H2AX and accumulation of ROS, which are indicative of cell differentiation and cell stress, respectively, in *Kras RelA* mice (Figure 3B and Supplemental Figure 3C). These effects seem to be RelA-dependent, as deletion of the superordinated kinase IKK2 in *Kras* mice led to significant upregulation of numerous differential gene signatures involved in myc signaling, metabolism, biosynthesis, cell stress, and cell cycle using Kyoto Encyclopedia of Genes and Genomes (KEGG) and transcription factor signature analysis (Supplemental Table 1, A and B) (1).

Cell stress of acinar cells, for example due to inflammation, is known to drive ADM. To analyze RelA involvement in ADM, we used an in vitro model for exocrine metaplastic conversion. Acinar pancreatic epithelial explants cultured in a collagen matrix differentiate to duct-like structures after recombinant human TGFα (TGFα) stimulation, simulating in vivo ADM

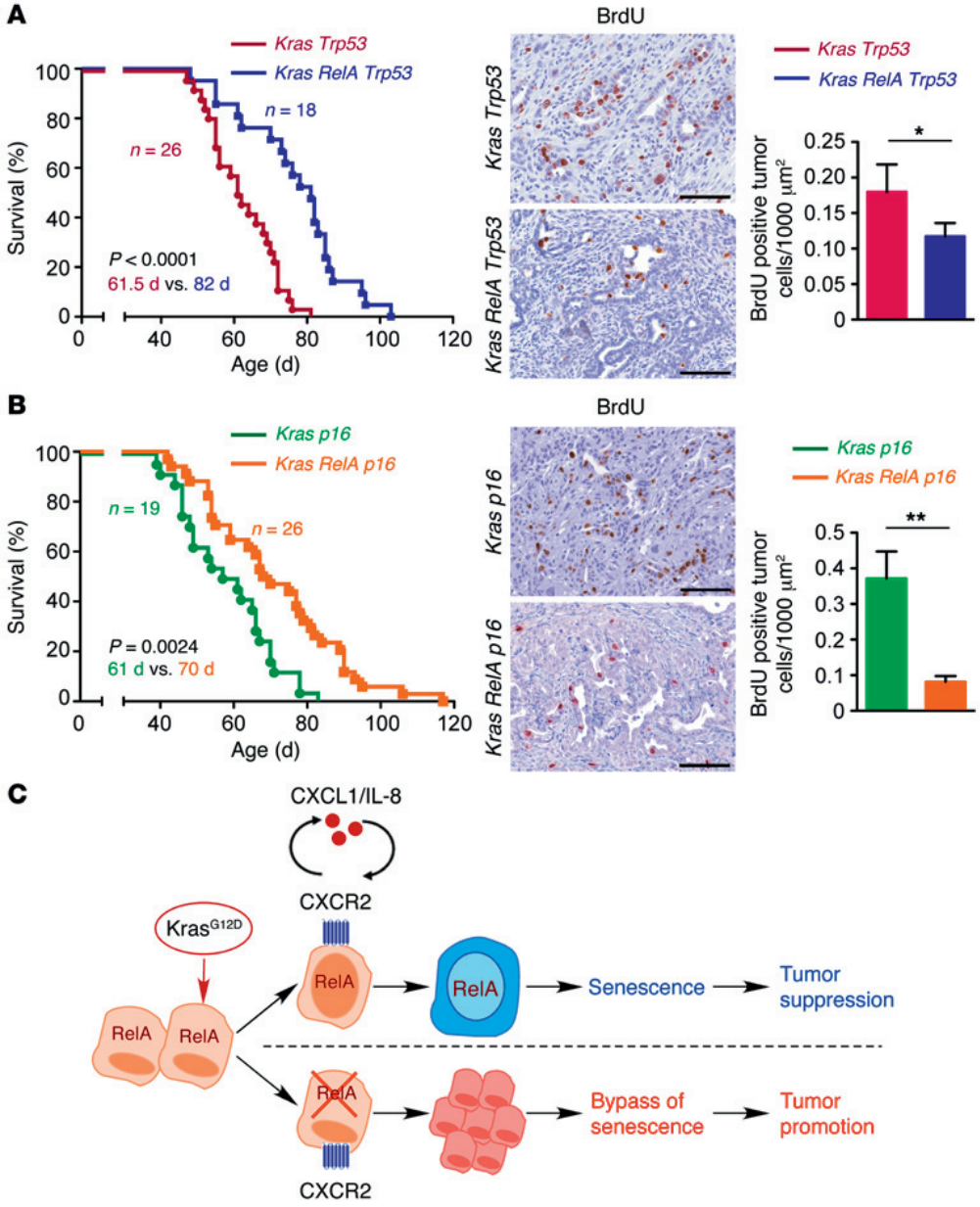

Figure 8. Abrogation of OIS in vivo illustrates dual role of RelA. (**A**) Kaplan-Meier curves documenting a median survival of 82 days in *Kras RelA Trp53* mice (n = 18; blue line) versus 61.5 days in *Kras Trp53* mice (n = 26; red line). $P < 0.0001$ by Mantel-Cox log rank test; n, number of mice. BrdU staining of PDAC tissue samples from *Kras Trp53* and *Kras RelA Trp53* mice. Scale bar: 100 µm. The number of BrdU-positive cells was counted per tumor area. Mean ± SD; n = 4; $^*P = 0.0266$ by unpaired t test; n, number of mice. (**B**) Kaplan-Meier analysis shows a median survival of 70 days in *Kras RelA p16* mice (n = 26; orange line) versus 61 days in *Kras p16* mice (n = 19; green line); $P = 0.0024$ by Mantel-Cox log rank test; n, number of mice. BrdU staining of PDAC tissue samples from *Kras p16* and *Kras RelA p16* mice. Scale bar: 100 µm. The number of BrdU-positive cells was counted per tumor area. Mean ± SD; n = 4; $^{**}P = 0.0012$ by unpaired t test; n, number of mice. (**C**) Schematic illustrating the dual role of RelA in pancreatic carcinogenesis. In early stages of tumorigenesis, the tumor-suppressive function of NF-κB is beneficial because it controls OIS by regulating the CXCL1/CXCR2 axis. However, as soon as OIS is bypassed during late stages of tumorigenesis, NF-κB supports tumor progression.

(Supplemental Figure 4A). Freshly harvested explants from pancreata of *Rela*$^{fl/fl}$ (hereafter referred to as *RelA*^{wt}) and *RelA*$^{fl/fl}$ *Ptf1a-Cre*^{ex1} (hereafter referred to as *RelA*$^{\Delta}$) littermates consisted of acinar cell clusters expressing α-amylase, but not the duct cell marker CK8/18 (Supplemental Figure 4B). Treated with 50 ng/ml TGFα for 5 days, 40.9% ± 3.7% of the *RelA*$^{\Delta}$ acinar explants displayed a duct-like morphology characterized by cystic structures lined with epithelial cells expressing the duct cell marker CK19. In contrast, only 24.2% ± 7.2% of acinar explants from *RelA*^{wt} pancreata transdifferentiated to duct-like structures upon TGFα treatment (Supplemental Figure 4, A, C, and D). To analyze ductal conversion in *RelA*^{wt} versus *RelA*$^{\Delta}$ acinar cells in an oncogenic *Kras* background, we isolated acinar cells from *Kras* and *Kras RelA* pancreata at an early time point to obtain maximal amount of exocrine tissue. These acinar cells were planted on collagen gel and were treated with 50 ng/ml TGFα for 5 days. A duct-like morphology was observed in 59.02% ± 0.14% of the *Kras RelA* acinar explants. In contrast, only 30.26% ± 0.09% of acinar explants derived from *Kras* pancreata transdifferentiated to duct-like structures (Supplemental Figure 4E).

These results are consistent with a central role of RelA in controlling NF-κB–mediated gene transcription. In the context of oncogenic *Kras*, RelA regulates cell stress and ADM-related pathways.

OIS in early mPanIN lesions in vivo depends on intact RelA function. Thus far, our data show that inactivation of RelA increases cell stress and facilitates mPanIN formation. However, how RelA mediates progression of mPanIN lesions to pancreatic cancer remained to be explored. Activation of the *Kras* oncogene can mobilize tumor suppressor networks to avert the hazard of malignant transformation. OIS represents such a network, blocking cell proliferation almost irreversibly, serving as a vital mechanism that protects against cancer. In pancreatic cancer, OIS is induced in early mPanIN, thereby impeding progression of preneoplastic lesions to PDAC (14). To identify senescent cells in situ, we

analyzed a panel of senescence-associated markers in pancreata from *Kras* and *Kras RelA* mice. The most commonly used biomarker of OIS in vivo is an elevated activity of senescence-associated β-galactosidase (SA-β-Gal), derived from the acidic lysosomal β-galactosidase (12). Quantification of SA-β-Gal–positive cells in low-grade mPanIN lesions from *Kras* and *Kras RelA* mice demonstrated loss of SA-β-Gal activity in *Kras RelA* mPanIN (Figure 4, A and B). In addition, the senescence marker decoy receptor 2 (DCR2; also known as TNFRSF10D) was significantly lower in *Kras RelA* pancreata than in *Kras* pancreata on both an mRNA expression and a protein level (Figure 4, C–E, and Supplemental Figure 5). Along the same lines, *p53* and *p21* mRNA and associated protein levels were downregulated in isolated pancreata of *Kras RelA* mice compared with *Kras* mice (Figure 4, C–E, and Supplemental Figure 5); mRNA levels of basic helix–loop–helix transcription factor *BHLHE40* (also known as *dec1*) also tend to be lower in *Kras RelA* mice (Figure 4C). Moreover, Western blot and immunohistological examinations revealed the downregulation of p16 and p19 in *Kras RelA* pancreata (Figure 4, D and E, and Supplemental Figure 5).

Recent studies have established that senescent cells secrete inflammatory cytokines and chemokines, extracellular proteases, and growth factors, collectively subsumed as the senescence-associated secretory phenotype (SASP). These factors are not only known to be NF-κB targets, but are also required to reinforce OIS. GSEA demonstrated a loss of the SASP signature in *Kras RelA* mice (Figure 4F).

Further, SASP is known to contribute to the surveillance and elimination of senescent cells through a tumor-suppressive immune response during the early stages of tumorigenesis (20, 21). To characterize the immune response in *Kras* and *Kras RelA* mice during pancreatic carcinogenesis, we digested the pancreata of 8-week-old mice and performed FACS analyses. In *Kras RelA* pancreata total macrophage population was significantly increased as shown by FACS using general macrophage markers ($CD11b^+F4/80^+$) (Supplemental Figure 6, A and B) and IHC (Supplemental Figure 6C). Among the total macrophage population, myeloid-derived suppressor cells (MDSCs; $CD11b^+Gr\text{-}1^+$), typically abundant within the pancreatic cancer microenvironment and implicated in immunosuppression, were more prominently found in neoplastic pancreata of *Kras RelA* than in *Kras* mice (Supplemental Figure 6D). FACS analysis further demonstrated an enrichment of macrophages expressing the additional M2 marker CD206 ($CD206^+CD11b^+F4/80^+$) in *Kras RelA* pancreata, indicative of an M2 polarization (Supplemental Figure 6, E and F). Furthermore, deletion of *Rela* in the pancreas of *Kras* mice led to decreased expression of genes associated with M1 activation, namely *Ifng*, *Tnf*, *Il12b*, *Cox2*, and *Il23a* (Supplemental Figure 6G).

Thus, our data indicate that RelA activation is required to reinforce OIS in mPanIN cells, which also impacts immune response. Deletion of *Rela* in neoplastic *Kras* pancreata supports a protumorigenic microenvironment. Subsets of protumorigenic M2 macrophages and MDSCs were found to be increased in the stroma of *Kras RelA* mice.

Activation of RelA-dependent signaling promotes OIS through CXCL1. Since OIS is induced in early mPanIN lesions, we isolated primary pancreatic duct epithelial cells (PDEC *Kras*) from *Kras* pancreata. Treatment of these cells with a specific NF-κB inhibitor (JSH-23) was accompanied by decreased SA-β-Gal activity (Figure 5A and Supplemental Figure 7A). JSH-23 has been demonstrated to block nuclear translocation and transcription activity of RelA (22). Given the documented effect of NF-κB on the expression of immune mediators (11), we used antibody arrays to monitor the expression profile of secreted cytokines and chemokines in conditioned media from PDEC *Kras* and PDEC *Kras* treated with JSH-23. As expected, inhibition of nuclear translocation and transcriptional activity of RelA specifically decreased the expression of certain inflammatory mediators, including G-CSF, GM-CSF, sICAM-1, CCl-5, TIMP-1, and TNF-α (Figure 5, B and C). Of the 40 cytokines and chemokines represented in this panel, CXCL1 (also known as KC) was most robustly downregulated in PDEC *Kras* treated with JSH-23 (Figure 5, B and C). The decrease in CXCL1 protein levels was corroborated by an increased SA-β-Gal activity in PDEC *Kras* incubated with CXCL1 for 48 hours (Figure 5D). Next, we investigated the involvement of CXCL1 in vivo by determining the cellular localization of *Cxcl1* mRNA expression in pancreata from 13-week-old *Kras* and *Kras RelA* mice using the RNAscope method for in situ mRNA detection. In *Kras* pancreata, *Cxcl1* mRNA expression was moderately to strongly present in the cytoplasm of most duct cells in mPanIN lesions, in acinar cells around mPanIN lesions, and in immune cells. Interestingly, *Cxcl1* mRNA was present in immune cells, only faintly present in a few duct cells, and absent in the majority of acinar cells in *Kras RelA* pancreata (Figure 5E). To determine the relevance of the observed link between the activation of RelA and CXCL1-dependent OIS, we used transgenic mice expressing *IL8*, the human orthologue of murine CXCL1 [*Tg(IL8)*, hereafter referred to as *IL-8tg*]. *IL-8tg* mice carry a bacterial artificial chromosome that encompasses the entire human *IL8* gene, including its regulatory elements (23). This mouse line was crossed to the *Kras RelA* strain to obtain LSL-$Kras^{G12D}$ $Rela^{fl/fl}$ *IL-8Tg* $Ptf1a\text{-}Cre^{ex1}$ mice (hereafter referred to as *Kras RelA IL-8tg* mice). Analysis and quantification of SA-β-Gal activity demonstrated a significantly higher percentage of SA-β-Gal–positive cells in low-grade lesions arising from *Kras RelA IL-8tg* pancreata compared with *Kras RelA* animals (Figure 5, F and G). Notably, IL-8 per se was sufficient to increase the number of SA-β-Gal–positive cells in low-grade mPanIN and to impede mPanIN progression in *Kras* animals (Supplemental Figure 7, B–D). But most strikingly, the phenotype of accelerated progression of mPanIN lesions in *Kras RelA* mice was nearly totally abrogated in the context of IL-8 expression (Figure 5, H and I). Coinciding with reinforcement of OIS and blocked mPanIN progression, induction of p53 in mPanIN was strongly detectable (Figure 5J). In line with the antioxidative function of p53, accumulation of ROS in mPanIN lacking RelA was also diminished in *Kras RelA IL-8tg mice* (Figure 5J).

Thus, these results strongly support the notion that CXCL1 contributes to the regulation of OIS via RelA activation in vivo and in vitro.

Systemic pharmacological and genetic inactivation of CXCR2 abrogates OIS and accelerates pancreatic carcinogenesis. Since CXCL1 acts through the chemokine receptor CXCR2, which is strictly expressed in PanIN lesions, but not in normal ductal epithelium, we then investigated whether CXCR2 is instrumental for reinforcement of OIS (Figure 6A). To this end, we treated

PDEC *Kras* with CXCL1 or with a combination of CXCL1 and a CXCR2 antagonist (SB225002) in vitro. The results demonstrated increased SA-β-Gal activity in PDEC *Kras* treated with CXCL1, but decreased SA-β-Gal activity in PDEC *Kras* treated with a combination CXCL1 and SB225002 (Figure 6B). To examine the relevance of the CXCR2 receptor in vivo, we treated 5-week-old *Kras* mice with SB225002 according to the protocol shown in Figure 6C or crossed LSL-$Kras^{G12D}$ *Pdx1-Cre* mice (referred to as **Kras* mice) to the $Cxcr2^{-/-}$ mouse line (LSL-$Kras^{G12D}$ *Pdx1-Cre* $Cxcr2^{-/-}$ mice, referred to hereafter as **Kras Cxcr2null*). The $Cxcr2^{-/-}$ mouse line lacks the receptor in the whole organism. We observed a dramatically decreased SA-β-Gal activity in low-grade mPanIN of the SB225002-treated group (Figure 6D) alongside accelerated tumorigenesis (Figure 6E). Similarly, **Kras Cxcr2null* mice revealed accelerated mPanIN progression; even some focal cancers developed in 18-week-old mice, which is normally not seen in **Kras* mice at this age (Figure 6, F and G).

Thus, our data suggest that either pharmacological or genetic systemic inactivation of CXCR2 leads to prevention of OIS, which in turn leads to accelerated pancreatic carcinogenesis.

Pancreas-specific inactivation of CXCR2 is sufficient to prevent OIS. To further corroborate the relevance of mPanIN-restricted CXCR2 for OIS in preneoplastic lesions we generated an additional **Kras* mouse line, lacking CXCR2 in the pancreas. To this end, **Kras* mice were crossed to floxed *Cxcr2* mice to obtain the LSL-$Kras^{G12D}$ $Cxcr2^{fl/fl}$ *Pdx1-Cre* line (referred to as **Kras Cxcr2* mice). Loss of CXCR2 in the pancreas resulted in impaired OIS and subsequently in increased proliferation (Figure 7A and Supplemental Figure 8, A and B). Histologically, mPanIN progression in **Kras Cxcr2* mice was accelerated (Supplemental Figure 8C). Notably, some **Kras Cxcr2* mice developed focal cancers similar to those in **Kras* mice lacking systemic CXCR2 expression. These observations were paralleled by decreased survival of **Kras* mice lacking CXCR2 either in mPanIN lesions (green line) or in the whole organism (blue line) (Figure 7B). To determine the relevance of the CXCL1/CXCR2 axis for the human disease, we stained human pancreatic cancer specimens for CXCR2 (Figure 7C). Similarly to our observations in mice, expression of CXCR2 was detectable in low-grade, but lost in high-grade, human PanIN (hPanIN) lesions. Transcript analysis of microdissected low-grade hPanIN lesions and human pancreatic cancer cells revealed significantly increased expression levels of *Cxcl1*, *Cxcl2*, and *Cxcl6* in low-grade hPanIN compared with human PDAC specimens (Figure 7D).

Moreover, we also investigated the expression of CXCR2 together with Ki-67, p53, and p16 in human normal pancreatic ducts as well as low-grade (hPanIN-1/2) and high-grade (hPanIN-3) hPanIN lesions by IHC. Supplemental Figure 8D demonstrates that CXCR2 and p16 decline as hPanIN lesions progress. In accordance with the induction of senescence in low-grade lesions, proliferation of these ducts is reduced (Supplemental Figure 8D). Conversely, p53 overexpression, which serves as a marker for the presence of p53 mutations, occurs only in high-grade hPanIN-3 lesions but is absent in low-grade hPanIN lesions (Supplemental Figure 8D), suggesting that expression of CXCR2 shares similarities with markers of OIS in human premalignant lesions (24).

These experiments demonstrate a direct impact of CXCR2 in ductal cells in the reinforcement of OIS in preneoplastic lesions during pancreatic carcinogenesis in a mouse model. Our data further provide evidence for the importance of the CXCL1/CXCR2 axis for pancreatic tumorigenesis in humans alike.

Reinforcement of OIS determines the dual role of RelA during pancreatic carcinogenesis. So far, our data indicate the significance of RelA in CXCL1/CXCR2-dependent OIS and its role as a tumor suppressor during the early stages of pancreatic tumorigenesis. To further genetically corroborate the implication of RelA in this novel and early mechanism of tumor surveillance, we took advantage of murine PDAC models that progress to pancreatic cancer via bypassing OIS. Since functional studies have demonstrated that senescence requires the p53 and p16/Rb pathways (25, 26), and their abrogation is necessary to bypass senescence, we crossed floxed *RelA* mice to *Kras* mice that lacked p53 or p16 in the pancreas (16). All mice progressed to PDACs. As expected, in the absence of OIS (data not shown), survival analysis demonstrated that survival of LSL-$Kras^{G12D}$ $Rela^{fl/fl}$ $Trp53^{fl/fl}$ $Ptf1a\text{-}Cre^{ex1}$ *(termed Kras RelA Trp53)* and LSL-$Kras^{G12D}$ $Rela^{fl/fl}$ $Ink4a^{fl/fl}$ $Ptf1a\text{-}Cre^{ex1}$ *(termed Kras RelA p16)* mice was significantly longer in comparison with LSL-$Kras^{G12D}$ $Trp53^{fl/fl}$ $Ptf1a\text{-}Cre^{ex1}$ *(termed Kras Trp53)* and LSL-$Kras^{G12D}$ $Ink4a^{fl/fl}$ $Ptf1a\text{-}Cre^{ex1}$ *(termed Kras p16)*, respectively (Figure 8, A and B). Established tumors in these mice revealed decreased proliferation after functional inactivation of RelA (Figure 8, A and B).

Taken together, these data clearly demonstrate a dual role of NF-κB/RelA activation in pancreatic carcinogenesis. In early stages of tumorigenesis, the tumor-suppressive function of NF-κB is beneficial because it controls OIS by regulating the CXCL1/CXCR2 axis (Figure 8C). However, as soon as OIS is bypassed during late stages of tumorigenesis, NF-κB supports tumor progression by enhancing proliferation of the transformed pancreatic cancer cells (Figure 8C).

Discussion

Our results illustrate several mechanisms that reveal the complexity of the IKK/NF-κB pathway during pancreatic carcinogenesis. Furthermore, they highlight several new aspects that need to be considered, especially when exploring the use of specific IKK/NF-κB and CXCR2 inhibitors as chemotherapeutic agents.

Recent studies have demonstrated that the components of the IKK complex IKK2 and NEMO drive progression of premalignant lesions to PDAC (1–3). However, because these kinase subunits have pleiotropic effects, it has remained unclear whether tumor promotion is directly mediated by the IKK/NF-κB pathway (10). Some studies have confirmed the tumor-enhancing function of the NF-κB subunit RelA in a mouse model of pulmonary adenocarcinoma (4). However, to date, no study has implicated RelA activation in spontaneous tumor formation in vivo in the pancreas. Using an in vivo model of pancreatic cancer, we investigated the function of RelA in the $Kras^{G12D}$ mouse line. Surprisingly, in contrast to IKK2 or NEMO, we noted rapid initiation and progression of preneoplastic lesions along with PDAC development in RelA-deficient $Kras^{G12D}$ mice, revealing a tumor-suppressive function for RelA. In contrast to the IKK complex, RelA is directly and immediately transferring cytoplasmic signals to the nucleus through binding of DNA, thus controlling transcription. However, blocked pancreatic carcinogenesis in IKK2/NEMO-deficient $Kras^{G12D}$ mice was not mediated directly by the NF-κB pathway, but through interlinked

pathways such as Notch, KLF, or IL-1/p62 (1–3). In fact, the IKK complex provides a basis for manifold cross-talk with other signaling pathways, as well as feedback circuits. In contrast to *Kras RelA* mice, comparative analysis of gene signatures revealed significant differences, including upregulation of numerous nonoverlapping pathways, in *Pdx1-Cre LSL-Kras^{G12D} IKK2$^{fl/fl}$* mice (Supplemental Table 1, A and B) (1). Loss of IKK2 resulted in induction of several pathways, mainly related to metabolism and biosynthesis, whereas functional inactivation of RelA only promoted cell stress and cell differentiation pathways. This further underlines substantial differences between the components of the IKK/NF-κB pathway. Although most studies have demonstrated a pro-oncogenic function of NF-κB, our findings are consistent with a tumor-suppressive function, as observed in other tumor models of the skin, the liver, and lymphomas (7, 9, 27, 28).

OIS is a failsafe mechanism that prevents the development of cancer in precancerous lesions of various tumors, including PDAC (29). Malignant cells are unable to undergo senescence, because of the loss of OIS effectors, such as p53 or p16 (30). The molecular mechanisms that regulate OIS during pancreatic oncogenesis are unknown. Using various mouse models of pancreatic cancer, we have provided novel findings that show that OIS requires activation of the RelA-dependent canonical NF-κB pathway during mPanIN progression. Senescence is mediated by cell-autonomous and non–cell-autonomous mechanisms that regulate OIS in a paracrine manner. Preneoplastic ductal cells that express *Kras^{G12D}* are not only the chief source of SASP components; mPanIN lesions are also the recipients, undergoing OIS through CXCR2 activation. The SASP comprises cytokines, chemokines, matrix metalloproteinases, and other proteins, most of which are regulated by NF-κB (11, 31–35). SASP components, such as IL-1β, IL-6, and CXCL1, were less prominently induced in *Kras* mice lacking RelA in the pancreas. Consequently, OIS was attenuated in these mice, whereas mice expressing *Kras^{G12D}* since embryonic development showed increased SA-β-Gal activity and widespread OIS in most early preneoplastic lesions (12). Our findings support the notion that induction of OIS in *Kras* mice necessitates the activation of RelA to regulate SASP (11, 29). RelA has been shown to cooperate with p53 in the execution of the senescence program (36). This interplay influences macrophage polarization and the subsequent targeting of senescent cells.

RelA also showed a potent effect on macrophage regulation. Tumor-associated macrophages can be polarized toward a classical, proinflammatory phenotype M1, or toward an alternative, anti-inflammatory M2 response. M1 macrophages are characterized by a proinflammatory cytokine profile and are potent killers of tumor cells, while M2 macrophages show mainly tumor-enhancing functions, promoting cell survival and proliferation (37, 38, 39). Interestingly, the senescent state triggered by *Kras^{G12D}* caused a significant increase in the secretion of factors known to promote M1 polarization, which is characterized by an increased propensity for cell killing and phagocytosis (40). Loss of RelA was associated with suppression of secretion of these factors and promotion with M2 polarization of macrophages and accumulation of MDSCs. MDSCs have been implicated in promoting tumor growth by suppressing antitumor immunity (41, 42). Interestingly, in the context of inflammation-associated tumorigenesis, recruitment of MDSCs was shown to depend on CXCL1/CXCR2. Recent work identifies CXCR2 as a new target for therapies aimed at inhibiting MDSC recruitment, providing a rationale for combining immune checkpoint inhibitors with agents designed to prevent MDSC-mediated immune suppression for cancer therapy (43). However, it seems that this mechanism is not crucial for the recruitment of MDSCs in the absence of OIS during *Kras*-induced pancreatic carcinogenesis. Beyond the CXCR2 ligands in mice (CXCL1, CXCL2/3, CXCL5, and CXCL7), several other factors, such as S100A8/A9, have been shown to attract myeloid cells to the tumor microenvironment (44). These factors do not only induce the accumulation of MDSCs; they are also secreted by MDSCs and by tumor cells to ensure the maintenance of functionally suppressive MDSCs within a tumor environment. Thus, rather than promoting inflammation, activation of RelA regulates the fine-tuning of tumor-inhibitory and tumor-promoting effects via SASP immune responses.

Of all SASP components, the CXCR2 ligand CXCL1 was shown to be required for OIS induction in vitro, whereas others, including IL-6 and IL-1β, have been shown to promote malignant phenotypes (45–47). Consistent with a previous study, PDECs that expressed *Kras^{G12D}* failed to undergo senescence without incubation with CXCL1 (15). CXCR2 in the pancreas of *Kras* mice is restricted to ductal cells. Although most studies have endorsed a pro-oncogenic function of CXCL1 and the human ortholog IL-8 in human tumors (48), our pharmacological and genetic approaches suggest a tumor surveillance role in pancreatic oncogenesis through the RelA-dependent regulation of the IL-8/CXCL1/CXCR2 axis. The CXCL1/CXCR2 axis is a critical regulatory system that reinforces growth arrest through senescence in vitro. Importantly, genetic and pharmaceutical blockage of CXCR2 in vivo mimicked a RelA-deficient phenotype, with reduced senescence and increased mPanIN progression. In contrast, overexpression of the human ortholog of IL-8 inhibited progression of preneoplastic lesions through expansion of senescent mPanIN lesions (25). However, the effects of CXCR2 on pancreatic oncogenesis appear to be context- and stage-dependent, because a recent study has demonstrated that CXCR2 promotes the development of PDAC in a mouse model (49). Notably, in this study activation of *Kras^{G12D}* was achieved by the *Pdx1-Cre* mouse line. Further, in the context of chronic inflammation–induced carcinogenesis in the colon, loss of CXCR2 suppresses inflammation-associated tumorigenesis. These effects have been attributed to the inhibition of infiltration of MDSCs into the colonic mucosa. However, in the context of spontaneous *Kras*-driven cancer development, CXCR2 and its ligands seem to play a central role in establishing OIS. Once OIS has been overcome, CXCR2 signaling seems to switch from a tumor suppressor to a tumor promoter (50).

In summary, we have examined the in vivo function of RelA during pancreatic oncogenesis, which comprises a dual mechanism (51–54). While on the one hand RelA inhibits the development of preneoplastic lesions by reinforcing senescence through the CXCL1/CXCR2 axis, its activation in established tumors promotes the cancer cell proliferation. Examining these context-dependent activities of RelA will be important for effective clinical use of NF-κB inhibitors. Furthermore, these findings underscore

that caution should be exercised when exploring the use of pharmaceuticals targeting the CXCR2 receptor as a therapeutic option for the treatment of various solid tumors.

Methods

Mice. LSL-*Kras*^{G12D} knock-in, *Ptf1a-Cre*^{ex1}, *RelA*$^{fl/fl}$ (termed *RelA*^{wt}), *Trp53*$^{fl/fl}$, *Ink4a*, and *Tg(IL8)* strains were interbred to obtain the compound mutant strains *Rela*$^{fl/fl}$ *Ptf1a-Cre*^{ex1} (termed *RelA*), LSL-*Kras*^{G12D} *RelA*$^{fl/fl}$ *Ptf1a-Cre*^{ex1} (termed *Kras RelA*), LSL-*Kras*^{G12D} *Tg(IL8) Ptf1a-Cre*^{ex1} (termed *Kras IL-8tg*), LSL-*Kras*^{G12D} *Rela*$^{fl/fl}$ *IL-8tg Ptf1a-Cre*^{ex1} (termed *Kras RelA IL-8tg*), LSL-*Kras*^{G12D} *Trp53*$^{fl/fl}$ *Ptf1a-Cre*^{ex1} (termed *Kras Trp53*), LSL-*Kras*^{G12D} *Rela*$^{fl/fl}$ *Trp53*$^{fl/fl}$ *Ptf1a-Cre*^{ex1} (termed *Kras RelA Trp53*), LSL-*Kras*^{G12D} *Ink4a*$^{fl/fl}$ *Ptf1a-Cre*^{ex1} (termed *Kras p16*), and LSL-*Kras*^{G12D} *RelA*$^{fl/fl}$ *Ink4a*$^{fl/fl}$ *Ptf1a-cre*^{ex1} (termed *Kras RelA p16*). Mutant LSL-*Kras*^{G12D} *Ptf1a-Cre*^{ex1} mice (termed *Kras,* the positive control) were used as control animals (19, 25, 55–58). LSL-*Kras*^{G12D} *Pdx1-Cre* (termed **Kras*), LSL-*Kras*^{G12D} *Cxcr2*$^{fl/fl}$ *Pdx1-Cre* (termed **Kras Cxcr2*), and LSL-*Kras*^{G12D} *Pdx1-Cre Cxcr2*$^{-/-}$ (termed **Kras Cxcr2null*) mice were obtained from Owen J. Sansom.

RNAscope method for in situ mRNA detection. In situ detection of *Cxcl1* transcripts in formalin-fixed paraffin-embedded (FFPE) pancreatic samples was performed using the RNAscope method (Advanced Cell Diagnostics) according to the manufacturer's instructions. Briefly, 4-μm FFPE pancreatic sections were pretreated with heat, deparaffinized, boiled with a pretreatment solution for 15 minutes, and submitted to protease digestion followed by hybridization for 2 hours with a target probe for *CXCL1*. Thereafter, an HRP-based signal amplification system was hybridized to the target probe before color development with 3,3′-diaminobenzidine tetrahydrochloride. Positive staining was defined as the presence of brown dots.The housekeeping gene *ubiquitin C* (*Ubc*) served as a positive control. The *DapB* gene, which is derived from a bacterial gene sequence, was used as a negative control.

Fluorescence-activated cell sorting (FACS). Single-cell suspensions were prepared from fresh pancreas and spleen. Pancreata were minced, incubated with 1.2 mg/ml collagenase type VIII (catalog C2139; Sigma-Aldrich) and 0.1 mg/ml soybean trypsin inhibitor (catalog T9003; Sigma-Aldrich) in PBS for 10 minutes at 37°C, and then passed through a Corning 70-μm Cell Strainer (catalog 352350; Corning). Spleens were crushed, passed through a 70-μm cell strainer, washed once with PBS/2% FCS, and treated with rbc lysis buffer (catalog R7757; Sigma-Aldrich) for 90 seconds to eliminate rbcs. Cell suspensions were stained in PBS/2% FCS with the following antibodies: CD45 (clone 30-F11), CD3e (clone 145-2C11), CD11b (clone M1/70), F4/80 (clone BM8; all from eBioscience); CD206 (clone C068C2), CD4 (clone GK1.5) (all from BioLegend); and Gr-1 (clone RB6-8C5) (Thermo Fisher Scientific). Flow cytometry analysis was performed using a Gallios flow cytometer (Beckman Coulter) after gating and exclusion of dead cells. Data were analyzed using a software package (FlowJo).

Accession number. Microarray data are available in the ArrayExpress database (www.ebi.ac.uk/arrayexpress) under accession number E-MTAB-3436.

Supplemental Methods. For all methods not listed here, please refer to the online Supplemental Methods section.

Author contributions

HA formulated hypotheses and designed experiments. ML performed the majority of experiments and analyzed data. JM, OS, DS, GJS, and TCW provided murine models. SMW contributed to flow cytometry sorting analyses. KND and HE analyzed microarray data. OK, MW, and TK performed several experiments. JS, IED, and BS provided patient samples and analyzed human data. ML and HA wrote the manuscript. JM, IED, MH, JMS, TCW, and RMS edited the manuscript.

Acknowledgments

We thank Chantal Geisert and Viktoria Mayr for excellent technical assistance. This work was supported by grants from Deutsche Forschungsgemeinschaft (AL 1174/5-1 and LE 3222/1-1) and Deutsche Krebshilfe (111646).

Address correspondence to: Hana Algül, II. Medizinische Klinik, Klinikum rechts der Isar, Technische Universität München, 81675 Munich, Germany. Phone: 49.89.4140.5215; E-mail: hana.alguel@mri.tum.de.

1. Ling J, et al. KrasG12D-induced IKK2/β/NF-κB activation by IL-1α and p62 feedforward loops is required for development of pancreatic ductal adenocarcinoma. *Cancer Cell*. 2012;21(1):105–120.
2. Maier HJ, Wagner M, Schips TG, Salem HH, Baumann B, Wirth T. Requirement of NEMO/IKKγ for effective expansion of KRAS-induced precancerous lesions in the pancreas. *Oncogene*. 2013;32(21):2690–2695.
3. Maniati E, et al. Crosstalk between the canonical NF-κB and Notch signaling pathways inhibits Pparγ expression and promotes pancreatic cancer progression in mice. *J Clin Invest*. 2011;121(12):4685–4699.
4. Bassères DS, Ebbs A, Levantini E, Baldwin AS. Requirement of the NF-kappaB subunit p65/RelA for K-Ras-induced lung tumorigenesis. *Cancer Res*. 2010;70(9):3537–3546.
5. Xia Y, et al. Reduced cell proliferation by IKK2 depletion in a mouse lung-cancer model. *Nat Cell Biol*. 2012;14(3):257–265.
6. Meylan E, et al. Requirement for NF-kappaB signalling in a mouse model of lung adenocarcinoma. *Nature*. 2009;462(7269):104–107.
7. Maeda S, Kamata H, Luo JL, Leffert H, Karin M. IKKbeta couples hepatocyte death to cytokine-driven compensatory proliferation that promotes chemical hepatocarcinogenesis. *Cell*. 2005;121(7):977–990.
8. Luedde T, et al. Deletion of NEMO/IKKgamma in liver parenchymal cells causes steatohepatitis and hepatocellular carcinoma. *Cancer Cell*. 2007;11(2):119–132.
9. Dajee M, et al. NF-kappaB blockade and oncogenic Ras trigger invasive human epidermal neoplasia. *Nature*. 2003;421(6923):639–643.
10. Perkins ND. The diverse and complex roles of NF-κB subunits in cancer. *Nat Rev Cancer*. 2012;12(2):121–132.
11. Chien Y, et al. Control of the senescence-associated secretory phenotype by NF-κB promotes senescence and enhances chemosensitivity. *Genes Dev*. 2011;25(20):2125–2136.
12. Caldwell ME, et al. Cellular features of senescence during the evolution of human and murine ductal pancreatic cancer. *Oncogene*. 2012;31(12):1599–1608.
13. Collado M, et al. Tumour biology: senescence in premalignant tumours. *Nature*. 2005;436(7051):642.
14. Guerra C, et al. Pancreatitis-induced inflammation contributes to pancreatic cancer by inhibiting oncogene-induced senescence. *Cancer Cell*. 2011;19(6):728–739.
15. Lee KE, Bar-Sagi D. Oncogenic KRas suppresses inflammation-associated senescence of pancreatic ductal cells. *Cancer Cell*. 2010;18(5):448–458.
16. Morton JP, et al. Mutant p53 drives metastasis and overcomes growth arrest/senescence in pancreatic cancer. *Proc Natl Acad Sci U S A*.

2010;107(1):246–251.
17. Collado M, Blasco MA, Serrano M. Cellular senescence in cancer and aging. *Cell*. 2007;130(2):223–233.
18. Moir JA, White SA, Mann J. Arrested development and the great escape — the role of cellular senescence in pancreatic cancer. *Int J Biochem Cell Biol*. 2014;57:142–148.
19. Algül H, et al. Pancreas-specific RelA/p65 truncation increases susceptibility of acini to inflammation-associated cell death following cerulein pancreatitis. *J Clin Invest*. 2007;117(6):1490–1501.
20. Kang TW, et al. Senescence surveillance of pre-malignant hepatocytes limits liver cancer development. *Nature*. 2011;479(7374):547–551.
21. Krizhanovsky V, et al. Senescence of activated stellate cells limits liver fibrosis. *Cell*. 2008;134(4):657–667.
22. Hu C, Sun L, Hu Y, Lu D, Wang H, Tang S. Functional characterization of the NF-kappaB binding site in the human NOD2 promoter. *Cell Mol Immunol*. 2010;7(4):288–295.
23. Asfaha S, et al. Mice that express human interleukin-8 have increased mobilization of immature myeloid cells, which exacerbates inflammation and accelerates colon carcinogenesis. *Gastroenterology*. 2013;144(1):155–166.
24. Schwitalla S, et al. Loss of p53 in enterocytes generates an inflammatory microenvironment enabling invasion and lymph node metastasis of carcinogen-induced colorectal tumors. *Cancer Cell*. 2013;23(1):93–106.
25. Campisi J. Aging, cellular senescence, and cancer. *Annu Rev Physiol*. 2013;75:685–705.
26. Tchkonia T, Zhu Y, van Deursen J, Campisi J, Kirkland JL. Cellular senescence and the senescent secretory phenotype: therapeutic opportunities. *J Clin Invest*. 2013;123(3):966–972.
27. Jing H, et al. Opposing roles of NF-κB in anti-cancer treatment outcome unveiled by cross-species investigations. *Genes Dev*. 2011;25(20):2137–2146.
28. Maeda S, et al. IκB kinaseβ/nuclear factor-κB activation controls the development of liver metastasis by way of interleukin-6 expression. *Hepatology*. 2009;50(6):1851–1860.
29. Rodier F, Campisi J. Four faces of cellular senescence. *J Cell Biol*. 2011;192(4):547–556.
30. Singh SK, Ellenrieder V. Senescence in pancreatic carcinogenesis: from signalling to chromatin remodelling and epigenetics. *Gut*. 2013;62(9):1364–1372.
31. Acosta JC, et al. A complex secretory program orchestrated by the inflammasome controls paracrine senescence. *Nat Cell Biol*. 2013;15(8):978–990.
32. Coppé JP, Desprez PY, Krtolica A, Campisi J. The senescence-associated secretory phenotype: the dark side of tumor suppression. *Annu Rev Pathol*. 2010;5:99–118.
33. Coppé JP, et al. Senescence-associated secretory phenotypes reveal cell-nonautonomous functions of oncogenic RAS and the p53 tumor suppressor. *PLoS Biol*. 2008;6(12):2853–2868.
34. Pérez-Mancera PA, Young AR, Narita M. Inside and out: the activities of senescence in cancer. *Nat Rev Cancer*. 2014;14(8):547–558.
35. Young AR, Narita M. SASP reflects senescence. *EMBO Rep*. 2009;10(3):228–230.
36. Lujambio A, et al. Non-cell-autonomous tumor suppression by p53. *Cell*. 2013;153(2):449–460.
37. Sica A, Bronte V. Altered macrophage differentiation and immune dysfunction in tumor development. *J Clin Invest*. 2007;117(5):1155–1166.
38. Murray PJ, Wynn TA. Protective and pathogenic functions of macrophage subsets. *Nat Rev Immunol*. 2011;11(11):723–737.
39. Mantovani A, Biswas SK, Galdiero MR, Sica A, Locati M. Macrophage plasticity and polarization in tissue repair and remodelling. *J Pathol*. 2013;229(2):176–185.
40. Biswas SK, Mantovani A. Macrophage plasticity and interaction with lymphocyte subsets: cancer as a paradigm. *Nat Immunol*. 2010;11(10):889–896.
41. Khaled YS, Ammori BJ, Elkord E. Myeloid-derived suppressor cells in cancer: recent progress and prospects. *Immunol Cell Biol*. 2013;91(8):493–502.
42. Lindau D, Gielen P, Kroesen M, Wesseling P, Adema GJ. The immunosuppressive tumour network: myeloid-derived suppressor cells, regulatory T cells and natural killer T cells. *Immunology*. 2013;138(2):105–115.
43. Highfill SL, et al. Disruption of CXCR2-mediated MDSC tumor trafficking enhances anti-PD1 efficacy. *Sci Transl Med*. 2014;6(237):237ra67.
44. Gebhardt C, Nemeth J, Angel P, Hess J. S100A8 and S100A9 in inflammation and cancer. *Biochem Pharmacol*. 2006;72(11):1622–1631.
45. Acosta JC, et al. Chemokine signaling via the CXCR2 receptor reinforces senescence. *Cell*. 2008;133(6):1006–1018.
46. Lesina M, et al. Stat3/Socs3 activation by IL-6 transsignaling promotes progression of pancreatic intraepithelial neoplasia and development of pancreatic cancer. *Cancer Cell*. 2011;19(4):456–469.
47. Quante M, et al. Bile acid and inflammation activate gastric cardia stem cells in a mouse model of Barrett-like metaplasia. *Cancer Cell*. 2012;21(1):36–51.
48. Matsuo Y, et al. CXCL8/IL-8 and CXCL12/SDF-1α co-operatively promote invasiveness and angiogenesis in pancreatic cancer. *Int J Cancer*. 2009;124(4):853–861.
49. Ijichi H, et al. Inhibiting Cxcr2 disrupts tumor-stromal interactions and improves survival in a mouse model of pancreatic ductal adenocarcinoma. *J Clin Invest*. 2011;121(10):4106–4117.
50. Katoh H, Wang D, Daikoku T, Sun H, Dey SK, Dubois RN. CXCR2-expressing myeloid-derived suppressor cells are essential to promote colitis-associated tumorigenesis. *Cancer Cell*. 2013;24(5):631–644.
51. Burgess DJ. Senescence. NF-κB shows its beneficial side. *Nat Rev Cancer*. 2011;11(12):832–833.
52. Klein U, Ghosh S. The two faces of NF-κB signaling in cancer development and therapy. *Cancer Cell*. 2011;20(5):556–558.
53. Perkins ND. NF-κB: tumor promoter or suppressor? *Trends Cell Biol*. 2004;14(2):64–69.
54. Tergaonkar V, Perkins ND. p53 and NF-κB crosstalk: IKKα tips the balance. *Mol Cell*. 2007;26(2):158–159.
55. Hingorani SR, et al. Preinvasive and invasive ductal pancreatic cancer and its early detection in the mouse. *Cancer Cell*. 2003;4(6):437–450.
56. Marino S, Vooijs M, van Der Gulden H, Jonkers J, Berns A. Induction of medulloblastomas in p53-null mutant mice by somatic inactivation of Rb in the external granular layer cells of the cerebellum. *Genes Dev*. 2000;14(8):994–1004.
57. Nakhai H, et al. Ptf1a is essential for the differentiation of GABAergic and glycinergic amacrine cells and horizontal cells in the mouse retina. *Development*. 2007;134(6):1151–1160.
58. Aguirre AJ, et al. Activated Kras and Ink4a/Arf deficiency cooperate to produce metastatic pancreatic ductal adenocarcinoma. *Genes Dev*. 2003;17(24):3112–3126.

Gastroenterology 2019;156:203–217

BASIC AND TRANSLATIONAL—PANCREAS

Levels of the Autophagy-Related 5 Protein Affect Progression and Metastasis of Pancreatic Tumors in Mice

Kivanc Görgülü,[1,*] **Kalliope N. Diakopoulos**,[1,*] Jiaoyu Ai,[1] Benjamin Schoeps,[2] Derya Kabacaoglu,[1] Angeliki-Faidra Karpathaki,[1] Katrin J. Ciecielski,[1] Ezgi Kaya-Aksoy,[1] Dietrich A. Ruess,[1] Alexandra Berninger,[1] Marlena Kowalska,[1] Marija Stevanovic,[1] Sonja M. Wörmann,[1] Thomas Wartmann,[3] Yue Zhao,[3] Walter Halangk,[3] Svetlana Voronina,[4] Alexey Tepikin,[4] Anna Melissa Schlitter,[5] Katja Steiger,[5,6] Anna Artati,[7] Jerzy Adamski,[7,8,9] Michaela Aichler,[10] Axel Walch,[10] Martin Jastroch,[11] Götz Hartleben,[8] Christos S. Mantzoros,[12] Wilko Weichert,[5] Roland M. Schmid,[1] Stephan Herzig,[8] Achim Krüger,[2] Bruno Sainz Jr,[13] Marina Lesina,[1,§] and Hana Algül[1,§]

[1]Klinik und Poliklinik für Innere Medizin II, Klinikum Rechts der Isar, Technische Universität München, Munich, Germany; [2]Institute of Molecular Immunology and Experimental Oncology, Klinikum Rechts der Isar, Technische Universität München, Munich, Germany; [3]Klinik für Chirurgie Bereich Experimentelle Operative Medizin, Universitätsklinikum Magdeburg, Magdeburg, Germany; [4]Institute of Translational Medicine, University of Liverpool, Liverpool, UK; [5]Institute of Pathology, Technische Universität München, Munich, Germany and German Cancer Consortium, Munich, Germany; [6]Comparative Experimental Pathology, Institute of Pathology, Technische Universität München, Munich, Germany; [7]Institute of Experimental Genetics, Genome Analysis Centre, Helmholtz Zentrum München, Neuherberg, Germany; [8]Institute for Diabetes and Cancer, German Center for Diabetes Research, Neuherberg, Germany; [9]Lehrstuhl für Experimentelle Genetik, Technische Universität München, Freising-Weihenstephan, Germany; [10]Research Unit Analytical Pathology, Helmholtz Zentrum München, Neuherberg, Germany; [11]Helmholtz Diabetes Center and German Diabetes Center, Helmholtz Zentrum München, Neuherberg, Germany; [12]Division of Endocrinology, Diabetes, and Metabolism, Beth Israel Deaconess Medical Centre, Harvard Medical School, Boston, Massachusetts; and [13]Department of Biochemistry, School of Medicine, Autónoma University of Madrid, Madrid, Spain

See editorial on page 17.

BACKGROUND AND AIMS: Cells in pancreatic ductal adenocarcinoma (PDAC) undergo autophagy, but its effects vary with tumor stage and genetic factors. We investigated the consequences of varying levels of the autophagy related 5 (Atg5) protein on pancreatic tumor formation and progression. **METHODS:** We generated mice that express oncogenic Kras in primary pancreatic cancer cells and have homozygous disruption of *Atg5* (*A5;Kras*) or heterozygous disruption of *Atg5* (*A5*$^{+/-}$*;Kras*), and compared them with mice with only oncogenic *Kras* (controls). Pancreata were analyzed by histology and immunohistochemistry. Primary tumor cells were isolated and used to perform transcriptome, metabolome, intracellular calcium, extracellular cathepsin activity, and cell migration and invasion analyses. The cells were injected into wild-type littermates, and orthotopic tumor growth and metastasis were monitored. *Atg5* was knocked down in pancreatic cancer cell lines using small hairpin RNAs; cell migration and invasion were measured, and cells were injected into wild-type littermates. PDAC samples were obtained from independent cohorts of patients and protein levels were measured on immunoblot and immunohistochemistry; we tested the correlation of protein levels with metastasis and patient survival times. **RESULTS:** *A5*$^{+/-}$*;Kras* mice, with reduced Atg5 levels, developed more tumors and metastases, than control mice, whereas *A5;Kras* mice did not develop any tumors. Cultured *A5*$^{+/-}$*;Kras* primary tumor cells were resistant to induction and inhibition of autophagy, had altered mitochondrial morphology, compromised mitochondrial function, changes in intracellular Ca^{2+} oscillations, and increased activity of extracellular cathepsin L and D. The tumors that formed in *A5*$^{+/-}$*;Kras* mice contained greater numbers of type 2 macrophages than control mice, and primary *A5*$^{+/-}$*;Kras* tumor cells had up-regulated expression of cytokines that regulate macrophage chemoattraction and differentiation into M2 macrophage. Knockdown of *Atg5* in pancreatic cancer cell lines increased their migratory and invasive capabilities, and formation of metastases following injection into mice. In human PDAC samples, lower levels of ATG5 associated with tumor metastasis and shorter survival time. **CONCLUSIONS:** In mice that express oncogenic Kras in pancreatic cells, heterozygous disruption of *Atg5* and reduced protein levels promotes tumor development, whereas homozygous disruption of *Atg5* blocks tumorigenesis. Therapeutic strategies to alter autophagy in PDAC should consider the effects of ATG5 levels to avoid the expansion of resistant and highly aggressive cells.

Keywords: Atg5 Levels; Pancreatic Carcinogenesis; Ca^{2+}; Mitochondria; Cathepsins.

*Authors share co-first authorship; §Authors share co-senior authorship.

Abbreviations used in this paper: **ADM, acinar-to-ductal metaplasia; Atg5, autophagy related 5; FBS, fetal bovine serum; FCS, fetal calf serum; PDAC, pancreatic ductal adenocarcinoma; PanIN, pancreatic intraepithelial neoplasia; shRNA, small hairpin RNA.**

Most current article

0016-5085/$36.00
https://doi.org/10.1053/j.gastro.2018.09.053

WHAT YOU NEED TO KNOW

BACKGROUND AND CONTEXT

Autophagy is considered a therapeutic target in pancreatic adenocarcinomas. As the effect of autophagy pathway inhibition remains unclear, the authors investigated the role of *Atg5*, an important autophagy regulator, in PDAC.

NEW FINDINGS

The authors correlate pancreatic malignancy with *Atg5* levels in mice and patients. Reduced *Atg5* levels enhance pancreatic cancer aggressiveness in vitro and in vivo through mechanisms including cathepsin activation and pro-tumorigenic M2-macrophage infiltration.

LIMITATIONS

Reduction of *Atg5*-levels influences a multitude of cellular functions collectively promoting pancreatic cancer progression and metastasis. Future studies may need to analyze the exact contribution of each of these pathways in pancreatic cancer.

IMPACT

Autophagy pathway inhibitors are utilized in PDAC-treatment. However, caution is required as reduced levels of an autophagy pathway regulator are correlated with metastasis/patient survival.

Pancreatic ductal adenocarcinoma (PDAC), the most common type of pancreatic cancer, frequently exhibits mutations in the *KRAS* oncogene, leading to constitutive activation of the KRAS-signaling pathway. Oncogenic KRAS has been shown to promote tumorigenesis through cell-autonomous (proliferation, migration, survival) and non-cell autonomous (tumor microenvironment) effects. In addition, it has also recently been associated with pro-tumorigenic alterations in cell metabolism, protein synthesis, cell growth, and stimulation of autophagy.[1] Autophagy is a central regulator of metabolism and cell homeostasis.[2,3] During baseline or cell stress/nutrient starvation–triggered autophagy, cytoplasmic constituents are engulfed into double-membrane autophagosomes and delivered to lysosomes for degradation and recycling. Autophagy typically orchestrates detoxification, release of nutrients, and restoration of cell homeostasis. Multiple autophagy genes (Atg) are involved in autophagosome formation. An important player is Atg5, which binds to Atg12-Atg16 and mediates conjugation of LC3 I to phosphatidylethanolamine, forming LC3 II. LC3 II is attached to the autophagosomal membrane and interacts with multiple adaptor proteins (eg, *Sqstm1*/p62) shuttling cargo molecules to autophagosomes.

Atg5 is required for formation of LC3 II–positive autophagosomes and maintenance of autophagic flux. Inhibition of autophagy by deletion of *Atg5* in the context of oncogene activation/tumor suppressor gene inhibition has been performed in multiple tissue types to study the role of autophagy during various stages of carcinogenesis.[3] Surprisingly, *Atg5*-deletion in the pancreas[4,5] and lung[6] has been shown to increase tumor initiation but decrease tumor progression, indicating a tumor stage–dependent action of autophagy. The underlying mechanisms of these phenotypes were proposed to be increased DNA damage, cell stress, apoptosis, and metabolic deficiencies.

Here we describe for the first time the opposing functions that varying levels of Atg5 have during pancreatic carcinogenesis. With the help of well-established models of in vitro and in vivo pancreatic carcinogenesis, we show that stages of pancreatic carcinogenesis critically depend on the levels of Atg5. Complete loss of *Atg5* in the pancreas during embryogenesis accelerates tumor initiation but blocks tumor progression, while monoallelic loss significantly increases tumor incidence and metastasis rate. Importantly, deletion of 1 *Atg5* allele and reduction of Atg5 protein levels increases PDAC aggressiveness through cell-autonomous and non–cell autonomous effects, collectively enhancing tumor malignancy. Small hairpin RNA (shRNA)–mediated knockdown of *Atg5* further highlights that the exact association of Atg5 levels with PDAC phenotype follows a non-linear pattern. Thus, our results not only provide novel evidence on the role of autophagy during PDAC development and progression, but also highlight the importance of exercising caution when blocking autophagy in PDAC.

Materials and Methods

All authors had access to the study data and reviewed and approved the final manuscript.

Mice

The $Atg5^{flox/flox}$,[7] $Ptf1a\text{-}cre^{ex1}$,[8] $LSL\text{-}Kras^{G12D}$ knock-in[9] strains were interbred to generate compound mutant $Atg5^{flox/flox}$; $Ptf1a\text{-}cre^{ex1}$; $LSL\text{-}Kras^{G12D}$ (termed *A5;Kras*), $Atg5^{flox/+}$;$Ptf1a\text{-}cre^{ex1}$; $LSL\text{-}Kras^{G12D}$ (termed $A5^{+/-}$;*Kras*), and $Ptf1a\text{-}cre^{ex1}$; $LSL\text{-}Kras^{G12D}$ (termed *Kras*) control animals. *TG(CAG-EGFP/Map1lc3b)53Nmz* transgenic mice (termed *GFP-LC3*)[10] interbred with $A5^{+/-}$;*Kras* mice to generate *A5;Kras* (termed *GFP-LC3;A5;Kras)*, $A5^{+/-}$;*Kras* (termed *GFP-LC3;*$A5^{+/-}$;*Kras)* or *Kras* (termed *GFP-LC3;Kras*) mice with concomitant GFP-LC3 expression were used for autophagosome detection. Littermate animals without $Ptf1a\text{-}cre^{ex1}$ expression were used for orthotopic transplantation and tail-vein injections. For all the experiments, mice were housed under specific pathogen-free conditions. All animal procedures were reviewed and approved by the Zentrum für Präklinische Forschung of the Technische Universität München, which follows the federal German guidelines for ethical animal treatment (Regierung von Oberbayern).

Statistical Analysis

Data are displayed as mean ± SD. Student *t* test was performed to compare the parameters for the groups by using GraphPad Prism (GraphPad, La Jolla, CA). Statistical significance was set at $*P < .05$, $**P < .01$, and $***P < .001$. Survival rates were calculated and displayed by the Kaplan–Meier method. Survival curves were compared by log-rank test using GraphPad Prism.

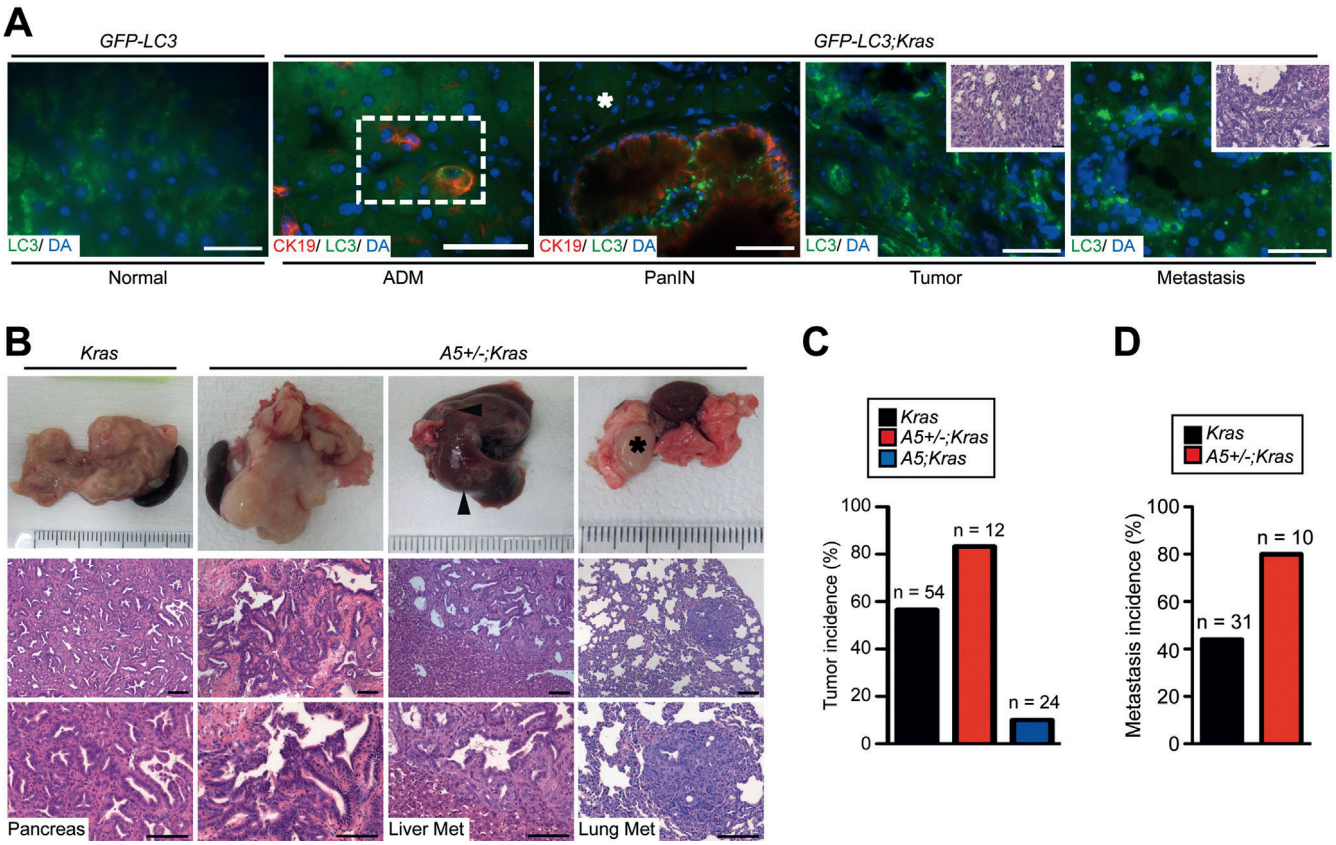

Figure 1. Monoallelic loss of *Atg5* influences metastatic load. (*A*) Autophagy in the pancreas of *GFP-LC3* transgenic mice under normal conditions and during PDAC progression in *GFP-LC3;Kras* mice. Tumor and liver metastasis are shown; *white square/white asterisk* indicate ADM/PanIN-adjacent acinar cells. DA, 4′,6-diamidino-2-phenylindole. (*B*) Representative pictures of pancreatic, liver, and lung tumors from *Kras* and $A5^{+/-}$;*Kras* mice; *black arrowheads/asterisk* point to metastatic focus in liver/lung, respectively. (*C*) Tumor incidence (%) in *Kras* (n = 54), $A5^{+/-}$;*Kras* (n = 12), and *A5;Kras* (n = 24) mice. (*D*) Metastasis incidence (%) in *Kras* (n = 31) and $A5^{+/-}$;*Kras* (n = 10) mice. Scale bars = 50 μm.

Results

Monoallelic Loss of Atg5 *Influences Metastatic Load*

Autophagy can be visualized in the pancreas as GFP-LC3–positive autophagosomes using *GFP-LC3* transgenic mice (Figure 1*A*). Under normal-fed conditions, GFP-LC3 puncta are visible in acinar cells. During pancreatic carcinogenesis, autophagosomes are detectable in premalignant acinar-to-ductal metaplasias (ADM), pancreatic intraepithelial neoplasias (PanIN), as well as in full-blown pancreatic tumors and metastasis (liver) of *GFP-LC3;Kras* mice. In addition, cells isolated from pancreatic tumors and their metastases are positive for GFP-LC3 autophagosomes (data not shown). Interestingly, PanIN-adjacent normal acinar cells lack GFP-LC3–positive puncta, despite harboring the oncogenic $Kras^{G12D}$ mutation (*white star*, Figure 1*A*). With complete loss of *Atg5* however, only a diffuse staining is visible (Supplementary Figure 1*A*). Autophagy is therefore present in each stage of pancreatic tumor formation and metastasis.

To elucidate the role of autophagy during PDAC, we generated mice with homozygous (*A5;Kras*) and heterozygous ($A5^{+/-}$;*Kras*) deletion of *Atg5* and compared them to autophagy-proficient *Kras* mice. As shown previously,[4] complete loss of *Atg5* accelerates tumor initiation by significantly enhancing ADM (Supplementary Figure 1*A*, *B*, and *D*) and increasing pancreas/body weight index at 4 weeks of age (Supplementary Figure 1*C*); however, *A5;Kras* mice only progress to PanIN-1 at 9 weeks of age (Supplementary Figure 1*B* and *E*) and do not develop more malignant stages of the disease (Supplementary Figure 1*E*). In fact, *A5;Kras* mice have reduced survival (Supplementary Figure 1*F*) associated with severe pancreatic degeneration, as shown by a significantly lower relative pancreatic weight starting at 18 weeks of age (Supplementary Figure 1*C*). $A5^{+/-}$;*Kras* mice did not differ in ADM/PanIN formation, pancreas/body weight ratio, or survival compared to *Kras* mice (Supplementary Figure 1*B*, *C*, *D*, *E*, and *F*). Of note, pancreatitis responses and pancreatitis-associated progression of ADM/PanIN-lesions were not different in all mouse lines (data not shown). Surprisingly however, monoallelic loss of *Atg5* significantly increased tumor and metastasis incidence, determined at the time of sacrifice, compared to autophagy-proficient and autophagy-deficient genotypes (Figure 1*B*, *C*, *D*, and Supplementary Table 1). As shown in Figure 1*B*, primary tumors formed in $A5^{+/-}$;*Kras* mice were characterized by a high degree of

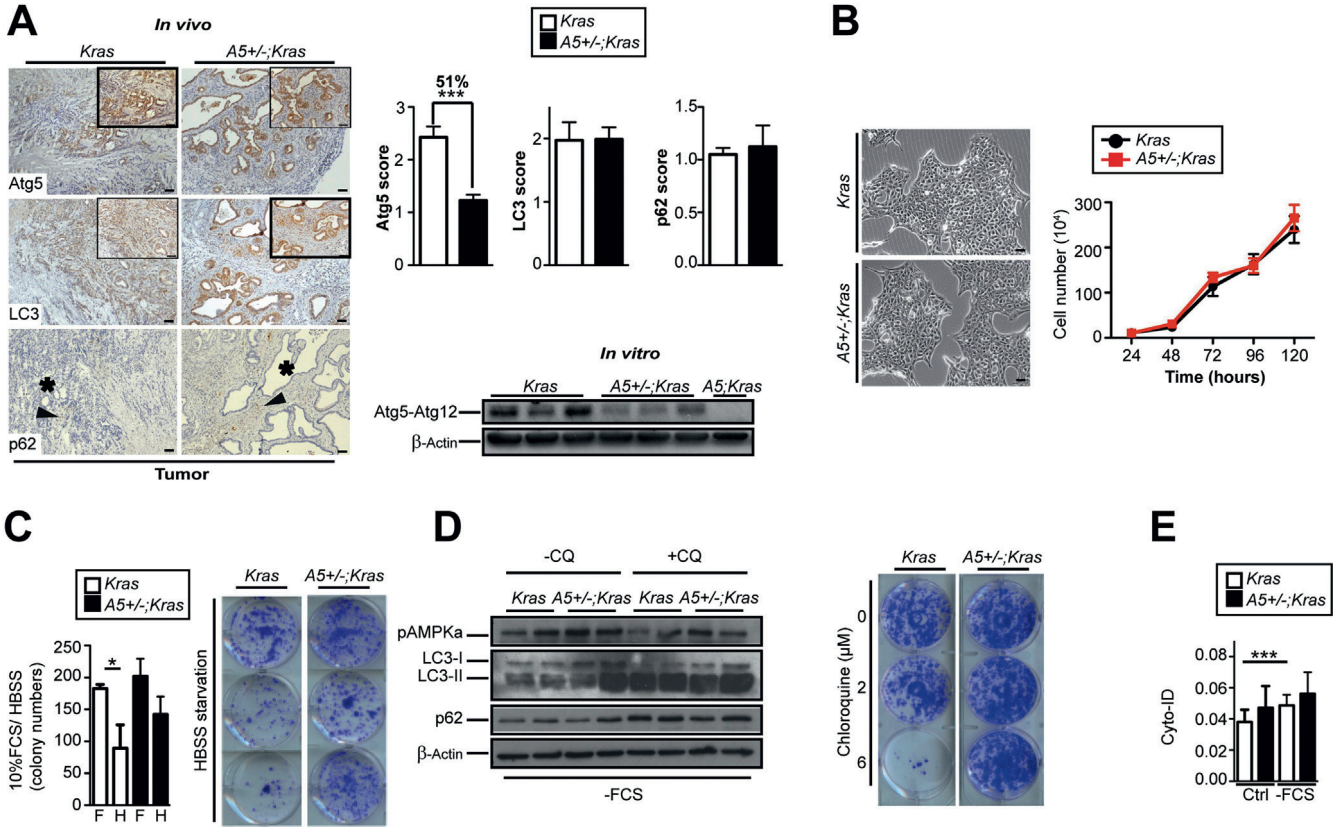

Figure 2. Monoallelic loss of *Atg5* affects cellular responses to autophagy activators and inhibitors. (*A*) Immunohistochemistry and scoring (score 1 [faint] – score 3 [strong]) of Atg5, LC3, and p62 in *Kras* and *A5*$^{+/-}$;*Kras* mouse tumors; *asterisks* highlight tumor structures and *arrowheads* tumor microenvironment; Atg5 detection in primary pancreatic tumor cells isolated from *Kras*, *A5*$^{+/-}$;*Kras*, and *A5;Kras* mice. (*B*) Morphology of *A5*$^{+/-}$;*Kras* and *Kras* cells (*left*); *Kras* and *A5*$^{+/-}$;*Kras* proliferation curve showing cell number $\times 10^4$ vs time (hours) after seeding (n = 3) (*right*). (*C*) Colony formation assay in *Kras* and *A5*$^{+/-}$;*Kras* cells after cultivation in 10% FCS-containing medium (F)Hank's balanced salt solution (HBSS) starvation (H) (n = 3) (*left*); representative picture of colony formation capacity in *Kras* and *A5*$^{+/-}$;*Kras* cells after HBSS-starvation (*right*). (*D*) Phospho-AMPKα, LC3-I/LC3-II, and p62 expression in *Kras* and *A5*$^{+/-}$;*Kras* cells, after FCS starvation, with/without chloroquine treatment (CQ) (*left*); representative picture of colony-formation capacity in *Kras* and *A5*$^{+/-}$;*Kras* cells after CQ treatment (*right*). (*E*) CYTO-ID fluorescence in *Kras* and *A5*$^{+/-}$;*Kras* cells after cultivation in medium with/without FCS (n > 3). Mean ± SD, *$P < .05$, ***$P < .001$. Scale bars = 50 μm.

histologic malignancy; at the same time multiple metastatic foci were visible in target tissues, a phenotype normally not present in autophagy proficient *Kras* mice.

Therefore, monoallelic and not biallelic loss of *Atg5* critically influences pancreatic tumor initiation, progression, and metastasis.

Autophagy Is Constitutively Active After Monoallelic Loss of Atg5 *Influencing Survival in Vitro*

To mechanistically examine the effect of monoallelic *Atg5* loss on PDAC, we first evaluated how monoallelic *Atg5* loss influences autophagy. As autophagic flux can be readily analyzed in vitro, we isolated primary pancreatic cancer cells from *Kras* and *A5*$^{+/-}$;*Kras* mice. During our study, 1 *A5;Kras* mouse from all *A5;Kras* mice analyzed (n = 24, Supplementary Figure 1*B*) stochastically developed PDAC. This cell line could not be propagated in vitro (data not shown) and was used only as a control for Atg5 protein expression analysis. Figure 2*A* shows Atg5 protein expression, detected as a complex with Atg12, in the cell line lysates. Importantly, reduction in Atg5 protein was evident in *A5*$^{+/-}$;*Kras* cells and in *A5*$^{+/-}$;*Kras* mice (Figure 2*A*). Cell morphology and cell proliferation capacities were not influenced (Figure 2*B*). Interestingly, however, while autophagic flux was not different between *Kras* and *A5*$^{+/-}$;*Kras* in vitro and in vivo (Figure 2*A* and *D*), autophagy regulation after treatment with autophagy activators or inhibitors was influenced. Specifically, starvation with Hank's balanced salt solution functionally affected *Kras* cells by significantly reducing colony numbers compared to 10% fetal calf serum (FCS)–containing medium (Figure 2*C*). Colony formation in *A5*$^{+/-}$;*Kras* cells was not compromised. FCS starvation led to an accumulation of LC3-II, which was even more evident in *Kras* vs *A5*$^{+/-}$;*Kras* cells after co-treatment with chloroquine (Figure 2*D*). Autophagic flux inhibition was validated by elevated p62 protein levels in both cell types, specifically however, in *Kras* cells after co-treatment with chloroquine (Figure 2*D*). AMPKα phosphorylation was slightly increased in *A5*$^{+/-}$;*Kras* cells, suggesting that AMPKα remains responsive to starvation in *A5*$^{+/-}$;*Kras* cells (Figure 2*D*). In

addition, increasing chloroquine treatment significantly affected colony formation only in *Kras* cells (Figure 2*D*). Finally, CYTO-ID–mediated quantification of autophagosomes after FCS starvation showed an elevation in autophagosome numbers only in *Kras* cells (Figure 2*E*). Of note, treatment of *Kras* and $A5^{+/-}$;*Kras* cells with various metabolic regulators (10% FCS, 6-AA, rotenone, galactose/glutamine, high glucose) did not differentially affect the colony-forming capacities of *Kras* and $A5^{+/-}$ *Kras* cells (Supplementary Figure 2*A*–*E*).

Thus, monoallelic loss of *Atg5* and reduced Atg5 protein levels lead to specific changes in autophagic regulation, making $A5^{+/-}$;*Kras* cell lines more resistant to standard autophagy stimulation and inhibition.

Monoallelic Loss of Atg5 *Increases Metastatic Properties of Cancer Cells in Vitro and in Vivo*

As $A5^{+/-}$;*Kras* mice had a higher tumor and metastasis incidence, we aimed to analyze in more detail the effect of *Atg5*-monoallelic loss on tumor and metastasis formation. In vitro experiments with *Kras* and $A5^{+/-}$;*Kras* cells revealed significantly increased anoikis resistance (Figure 3*A*), migration, invasion, and cell spreading in $A5^{+/-}$;*Kras* cells (Figure 3*B*), all of which influence metastatic capacities of tumor cells. Filopodia formation, an indicator of cell spreading, was also clearly detectable in $A5^{+/-}$;*Kras* cells while *Kras* cells displayed only small protrusions (Figure 3*B*). Tumor formation after orthotopic transplantation was similar in *Kras* and $A5^{+/-}$;*Kras* cell lines, with both cell lines

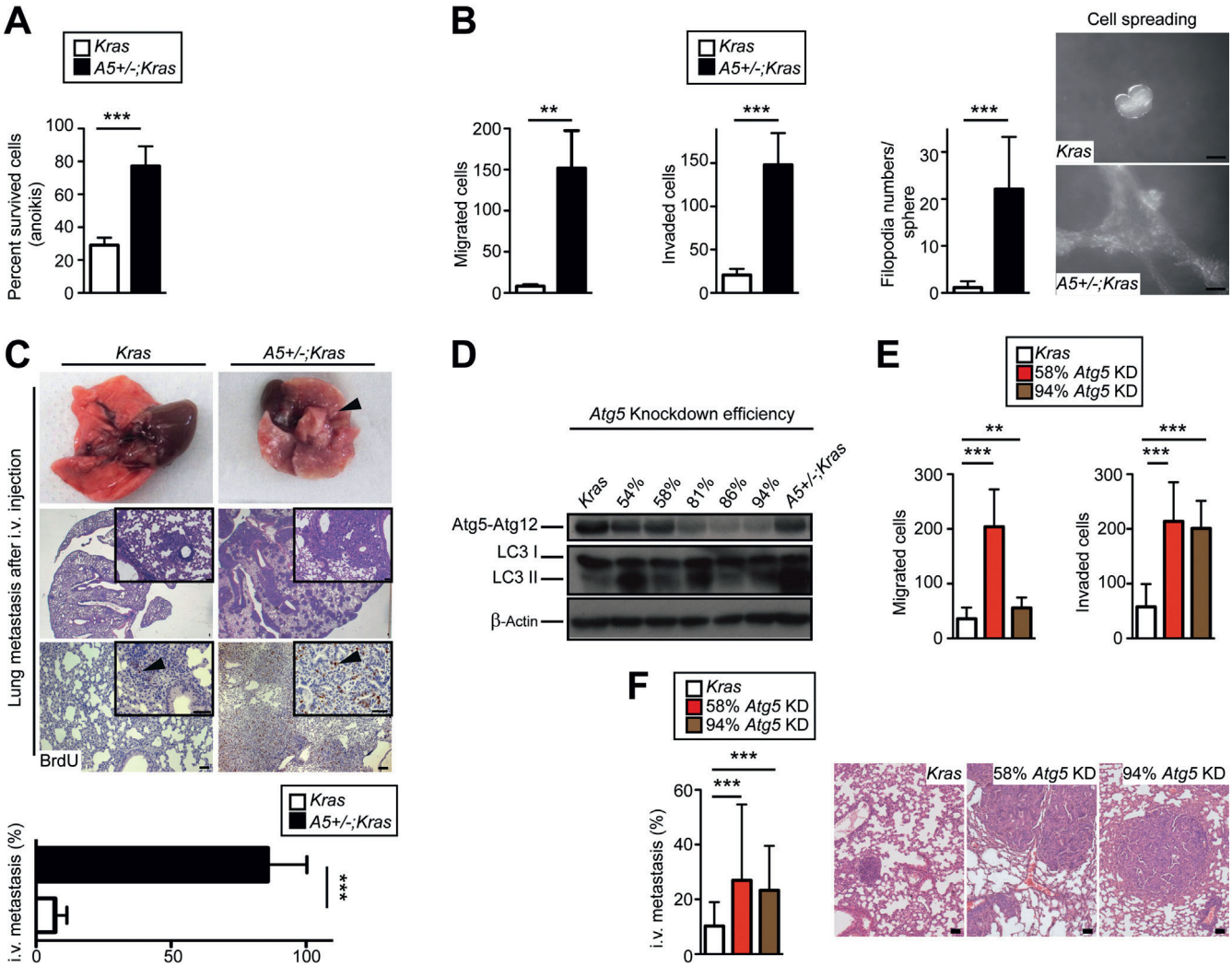

Figure 3. Monoallelic loss of *Atg5* increases metastatic properties of cancer cells in vitro and in vivo. (*A*) Anoikis assay with *Kras* and $A5^{+/-}$;*Kras* cells (%). (*B*) Quantification of migration (*left*), invasion (*middle*), and filopodia numbers/sphere with representative picture of cell spreading/filopodia formation in *Kras* and $A5^{+/-}$;*Kras* cells (*right*). (*C*) Lung tumors after tail-vein injection (i.v.) of *Kras* and $A5^{+/-}$;*Kras* cells; *black arrowheads* indicate tumors or bromodeoxyuridine-positive cells (*top*); quantification of lung metastasis (% area) after i.v. *Kras* and $A5^{+/-}$;*Kras* cells (n = 6) (*bottom*). (*D*) Western blot of Atg5-Atg12 and LC3I/II in *Kras*, $A5^{+/-}$;*Kras* and *Kras* cells after 54%, 58%, 81%, 86%, and 94% shRNA-mediated knockdown of *Atg5*. (*E*) Migration (*left*), invasion (*right*) of *Kras* vs *Kras* cells with 58%, 94% knockdown (KD) of *Atg5*. (*F*) Quantification of lung tumor formation after tail-vein injection (i.v.) of *Kras* and *Kras* cells with 58%, 94% KD of *Atg5* (% area); representative H&E pictures are included. Mean ± SD (n > 3), ***$P < .001$, **$P < .01$. Scale bars = 50 μm.

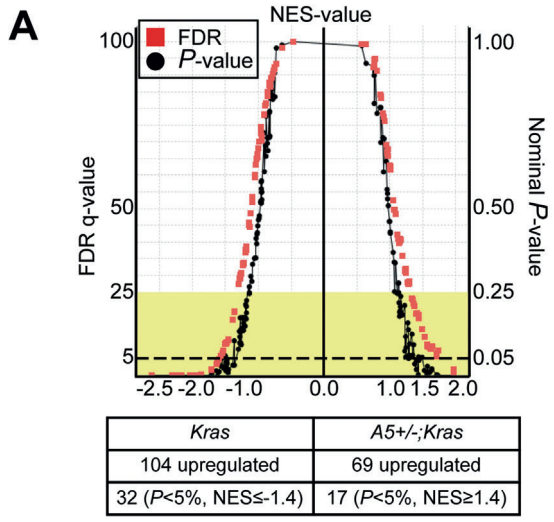

Kras	*A5+/-;Kras*
104 upregulated	69 upregulated
32 (*P*<5%, NES≤-1.4)	17 (*P*<5%, NES≥1.4)

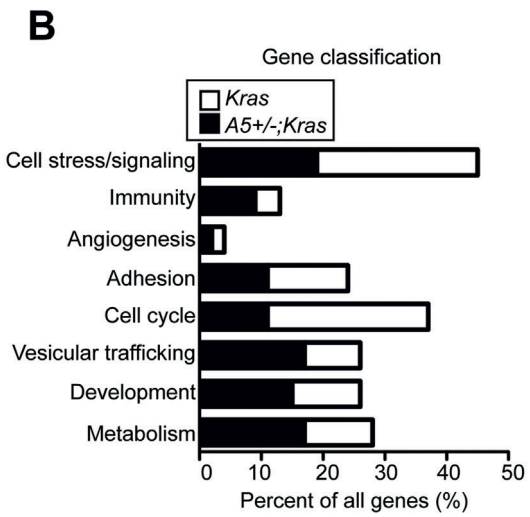

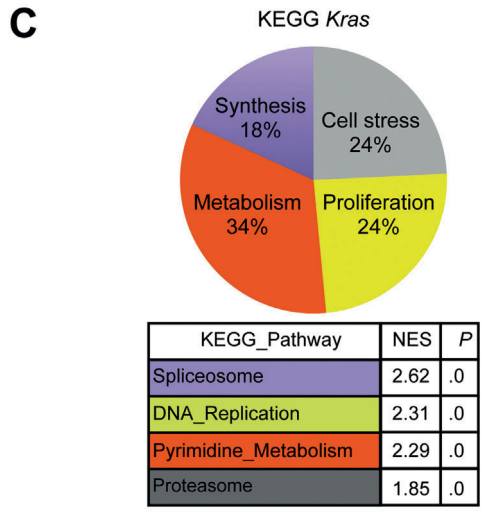

KEGG_Pathway	NES	*P*
Spliceosome	2.62	.0
DNA_Replication	2.31	.0
Pyrimidine_Metabolism	2.29	.0
Proteasome	1.85	.0

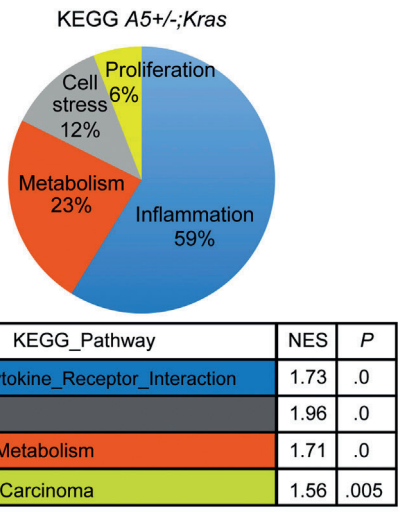

KEGG_Pathway	NES	*P*
Cytokine_Cytokine_Receptor_Interaction	1.73	.0
Lysosome	1.96	.0
Galactose_Metabolism	1.71	.0
Basal_Cell_Carcinoma	1.56	.005

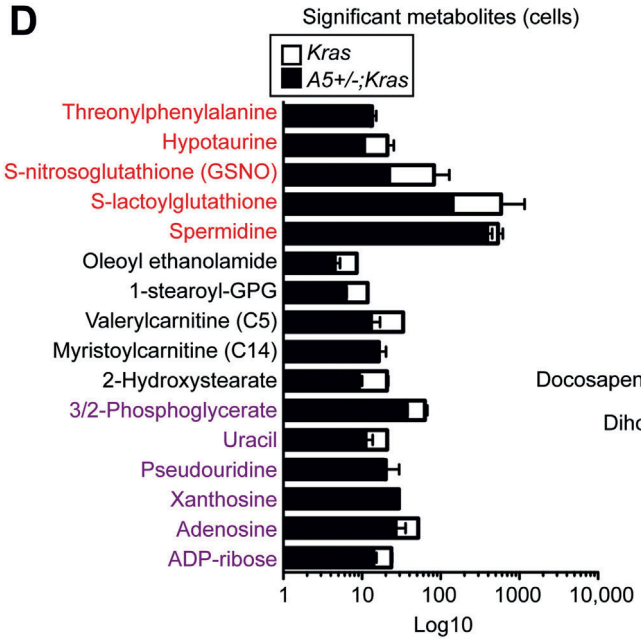

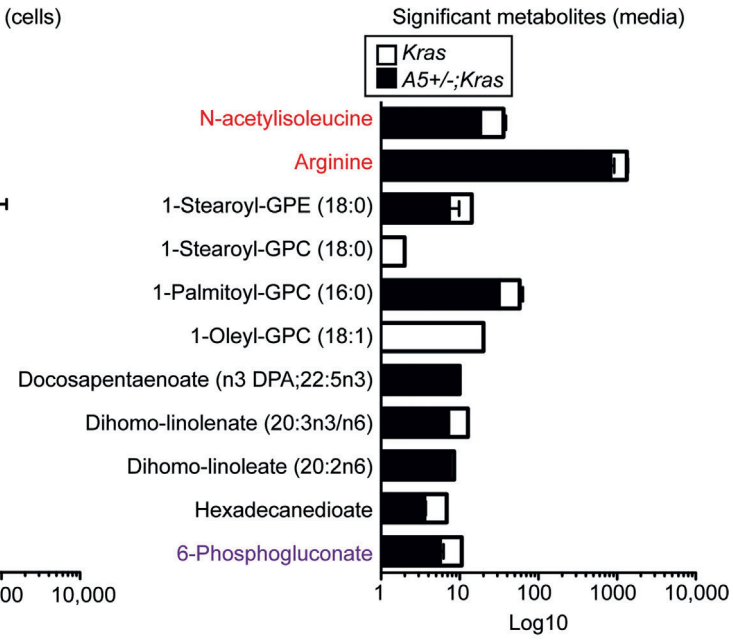

forming CK19-positive ductal tumors, morphologically resembling primary tumors (Supplementary Figure 3*A*). However, metastasis incidence after orthotopic transplantation was significantly increased in $A5^{+/-}$;*Kras* cells, with cells metastasizing to sites, including lymph nodes, liver, lung, and spleen (Supplementary Figure 3*B*). In a second model for target tissue colonization, significantly more lung tumors were formed after tail-vein injection of wild-type mice with $A5^{+/-}$;*Kras* vs *Kras* cells (Figure 3*C*). Body weight of mice, as an indicator of cachexia, was also reduced after injection with $A5^{+/-}$;*Kras* cells (Supplementary Figure 3*C*). In addition to lung tumor formation, some mice exhibited liver and spleen metastasis, implying higher aggressiveness of pancreatic tumor cells after monoallelic loss of *Atg5* (Supplementary Figure 3*D*). Proliferation of lung tumors (Figure 3*C*), as well as in vitro proliferation of $A5^{+/-}$;*Kras* cell lines after re-isolation from lung tumors (Supplementary Figure 3*D*), was also increased.

To elucidate the association between *Atg5* expression levels and PDAC malignancy, we knocked down *Atg5* in *Kras* cell lines using shRNAs with various knockdown efficiencies (54%, 58%, 81%, 86%, and 94%). All shRNAs were able to affect *Atg5* expression levels with the aforementioned efficiency at the mRNA (data not shown) and protein level (Figure 3*D*). As 58% *Atg5* knockdown resembles the situation after monoallelic loss of *Atg5*, we continued with these cells for further analyses. We also utilized 94% *Atg5* knockdown cells to determine whether the levels at which *Atg5* influences PDAC phenotype coincide with a certain percentage. Importantly, knock down of *Atg5* by 58% or 94% significantly enhanced migration and invasion in vitro (Figure 3*E*) as well as lung metastasis in vivo (Figure 3*F*). Colony formation after cultivation in 10% FCS-containing medium was not affected (Supplementary Figure 3*E*).

Therefore, our data suggest that monoallelic loss of *Atg5* during embryonic development as well as shRNA-mediated *Atg5* dosage reduction increase metastatic capacities and aggressiveness of cells in vitro and in vivo.

Monoallelic Loss of Atg5 *Is Sufficient to Induce Transcriptional and Metabolic Changes*

Autophagy is known to regulate transcription.[11] In addition, the autophagy–lysosomal pathway is controlled on a transcriptional level in PDAC.[12] To investigate how monoallelic loss of *Atg5* increases tumor cell metastasis and aggressiveness, we performed transcriptomic analyses in *Kras* and $A5^{+/-}$;*Kras* pancreatic tumor cells. Surprisingly, loss of 1 allele of *Atg5* was sufficient to change transcriptomic pathway regulation on a large scale. Gene enrichment analysis revealed that loss of 1 allele of *Atg5* led to a reduction in the number of up-regulated pathways by half (Figure 4*A*). Functional classification of the most significantly regulated genes (Supplementary Figure 4*C*) identified multiple cellular functions affected by monoallelic loss of *Atg5* (Figure 4*B*). Most importantly, an increase was seen in metabolism, immunity, development, and vesicular trafficking/homeostasis associated cellular functions; a decrease was seen in adhesion and cell cycle associated cellular functions (Figure 4*B*). Classification of Kyoto Encyclopedia of Genes and Genomes pathways confirmed the increase in inflammation and the decrease in proliferation/synthesis-associated pathways in $A5^{+/-}$;*Kras* cells (Figure 4*C*, Supplementary Figure 4*B*). Interestingly, the gene set associated with lysosomal function was enriched in $A5^{+/-}$;*Kras* cells (Figure 4*C*, Supplementary Figure 4*B*), further supporting a deregulation in vesicular homeostasis. Of note, gene enrichment analysis using the Transcription Factor Binding Motif database further supported the enrichment of development and inflammation-associated gene sets and the down-regulation of proliferation-associated gene sets in $A5^{+/-}$;*Kras* cells (Supplementary Figure 4*A* and *B*).

Because autophagy influences metabolic pathways, we performed non-targeted metabolic profiling in *Kras* and $A5^{+/-}$;*Kras* cell lines and their supernatants (Figure 4*D*). Importantly, $A5^{+/-}$;*Kras* cells contained increased amounts of nucleotides and spermidine, representing deregulated proliferation, elevated amounts of oxidative and cell stress-associated metabolites (eg, *S*-nitrosoglutathione, hypotaurine, S-lactoylglutathione, involved in oxidative stress, and ADP-ribose connected with cell stress), increased 3/2-phosphoglycerate implicated in glucose metabolism, and changes in the amounts of fatty acids engaged in energy metabolism (eg, myristoylcarnitine, valerylcarnitine). Supernatants of $A5^{+/-}$;*Kras* cells showed changes in lysolipids (eg, 1-Stearoyl-GPE) and other lipids (eg, polyunsaturated fatty acids), indicative of changes in membrane composition/signaling; arginine, suggesting an influence on the immune microenvironment (macrophages); and 6-phosphogluconate, a metabolite associated with the pentose phosphate pathway.

Thus, monoallelic loss of *Atg5* is sufficient to induce global transcriptomic and metabolomic changes, mostly in pathways associated with metabolism, inflammation, and vesicle homeostasis.

Monoallelic Loss of Atg5 *Reduces Mitochondrial Functionality*

To gain further insight into the effect of monoallelic *Atg5*-loss on metabolism, we performed a series of

Figure 4. Monoallelic loss of *Atg5* leads to global changes in metabolism, inflammation, and vesicle homeostasis. (*A*) Normalized Enrichment Score (NES) vs significance plot illustrating gene sets, identified by Gene Set Enrichment Analysis (GSEA), enriched in either *Kras* or $A5^{+/-}$;*Kras* pancreatic tumor cells (n = 3); enriched pathways are localized beneath *dotted line*. (*B*) Functional classification of most highly regulated genes identified by GSEA in *Kras* and $A5^{+/-}$;*Kras* cells (percent of all significantly up-regulated genes; Supplementary Figure 4*C*). (*C*) Classification of significantly enriched gene sets into categories for *Kras* (*left*) and $A5^{+/-}$;*Kras* (*right*) cells (*P* value 0.0 indicates $P < .001$). (*D*) Classification of significantly up-regulated metabolites in *Kras* and $A5^{+/-}$;*Kras* cells (*left*) and their supernatants (media, *right*); amino acids/peptides = *red*; lipids = *black*; nucleotides/carbohydrates = *purple*; mean ± SD (n = 3).

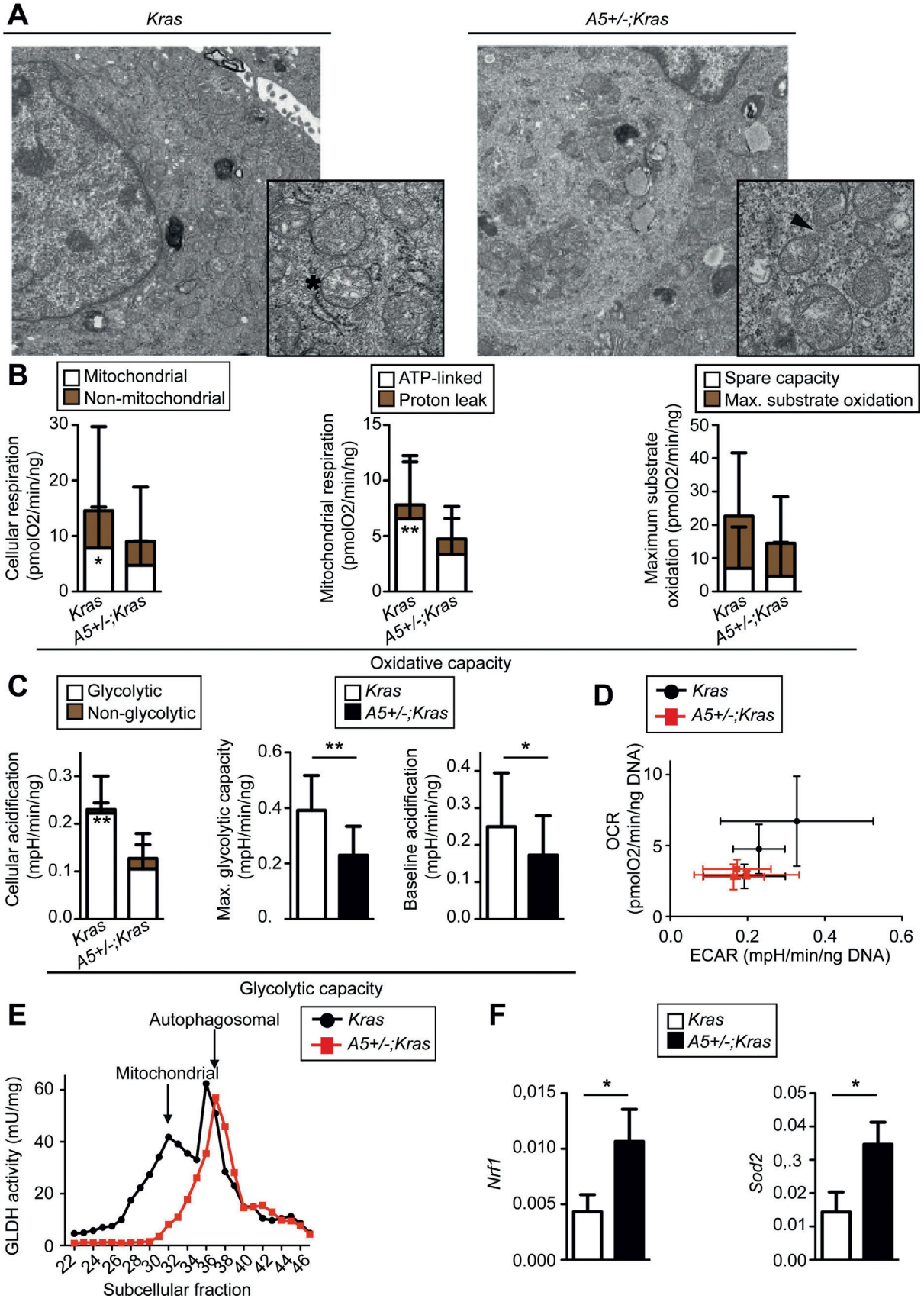
A
Kras
A5+/-;Kras
B
Mitochondrial
Non-mitochondrial
Cellular respiration (pmolO2/min/ng)
ATP-linked
Proton leak
Mitochondrial respiration (pmolO2/min/ng)
Spare capacity
Max. substrate oxidation
Maximum substrate oxidation (pmolO2/min/ng)
Kras
A5+/-;Kras
Oxidative capacity
C
Glycolytic
Non-glycolytic
Cellular acidification (mpH/min/ng)
Max. glycolytic capacity (mpH/min/ng)
Baseline acidification (mpH/min/ng)
D
OCR (pmolO2/min/ng DNA)
ECAR (mpH/min/ng DNA)
Glycolytic capacity
E
Autophagosomal
Mitochondrial
GLDH activity (mU/mg)
Subcellular fraction
F
Nrf1
Sod2

experiments related to mitochondrial functionality and cell stress. Electron microscopy revealed changes in mitochondrial morphology. In particular, there was an increase in mitochondrial fission and differences in cristae stacking between *Kras* and *A5*$^{+/-}$;*Kras* cells (Figure 5*A*). Protein expression analyses illustrated slight increases in oxidative phosphorylation–associated mitochondrial proteins (COX II/IV, ATP Core 2), in mitochondrial stress-associated SOD2, and in endoplasmic reticulum–stress associated BiP (Supplementary Figure 5*A*). Endoplasmic reticulum stress was also indicated by an elevation in the spliced form of *Xbp1* (Supplementary Figure 5*A*). Expression of p53, however, was not influenced (data not shown). Mitochondrial function was further assessed by detailed comparison of oxidative and glycolytic capacities in *Kras* and *A5*$^{+/-}$;*Kras* cell lines (Figure 5*B–D*). We detected a decrease in oxidative capacity, as evidenced by cellular respiration rate, mitochondrial respiration rate, and maximum substrate oxidation rate, at the expense of mitochondrial ATP production (Figure 5*B*). In addition, *A5*$^{+/-}$;*Kras* cells showed a reduction in glycolysis, as evidenced by decreased cellular acidification rates, maximum glycolytic capacity, and baseline acidification rate (Figure 5*C*). Mitochondrial coupling efficiency did not show any significant change (Supplementary Figure 5*B*). Figure 5*D* verifies these results in an oxygen consumption rate vs extracellular acidification plot, showing a weakening in metabolic activity in *A5*$^{+/-}$;*Kras* cells. This is indicated by the movement of the *A5*$^{+/-}$;*Kras* cell line measurements towards both lower oxygen consumption rate and lower extracellular acidification rate, demonstrating decreased ATP turnover. Interestingly, cellular fractionation experiments revealed a displacement in the mitochondrial fraction as detected by glutamate dehydrogenase activity. In particular, mitochondria were shifted toward the autophagosomal fraction, indicating decreased integrity of mitochondria (Figure 5*E*). Finally, messenger RNA expression levels of *Nrf1* and mitochondrial *Sod2* were increased, corroborating the elevated mitochondrial stress (Figure 5*F*); *Nrf2* and cytosolic *Sod1* were not changed (Supplementary Figure 5*C*).

Concluding, monoallelic loss of *Atg5* affects cellular homeostasis by altering mitochondrial morphology and compromising mitochondrial function.

Atg5 *Level Influences Intracellular* Ca^{2+} *Flux and Extracellular Cathepsin Activity*

Mitochondria play an important role in buffering intracellular Ca^{2+} levels and are thus closely linked to Ca^{2+} fluctuations. In addition, Ca^{2+} responses influence mitochondrial function/morphology, gene transcription,[13–15] vesicle trafficking, cellular migration, and lamellipodia formation at the front of migrating cells.[16] Thus, we examined in more detail cellular Ca^{2+} responses as a putative mechanism connecting our observations. In support, Ca^{2+} responses of *Kras* and *A5*$^{+/-}$;*Kras* cells after treatment with 0.01% or 0.05% fetal bovine serum (FBS) were significantly different (Figure 6*A*). Cytosolic Ca^{2+} responses in *A5*$^{+/-}$;*Kras* cells were characterized by higher amplitudes and only 1 peak of Ca^{2+} elevation. Moreover, the number of FBS-responding cells was slightly elevated in *A5*$^{+/-}$;*Kras* vs *Kras* cells (Supplementary Figure 6*A*). S100a4, a $Ca2^{2+}$-binding protein associated with increased metastatic capacities, was found highly expressed in *A5*$^{+/-}$;*Kras* tumors compared to only a low-level expression in *Kras* tumors. The higher PanIN orders and established PDAC structures were particularly positive for S100a4 expression (Figure 6*B*).

Lysosomal trafficking and exocytosis of lysosomal cathepsins is also regulated by intracellular Ca^{2+} fluctuations.[17] Quantification of lysosomal cathepsin activities in cell culture supernatants revealed a significantly higher activity of cathepsin L and cathepsin D (Figure 6*C*), whereas cathepsin B was not affected (Supplementary Figure 6*B*). Protein levels of the respective pro-cathepsins also showed a tendency towards increased amounts in *A5*$^{+/-}$;*Kras* cells (Supplementary Figure 6*B*). In addition, copy number of genes associated with lysosomes indicated a difference in regulation between normal pancreas and pancreatic cancer samples (Supplementary Figure 6*D*).

Furthermore, we functionally evaluated the importance of extracellular cathepsin activity in cell spreading and invasion. For this, we treated *Kras* and *A5*$^{+/-}$;*Kras* cells with the cathepsin inhibitor E64d, and quantified the number of filopodia per sphere (Figure 6*D*) and the number of Matrigel-invaded cells (Figure 6*E*). While the number of colonies formed by *Kras* and *A5*$^{+/-}$;*Kras* cells did not change after E64d-treatment (Supplementary Figure 6*C*), cell spreading and invasive capacities were significantly reduced in *A5*$^{+/-}$;*Kras* cells (Figure 7*D* and *E*). Of note, E64d did not affect filopodia formation and invasive capacities of *Kras* cells (data not shown).

In summary, levels of *Atg5* significantly influence cellular Ca^{2+} responses and lysosomal enzyme activities, which are required for increased cell spreading and invasion.

Monoallelic Loss of Atg5 *Induces Pro-Tumorigenic Inflammation*

Changes in inflammation have been shown to promote tumorigenesis and cancer cell invasion/metastasis.

Figure 5. Monoallelic loss of *Atg5* reduces mitochondrial functionality and increases endoplasmic reticulum stress. (*A*) Transmission electron microscopy pictures of *Kras* and *A5*$^{+/-}$;*Kras* cells (4000×, 20,000×); *asterisk/black arrowhead* indicate mitochondria/mitochondrial fission. (*B*) Oxidative capacity (pmolO_2/min) of *Kras* and *A5*$^{+/-}$;*Kras* cells normalized to protein or DNA (ng) ($n \geq 30$). (*C*) Glycolytic capacity (mpH/min) of *Kras* and *A5*$^{+/-}$;*Kras* cells normalized to protein or DNA (ng) ($n = 9$). (*D*) Oxygen consumption rate (pmolO_2/min/ng DNA) vs extracellular acidification rate (mpH/min/ng DNA) for *Kras* and *A5*$^{+/-}$;*Kras* cells. (*E*) Mean glutamate dehydrogenase (GLDH) activity (mU/mg protein) distribution into density fractions (with decreasing density from 22 to 46) in *Kras* and *A5*$^{+/-}$;*Kras* cell extracts ($n = 4$). (*F*) Quantitative reverse transcriptase polymerase chain reaction of *Nrf1* and *Sod2* normalized to *cyclophilin* ($n = 3$). Mean ± SD, $^{*}P < .05$; $^{**}P < .01$.

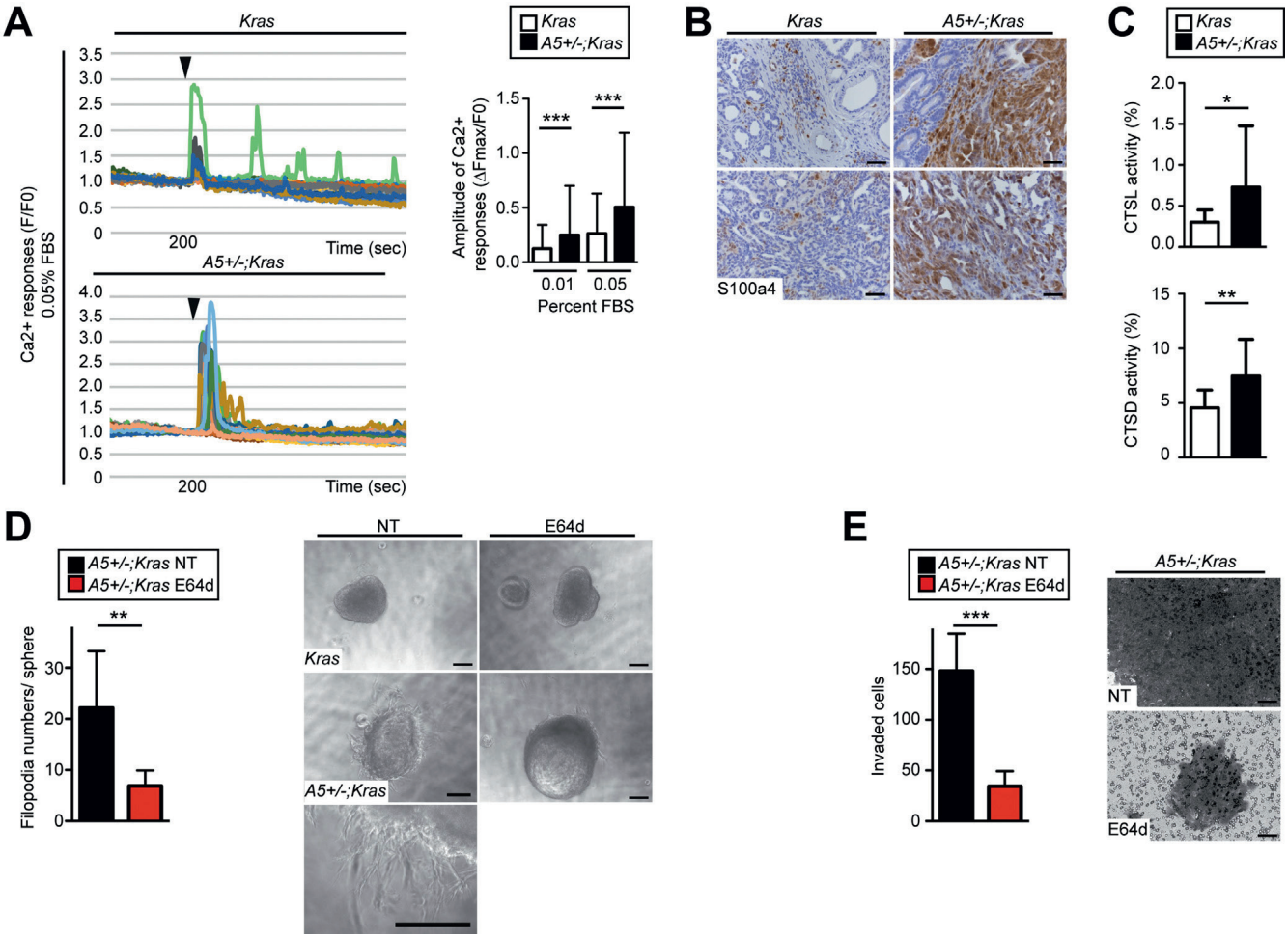

Figure 6. *Atg5*-dependent changes in Ca2+ signaling, extracellular cathepsin levels and filopodia formation: determinants of metastatic potential. (*A*) Representative recordings (*left*) and amplitude (*right*) of cytosolic Ca^{2+} responses (as described in Supplementary Methods) in *Kras* and $A5^{+/-}$;*Kras* cells after FBS-stimulation (at 200 seconds, marked with *black arrowhead*) (n > 170). (*B*) S100a4 immunohistochemistry in *Kras* and $A5^{+/-}$;*Kras* mice. (*C*) Cathepsin L (CTSL) and cathepsin D (CTSD) extracellular activity (percent extracellular activity vs total activity) as measured from supernatants of *Kras* and $A5^{+/-}$;*Kras* cells (n = 15). (*D*) Quantification of filopodia numbers/sphere in $A5^{+/-}$;*Kras* cells after E64d treatment compared to no treatment (NT) (n > 3) (*left*); representative bright field picture of cell spreading and filopodia (*right*). (*E*) Quantification of invaded $A5^{+/-}$;*Kras* cells after E64d treatment or NT (n > 3) (*left*); representative picture of invaded cells (*right*). Mean ± SD, $^{*}P < .05$; $^{**}P < .01$; $^{***}P < .001$. Scale bars = 50 μm.

Our transcriptomic results identified alterations in inflammatory pathways. Moreover, extracellular arginine levels, known to influence pro-tumorigenic M2- vs pro-inflammatory M1-macrophages, were increased in $A5^{+/-}$;*Kras* vs *Kras* cells. Thus, we aimed to elucidate the effect of *Atg5*-monoallelic loss on macrophage-mediated inflammation. Firstly, we examined the cytokine/chemokine profile of *Kras* and $A5^{+/-}$;*Kras* cells in cell culture supernatants (Supplementary Figure 7*A*). Quantification of dot-plot pixel intensity revealed up-regulation of cytokines involved in macrophage chemoattraction (CXCL1, CXCL12), M2-differentiation (M-CSF, CXCL12, IL10, CXCL2, IL1ra, CXCL10), and tumor progression/metastasis (tumor necrosis factor–α) in $A5^{+/-}$;*Kras* vs *Kras* cells, while cytokines important for M1-polarization (granulocyte-macrophage colony-stimulating factor), M1-chemoattraction (soluble intercellular adhesion molecule-1), and granulocyte attraction (granulocyte colony-stimulating factor) were down-regulated. To analyze in more detail the effect of *Kras* and $A5^{+/-}$;*Kras* cells on the inflammatory microenvironment, we treated undifferentiated macrophages with the cell culture supernatants of *Kras* and $A5^{+/-}$;*Kras* cells and characterized the changes in macrophage morphology, as described previously.[18] Supernatants from *Kras* cells induced macrophage differentiation into the M1-subtype; supernatants form $A5^{+/-}$;*Kras* cells on the other hand shifted differentiation toward the M2-subtype, (increased cell elongation, Supplementary Figure 7*B*), confirmed by elevated levels of arginase 1 expression (Supplementary Figure 7*B*). Moreover, we assessed the in vivo ability of *Kras* and $A5^{+/-}$;*Kras* cells to attract macrophages by quantifying F4/80 and CD206 in the original pancreatic tumor tissues of these mice (Supplementary Figure 7*C*). Importantly, F4/80- and CD206-macrophage numbers were clearly elevated in $A5^{+/-}$;*Kras* tumors, indicating more CD206 and thus M2-macrophages after monoallelic loss of *Atg5*. More F4/80 and arginase

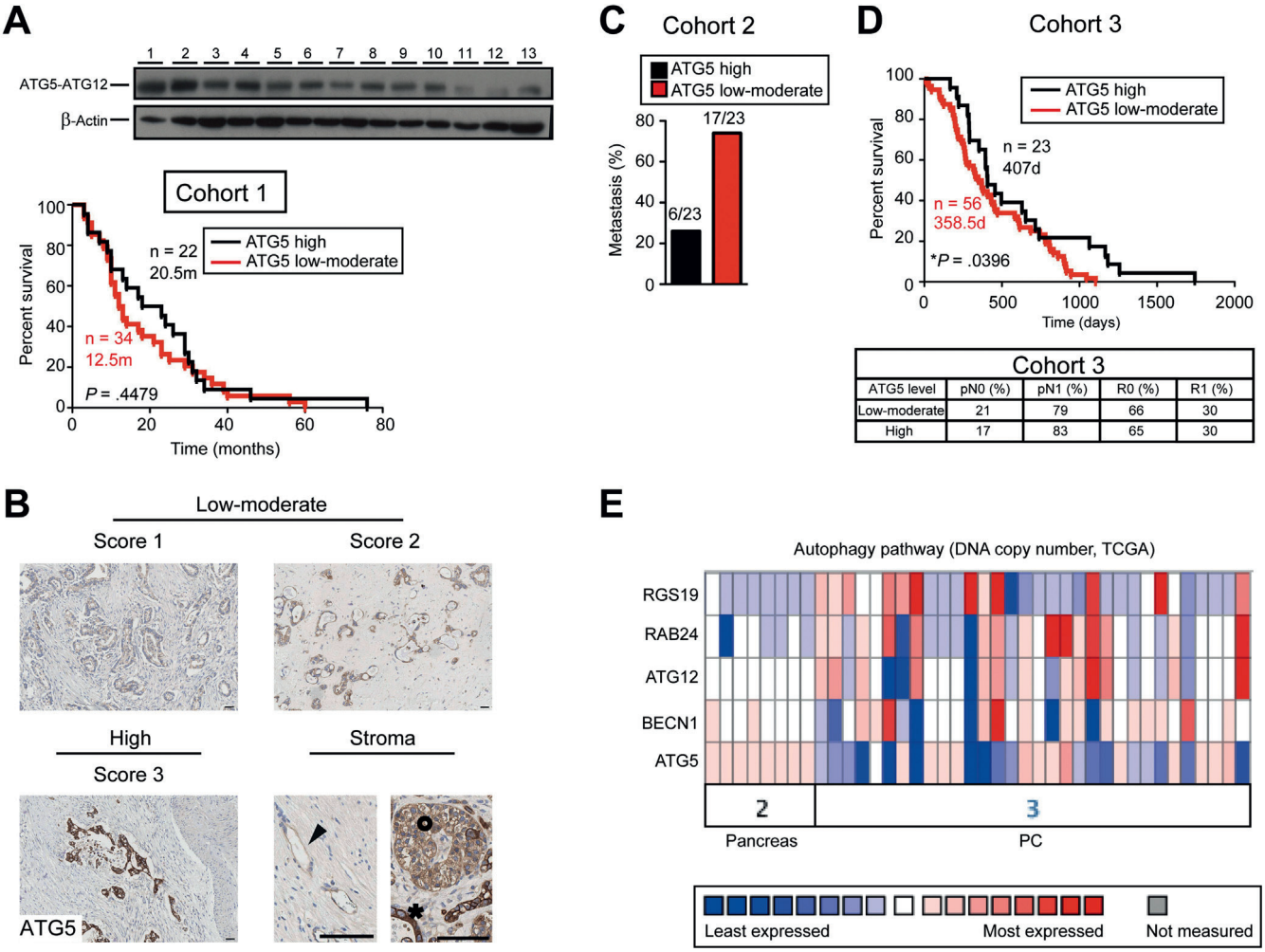

Figure 7. Lower levels of *ATG5* gene and protein levels correlate with human pancreatic cancer aggressiveness. (*A*) ATG5-ATG12 protein levels in human pancreatic cancer samples (*top*); Kaplan-Meier survival analysis (months) with cohort 1 patients separated into high (ATG5 to β-actin ratio $\geq$0.5; n = 22, median survival 20.5 months) vs low–moderate (ATG5 to β-actin ratio $<$0.5; n = 34, median survival 12.5 months) ATG5 expression groups (P = .4479). (*B*) Representative ATG5 immunohistochemistry in primary human PDAC tissues separated into Score 1/2 (low–moderate) and score 3 (high); *asterisk/arrowhead/circle* mark epithelial cancer/endothelial/islet cells. (*C*) Distant metastasis incidence (%) in n = 23 cohort 2 patients separated into high (n = 6) vs low–moderate (n = 23) ATG5 expression groups according to (*B*). (*D*) Kaplan-Meier survival analysis (days) with cohort 3 patients separated into high (n = 23, median survival 407 days) vs low–moderate (n = 56, median survival 358.5 days) ATG5 expression groups according to (*B*) (*P = .0396, *top*); *table* shows lymph node infiltration (%, pN0, pN1) and resection status (%, R0, R1) (*bottom*). (*E*) Illustration of autophagy-associated DNA copy number gain (*red*) or loss (*blue*) (The Cancer Genome Atlas data) in normal vs pancreatic cancer (PC) samples; *blue bars* correlate to less than hemizygous, *white* to hemizygous, and *red* to more than hemizygous levels. Scale bars = 50 μm.

1–positive M2-macrophages were also attracted into the lungs of mice after tail-vein injection of $A5^{+/-}$;*Kras* compared to *Kras* cells (Supplementary Figure 7*D*), further supporting the in vitro and in vivo results (Supplementary Figure 7*B* and *C*).

To determine whether macrophages critically influence the metastatic capabilities of $A5^{+/-}$;*Kras* cells, we depleted macrophages in wild-type mice using liposomal-clodronate. Subsequently, we performed tail-vein injection of $A5^{+/-}$;*Kras* cells and analyzed lung tissue metastasis. Clodronate treatment was able to deplete most on the macrophages, as shown by F4/80 immunohistochemistry (Supplementary Figure 7*E, right*). Interestingly, macrophage depletion significantly reduced metastasis of $A5^{+/-}$;*Kras* cells compared to control liposome-treated mice, highlighting the importance of infiltrating macrophages in potentiating metastasis.

Consequently, monoallelic loss of *Atg5* induces changes in cytokine/chemokine secretion from tumor cells resulting in accumulation of M2-macrophages, ultimately shaping the inflammatory microenvironment to critically favor tumor aggressiveness and promote tumor metastasis.

Levels of ATG5 Are Correlated to Human Pancreatic Cancer Aggressiveness

To establish a connection between the mouse model results and human pancreatic cancer, we analyzed ATG5

protein levels in 3 independent patient cohorts (Supplementary Tables 2, 3, and 4). ATG5-ATG12 protein expression in lysates from pancreatic tumor patients (Cohort 1) was different between the samples (Figure 7*A, top*). Grouping the patients into ATG5 high vs ATG5 low–moderate expression indicated a trend towards reduced survival in the low–moderate ATG5-expression group (Figure 7*A, bottom*). Due to the variations in tumor cellularity and the limitations of Western blotting, we performed ATG5 immunohistochemistry (cohorts 2 and 3). As expected and already described (Human Protein Atlas), ATG5 is expressed not only in the pancreatic epithelial tumor structures but also in other cell types (eg, endothelial and islet cells) in the tissue (Figure 7*B*). After establishing an ATG5-expression score (score 1, score 2, and score 3), we divided the patients into low–moderate (score 1 and score 2) and high (Score 3) ATG5 expression (Figure 7*B*). Applying this analysis on a small distant metastatic patient cohort (cohort 2) showed a higher metastasis incidence in the low–moderate ATG5 expressing patients (Figure 7*C*). Furthermore, we could significantly correlate reduced survival with lower ATG5 expression in a larger cohort of patients undergoing pancreatic cancer resection (cohort 3, Figure 7*D*). Because lymph node and resection status was not different between the groups, ruling out important confounding factors (Figure 7*D*), these analyses very likely reflect the re-occurrence of metastases and thus aggressiveness of the tumors. Of note, metastatic relapse in resected patients determines survival. Finally, The Cancer Genome Atlas databank analysis identified a reduction in *ATG5* copy numbers between pancreatic cancer samples and normal human pancreas (Figure 7*D*).

Thus, lower levels of ATG5 are associated with increased pancreatic cancer metastasis and patient survival.

Discussion

Autophagy has been shown to play a dual role in tumorigenesis of different tissue types.[3,19] Particularly, autophagy seems to accelerate tumor initiation while blocking progression of pre-neoplastic lesions, as exemplified in PDAC.[2] Studies have mainly made use of models with complete loss of autophagic function, a fact that is rarely seen in human patients. Therefore, we aimed to analyze the effect of varying levels of Atg5 on PDAC development. Surprisingly, complete loss of *Atg5* blocks tumorigenesis, while monoallelic loss of *Atg5* promotes tumorigenesis and metastasis. We suggest cell intrinsic changes in mitochondrial homeostasis, Ca^{2+} responses, autophagy regulation, and lysosomal cathepsin activation, as well as changes in the inflammatory tumor microenvironment to be crucial for aggressiveness of pancreatic cancer. Importantly, shRNA-mediated *Atg5* dosage regulation also increased metastatic capabilities of pancreatic cancer cells, indicating that a simple decrease in Atg5 levels is sufficient to influence PDAC metastasis. The clinical significance of this observation is supported by the analysis of 3 independent human pancreatic cancer cohorts verifying an association between ATG5 levels and PDAC metastasis and patient survival.

Autophagy is closely connected with PDAC and multiple pathways influence this interaction, for example, reactive oxygen species levels, endoplasmic reticulum stress, hypoxia, mitochondrial metabolism, and the surrounding tumor microenvironment.[2] Past studies have shown that the interplay between oncogenic *Kras* and autophagy during PDAC progression is also regulated by other genetic alterations, but contradictory results did not enable clear conclusions.[4,5] Our initial analysis of sequential pancreatic cancer stages implicated targeted induction of autophagy during PDAC development, confirming past results on gradual elevation of baseline autophagy during carcinogenesis.[2] The importance of autophagy in pancreatic cancer progression was further verified by homozygous deletion of *Atg5*, confirming past results.[4] Along the same line, whole-body inhibition of autophagy was recently shown to control tumor cell growth via intrinsic and extrinsic mechanisms in mice.[20] Unlike complete loss of *Atg5*, however, monoallelic loss resulted in a higher tumor incidence and metastasis occurrence. *Atg5* dosage regulation through shRNA-mediated knockdown also enhanced metastatic capabilities of pancreatic cancer cells, indicating that although there is a clear phenotypic difference between complete presence, partial presence, and complete absence of *Atg5*, the phenotypic effect follows *Atg5* dosage in a nonlinear fashion. So far, only one published study has uncovered a connection between monoallelic deletion of *Atg5* and increased metastasis in melanoma supporting our results.[21] Nonetheless, the underlying mechanisms for the phenotype in melanoma are still obscure.

Atg5, as apart of the Atg-conjugation system, is required for autophagic flow. Atg-mediated closure of autophagosomes is necessary for subsequent lysosomal degradation and recycling of membrane components.[22] Upon complete loss of *Atg5* in the pancreas, autophagosomes accumulate in acinar cells and degradation is blocked.[11] However, the impact of *Atg5* monoallelic loss on autophagic flux remains unclear. In $A5^{+/-}$;*Kras* cells and tumors, we detected decreased Atg5 protein expression. Interestingly, reduced protein amounts did not result in an apparent negative consequence on autophagy, as $A5^{+/-}$;*Kras* cells were more resistant to autophagy inhibitors or activators and functionally not affected. Multiple non-canonical autophagy and intracellular degradation pathways exist that might compensate for monoallelic loss of *Atg5* (eg, microautophagy, chaperone-mediated autophagy, non-canonical autophagy independent of various core autophagy proteins, selective autophagy, and macropinocytosis).[23,24] In order to fully illuminate the effect of monoallelic *Atg5* loss on autophagy-associated pathways and to extent pancreatic tumor progression, more future studies are required. Therefore, our present results show that monoallelic loss of *Atg5* enhanced autophagy levels in a cell-intrinsic manner, indicating active adaptation of pancreatic cancer cells.

Loss of 1 allele of *Atg5* significantly changed not only autophagy regulation, but also tumor cell behavior by enhancing migration and invasion. Importantly, *Atg5*-heterozygous cell lines could form tumors in hosts and had a higher capacity to metastasize to distant organs. Metastasis is a multistep process involving a plethora of cellular adaptations.[25] Mitochondria,[26] Ca^{2+} oscillations,[27] extracellular matrix degradation,[28] and the tumor microenvironment[29] have been shown to determine tumor malignancy and dissemination. Interestingly, we could detect changes in mitochondrial homeostasis with loss of 1 allele of *Atg5*. Specifically, mitochondrial function was reduced, while distinct mitochondrial stress markers were up-regulated. Mitochondrial turnover was also affected, as more fission events could be documented along with an increase of mitochondrial mass in the autophagosomal fraction, indicating uptake of damaged mitochondria. Past studies have shown that increased mitochondrial fission and fragmentation supports tumor cell growth, invasion, and migration.[26] Moreover, mitochondrial metabolism is necessary to support cancer cell dissemination, while a certain degree of cell stress is required for tumor cells to alter their mitochondrial programming and promote cellular adaptation.[30–32] Mitochondria are also known to influence Ca^{2+} signaling amplitude and propagation rate by sequestering Ca^{2+}. Especially in polarized pancreatic acinar cells, where a considerable portion of mitochondria are localized in the apical part of the cell, Ca^{2+} transients are effectively confined and spatially regulated.[13] Interestingly, intracellular Ca^{2+} fluctuations are involved in tumor cell dissemination influencing migration and vesicle trafficking.[16,33] Along these lines, monoallelic loss of *Atg5* influenced FBS-mediated migration/invasion, FBS-induced Ca^{2+} responses as well as expression of Ca^{2+} handling proteins. In support, *Atg5* expression was recently linked to heightened tumor cell metastasis via disrupting the V1Vo ATPase, which is closely connected to cytosolic Ca^{2+}, indicating a pathway through which a autophagy-related gene can promote metastasis in an autophagy-independent manner.[34] Therefore, monoallelic loss of *Atg5* might establish an intermediate stress level in tumor cells disturbing mitochondrial homeostasis and to a certain extent Ca^{2+} signaling, heightening their aggressive and metastatic potential.

Tumor cell invasion further requires digestion of extracellular matrix, which can be achieved through lysosomal cathepsins.[28] Lysosomes are highly responsive to changes in intracellular Ca^{2+} fluxes via expression of Ca^{2+} channels. One such channel is TRPM2, which is specifically activated by intracellular adenosine diphosphoribose.[35] Adenosine diphosphoribose was elevated in $A5^{+/-}$;*Kras* compared to *Kras* cells. Lysosomal Ca^{2+} signaling is connected to the autophagy process.[36] In addition, lysosomes contain cysteine cathepsins, which are not only responsible for degradation, but also play a role in autophagy, metabolism, and lysosome-mediated cell death. Cathepsins regulate the numbers of autophagosomes and lysosomes.[37] Our data pointed to a heightened level of autophagy in $A5^{+/-}$;*Kras* cells. $A5^{+/-}$;*Kras* cells exhibited enhanced extracellular cathepsin activation. Importantly, cathepsin activation in the extracellular medium was required and sufficient to enable invasion of cancer cells. Monoallelic loss of *Atg5* may in this scenario initiate multiple cellular changes starting with mitochondrial and Ca^{2+} homeostasis. Affected Ca^{2+} homeostasis may influence lysosomal numbers and fusions with autophagosomes, aggravated even further by the direct effects of *Atg5* on autophagy levels. In addition, it was shown that the interaction of Atg5-Atg12 with the tethering factor TECPR1 (tectonin β-propeller repeat containing 1) is crucially involved in the initiation of autophagosomal/lysosomal fusion to promote autophagic flux.[38] In this context, monoallelic loss of *Atg5* could be tightly interrelated to impaired lysosomal biogenesis and fusion. A hindered autolysosomal maturation process may thus lead to an accidental activation of pro-cathepsins and subsequently their release into the extracellular medium, ultimately promoting migration, invasion, and metastasis.

Lysosomal homeostasis can also affect the immune system and cytokine secretion, especially in conjunction with cathepsin activities.[39] The inflammatory tumor microenvironment is crucial in facilitating spontaneous PDAC development and amplifying the metastatic process. Anti-inflammatory M2-macrophages, regulatory lymphocytes, and neutrophils have been shown to potentiate PDAC.[29,40] Interestingly, we saw a shift in the cytokine profile of $A5^{+/-}$;*Kras* cells towards cytokines involved in promoting pro-tumorigenic M2-macrophages. In support of all of these data, we also detected more M2-macrophages in the original $A5^{+/-}$;*Kras* primary pancreatic tumors, as well as in the lung tumors formed after tail-vein injection of $A5^{+/-}$;*Kras* cell lines. Importantly, depleting macrophages significantly reduced $A5^{+/-}$;*Kras* cell metastasis in vivo, highlighting the importance of macrophages in potentiating metastasis. Consequently, monoallelic loss of *Atg5* leads to cell-intrinsic changes, which ultimately affect the tumor microenvironment favoring metastatic spread.

So far, only the autophagy protein Beclin-1 has been found monoallelically deleted in a variety of cancer types, such as breast, ovarian, and prostate cancer. In support of these findings *Beclin-1* heterozygous mice display frequent spontaneous malignancies.[41] Our study expands the spectrum of monoallelically affected autophagy genes to *Atg5*, correlating ATG5 protein expression with metastasis and survival in 3 independent human pancreatic cancer cohorts. Clinical trials on pancreatic cancer patients are currently evaluating autophagy inhibitors, such as chloroquine in adjuvant therapies combined with gemcitabine (ClinicalTrials.gov ID NCT01777477[42]). However, autophagy inhibitors are not only less specific, but very likely to only partially impede autophagic flux.[43] As we have shown that monoallelic loss of *Atg5* leads to chloroquine resistance and higher metastatic spread, administration of chloroquine may thus generate resistant cancer cell clones with heightened aggressiveness. Therefore, our data alert toward

increased awareness when applying autophagy blockers in clinical trials for pancreatic cancer patients.

Supplementary Material

Note: To access the supplementary material accompanying this article, visit the online version of *Gastroenterology* at www.gastrojournal.org, and at https://doi.org/10.1053/j.gastro.2018.09.053.

References

1. Zeitouni D, Pylayeva-Gupta Y, Der CJ, et al. KRAS mutant pancreatic cancer: no lone path to an effective treatment. Cancers (Basel) 2016;8.
2. New M, Van Acker T, Long JS, et al. Molecular pathways controlling autophagy in pancreatic cancer. Front Oncol 2017;7:28.
3. Santana-Codina N, Mancias JD, Kimmelman AC. The role of autophagy in cancer. Annu Rev Cancer Biol 2017;1:19–39.
4. Rosenfeldt MT, O'Prey J, Morton JP, et al. p53 status determines the role of autophagy in pancreatic tumour development. Nature 2013;504:296–300.
5. **Yang A, Rajeshkumar NV**, Wang X, et al. Autophagy is critical for pancreatic tumor growth and progression in tumors with p53 alterations. Cancer Discov 2014;4:905–913.
6. Rao S, Tortola L, Perlot T, et al. A dual role for autophagy in a murine model of lung cancer. Nat Commun 2014;5:3056.
7. Hara T, Nakamura K, Matsui M, et al. Suppression of basal autophagy in neural cells causes neurodegenerative disease in mice. Nature 2006;441:885–889.
8. **Nakhai H, Sel S**, Favor J, et al. Ptf1a is essential for the differentiation of GABAergic and glycinergic amacrine cells and horizontal cells in the mouse retina. Development 2007;134:1151–1160.
9. Jackson EL, Willis N, Mercer K, et al. Analysis of lung tumor initiation and progression using conditional expression of oncogenic K-ras. Genes Dev 2001;15:3243–3248.
10. Mizushima N, Yamamoto A, Matsui M, et al. In vivo analysis of autophagy in response to nutrient starvation using transgenic mice expressing a fluorescent autophagosome marker. Mol Biol Cell 2004;15:1101–1111.
11. Diakopoulos KN, Lesina M, Wormann S, et al. Impaired autophagy induces chronic atrophic pancreatitis in mice via sex- and nutrition-dependent processes. Gastroenterology 2015;148:626–638 e17.
12. Perera RM, **Stoykova S, Nicolay BN**, et al. Transcriptional control of autophagy-lysosome function drives pancreatic cancer metabolism. Nature 2015;524:361–365.
13. Gunter TE, Yule DI, Gunter KK, et al. Calcium and mitochondria. FEBS Lett 2004;567:96–102.
14. Gomes LC, Scorrano L. Mitochondrial morphology in mitophagy and macroautophagy. Biochim Biophys Acta 2013;1833:205–212.
15. Boland ML, Chourasia AH, Macleod KF. Mitochondrial dysfunction in cancer. Front Oncol 2013;3:292.
16. Tsai FC, Meyer T. Ca2+ pulses control local cycles of lamellipodia retraction and adhesion along the front of migrating cells. Curr Biol 2012;22:837–842.
17. Settembre C, Fraldi A, Medina DL, et al. Signals from the lysosome: a control centre for cellular clearance and energy metabolism. Nat Rev Mol Cell Biol 2013;14:283–296.
18. **McWhorter FY, Wang T**, Nguyen P, et al. Modulation of macrophage phenotype by cell shape. Proc Natl Acad Sci U S A 2013;110:17253–17258.
19. Guo JY, White E. Autophagy, metabolism, and cancer. Cold Spring Harb Symp Quant Biol 2016;81:73–78.
20. Yang A, Herter-Sprie G, Zhang H, et al. Autophagy sustains pancreatic cancer growth through both cell-autonomous and nonautonomous mechanisms. Cancer Discov 2018;8:276–287.
21. Garcia-Fernandez M, Karras P, Checinska A, et al. Metastatic risk and resistance to BRAF inhibitors in melanoma defined by selective allelic loss of ATG5. Autophagy 2016;12:1776–1790.
22. Koyama-Honda I, Tsuboyama K, Mizushima N. ATG conjugation-dependent degradation of the inner autophagosomal membrane is a key step for autophagosome maturation. Autophagy 2017;13:1252–1253.
23. Dupont N, Nascimbeni AC, Morel E, et al. Molecular Mechanisms of Noncanonical Autophagy. Int Rev Cell Mol Biol 2017;328:1–23.
24. Recouvreux MV, Commisso C. Macropinocytosis: a metabolic adaptation to nutrient stress in cancer. Front Endocrinol (Lausanne) 2017;8:261.
25. Pachmayr E, Treese C, Stein U. Underlying mechanisms for distant metastasis—molecular biology. Visc Med 2017;33:11–20.
26. Chen H, Chan DC. Mitochondrial dynamics in regulating the unique phenotypes of cancer and stem cells. Cell Metab 2017;26:39–48.
27. White C. The regulation of tumor cell invasion and metastasis by endoplasmic reticulum-to-mitochondrial Ca2+ transfer. Front Oncol 2017;7:171.
28. Fonovic M, Turk B. Cysteine cathepsins and extracellular matrix degradation. Biochim Biophys Acta 2014;1840:2560–2570.
29. Nielsen MF, Mortensen MB, Detlefsen S. Key players in pancreatic cancer-stroma interaction: cancer-associated fibroblasts, endothelial and inflammatory cells. World J Gastroenterol 2016;22:2678–2700.
30. Altieri DC. Mitochondria on the move: emerging paradigms of organelle trafficking in tumour plasticity and metastasis. Br J Cancer 2017;117:301–305.
31. Amoedo ND, Rodrigues MF, Rumjanek FD. Mitochondria: are mitochondria accessory to metastasis? Int J Biochem Cell Biol 2014;51:53–57.
32. Porporato PE, Payen VL, Perez-Escuredo J, et al. A mitochondrial switch promotes tumor metastasis. Cell Rep 2014;8:754–766.
33. Okeke E, Parker T, Dingsdale H, et al. Epithelial-mesenchymal transition, IP3 receptors and ER-PM

junctions: translocation of Ca2+ signalling complexes and regulation of migration. Biochem J 2016;473:757–767.
34. Guo H, Chitiprolu M, Roncevic L, et al. Atg5 disassociates the V1V0-ATPase to promote exosome production and tumor metastasis independent of canonical macroautophagy. Dev Cell 2017;43:716–730 e7.
35. Lange I, Yamamoto S, Partida-Sanchez S, et al. TRPM2 functions as a lysosomal Ca2+-release channel in beta cells. Sci Signal 2009;2:ra23.
36. Di Paola S, Scotto-Rosato A, Medina DL. TRPML1: The Ca(2+)retaker of the lysosome. Cell Calcium 2018;69:112–121.
37. Man SM, Kanneganti TD. Regulation of lysosomal dynamics and autophagy by CTSB/cathepsin B. Autophagy 2016;12:2504–2505.
38. Chen D, Fan W, Lu Y, et al. A mammalian autophagosome maturation mechanism mediated by TECPR1 and the Atg12-Atg5 conjugate. Mol Cell 2012;45:629–241.
39. Nabar NR, Kehrl JH. The transcription factor EB links cellular stress to the immune response. Yale J Biol Med 2017;90:301–315.
40. Wormann SM, Diakopoulos KN, Lesina M, et al. The immune network in pancreatic cancer development and progression. Oncogene 2014;33:2956–2967.
41. Qu X, Yu J, Bhagat G, et al. Promotion of tumorigenesis by heterozygous disruption of the beclin 1 autophagy gene. J Clin Invest 2003;112:1809–1820.
42. **Wolpin BM, Rubinson DA**, Wang X, et al. Phase II and pharmacodynamic study of autophagy inhibition using hydroxychloroquine in patients with metastatic pancreatic adenocarcinoma. Oncologist 2014;19:637–638.
43. Mizushima N, Yoshimori T, Levine B. Methods in mammalian autophagy research. Cell 2010;140:313–326.

Author names in bold designate shared co-first authorship.

Received December 23, 2017. Accepted September 28, 2018.

Reprint requests
Address requests for reprints to: Hana Algül, MD, MPH, Klinik und Poliklinik für Innere Medizin II, Klinikum Rechts der Isar, Technische Universität München, 81675 Munich, Germany. e-mail: hana.alguel@mri.tum.de; fax: (49) 89-4140-7869; Marina Lesina, PhD, Klinik und Poliklinik für Innere Medizin II, Klinikum Rechts der Isar, Technische Universität München, 81675 Munich, Germany. e-mail: marina.lesina@tum.de; fax: (49) 89-4140-7869.

Acknowledgments
The authors thank Gabriele Mettenleiter (electron microscopy), Marion Mielke (immunohistochemistry), the tissue bank of the Institute of Pathology of the Technische Universität München (MTBIO), and Franziska Braun (cathepsin, glutamate dehydrogenase measurements) for technical assistance. The authors want to deeply acknowledge Prof. Walter Halangk, who in the course of the revision of this manuscript passed away. The authors are grateful for his very valuable contribution. Thus, the authors want to dedicate this manuscript to him.

Author contributions: K.G. and K.N.D. designed and performed experiments, analyzed data, and prepared the manuscript. J.A., M.S., D.K., A.F.K., K.J.C, E.K.-A., D.A.R., A.B., M.K., S.M.W., M.L. provided experimental support. B.S. provided *Atg5*-knockdown cell lines. T.W., Y.Z., and W.H. performed cathepsin and glutamate dehydrogenase measurements. S.V. and A.T. performed Ca2+ measurements. A.M.S., K.S., W.W. supplied human PDAC samples and performed ATG5 scoring. A.A. and J.A. performed metabolomic experiments. M.A. and A.W. performed electron microscopy. M.J. carried out mitochondrial respiratory measurements. G.H. conducted CYTO-ID experiments. A.K., C.S.M, S.H., B.S. Jr, and R.M.S revised the manuscript. H.A. and M.L. designed experiments, analyzed data, and revised the manuscript.

Transcript profiling: Microarray data are available in the ArrayExpress database at EMBL-EBI (https://www.ebi.ac.uk/arrayexpress/) under accession number E-MTAB-6275.

Conflicts of interest
The authors disclose no conflicts.

Funding
This study was supported in part by the Mildred-Scheel-Professur der Deutschen Krebshilfe 111464, DFG AL 1174/6-1 to H.A., DFG DI 2299/1-1 to K.N.D., DFG SFB1321 (S01) to K.S. and W.W., and the German Federal Ministry of Education and Research to the German Center for Diabetes Research (DZD e.V.) to J.A.

Supplementary Materials and Methods

Quantification of Relative Pancreatic Weight, Tumor Incidence, and Metastasis Incidence

Kras, *A5*$^{+/-}$*; Kras*, and *A5; Kras* mice were sacrificed at 4, 9, and 18 weeks of age or at the time point of sickness. Relative pancreatic weight was calculated from the pancreas and body weight obtained during sacrifice (pancreas weight/body weight). Tumor incidence and metastasis incidence (percent of tumor or metastasis-positive mice relative to all mice sacrificed) was calculated after histologic examination. Metastasis-positive mice were mice with metastasis in liver, lung, or diaphragm from the pool of pancreatic tumor–positive mice. Ascites, lymph node, spleen, or kidney infiltration was also evaluated (see Supplementary Table 1).

Detection of GFP-LC3 Puncta

GFP-LC3 mice with or without concomitant *Kras* expression were sacrificed after standard fed conditions. Pancreas was snap frozen in freezing medium (Tissue-Tek O.C.T. Compound; Weckert Labortechnik, Germany) and 7- to 10-μm-thick cryosections were mounted on adhesive-coated slides. Sections were air-dried, fixed in 100% ethanol for 8 minutes at room temperature (RT), washed with phosphate buffered saline (PBS) and covered with 4′,6-diamidino-2-phenylindole (DAPI) containing mounting medium (H-1200; Vector Laboratories, Burlingame, CA). Sections were processed and kept in the dark until analysis. Puncta formation was detected by analysis of green fluorescence (EX/EM 470/525 nm) with fluorescence microscopy (Zeiss Axiovert 200M; Carl Zeiss NTS GmbH, Oberkochen, Germany).

Tumor Cell Isolation and Cultivation

Primary pancreatic tumor cell lines were established from isolated murine pancreatic tumors. To establish the cell lines, pieces of pancreatic tumor tissue from *Kras*, *A5*$^{+/-}$; *Kras*, and *A5; Kras* mice were placed in full culture medium (see below) and tumor cells were allowed to grow out of the tissue. Cell lines were routinely cultured under standard conditions (5% CO_2, 37°C) in culture media (Dulbecco's modified Eagle medium [DMEM] supplemented with 10% FBS (#10082147; Gibco, Gaithersburg, MD), 1% penicillin-streptomycin (Pen-Strep) (#1500-063; Gibco), 1% non-essential amino acids (#11140050; Gibco). On average, cells were passaged 5 times before any experiments.

Knockdown of mAtg5

Experimental procedures were followed as described previously.[1]

Transfection of 293T Cells for Production of Lentiviral Particles. The 5 × 10^6 293T cells were seeded in 10-cm dishes. After 1 day, media was replaced and co-transfection of transfer plasmids purchased from Sigma Aldrich (St Louis, MO; TRCN0000327456 (54% knockdown, validated), TRCN0000327358 (58% knockdown, validated), TRCN0000363558 (81% knockdown, validated), TRCN0000375754 (86% knockdown, validated), and TRCN0000099432 (94% knockdown, validated) with lentiviral packaging plasmids (pMD.GP, pRSV-rev, pMD.G) was performed using Lipofectamine 2000 (ThermoFisher Scientific, Waltham, MA). shRNA that does not target any known human or mouse gene (shNT) was used as a control. Two days later, lentiviral particles were harvested from the supernatant and frozen at –80°C.

Transduction of Target Cells With mATG5 Knockdown Constructs. Target *Kras* cells were seeded in 6-cm dishes. One day later, media was aspirated and 1 mL lentiviral suspension was added to cells in presence of 8 μg/mL Polybrene (Sigma Aldrich). After 2 hours at 37°C, 4 mL media was added. Selection of transduced cells was performed using 10 μg/mL puromycin.

Experimental Analysis. Cells were tested in Western blotting for Atg5, LC3, and β-actin expression (as described below) and the knockdown percentage were confirmed. Cells with 54%, 58%, 81%, 86%, and 94% mAtg5-knockdown were further used in colony formation (full medium, 10% FCS), Boyden Chamber migration, invasion, and tail-vein injection experiments as described below. Experiments were performed in triplicate.

In Vitro Cathepsin Activity Measurements

Activities of cathepsins B, L, and D were intra- and extracellularly assessed in cell lysates and culture media of primary pancreatic tumor cell lines. Tumor cells were separated from culture media by centrifugation at 1000*g* for 10 minutes. Then, cell pellet and culture medium were snap frozen. After thawing, tumor cells were subsequently resuspended in ice-cold homogenization buffer (5 mM MOPS [pH 6.5], 250 mM sucrose, 1 mM Mg_2SO_4, 0.13% Triton X100l) and lysed by sonication. Cathepsin B and -L were determined as Ca074- and N1760-sensitive activity in assay buffer (50 mM sodium phosphate buffer [pH 5.5], 1 mM EDTA, and 1 mM dithiothreitol) using the fluorogenic substrates Z-Arg-Arg-7-amino-4-methylcoumarin A (10 μM, #31213-v; Pepta Nova, Sandhausen, Germany) and Z-Phe-Arg-7-amino-4-methylcoumarin (10 μM, #3095-v; Pepta Nova), respectively. Cathepsin D activity was measured in 50 mM sodium acetate buffer (pH 4.0) using the fluorogenic substrate Mca-Gly-Lys-Pro-Ile-Leu-Phe-Phe-Arg-Leu-Lys(Dnp)-D-Arg-NH2 (10 μM, #3200-v; Pepta Nova). The release of 7-amido-4-methylcoumarin was kinetically monitored for 10 minutes at the excitation/emission wavelength of 360/438 nm in a Safire microplate reader (Tecan, Grödig, Austria) by spectrofluorometry. Intra- and extracellular portions of cathepsin activities were normalized to the protein concentration in cell lysates determined by Bio-Rad (Hercules, CA) protein assay kit.

Subcellular Fractionation by Isopycnic Percoll Density Centrifugation and Measurement of Glutamate Dehydrogenase Activity

To analyze distribution and integrity of mitochondria in subcellular fractions pelleted tumor cells harvested from primary pancreatic tumor cells lines (produced as described here) were resuspended in HS buffer (250 mM sucrose,

10 mM citric acid, 0.5 mM EGTA, 0.1 mM MgSO4 [pH 6.0]) and homogenized by 5 strokes using a Dounce homogenizer. After centrifugation at 100*g* post-nuclear supernatant was applied onto an isotonic 50% (v/v) Percoll/HS buffer solution (as described here) at pH 7.27 and subsequently separated by isopycnic centrifugation at 50,000*g* for 45 minutes at 4°C. After separation, the Percoll gradient was portioned in 46 fractions using a peristaltic pump beginning from the bottom and fractions were stored at –80°C until further use.

Activity of glutamate dehydrogenase as a marker of mitochondrial distribution in subcellular fractions was determined spectrophotometrically at 340 nm according to $NADH_2$ oxidation with 2-oxoglutarate and NH_4^+ as a substrate by the method of Schmidt.[2]

Immunoblotting

For immunoblotting, *Kras*, *A5*$^{+/-}$; *Kras*, and *A5; Kras* cells were pelleted and snap frozen. Cell pellets were resuspended in ice-cold protein lysis buffer (50 mM HEPES [pH 7.9], 150 mM NaCl, 1 mM EDTA [pH 8.0], 0.5% NP-40 [Roche, Basel, Switzerland], 10% glycerol) supplemented with protease/phosphatase inhibitors (SERVA, Heidelberg, Germany), sonicated, and kept on ice. Extracellular proteins secreted into the culture medium were concentrated by trichloroacetic acid precipitation (final concentration 6%) in the presence of 2% Na-deoxycholate by the method Bensadoun and Weinstein.[3] Concentration was determined by Bio-Rad protein Assay kit and concentration of all samples was set to 4 mg/mL. All samples were cooked for 5 minutes at 95 Celcius in Laemmli buffer (300 mM Tris-HCl [pH 6.8], 10% (w/v) sodium dodecyl sulfate, 50% (v/v) glycerol, 0.05% (w/v) Bromphenole blue, and 5% (v/v) β-mercaptoethanol) except when used for detection of mitochondrial oxidative phosphorylation complexes. Protein lysates were separated by sodium dodecyl sulfate gel electrophoresis and transferred to polyvinylidene fluoride membranes. After overnight incubation with primary antibody at 4°C, proteins were detected using horseradish peroxidase–conjugated secondary antibodies anti-mouse (NA931V; GE Healthcare Life Sciences, Chicago, IL), anti-rabbit (NA934V; GE Healthcare Life Sciences) or anti-guinea pig (A7289; Sigma) and Amersham enhanced chemiluminescence reagent (GE Healthcare Life Sciences). The primary antibodies used include: anti-Atg5 (1/1000) (NB110-53818; Novus Biologicals, Littleton, CO), anti-p62 (1/1000) (GP62-C; Progen, Heidelberg, Germany), anti-LC3 (1/1000) (PD014; MBL International, Woburn, MA), anti-cathepsin B (1/5000) (AF965; R&D Systems, Minneapolis, MN), anti-p53 (1/500) (NCL-p53-CM5p Novocastra, Newcastle upon Tyne, UK), anti-cathepsin L (1/5000) (AF1515; R&D Systems) anti-cathepsin D (1/5000) (cs-10725; Santa Cruz Biotechnology, Santa Cruz, CA), anti-phospho-AMPKα (1/1000) (2535; Cell Signaling Technology, Danvers, MA), anti-AMPKα (1/1000) (2532; Cell Signaling Technology), anti–phospho-S6 (1/1000) (2211; Cell Signaling Technology, anti-SOD2 (1/1000) (ADI-SOD-111; Enzo, Farmingdale, NY), anti-BiP (1/1000) (AB21685; Abcam, Cambridge, UK), anti-MitoProfile Total OXPHOS Rodent Western Blot antibody cocktail (1/1000) (MS604; Mitosciences, Eugene, OR), anti–β-actin (1:2000) (A5441; Sigma).

Histochemistry and Immunohistochemistry

For proliferation analysis, mice were labeled with 50 μg bromodeoxyuridine (B5002; Sigma) per gram body weight by intraperitoneal injection and sacrificed 2 hours later. Pancreas was fixed in 4% (wt/vol) paraformaldehyde in PBS overnight at 4°C and embedded in paraffin wax. Tissue sections of 2-μm thickness were mounted on adhesive-coated slides and stained with H&E.

For immunohistochemistry standard procedures were applied. Briefly, after deparaffinization and rehydration, heat-induced antigen retrieval with 0.01M citrate (pH 6.0) was utilized. Endogenous peroxidase was blocked with 3% hydrogen peroxide for 15 minutes at RT in the dark. Unspecific binding was blocked with 5% serum for 1 hour at RT. Slides were incubated with primary antibodies diluted in blocking solution over night at 4°C. Primary antibodies used include: anti-bromodeoxyuridine (1/250) (MCA2060 AbD Serotec, Killington, UK), anti-F4/80 (1/100) (MF-48000; Invitrogen, Carlsbad, CA), anti-CK19 (1/200) (TROMA III Developmental Studies Hybridoma Bank), anti-arginase 1 (1/500) (610708; BD Transduction Laboratories, Woburn, MA), anti-S100a4 (1/800) (13018; Cell Signaling Technology), anti-MMR/CD206 (1/100) (AF2535; R&D Systems Bio-Techne), anti-Atg5 (1/100) (NB110-53818; Novus Biologicals), anti-p62 (1/100) (GP62-C; Progen), and anti-LC3 (1/100) (PD014; MBL International). Secondary antibodies including biotinylated anti-rabbit in goat (BA 1000; Vector Laboratories), anti-mouse in goat (BA 9200; Vector Laboratories), and anti-rat in rabbit (BA 4000; Vector Laboratories) were applied for 1 hour at RT and avidin-biotin peroxidase complex for biotinylated secondary antibodies was then added according to manufacturer directions (Vector Laboratories). Staining was developed with DAB reagent (Vector Laboratories). For arginase 1 and S100a4 detection streptavidin/biotin blocking kit (SP2002; Vector) was used during the staining procedure to reduce background, according to manufacturer instructions. Hematoxylin was used for counterstaining.

Acinar-to-Ductal Metaplasia and Pancreatic Intraepithelial Neoplasia Quantifications

Paraffin-embedded tissue sections from 4-week-old *Kras*, *A5*$^{+/-}$; *Kras*, *A5; Kras* were stained for H&E and photographed at 100× magnification. The number of ADMs was determined in each picture using Zeiss AxioVision software (Carl Zeiss NTS GmbH). Measurements from multiple photographs per tissue slide were summed up and expressed as ADM per high-power field. Results were then averaged according to genotype. In a similar fashion, paraffin-embedded tissue sections from 9- and 18-week-old *Kras*, *A5*$^{+/-}$; *Kras*, *A5; Kras* were stained for H&E and photographed at 100× magnification. PanINs were classified according to

Gene	Forward primer	Reverse primer
Sod1	GTCCGTCGGCTTCTCGTCT	CACAACTGGTTCACCGCTTG
Sod2	ACACATTAACGCGCAGATCA	ATATGTCCCCCACCATTGAA
Nrf1	TCTCACCCTCCAAACCCAAC	CCCGACCTGTGGAATACTTG
Nrf2	TTCTTTCAGCAGCATCCTCTCCAC	ACAGCCTTCAATAGTCCCGTCCAG
Xbp1	ACACGCTTGGGAATGGACAC	CCATGGGAAGATGTTCTGGG
Cyclophilin	ATGGTCAACCCCACCGTGT	TTCTGCTGTCTTTGGAACTTTGTC

PanIN-1/-2/-3 and total numbers were expressed as PanIN/high-power field. Results were then averaged according to genotype and age group.

Co-Immunofluorescence

Cryosections of GFP-LC3 transgenic pancreas were processed as described. Unspecific binding was blocked with 5% serum at RT and incubated over night at 4°C with the primary antibody. Anti-CK19 primary antibody (TROMA III Developmental Studies Hybridoma Bank) was diluted in blocking solution (1/200). The following day, secondary antibody anti-rat in goat Alexa Fluor 568 (1/300) (A11077; Invitrogen) was applied for 1 hour at RT. In the end, slides were covered with DAPI-containing mounting medium (H-1200 Vector Laboratories) and analyzed with fluorescence microscopy (Zeiss Axiovert 200M).

Transmission Electron Microscopy

For transmission electron microscopy *Kras* and $A5^{+/-}$; *Kras* cells were collected and fixed in 2.5% electron microscopy grade glutaraldehyde in 0.1M sodium cacodylate buffer (pH 7.4) (Science Services, Munich, Germany), post-fixed in 2% aqueous osmium tetraoxide,[4] dehydrated in gradual ethanol (30%–100%) and propylene oxide, embedded in Epon (Merck, Darmstadt, Germany) and cured for 24 hours at 60°C. Pellets were cut in semi-thin sections and stained with toluidine blue. Ultrathin sections of 50 nm were collected onto 200 mesh copper grids, stained with uranyl acetate and lead citrate before examination by transmission electron microscopy (Zeiss Libra 120 Plus, Carl Zeiss NTS GmbH, Oberkochen, Germany). Pictures were acquired using a Slow Scan CCD-camera and iTEM software (Olympus Soft Imaging Solutions, Münster, Germany).

RNA Extraction and Quantitative Real-Time Polymerase Chain Reaction

For RNA extraction, *Kras* and $A5^{+/-}$; *Kras* cells were collected in RLT lysis buffer (1015762; Qiagen, Venlo, The Netherlands) supplemented with 1% β-mercaptoethanol (M6250; Sigma) and snap-frozen. Subsequently, RNA was extracted using the RNeasy Mini Kit (74104; Qiagen). SuperScript II Reverse Transcriptase (18064-014; Invitrogen) was used for complementary DNA synthesis. Quantitative real-time polymerase chain reaction was carried out using a StepOne Plus Real-Time PCR System (Applied Biosystems, Foster City, CA) in combination with Power SYBR Green PCR Master Mix (4368577; Applied Biosystems). Target messenger RNA expression was normalized to endogenous *cyclophillin* and quantified by the ΔΔCT method. Primer sequences are provided.

For detection of spliced *Xbp1*, complementary DNA was subjected to polymerase chain reaction with a primer set detecting both unspliced and spliced *Xbp1* (unspliced *Xbp1u* 171 bp, spliced *Xbp1s* 145 bp). PCR products were separated by agarose gel electrophoresis. *Cyclophilin* was used as control.

Microarray Data Analysis

For transcriptomic analysis, *Kras* and $A5^{+/-}$; *Kras* tumor cells were harvested after PBS-washing in RLT lysis buffer supplemented with 1% β-mercaptoethanol, as described. Cell suspensions were snap-frozen and stored at −80°C. RNA isolation from tumor cell suspensions and Affymetrix GeneChip (*Mus musculus*) Mouse Gene 1.0 ST Array was conducted by the service facility KFB Center of Excellence for Fluorescent Bioanalytics (Regensburg, Germany, www.kfb-regensburg.de). Microarray data were analyzed by using the Gene Set Enrichment Analysis software (Broad Institute, Cambridge, MA). A Normalized Enrichment Score (NES) of $\geq$1.0 and a nominal P value of $<$.05 were used to evaluate significantly up-regulated pathways according to Kyoto Encyclopedia of Genes and Genomes and Transcription Factor Binding Motif databases. Pathways were subsequently separated into groups depending on their description in the respective database. A heat map of the most highly regulated genes computed by GSEA was used and the genes were further classified according to their function. Genes belonging to one functional group were depicted as percentage related to the entire number of highly regulated genes. A NES vs nominal P value diagram was provided to indicate the total number of regulated (NES $\geq$ 0.5) and significantly regulated (NES $\geq$ 1.4, nominal P value $<$.05) pathways detected in the Kyoto Encyclopedia of Genes and Genomes database. Microarray data are available in the ArrayExpress database at EMBL-EBI (https://www.ebi.ac.uk/arrayexpress/) under accession number E-MTAB-6275.

Non-Targeted Metabolomic Measurements

Liquid chromatography tandem mass spectrometry–based non-targeted metabolomics analysis was conducted

at the Genome Analysis Centre, Helmholtz Zentrum München as described previously.[5] About 1×10^6 pancreatic cancer cells were required for the analysis. In brief, 0.375×10^6 *Kras* or *A5*$^{+/-}$; *Kras* cells were seeded in duplicates in a 6-well plate with 2 mL culture medium and grown for 48 hours until 80%–90% confluent and an approximate number of 0.5×10^6 was reached. Cells were washed 2 times with PBS (37°C). Dry ice-cold 80% v/v methanol (400 μL) containing 4 recovery standard compounds to monitor extraction efficiency was added to the cells to cover them immediately. Cells were scraped and the cell suspension was transferred into precooled (dry ice) 2-mL screwcap micro tubes (Sarstedt Micro Tube, 2 mL, PP [reference #72.694.005]) filled with 160 mg glass beads. Another 100 μL of dry ice-cold methanol extraction solvent to wash the well was added and transferred to the micro tube. Suspensions of two 6-well plates were pooled into one tube to obtain a sample of 1×10^6 cells in 1-mL cell suspension. The samples were stored immediately at −80°C until metabolomic analysis was performed. The metabolites were assigned to cellular pathways based on PubChem, Kyoto Encyclopedia of Genes and Genomes, and the Human Metabolome Database. Metabolic pathways were described as significantly up- or down-regulated, when metabolites assigned to those specific pathways were increased or decreased, respectively. Values depicted correspond to the absolute values normalized in terms of raw area counts after liquid chromatography/mass spectrometry–based metabolomic analysis.

Oncomine Database

The oncomine database (www.oncomine.org) was used to search for autophagy and lysosomal function-associated genes. GO Biological Process-Autophagy or GO Cellular Component-Lysosome was used as concept; primary filters selected were Cancer vs Normal Analysis and Pancreatic Cancer; pathology subtypes M1+, N1+, T4 according to TNM-staging were subsequently applied. DNA Copy Number ($\log_2$ copy number units) retrieved from The Cancer Genome Atlas (TCGA Research Network, http://cancergenome.nih.gov/) was used to illustrate copy number gain or loss in human pancreatic cancer samples vs normal pancreas samples.

Measurement of Mitochondrial Metabolism by Seahorse Analyzer

Measurements of oxygen consumption rate were performed with a XF extracellular flux analyzer as described previously.[7] Briefly, *Kras* and *A5*$^{+/-}$;*Kras* tumor cells were seeded at a density of 1×10^5 cells per well in a XF24 cell culture microplate. DMEM (4.5 g/L glucose, +L-glutamine, -pyruvate [pH 7.6] at RT) supplemented with 10% heat-inactivated FBS (Gibco) and 1% Pen-Strep was used for cell culturing. On the day of assay (24 hours after seeding), medium was exchanged to non-carbonated Seahorse measurement medium and the XF24 plate was transferred to a temperature-controlled (37°C) XF24 Extracellular Flux analyzer (Seahorse Bioscience, Billerica, MA) and equilibrated for 10 minutes. To determine the basal respiration four assay cycles (1-minute mix, 2-minute wait and 3-minute measuring period) were used. Then oligomycin (4 μM) was added by automatic pneumatic injection (3 assay cycles) to inhibit ATP synthase and thus approximate the proportion of respiration used to drive ATP synthesis vs proton leak-linked respiration. Oligomycin was followed by an injection of FCCP (carbonyl cyanide p-trifluoromethoxyphenylhydrazone) (0.5 μM) to completely dissipate proton motive force and maximally stimulate mitochondrial respiration (3 assay cycles), thus determining spare respiratory capacity and substrate oxidation capacity. An injection of rotenone (4 μM) and antimycin A (2 μM) was used to correct for the non-mitochondrial respiration rate (3 assay cycles), which was subtracted from all the other rates. Coupling efficiency was calculated as the oligomycin-sensitive fraction of mitochondrial respiratory activity, estimating the proportion of basal respiration used to drive ATP synthesis. To determine extracellular acidification rates for glycolysis, experiments were ended by injection of 2-deoxy-D-glucose, 100 mM), correcting for non-glycolytic acidification. Injection of 2-deoxy-D-glucose enabled calculation of glycolytic acidification. Data obtained after oligomycin treatment induce glycolytic capacity. Oxygen consumption rate was plotted against extracellular acidification rates to illustrate oxidative vs glycolytic metabolism in cancer cells. Raw data were normalized to either protein or DNA content (ng).

Cell Morphology Analysis and Quantification of Cell Proliferation

To analyze cell morphology, *Kras* and *A5*$^{+/-}$; *Kras* were seeded in 6-well plates. Twenty-four hours after seeding, pictures were acquired with the Zeiss AxioVision Imager A1 using a magnification of 100×. For quantification of proliferation, 5×10^4 *Kras* and *A5*$^{+/-}$; *Kras* cells were seeded per well in a 6-well plate. The culture media was changed every other day. Cells were counted after trypsinization every 24 hours up to 120 hours using the Neubauer counting chamber. Full medium DMEM supplemented with 10% FBS (#10082147; Gibco), 1% Pen-Strep (#1500-063; Gibco), 1% non-essential amino acids (#11140050; Gibco) was used for cell culture.

Autophagic Flux Measurement Using CYTO-ID

To analyze autophagosome accumulation, *Kras* and *A5*$^{+/-}$; *Kras* were seeded in triplicates in 96-well plates and allowed to adhere overnight. Half of the cells were kept in full medium and compared to cells cultivated overnight in serum-free medium. Autophagosome accumulation was analyzed by using the CYTO-ID Autophagy Detection Kit (ENZ-51031; Enzo) according to the manufacturer's instructions. Fluorescence was detected using a Varioscan Lux (Thermo scientific) microplate reader.

Colony Formation and Cell Treatments

For the cologenic assay, 3×10^2 *Kras* and $A5^{+/-}$; *Kras* cells were plated in triplicates 6-well plates and grown for 10 days in culture media. Colonies were stained with 2% crystal violet (C3886; Sigma), washed with water, and their area was quantified using ImageJ software (National Institutes of Health, Bethesda, MD). Treatments during the clonogenic assays include: 10% FCS-containing medium, serum-free Hank's balanced salt solution–containing medium (GIBCO-14025092, 1:20 dilution of normal medium), chloroquine in full medium (2 μM and 6 μM, C6628; Sigma), 6-aminonicotinamide in full medium (10 μM and Sigma-A68203), Rotenone in full medium (15 nM and Sigma-R8875), galactose and glutamine in glucose-free medium (galactose 10 mM and glutamine 4 mM, D-(+)-galactose, Sigma-G5388 and GlutaMAX-I, GIBCO-35050061, DMEM, no glucose, GIBCO-11966-025), high glucose in glucose-free medium (25 mM and GIBCO-A2494001).

Anoikis Assay

For the anoikis assay, 6-well plates were coated with poly-HEMA (20 mg/mL) (P3932; Sigma) dissolved in 96% ethanol. Then 5×10^5 *Kras* and $A5^{+/-}$; *Kras* cells were seeded in triplicates and cultured for 48 hours in culture media. Surviving cells in the media were calculated using the Neubauer counting chamber.

Boyden Chamber Migration Assay

Then 1.5×10^5 *Kras* and $A5^{+/-}$; *Kras* cells were seeded in triplicates in 6-well plates until confluence. One hundred microliters serum-free medium was added to upper chamber and 200 μL cells were added to chamber (2.5×10^5/mL in serum-free medium). Seven hundred and fifty microliters full medium was added to lower chamber. Boyden-Chamber Assay plate was incubated at 37°C for 12–16 hours. After incubation, medium was removed from upper chamber and chambers were washed twice with PBS. Cells were fixed with formaldehyde (3.7% in PBS) for 2 minutes and washed with PBS twice. To permeabilize cells, 100% methanol was added to chambers for 20 minutes. After removing methanol chambers were washed twice with PBS. Chambers were placed into wells and stained with Giemsa at RT for 15 minutes. After removing Giemsa solution, chambers were washed twice with PBS. Non-migrated cells were scraped off with cotton swabs from the membranes. Migrated cells were counted under a light microscope.

Invasion Assay

The 6.5-mm Transwell (#CLS3464; Sigma, Corning Costar) with 8.0-μm pore polyester membrane insert was used in 24-well culture plates. The upper surface of the membrane was coated with 100 μL mixed Matrigel (Corning Life Sciences, Teterboro, NJ) per well. The Matrigel was incubated at 37°C for gelling. Then 5×10^4 *Kras* and $A5^{+/-}$; *Kras* cells were seeded in triplicate with 200 μL serum-free DMEM in the upper chamber. The lower chamber was filled with 750 μL culture media. After 48 hours, the cells were fixed by formaldehyde 3.7% in PBS, permeabilized with 100% methanol, and stained with crystal violet. Cells that invaded to the lower surface area of the membrane were calculated by counting stained cells. E64d (100 μM and E3132-Sigma) was used to inhibit cathepsin activity. Filopodia were quantified after 36 hours of seeding.

Orthotopic Transplantation

Littermates of $A5^{+/-}$; *Kras* mice 8 weeks of age were injected orthotopically into the pancreas with 1×10^6 of either *Kras* or $A5^{+/-}$; *Kras* tumor cell suspensions (resuspended in a solution of Matrigel [Corning 354234]/DMEM without supplements in a ratio of 4:1) using a 26-gauge needle. The mice were sacrificed 30 days after injection, or earlier when they reached sickness criteria. Pancreatic tissues were collected, embedded in paraffin, and stained with H&E. Lung, liver, lymph nodes, kidney, spleen, and duodenum were also collected and processed in the same way. Occurrence of tumors and metastasis was quantified and representative macroscopic and microscopic pictures were taken.

Tail-Vein Injection

Littermates of $A5^{+/-}$; *Kras* mice 8 weeks of age were injected intravenously through the tail vein with 1×10^6 of either *Kras* or $A5^{+/-}$; *Kras* tumor cell suspensions (resuspended in 0.9% saline solution) using a 26-gauge needle. The mice were sacrificed 20 days after injection, or earlier when they reached sickness criteria. The lungs were collected, embedded in paraffin, and stained with H&E. Mice were classified as metastasis positive or negative and representative macroscopic and microscopic pictures were taken. Body weight at time of sacrifice was measured to establish levels of cachexia. Metastatic tumor cells were re-isolated from pieces of lung tissue to determine cell morphology and survival capacity.

Liposomal Clodronate Treatment

For macrophage depletion in wild-type mice, clodronate-loaded liposomes (CP-010-010, Liposoma, Amsterdam, The Netherlands) were used. As control, mice were injected with control liposomes (PBS). For the experiment, mice were injected intraperitoneally (mL/mouse) as follows:

Before tail-vein injection			After tail-vein injection		
Day –8	Day –4	Day 0	Day 4/8	Day 12/16	Day 20
0.2 mL	0.2 mL	0.1 mL	0.1 mL	0.1 mL	0.1 mL

Clodronate- and PBS-treated mice were injected with $A5^{+/-}$;*Kras* cells (biologic duplicates) into the tail vein (at day 0 according to the scheme above) to analyze the influence of macrophages on metastasis in the lung. Experiments were performed with at least 5 mice per group. Mice were sacrificed 21 days after tail-vein injection due to sickness. Spleens of mice were analyzed after the experiments for

F4/80 immunohistochemistry as described. Lung metastasis was quantified as described below.

Cytokine Array

In order to detect cellular cytokine profile supernatants of *Kras* and *A5*$^{+/-}$; *Kras* cells were collected and processed as described here for immunoblotting. Lysates were then used according to the manufacturer's instructions (Mouse Cytokine Array Panel A, Catalog Number ARY006; R&D Systems). Pixel intensity of individual plots was quantified using ImageJ software. The average of 2 spots corresponding to 1 cytokine was used to compare cytokine profile according to genotype.

Macrophage Differentiation Assay

To detect the effect of *Kras* and *A5*$^{+/-}$; *Kras* cells on macrophage phenotype, *Kras* and *A5*$^{+/-}$;*Kras* cells were seeded in 6-well plates and cultivated for 48 hours. Supernatants were collected and applied on raw macrophages (RAW 264.7; ATCC TIB-71) cultivated in DMEM supplemented with 10% FBS (#10082147; Gibco), 1% Pen-Strep (#1500-063; Gibco), and 1% non-essential amino acids (#11140050; Gibco). Macrophage phenotype was monitored and assessed by microscopy as described previously.[6]

For arginase-1 immunofluorescence macrophages were treated as described here and subsequently stained with anti-arginase 1 (1/500) (610708; BD Transduction Laboratories). Briefly, unspecific binding was blocked with 5% serum at RT and cells were incubated overnight at 4°C with the primary antibody. The following day, secondary antibody anti-mouse in goat Alexa Fluor 488 (1/300) (A-11001l; Invitrogen) was applied for 1 hour at RT. In the end, slides were covered with DAPI-containing mounting medium (H-1200; Vector Laboratories) and analyzed with fluorescence microscopy (Zeiss Axiovert 200M).

Measurement of Ca^{2+} Responses

To measure Ca^{2+} responses, *Kras* and *A5*$^{+/-}$;*Kras* cells were loaded with Fluo-4 by incubation with Fluo-4/AM (5 μM) for 60 minutes at RT (approximately 23°C) in Na-HEPES–based solution (140 mM NaCl, 4.7 mM KCl, 1.13 mM $MgCl_2$, 10 mM HEPES, 10 mM glucose, 1.8 mM $CaCl_2$ [pH 7.4]). After that cells were washed by perfusion (gravity-based perfusion system) with the Na-HEPES–based solution and imaged every 2 seconds over a time period of 800 seconds using a Zeiss 510 confocal made (excitation 488 nm, emission LP505). Heat-inactivated FBS (0.01% or 0.05% diluted in the Na-HEPES–based based solution) was applied when 200 seconds of recording were reached.

Fluorescent responses (F) were normalized to fluorescence F_0 recorded before the addition of FBS (average fluorescence value for measurements recorded during 190–200 seconds time interval). Amplitude of cytosolic Ca^{2+} responses was determined by the equation $(F_{max} - F_0) / F_0 = \Delta F_{max} / F_0$, with F_{max} corresponding to the maximum Fluo-4 fluorescence measured during the 200- to 500-second interval. Amplitude of cytosolic Ca^{2+} responses of each single cell over 5 minutes of FBS application was measured and the amplitudes were then averaged for each genotype ($n > 170$ cells for each genotype).

Cells responding to FBS were defined as cells exciding 20% elevation threshold of normalized fluorescence (F/F_0) in the first 5 minutes of FBS application.

Quantification of Primary Tumor and Metastasis Burden (Intravenous and Orthotopic Transplantation; Also With Liposomal Clodronate Treatments)

For quantification of primary tumor and metastasis burden (in all orthotopic transplantation and tail-vein injection experiments) 2-μm tissue slices were stained with H&E. Per H&E slide multiple pictures at 100× magnification were taken. Area (μm^2) of tumor foci in pancreas and/or lung tissues was calculated and expressed as percents to all tissue area using a proprietary software package (Zeiss AxioVision). Statistical analysis was done in between the genotypes (mean ± SD, Student *t* test).

Quantification of F4/80-Positive and CD206-Positive Macrophages

For quantification of F4/80-positive macrophages in the lungs of tail-vein–injected mice, tissue sections were stained for F4/80 via immunohistochemistry, as described here. Sections were subsequently photographed at 200× magnification. Number of positive cells was determined with Zeiss AxioVision software. Sum from multiple photographs per tissue slide were generated and expressed in relation to the number of high power fields counted. Results were then averaged by genotype.

F4/80-positive and CD206-positive macrophages were also quantified in the original tumors of *Kras* and *A5*$^{+/-}$;*Kras* mice. For this, tissue slides were stained with the respective antibodies and the percent of positive nuclei/all nuclei was determined.

Human Sample Analysis

For ATG5 immunoblotting, a total of 67 human PDAC samples (Supplementary Table 2, cohort 1) collected from the MTBIO tissue bank of the Institute of Pathology at the Technical University Munich, were analyzed as described here. Band density was quantified by using ImageJ software and normalized to β-actin. From these 67 patients, 56 with known survival were grouped into ATG5 low-moderate expression (ATG5/β-actin ratio <0.5) and high expression (ATG5/β-actin ratio ≥ 0.5) and used for Kaplan-Meier survival analysis with GraphPad Prism software (GraphPad).

For ATG5 immunohistochemistry, 2 different cohorts (cohort 2 and cohort 3) were used. Cohort 2 consisted of 26 primary PDACs and their corresponding distant metastases that were resected between 2008 and 2013 at the University Hospital Heidelberg (Supplementary Table 3). The use of this tumor cohort for biomarker analysis has been approved by the ethics commission of the Klinikum Rechts der Isar, Technische Universität München (403/17S). Primary tumor samples were used for ATG5 immunohistochemistry as described below for cohort 3, and 19 of these

were evaluated as described below for cohort 3. In this analysis, 4 patients from cohort 3 also exhibiting distant metastasis were included as well. The percentages of patients with distant metastasis in the low–moderate and in the high ATG5-expressing groups were calculated as described below for cohort 3.

Cohort 3 consisted of a patient cohort with primary resected PDACs. The cohort was investigated previously in several studies[8–10] and included 200 individuals (Supplementary Table 4) that received partial pancreatoduodenectomy for PDAC between 1991 and 2006 at the Charité University Hospital Berlin. The use of this tumor cohort for biomarker analysis has been approved by the Charité University ethics committee (EA1/06/2004).

Tissue microarrays of both immunohistochemistry cohorts were generated as described previously.[8,11] In detail, 3 tumor cores (diameter 1.5 mm) of representative tumor areas selected by a board-certified pathologist on H&E-stained slides were punched out of formalin-fixed, paraffin-embedded tissue blocks and arranged in a newly generated paraffin block. Tissue microarrays were made using a tissue microarrayer (Beecher Instruments, Sun Prairie, WI). Staging of both cohorts followed the World Health Organization recommendations at the time of cohort generation (TNM classification, 7th edition). Clinical and demographic information was obtained from the respective institutional patient databases, by reviewing medical charts and pathological reports. Patient follow-up data were obtained from clinical records and via direct contact with patients and/or their relatives. For Immunohistochemistry, 2-μm sections prepared with a rotary microtome (HM355S; ThermoFisher Scientific) were collected from 134 patients in this cohort (Supplementary Table 3). Immunohistochemistry was performed using a Bond RXm system (Leica, Wetzlar, Germany, all reagents from Leica) with a primary antibody against ATG5 (NB110-53818; Novus Biologicals). Briefly, slides were deparaffinized using deparaffinization solution, pretreated with Epitope retrieval solution 1 (corresponding to citrate buffer pH 6) for 20 minutes. Antibody binding was detected with a polymer refine detection kit without post primary reagent and visualized with DAB as a dark-brown precipitate. Counterstaining was done with hematoxylin. The membranous ATG5 was scored according to the percentage and intensity of positive cells on a 0 to 3+ scale (negative as score 0, faint expression as score 1+, moderate expression as score 2+ and strong expression as score 3+; see Figure 7B for a panel of staining). Kaplan-Meier survival analysis was performed by GraphPad Prism software, with a total of 79 patients from the 134. Patients with no available survival and patients with no death follow-up were removed from the analysis. The 2 groups in the Kaplan-Meier analysis included low–moderate ATG5-expressing patients (with scores 1 and 2) and high ATG5-expressing patients (score 3). Lymph node status and resection status in these patients was expressed as percent of patients referring to the total patients belonging to the 2 groups.

An overview of the 3 different cohorts used can be found in the following table:

Cohort number	Status	Site	Analysis	Patients, n
1	Postoperative	Primary	Western blot	56
2	Palliative/ metastatic	Primary	IHC	23
3	Postoperative	Primary	IHC	79

IHC, immunohistochemistry.

Supplementary References

1. Cui H, Seubert B, Stahl E, et al. Tissue inhibitor of metalloproteinases-1 induces a pro-tumourigenic increase of miR-210 in lung adenocarcinoma cells and their exosomes. Oncogene 2015;34:3640–3650.
2. Bergmeyer HU, Bergneyer J, Grassl M. Methods of Enzymatic Analysis. Weinheim: Verlag Chemie, 1983.
3. Bensadoun A, Weinstein D. Assay of proteins in the presence of interfering materials. Anal Biochem 1976; 70:241–250.
4. Dalton AJ. A chrom-osmium fixative for electron microscopy. Anat Rec 1955;121:281.
5. Diakopoulos KN, Lesina M, Wormann S, et al. Impaired autophagy induces chronic atrophic pancreatitis in mice via sex- and nutrition-dependent processes. Gastroenterology 2015;148:626–638 e17.
6. **McWhorter FY, Wang T**, Nguyen P, et al. Modulation of macrophage phenotype by cell shape. Proc Natl Acad Sci U S A 2013;110:17253–17258.
7. Oelkrug R, Goetze N, Exner C, et al. Brown fat in a protoendothermic mammal fuels eutherian evolution. Nat Commun 2013;4:2140.
8. **Noll EM, Eisen C, Stenzinger A, Espinet E**, et al. CYP3A5 mediates basal and acquired therapy resistance in different subtypes of pancreatic ductal adenocarcinoma. Nat Med 2016;22:278–287.
9. Schlitter AM, Jesinghaus M, Jager C, et al. pT but not pN stage of the 8th TNM classification significantly improves prognostication in pancreatic ductal adenocarcinoma. Eur J Cancer 2017;84:121–129.
10. **Muckenhuber A, Berger AK**, Schlitter AM, et al. Pancreatic ductal adenocarcinoma subtyping using the biomarkers hepatocyte nuclear factor-1A and cytokeratin-81 correlates with outcome and treatment response. Clin Cancer Res 2018;24:351–359.
11. Stenzinger A, Endris V, Klauschen F, et al. High SIRT1 expression is a negative prognosticator in pancreatic ductal adenocarcinoma. BMC Cancer 2013;13:450.

Author names in bold designate shared co-first authorship.

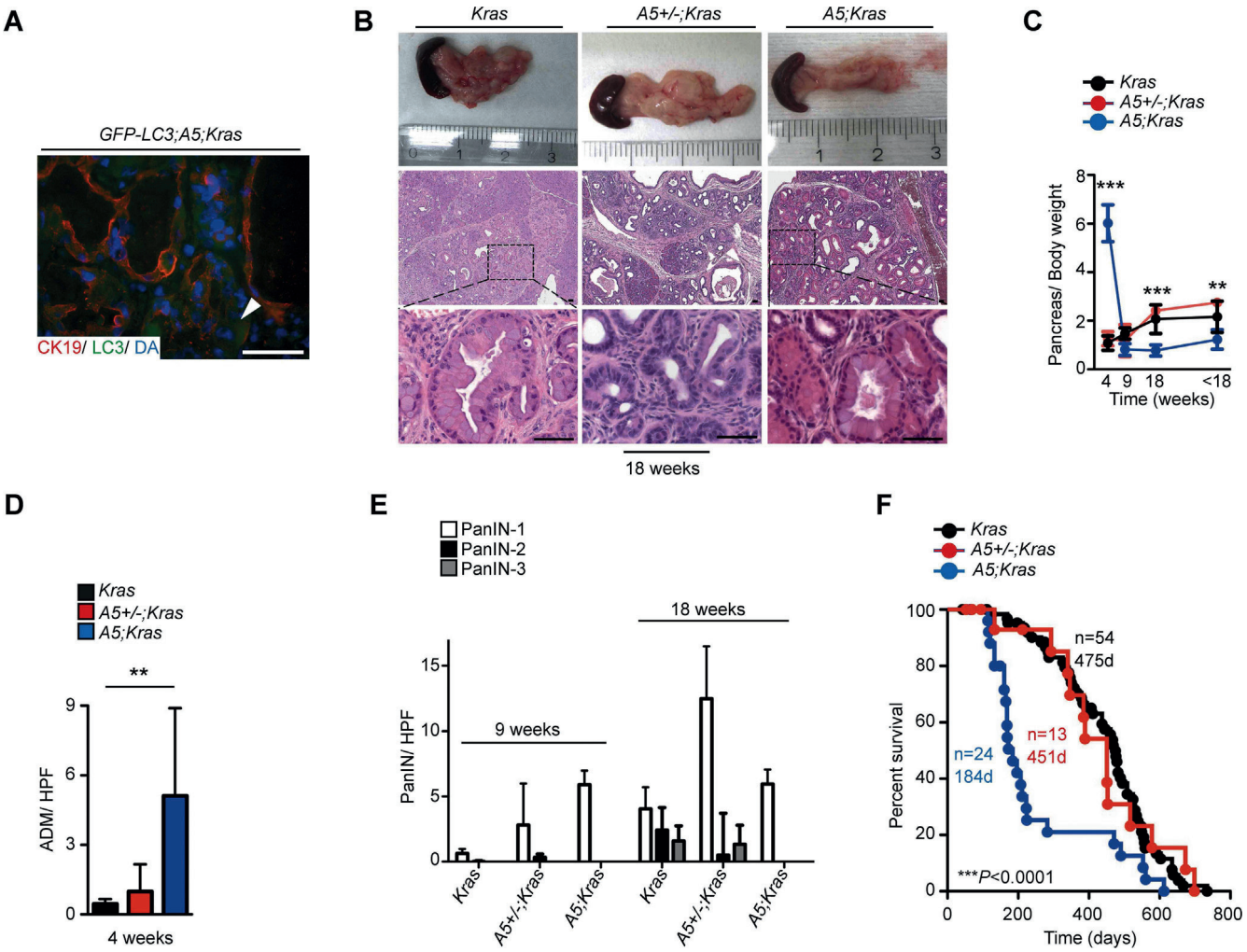

Supplementary Figure 1. Relating to Figure 1. (*A*) GFP-LC3 and CK19 immunofluorescence of *A5;Kras* mice expressing transgenic *GFP-LC3*; *white arrowhead* indicates diffuse GFP-LC3 staining; nuclei are detected with DAPI. (*B*) Macroscopic and microscopic appearance of pancreata from 18-week-old *Atg5*-deficient (*A5;Kras*) and *Atg5* heterozygous mice ($A5^{+/-}$;*Kras*) compared to 18-week-old *Atg5* proficient mice (*Kras*); oncogenic Kras is expressed in all groups of mice. (*C*) Pancreas to body weight ratio in 4-/9-/18-/ and more than 18-week-old *Kras*, $A5^{+/-}$;*Kras*, and *A5;Kras* mice ($n \geq 3$). (*D*) Quantification of ADM per high power field (HPF) in 4-week-old *Kras*, $A5^{+/-}$;*Kras*, *A5;Kras* mice ($n \geq 4$). (*E*) Quantification of PanIN-1/-2/-3 per HPF in 9-/18-week-old *Kras*, $A5^{+/-}$;*Kras*, and *A5;Kras* mice ($n \geq 3$). (*F*) Kaplan-Meier survival curve of *Kras* ($n = 54$), $A5^{+/-}$;*Kras* ($n = 13$), and *A5;Kras* ($n = 24$) mice (median survival 475, 451, and 184 days respectively; ***$P < .0001$ comparing *Kras* and *A5;Kras*). Mean ± SD, *$P < .05$; **$P < .01$; ***$P < .001$. Scale bars = 50 μm.

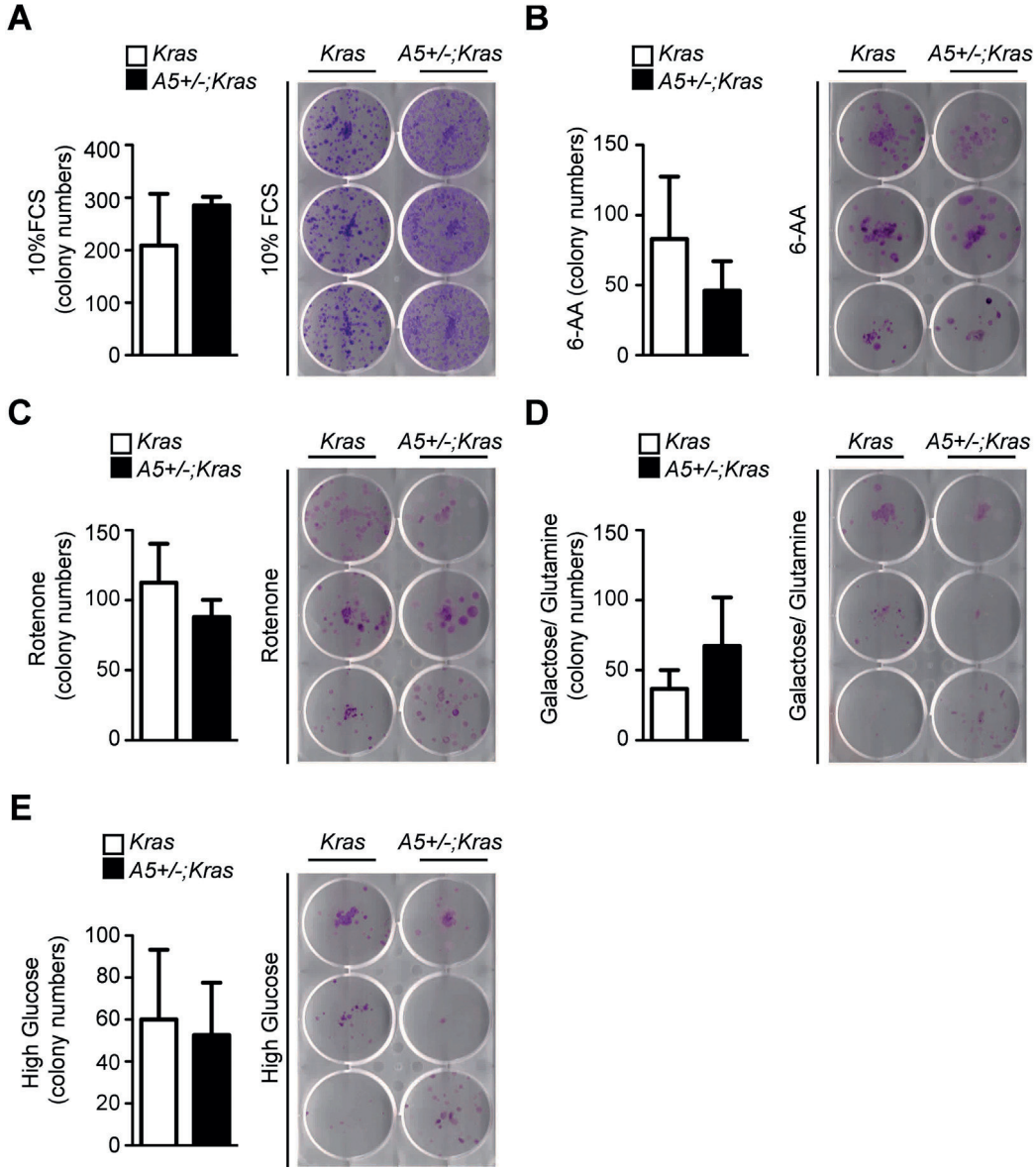

Supplementary Figure 2. Relating to Figure 2. Colony-formation assays in *Kras* and *A5*$^{+/-}$;*Kras* cells after (*A*) 10% FCS cultivation, (*B*) 6-aminonicotinamide (6-AA), (*C*) rotenone, (*D*) galactose/glutamine, and (*E*) high glucose treatment. Graphs are shown on the *left*, representative pictures on the *right*. Mean ± SD (n = 3).

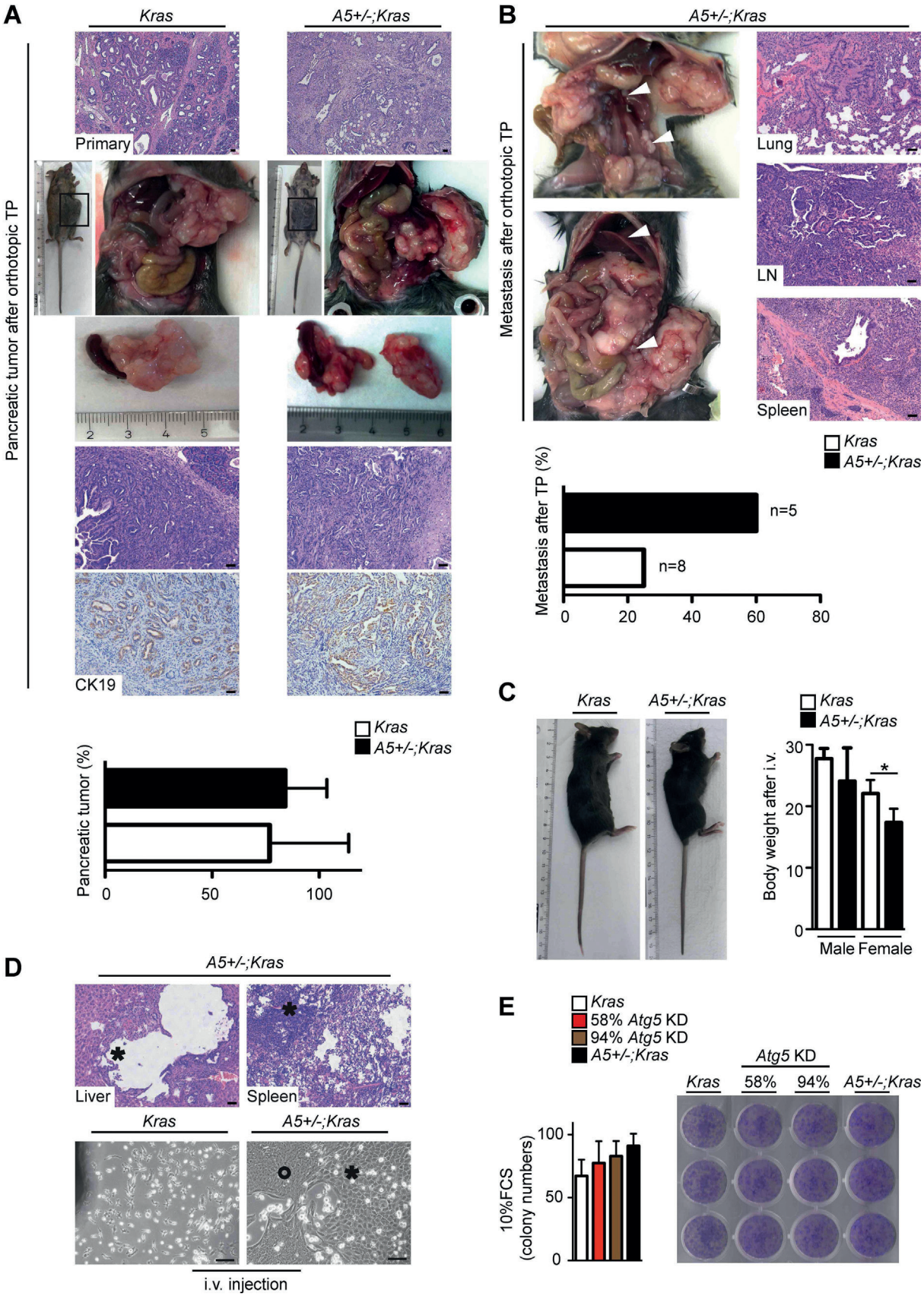
A
Kras
A5+/-;Kras
Primary
Pancreatic tumor after orthotopic TP
CK19
Kras
A5+/-;Kras
Pancreatic tumor (%)
0
50
100
B
A5+/-;Kras
Metastasis after orthotopic TP
Lung
LN
Spleen
Kras
A5+/-;Kras
Metastasis after TP (%)
n=5
n=8
0
20
40
60
80
C
Kras
A5+/-;Kras
Kras
A5+/-;Kras
Body weight after i.v.
30
20
10
0
*
Male Female
D
A5+/-;Kras
Liver
Spleen
Kras
A5+/-;Kras
i.v. injection
E
Kras
58% Atg5 KD
94% Atg5 KD
A5+/-;Kras
Atg5 KD
Kras
58%
94%
A5+/-;Kras
10%FCS
(colony numbers)
100
50
0

Supplementary Figure 3. Relating to Figure 3. (*A*) Representative macroscopic and microscopic pictures of pancreatic tumors from wild-type mice after orthotopic transplantation (TP) of *Kras* and *A5*$^{+/-}$;*Kras* cells; primary tumors are shown on the top, tumors formed after TP in the fourth picture from the top, and CK19 immunohistochemistry on the bottom; quantification of primary pancreatic tumor burden in mice after orthotopic TP of *Kras* and *A5;Kras* cell lines (% area of tumor tissue, n $>$ 3) (*bottom*). (*B*) Representative macroscopic and microscopic pictures of metastasis (lung, lymph node [LN], spleen) after TP of *A5*$^{+/-}$;*Kras* cells into wild-type mice; *white arrowheads* indicate metastasis (*top*); metastasis incidence (%) after TP of *Kras* and *A5*$^{+/-}$;*Kras* cells (n $\geq$ 5) (*bottom*). (*C*) Representative macroscopic picture of wild-type mice after tail vein (intravenous [i.v.]) injection of *Kras* and *A5*$^{+/-}$;*Kras* cells (*left*), and quantification of body weight in male and females (n $\geq$ 3) (right). (*D*) H&E picture of liver and spleen metastasis after i.v. of *A5*$^{+/-}$;*Kras* cells; asterisks indicate metastasis (*top*); representative bright field pictures of *Kras* and *A5*$^{+/-}$;*Kras* cells isolated from the lung of wild-type mice after i.v.; *asterisk* and *circle* indicate 2 different cell populations (*bottom*). (*E*) Colony-formation assay in *Kras*, *A5*$^{+/-}$;*Kras*, and *Kras* cells after 58%, 94% knockdown (KD) of *Atg5* (n $>$ 3) (*left*); representative pictures are shown (*right*); cells were cultivated in medium with 10% FCS. Mean $\pm$ SD, *$P <$ .05. Scale bars $=$ 50 μm.

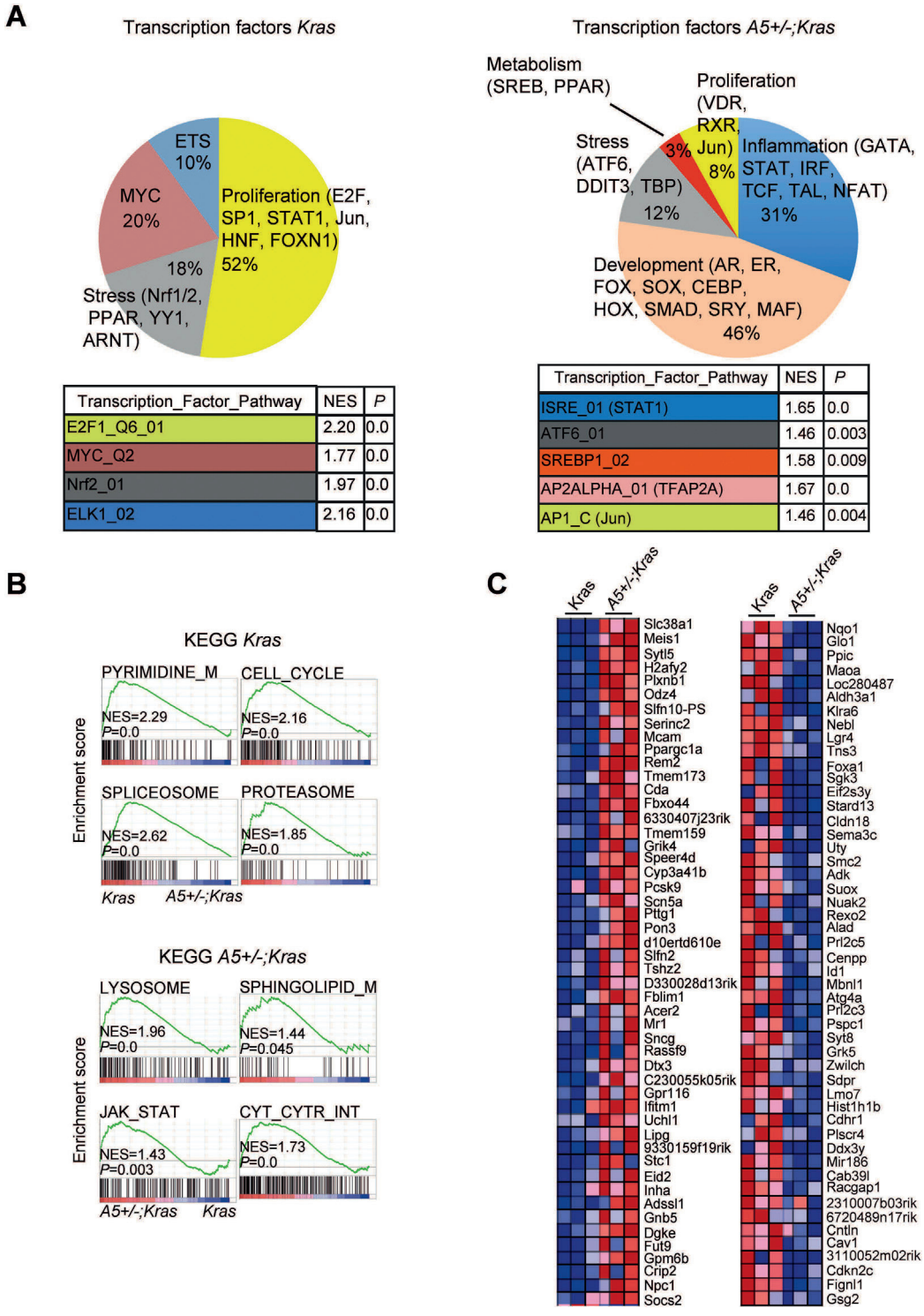

Transcription_Factor_Pathway	NES	P
E2F1_Q6_01	2.20	0.0
MYC_Q2	1.77	0.0
Nrf2_01	1.97	0.0
ELK1_02	2.16	0.0

Transcription_Factor_Pathway	NES	P
ISRE_01 (STAT1)	1.65	0.0
ATF6_01	1.46	0.003
SREBP1_02	1.58	0.009
AP2ALPHA_01 (TFAP2A)	1.67	0.0
AP1_C (Jun)	1.46	0.004

Supplementary Figure 4. Relating to Figure 4. (*A*) Classification of significantly enriched gene sets into categories, based on Transcription Factor Binding Motif database for *Kras* (*left*) and *A5*$^{+/-}$;*Kras* (*right*) cells; *pie charts* show classification and *tables* highlight examples of enriched pathways (NES $\geq$ 1.0, $P < .05$; P value 0.0 indicates $P < .001$). (*B*) GSEA diagrams of significantly enriched Kyoto Encyclopedia of Genes and Genomes pathways found in *Kras* (*top*) and *A5*$^{+/-}$;*Kras* (bottom) cells. (*C*) Heat map of most highly regulated genes identified by GSEA in *Kras* and *A5*$^{+/-}$;*Kras* cells.

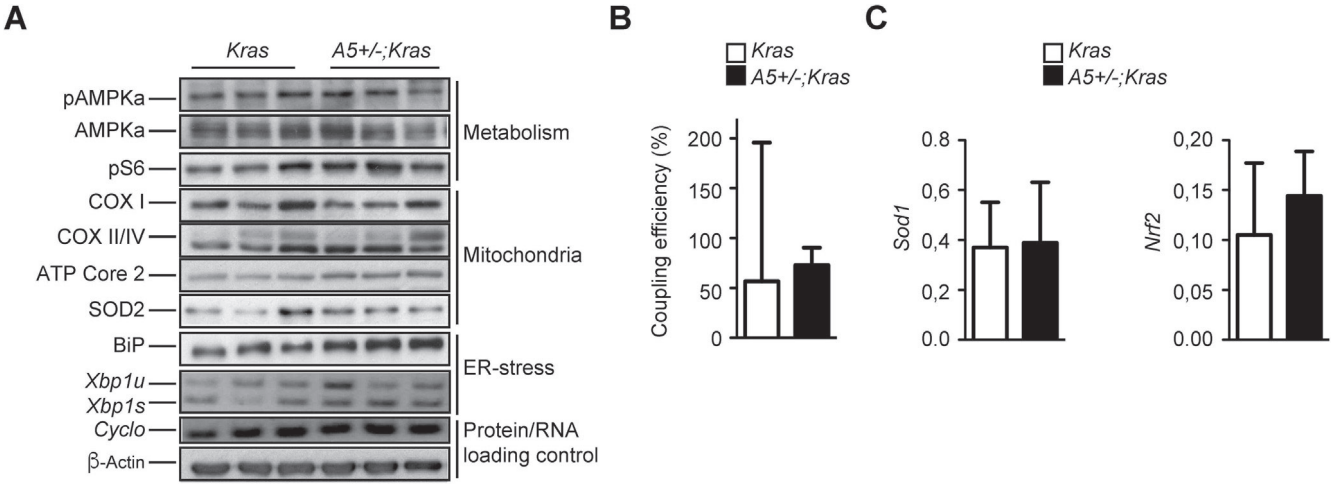

Supplementary Figure 5. Relating to Figure 5. (*A*) Analysis of phospho-AMPKα, AMPKα, phospho-S6, mitochondrial complexes (COX I, COX II/IV, ATP Core 2), SOD2, and BiP in protein lysates and *Xbp1* splicing (*Xbp1u* = unspliced, *Xbp1s* = spliced) in RNA preparations from *Kras* and *A5*$^{+/-}$;*Kras* cells; β-actin and *cyclophilin* were used as loading controls. (*B*) Coupling efficiency (%) of mitochondria in *Kras* and *A5*$^{+/-}$;*Kras* cells as measured by seahorse (n $\geq$ 30). (*C*) Quantitative real-time polymerase chain reaction of *Sod1* and *Nrf2* in mRNA extracts from *Kras* and *A5*$^{+/-}$;*Kras* cells; data are normalized to *cyclophilin* (n = 3). Mean $\pm$ SD.

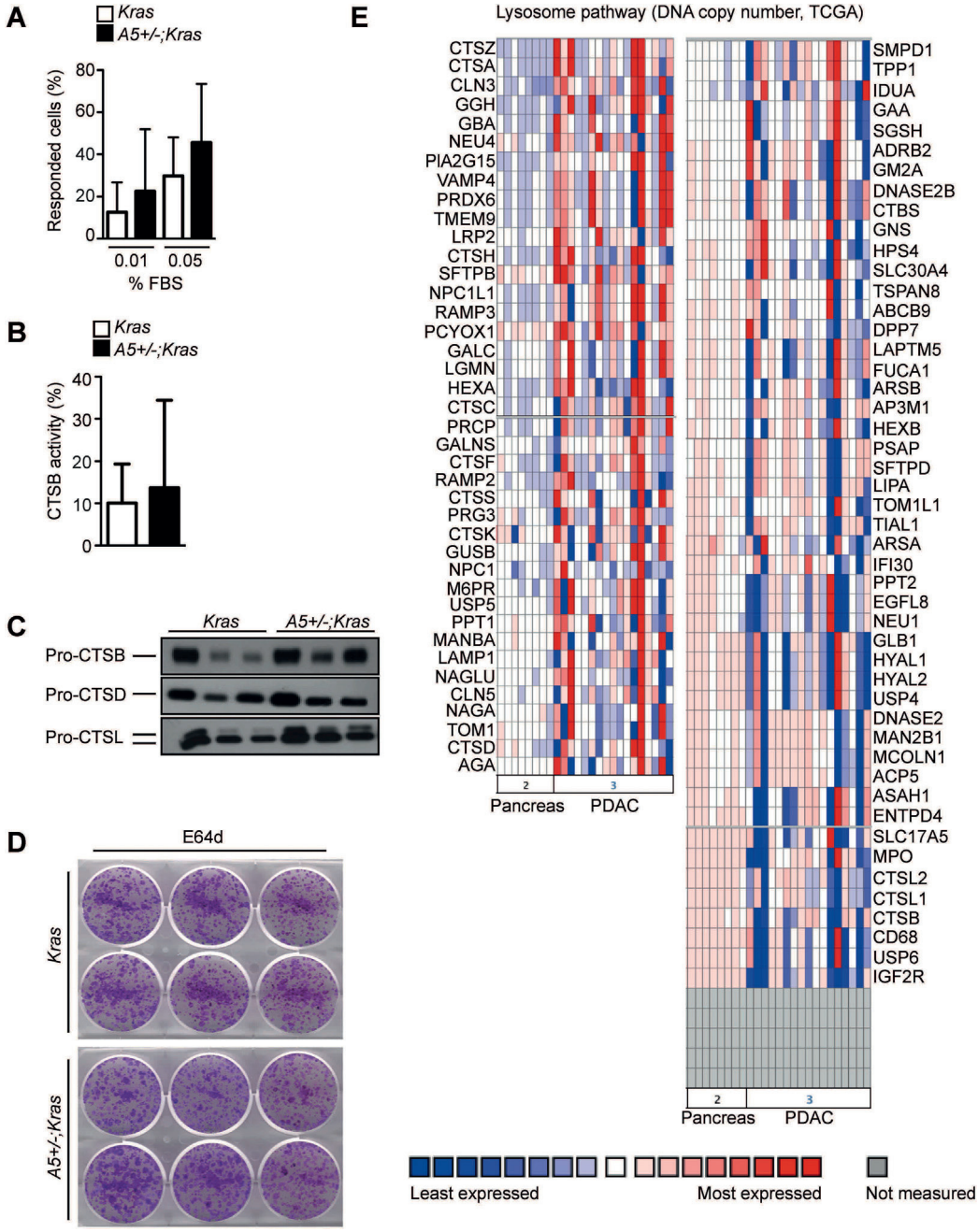

Supplementary Figure 6. Relating to Figure 6. (*A*) Proportions of *Kras* and *A5*$^{+/-}$;*Kras* cells producing Ca^{2+} responses after stimulation with 0.01% or 0.05% FBS (n > 170). (*B*) Cathepsin B (CTSB) extracellular activity (% extracellular activity vs total activity) as measured from supernatants of *Kras* and *A5*$^{+/-}$;*Kras* cells (n = 15). (*C*) Western blot analysis of pro-cathepsin B (Pro-CTSB), pro-cathepsin D (CTSD), and pro-cathepsin L (Pro-CTSL) in supernatants of *Kras* and *A5*$^{+/-}$;*Kras* cells. (*D*) Colony-formation assay in *Kras* and *A5*$^{+/-}$;*Kras* cells after cultivation with E64d. (*E*) Illustration of lysosome-associated DNA copy number gain (*red*) or loss (*blue*) (The Cancer Genome Atlas data) in normal pancreas vs PDAC samples (log2 copy number units). Mean ± SD.

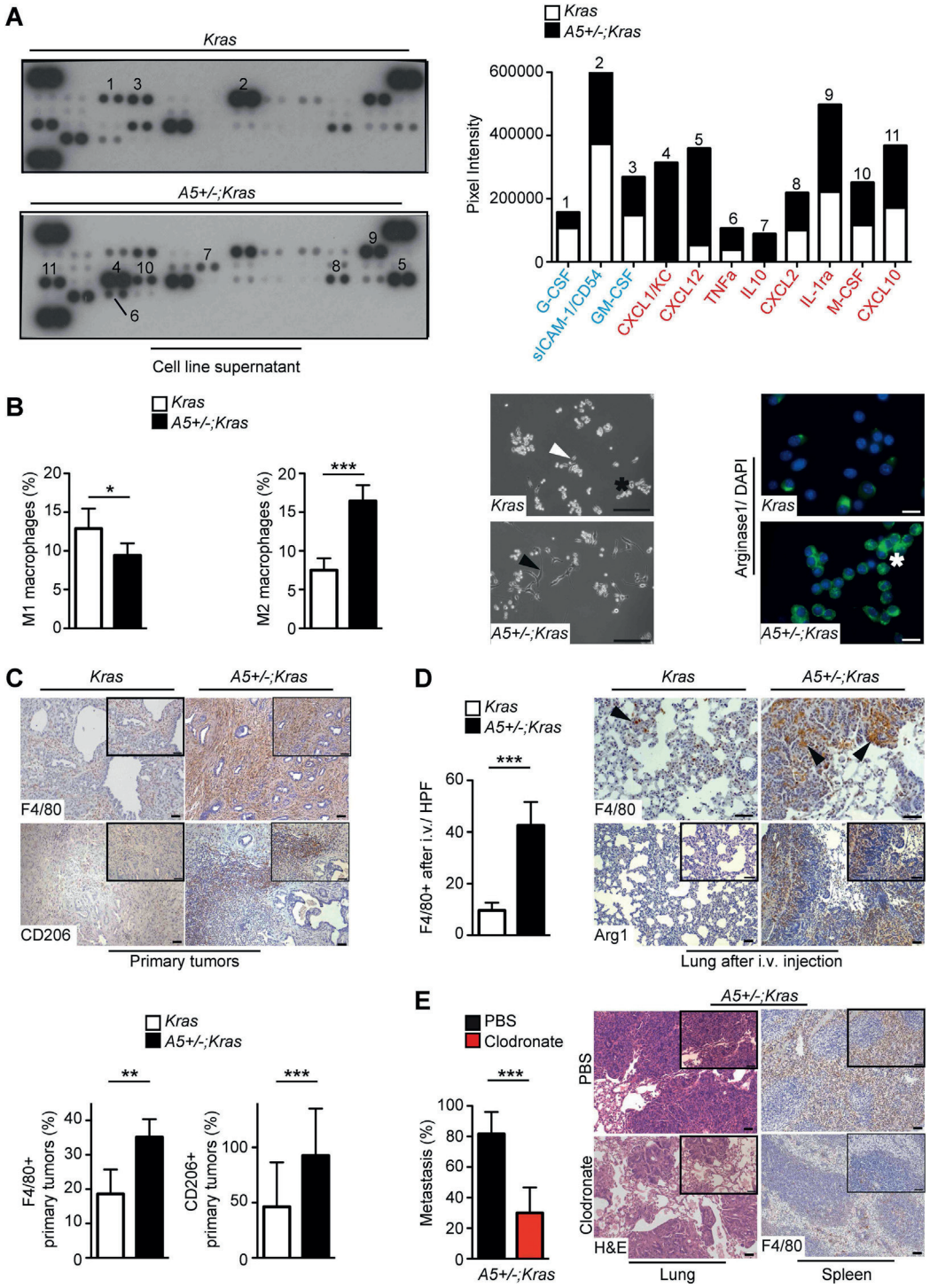

Supplementary Figure 7. Monoallelic loss of *Atg5* induces pro-tumorigenic inflammation. (*A*) Cytokine profile expression shown by immunoblotting of protein lysates from *Kras* and *A5*$^{+/-}$;*Kras* supernatants (*left*); quantification of average pixel intensity between 2 dots corresponding to the same cytokine; numbers above graph correspond to dot-position in plot (n = 1). (*B*) Quantification of M1 and M2 macrophages (% of all macrophages) according to their morphology after stimulation with supernatants from *Kras* and *A5*$^{+/-}$;*Kras* cells (n ≥ 3); representative bright-field pictures are shown indicating morphology of undifferentiated (*asterisk*), M1 (*white arrowhead*), and M2 (*black arrowhead*) macrophages (*left*); arginase-1 immunofluorescence in macrophages after stimulation with supernatants from *Kras* and *A5*$^{+/-}$;*Kras* cells; nuclei are detected with DAPI (*right*). (*C*) Representative immunohistochemistry pictures of F4/80 and CD206 in primary tumors from *Kras* and *A5*$^{+/-}$;*Kras* mice (*top*); quantification of F4/80 and CD206-positive macrophages (% positive nuclei) in *Kras* and *A5*$^{+/-}$;*Kras* primary tumors (n > 3). (*D*) Immunohistochemical quantification of F4/80-positive cells per high power field (HPF) in the lungs of mice after tail vein injection (i.v.) with *Kras* and *A5*$^{+/-}$;*Kras* cells (n = 20) (*left*); representative F4/80 and arginase 1 (Arg1) immunohistochemistry in tissue sections from the lungs of mice after tail vein injection (i.v.) with *Kras* and *A5*$^{+/-}$;*Kras* cells; *black arrowheads* indicate F4/80-positive macrophages (*right*). (*E*) Quantification of lung metastasis (% area) after tail vein injection of *A5*$^{+/-}$;*Kras* cells into PBS or clodronate-treated wild-type mice (n > 3) (*left*); representative H&E pictures of the lung and F4/80 immunohistochemistry pictures of the spleen after the respective treatments. Mean ± SD, **P* < .05; ***P* < .01; ****P* < .001. Scale bars = 50 μm.

Supplementary Table 1. PDAC and Metastasis in *A5*$^{+/-}$;*Kras* Mice

ID	Sex	Age, *d*	PDAC	Histology	Liver	Lung	Diaphragm	Ascites	Others
7135	F	698	Y	D	N	N	N	N	
9138	F	293	Y	D	Y	N	N	N	LN
9137	F	340	Y	D	Y	Y	Y	Y	LN
9384	F	453	Y	D	Y	Y	Y	Y	Spl
2835	M	389	Y	U	N	N	N	N	—
M5683	M	133	N	N	N	N	N	N	—
M5681	M	346	Y	D	Y	Y	Y	Y	LN
M5617	F	385	Y	D	N	Y	N	N	—
M5618	M	451	Y	D	N	Y	Y	N	—
M5551	M	578	Y	D	Y	Y	N	Y	LN
P642	M	673	Y	D	Y	N	Y	Y	LN/Spl/Kd
M6215	F	451	N	N	N	N	N	N	—

NOTE. List of *A5*$^{+/-}$;*Kras* mice that were used for PDAC and metastasis quantification; mouse number (ID), sex, age, PDAC incidence, histology, liver/lung/diaphragm metastasis, ascites incidence, and other abnormalities are presented.
D, ductal; F, female; Kd, kidney infiltration; LN, lymph node infiltration; M, male; Y, yes; N, no; Spl, spleen infiltration; U, undifferentiated.

Supplementary Table 2. Human Pancreatic Cancer Patient Cohort (Postoperative, Cohort 1)

Histology	T	N	M	G	Survival, *mo*	ATG5	Stage
PDAC	4	1	1	3	13	1.035	IV
PDAC	3	1	1	3	12	0.304	IV
PDAC	3	1	1	3	9	0.460	IV
PDAC	3	1	1	3	11	0.030	IV
PDAC	3	1	1	2	7	0.000	IV
PDAC	4	1	0	3	9	0.472	III
PDAC	4	1	0	3	12	0.144	III
PDAC	4	1	x	2	17	0.369	III
PDAC	4	1	x	2	5	0.294	III
PDAC	3	1	0	4	13	0.529	III
PDAC	3	1	0	3	26	0.624	IIB
PDAC	3	1	x	3	10	0.554	IIB
PDAC	3	1	x	3	29	0.685	IIB
PDAC	3	1	x	3	29	0.698	IIB
PDAC	3	1	0	3	7	0.873	IIB
PDAC	3	1	0	3	4	0.769	IIB
PDAC	3	1	0	3	5	0.016	IIB
PDAC	3	1	0	3	3	0.488	IIB
PDAC	3	1	0	3	Lost to FU	0.621	IIB
PDAC	3	1	0	3	10	0.491	IIB
PDAC	3	1	0	3	4	0.526	IIB
PDAC	3	1	0	3	14	1.308	IIB
PDAC	3	1	0	3	9	0.966	IIB
PDAC	3	1	0	3	17	1.005	IIB
PDAC	3	1	0	3	11	0.428	IIB
PDAC	3	1	0	3	Lost to FU	0.838	IIB
PDAC	3	1	0	3	Lost to FU	0.042	IIB
PDAC	3	1	0	2	3	0.380	IIB
PDAC	3	1	0	2	29	0.382	IIB
PDAC	3	1	0	2	25	0.350	IIB
PDAC	3	1	0	2	34	0.649	IIB
PDAC	3	1	0	2	46	0.548	IIB
PDAC	3	1	0	2	31	0.758	IIB
PDAC	3	1	0	2	Lost to FU	0.167	IIB
PDAC	3	1	0	2	10	0.115	IIB
PDAC	3	1	0	2	40	0.157	IIB
PDAC	3	1	0	2	3	0.964	IIB
PDAC	3	1	x	2	13	0.258	IIB
PDAC	3	1	x	2	10	0.255	IIB
PDAC	3	1	0	1	24	0.777	IIB
PDAC	3	1	0	1	56	0.210	IIB
PDAC	3	1	X		14	0.535	IIB
PDAC	2	1	0	1	23	0.101	IIB
PDAC	1	1	0	3	60	0.047	IIB
PDAC	3	0	0	3	4	0.805	IIA
PDAC	3	0	0	3	31	0.461	IIA
PDAC	3	0	x	3	18	0.486	IIA
PDAC	3	0	x	3	8	0.539	IIA
PDAC	3	0	0	3	76	2.504	IIA
PDAC	3	0	0	3	10	0.653	IIA
PDAC	3	0	0	3	Lost to FU	0.502	IIA
PDAC	3	0	0	2	32	0.911	IIA
PDAC	3	0	x	2	21	0.303	IIA
PDAC	3	0	0	2	10	0.052	IIA
PDAC	3	0	x	2	39	0.388	IIA
PDAC	3	0	0	2	36	0.298	IIA
PDAC	3	0	0	2	30	1.674	IIA
PDAC	3	0	0	2	18	0.572	IIA
PDAC	3	0	0	2	Lost to FU	0.405	IIA
PDAC	3	0	x	1	23	0.747	IIA
PDAC	3	0	x	1	34	0.181	IIA
PDAC	2	0	0	3	Lost to FU	0.533	IB
PDAC	2	0	0	2	23	0.098	IB
PDAC	—	—	—	—	—	0.848	—
PDAC	—	—	—	—	—	0.006	—
PDAC	—	—	—	—	—	0.312	—
PDAC	—	—	—	—	—	0.493	—

NOTE. List of the analyzed human pancreatic cancer samples for ATG5-Western blot (n = 67), collected from the MTBIO tissue bank of the Institute of Pathology at the Technical University Munich. Histology (PDAC), extent of primary tumor (T), lymph node infiltration (N), metastasis (M), tumor differentiation grade (G), survival, ATG5 protein expression normalized to β-actin and quantified by ImageJ software (ATG5), and tumor stage are shown. Samples lost to FU and unknown survival time were not used in the analysis. The last 4 samples did not have patient data and were excluded from the study.
FU, follow-up.

Supplementary Table 3. Human Pancreatic Cancer Patient Cohort (Palliative/Metastatic, Cohort 2)

Histology	ATG5	M1
PDAC	2.3	HEP, PER
PDAC	3	HEP
PDAC	—	HEP
PDAC	2.8	HEP
PDAC	1	HEP
PDAC	—	HEP, PER, ADR
PDAC	—	HEP
PDAC	2.9	HEP
PDAC	—	HEP
PDAC	2	PER
PDAC	2	PER
PDAC	2.8	PER
PDAC	3	HEP
PDAC	2.1	HEP
PDAC	1.8	HEP
PDAC	2.5	HEP
PDAC	2	SKI
PDAC	2.9	HEP
PDAC	1.9	HEP
PDAC	—	HEP
PDAC	—	HEP
PDAC	3	HEP
PDAC	2.1	HEP
PDAC		SKI
PDAC	3	HEP
PDAC	3	HEP

NOTE. List of the analyzed human pancreatic cancer samples for ATG5-immunohistochemistry (n = 26). Each row represents 1 individual diagnosed with PDAC and exhibiting distant metastasis (M1). Patients were resected between 2008 and 2013 at the University Hospital Heidelberg. ATG5 protein was detected by immunohistochemistry; membranous ATG5 was scored according to the percentage and intensity of positive cells on a 0 to 3+ scale (negative as score 0, faint expression as score 1+, moderate expression as score 2+ and strong expression as score 3+). The sum score is provided in the second column. Patients without ATG5 score were excluded from the analysis.
ADR, adrenal; HEP, hepatic; PER, peritoneal; SKI, skin.

Supplementary Table 4. Human Pancreatic Cancer Patient Cohort (Postoperative, Cohort 3)

ATG5	Death	Survival, *d*	pN	pM	pT	Sex	Age, *y*	Stage	R
2.7	1	431	0	0	2	F	74	I	0
2	1	898	1	0	2	F	75	IIB	0
1	0	—	0	0	3	F	64	IIA	0
2.7	0	5748	1	0	3	F	56	IIB	1
3	1	278	1	0	3	M	47	IIB	0
1	1	780	1	0	2	M	67	IIB	0
3	1	407	1	0	3	F	62	IIB	0
2.4	1	452	1	1	3	M	31	IV	1
3	1	1166	1	0	2	F	63	IIB	0
2.5	1	215	0	0	2	F	58	I	0
3	1	629	1	0	2	M	53	IIB	1
2.8	1	329	1	0	3	F	62	IIB	0
2.8	1	46	0	0	2	F	61	I	0
2.9	1	406	1	0	3	M	69	IIB	0
2.1	1	236	0	0	2	F	70	I	1
2.6	0	2459	0	0	2	F	71	I	—
2.6	—	—	1	0	2	M	64	IIB	0
2.2	1	862	1	0	2	F	64	IIB	0
2.3	1	448	1	0	2	M	71	IIB	0
2.5	0	2302	1	0	2	M	64	IIB	—
3	1	287	1	0	3	F	47	IIB	1
3	0	305	1	0	3	M	62	IIB	—
1.3	1	945	1	0	3	F	75	IIB	0
2.2	1	832	1	0	3	F	62	IIB	0
2.9	1	685	0	0	3	F	59	IIA	—
1.2	—	—	1	0	3	M	50	IIB	0
2	1	—	1	0	2	M	60	IIB	—
1.3	0	2049	0	0	3	M	63	IIA	0
2.2	—	—	1	0	3	M	66	IIB	0
2.9	1	1045	1	0	3	F	49	IIB	0
2.9	0	2104	0	0	2	F	64	I	0
3	1	1743	1	0	2	M	71	IIB	0
2.2	—	—	1	0	3	F	59	IIB	0
1.2	0	—	0	0	3	M	59	IIA	0
2.9	1	744	1	0	3	F	73	IIB	1
3	1	740	1	0	3	M	50	IIB	0
3	1	1258	0	0	3	F	62	IIA	0
2.5	1	809	1	0	3	F	61	IIB	0
3	1	167	1	0	3	M	66	IIB	0
2	1	348	1	0	3	F	59	IIB	1
2.2	1	911	1	0	3	M	64	IIB	0
2.5	1	779	0	0	3	F	69	IIA	0
2.9	1	471	0	0	2	F	76	I	0
2.3	1	125	1	0	3	M	63	IIB	0
2.2	0	1427	0	0	3	M	65	IIA	1
3	1	395	0	0	3	M	60	IIA	0
1.2	1	—	1	0	2	F	77	IIB	—
3	1	—	1	0	3	M	38	IIB	—
2	1	—	1	0	3	F	76	IIB	1
3	0	—	1	0	3	M	63	IIB	1
3	—	—	1	0	3	F	65	IIB	0
2.6	1	432	0	0	2	F	69	I	0
2.7	1	805	1	0	3	M	—	IIB	—
2.2	0	2644	0	0	3	F	62	IIA	—
3	1	496	1	0	3	F	79	IIB	—
2.8	1	198	1	0	3	M	49	IIB	0
3	1	—	1	0	3	M	70	IIB	—
3	1	404	1	0	3	M	73	IIB	—
2.8	1	—	0	0	3	F	77	IIA	—
2	1	902	1	0	3	F	73	IIB	—
2.8	1	112	1	1	3	M	55	IV	0
3	1	715	1	0	3	M	64	IIB	0
3	1	209	1	0	3	F	51	IIB	0
2.8	1	260	1	0	3	M	51	IIB	0
3	1	353	1	0	3	F	67	IIB	0
3	0	—	1	0	3	M	48	IIB	—
1.8	1	611	1	0	3	F	78	IIB	0
2.9	1	98	1	0	3	F	63	IIB	0
2.7	1	28	0	0	3	F	74	IIA	1
2.7	0	2645	1	0	2	M	53	IIB	0
2	0	—	0	0	2	F	59	I	0
3	0	2609	1	0	3	M	69	IIB	0
2.8	1	—	1	0	3	M	72	IIB	0
2.8	1	255	1	0	3	M	74	IIB	0
3	1	—	0	0	3	M	78	IIA	0
2.9	1	184	0	0	4	F	72	III	0
3	1	291	1	0	3	F	69	IIB	0
3	0	1273	0	0	3	M	56	IIA	0
3	1	1183	0	0	3	M	50	IIA	0
2.6	1	96	1	0	3	F	75	IIB	1
3	1	—	1	0	3	M	57	IIB	0
0.7	1	—	1	0	4	F	70	III	0
3	1	1064	1	0	3	M	72	IIB	1
2	1	288	1	0	3	F	61	IIB	0
2.8	1	192	1	0	4	M	57	III	1
2.8	1	370	1	0	3	F	74	IIB	0
2.9	1	1186	1	0	3	F	72	IIB	0
3	1	394	0	0	3	M	69	IIA	1
3	0	17	1	0	3	F	68	IIB	1
1	1	369	0	0	3	F	79	IIA	1
2.8	—	—	1	0	3	F	62	IIB	1
2.8	0	7	1	0	3	M	60	IIB	1
3	1	59	1	0	3	F	61	IIB	1
3	1	289	1	0	4	M	60	III	1
3	—	—	1	0	3	M	70	IIB	0
2.2	—	—	0	0	1	M	66	I	0
3	1	222	1	0	3	M	61	IIB	1
2.05	0	415	0	0	3	F	81	IIA	0
3	1	653	1	1	3	F	46	IV	0
2	1	12	1	0	4	M	69	III	1
3	—	—	1	0	3	M	59	IIB	1
2.8	0	12	1	0	3	M	67	IIB	0
2.8	1	205	1	0	3	M	69	IIB	1
3	—	—	1	0	4	M	73	III	0
2.5	1	615	1	0	3	M	54	IIB	1
2.3	1	263	1	0	3	M	67	IIB	1
2.7	—	—	0	0	3	M	65	IIA	0
2	1	915	0	0	3	M	68	IIA	0
3	—	—	1	0	3	M	75	IIB	0
2	1	316	1	0	3	M	64	IIB	0
3	1		1	0	2	M	73	IIB	0
1.8	0	1079	1	0	3	F	59	IIB	0
3	1	455	1	0	3	M	56	IIB	0
2.7	0	210	1	0	3	M	43	IIB	1
1.2	1	603	1	0	3	F	58	IIB	1
2.8	0	865	1	0	3	F	57	IIB	0
2.3	—	—	1	0	3	M	77	IIB	1
3	0	311	1	0	3	M	61	IIB	0
2.3	1	199	1	1	3	M	41	IV	0

Supplementary Table 4. Continued

ATG5	Death	Survival, *d*	pN	pM	pT	Sex	Age, *y*	Stage	R
2.9	0	866	0	0	3	M	75	IIA	0
2.2	1	582	1	0	3	M	75	IIB	0
2.1	—	—	1	0	3	F	75	IIB	1
2.3	1	265	1	0	4	M	74	III	1
2	0	696	1	0	3	F	66	IIB	0
2.2	1	185	1	0	3	M	51	IIB	1
2.1	1	268	1	0	3	F	81	IIB	0
2.9	0	586	0	0	3	M	69	IIA	0
1.5	0	5	0	0	3	F	69	IIA	0
2.2	1	1104	1	0	3	F	68	IIB	0
2.6	1	324	1	0	3	F	68	IIB	1
2.2	1	380	1	0	3	M	58	IIB	0
2.3	1	249	1	0	3	F	63	IIB	0
2.3	1	166	1	0	3	M	72	IIB	0
2.8	1	216	1	0	3	M	55	IIB	1

NOTE. List of the analyzed human pancreatic cancer samples for ATG5-immunohistochemistry (n = 134). Each row represents 1 individual diagnosed with PDAC at the Charité University Hospital Berlin. Event of death (1 = yes, 0 = no), survival, lymph node status (pN), metastasis status (pM), tumor stage (pT), patient characteristics (sex, age), Union for International Cancer Control tumor staging, and resection margin (R) are shown. ATG5 protein was detected by immunohistochemistry; membranous ATG5 was scored according to the percentage and intensity of positive cells on a 0 to 3+ scale (negative as score 0, faint expression as score 1+, moderate expression as score 2+ and strong expression as score 3+). The sum score is provided in the first column. Patients without death event and no registered survival were removed from the analysis.
F, female; M, male.

Cell Reports
Medicine

Article

Extensive preclinical validation of combined RMC-4550 and LY3214996 supports clinical investigation for KRAS mutant pancreatic cancer

Graphical abstract

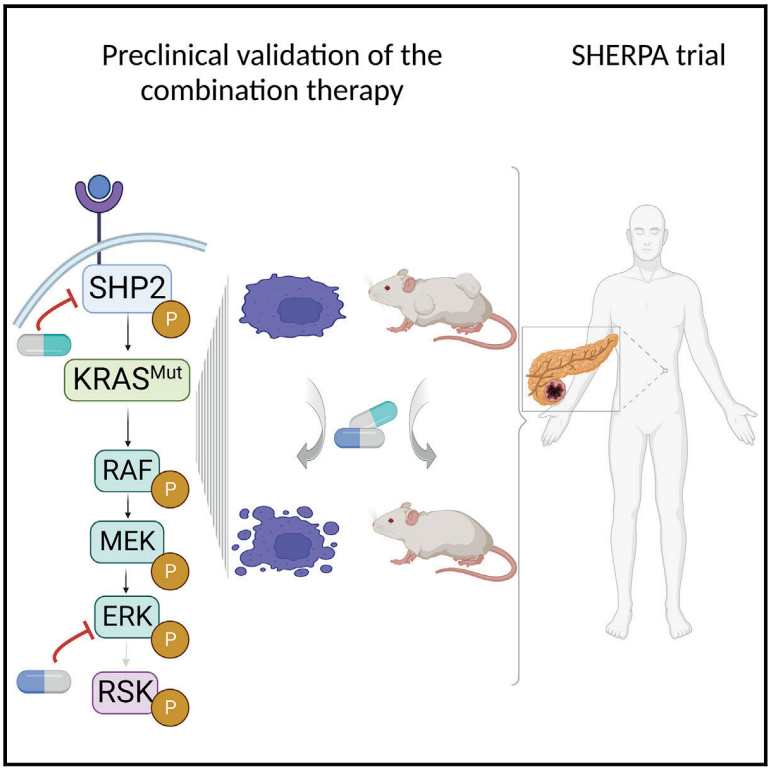

Authors

Katrin J. Frank, Antonio Mulero-Sánchez, Alexandra Berninger, ..., Hana Algül, Marina Lesina, Sara Mainardi

Correspondence

s.mainardi@nki.nl

In brief

KRAS mutant pancreatic tumors have poor prognosis and few therapeutic options. Here, Frank et al. show that the combination of RMC4550 (SHP2 inhibitor) and LY3214996 (ERK inhibitor) effectively impairs tumor growth and induces tumor regression in multiple *in vivo* models of PDAC.

Highlights

- SHP2 and ERK co-inhibition is synergistic and triggers apoptosis in PDAC *in vitro*
- The combination is tolerated and promotes tumor regression in multiple *in vivo* models
- Non-invasive PET-CT scans can monitor early response to the therapy
- The SHERPA phase 1a/1b trial will investigate the combination clinically

Frank et al., 2022, Cell Reports Medicine *3*, 100815
November 15, 2022
https://doi.org/10.1016/j.xcrm.2022.100815

CellPress

Cell Reports Medicine

CellPress
OPEN ACCESS

Article

Extensive preclinical validation of combined RMC-4550 and LY3214996 supports clinical investigation for KRAS mutant pancreatic cancer

Katrin J. Frank,[1,10] Antonio Mulero-Sánchez,[2,10] Alexandra Berninger,[1,10] Laura Ruiz-Cañas,[3,4] Astrid Bosma,[2] Kıvanç Görgülü,[1] Nan Wu,[1] Kalliope N. Diakopoulos,[1] Ezgi Kaya-Aksoy,[1] Dietrich A. Ruess,[5] Derya Kabacaoğlu,[1] Fränze Schmidt,[1] Larissa Kohlmann,[1] Olaf van Tellingen,[6] Bram Thijssen,[2] Marieke van de Ven,[7] Natalie Proost,[7] Susanne Kossatz,[8,9] Wolfgang A. Weber,[8] Bruno Sainz, Jr.,[3,4] Rene Bernards,[2] Hana Algül,[1] Marina Lesina,[1,10] and Sara Mainardi[2,10,11,*]

[1]Comprehensive Cancer Center Munich at Klinikum rechts der Isar, Technische Universität München, 81675 Munich, Germany
[2]Division of Molecular Carcinogenesis, Oncode Institute, The Netherlands Cancer Institute, Plesmanlaan 121, 1066CX Amsterdam, the Netherlands
[3]Department of Biochemistry, Universidad Autónoma de Madrid (UAM) and Instituto de Investigaciones Biomédicas "Alberto Sols" (IIBM), CSIC-UAM, 28029 Madrid, Spain
[4]Chronic Diseases and Cancer, Area 3, Instituto Ramón y Cajal de Investigación Sanitaria (IRYCIS), 28034 Madrid, Spain
[5]Department of General and Visceral Surgery, Center of Surgery, Medical Center-University of Freiburg, 79106 Freiburg, Germany
[6]Division of Pharmacology, The Netherlands Cancer Institute, 1066CX Amsterdam, the Netherlands
[7]Mouse Clinic for Cancer and Aging Research, Preclinical Intervention Unit, The Netherlands Cancer Institute, 1066CX Amsterdam, the Netherlands
[8]Department of Nuclear Medicine at Klinikum Rechts der Isar and Central Institute for Translational Cancer Research (TranslaTUM), Technische Universität München, 81675 Munich, Germany
[9]Department of Chemistry, Technische Universität München, 85748 Munich, Germany
[10]These authors contributed equally
[11]Lead contact
*Correspondence: s.mainardi@nki.nl
https://doi.org/10.1016/j.xcrm.2022.100815

SUMMARY

Over 90% of pancreatic cancers present mutations in KRAS, one of the most common oncogenic drivers overall. Currently, most KRAS mutant isoforms cannot be targeted directly. Moreover, targeting single RAS downstream effectors induces adaptive resistance mechanisms. We report here on the combined inhibition of SHP2, upstream of KRAS, using the allosteric inhibitor RMC-4550 and of ERK, downstream of KRAS, using LY3214996. This combination shows synergistic anti-cancer activity *in vitro*, superior disruption of the MAPK pathway, and increased apoptosis induction compared with single-agent treatments. *In vivo*, we demonstrate good tolerability and efficacy of the combination, with significant tumor regression in multiple pancreatic ductal adenocarcinoma (PDAC) mouse models. Finally, we show evidence that ^{18}F-fluorodeoxyglucose (FDG) positron emission tomography (PET) can be used to assess early drug responses in animal models. Based on these results, we will investigate this drug combination in the SHP2 and ERK inhibition in pancreatic cancer (SHERPA; ClinicalTrials.gov: NCT04916236) clinical trial, enrolling patients with *KRAS*-mutant PDAC.

INTRODUCTION

Pancreatic cancer is the third leading cause of cancer-related deaths in Western countries and the seventh worldwide and is predicted to become the second most common cause of cancer mortality in the US in the next 20 to 30 years.[1–3] The 5-year survival rate of patients suffering from pancreatic ductal adenocarcinoma (PDAC) is only 10% as diagnosis is often made when disease is already advanced, and therapeutic options are limited. Over the last years, the genomic landscape of PDAC has emerged, and recurrent mutations have been identified.[4,5] Recently, the discovery of a subset of patients with PDAC bearing germline alterations in *BRCA1/2* and *PALB2*, which cause homologous repair deficiency (HRD), has led to the approval of PARP inhibitors as the first targeted therapy for HRD-pancreatic cancer.[6] However, *BRCA1/2* and *PALB2* mutants are present in only 5%–9% of patients with PDAC[7] compared with over 90% of patients that carry tumors bearing *KRAS* mutations, and, to date, no other non-cytotoxic, targeted therapies have been approved.

It has been widely demonstrated that *KRAS* mutations constitute an early initiating event in the pancreatic tumorigenic

process[8] and that pancreatic adenocarcinomas retain a high dependency on RAS signaling,[9,10] thus making KRAS the ideal therapeutic target for pancreatic cancer. However, for more than three decades, research on the direct targeting of RAS has proven to be a very challenging task. Only recently have $KRAS^{G12C}$-specific inhibitors entered clinical development,[11–13] and some, like sotorasib and adagrasib, have shown initial clinical responses,[14–16] leading to sotorasib being the first drug approved by the US Food and Drug Administration (FDA) for the treatment of $KRAS^{G12C}$-driven non-small cell lung cancer.

Unfortunately, the G12C variant represents only 1% of *KRAS* mutations in pancreatic cancer, with the most frequent amino acid substitutions being G12D (41%), G12V (34%), and G12R (16%).[17] For those most common mutations, targeted inhibitors have not yet been developed; therefore, most translational studies have been aimed at blocking downstream RAS effectors mainly in the MAPK or PI3K-AKT pathways.[18–21] Unfortunately, attempts to target RAS downstream effectors have been hampered by compensatory feedback mechanisms, often involving reactivation of receptor tyrosine kinases.[22] This notion, together with advances in KRAS biophysics and structural biology studies, undermined the old paradigm of mutant KRAS being constitutively active and made it clear that it is possible to reduce mutant RAS activation by combining inhibition of upstream and downstream nodes in the RAS-MAPK pathway. In particular, the ubiquitously expressed non-receptor protein tyrosine phosphatase SHP2, encoded by the *PTPN11* gene, has been identified as a useful upstream target[23–25] as it is involved in signal transduction downstream of multiple growth factor, cytokine, and integrin receptors.[26] Potent and specific allosteric inhibitors of SHP2 have recently been developed and have entered clinical trials,[27] holding great promise for receptor tyrosine kinase (RTK)-driven tumors. Nonetheless, so far, the question regarding the most beneficial drug combination for KRAS-driven pancreatic cancer remains.

MEK inhibitors have been tested extensively in *KRAS*-mutant PDAC, as well as other solid tumors, with poor results.[28–30] This is primarily attributable to their highly toxic profile and adverse side effects as well as the above-mentioned feedback reactivation of the MAPK pathway.[22,31] In contrast, inhibitors of ERK, directly downstream of MEK, have only recently been introduced into clinical studies[32] and seem auspicious with regard to their toxicity profile. In the present study, we explore the tolerability and efficacy of combining the allosteric SHP2 inhibitor RMC-4550 with the ATP-competitive, selective ERK inhibitor LY3214996 in multiple *in vitro* and *in vivo* models of murine and human PDAC. Based on the data reported here, we developed the phase 1a/1b SHP2 and ERK inhibition in pancreatic cancer (SHERPA) clinical trial (ClinicalTrials.gov: NCT04916236).

RESULTS

Combinatorial effect *in vitro*

In a previous study, we showed promising *in vitro* and *in vivo* results to support combined SHP2 and MEK inhibition for the treatment of pancreatic cancer.[23,24] While the reported combinatorial strategy is sound, the frequently observed side effects and the common occurrence of resistance associated with MEK inhibitors like trametinib[31,33,34] led us to search for possible alternatives. Since reactivation of ERK is a major mechanism hampering MEK inhibitor (MEKi) efficacy,[22,33,35,36] we hypothesized that direct ERK inhibition might be a worthwhile strategy. The recently developed ERK inhibitor LY3214996[37] was shown to be a selective, potent, and reversible ATP-competitive inhibitor of ERK1/2 activity in KRAS- and BRAF-mutant cell lines. In parallel, RMC-4550 a selective allosteric SHP2 inhibitor was developed with a mode of action similar to the Novartis' SHP099 but with slightly higher potency.[38]

Since LY3214996 and RMC-4550 have not yet been studied in combination, we first investigated the effects of combined treatment on MAPK activity, proliferation, and apoptosis *in vitro*. First, we analyzed the inhibitors' capacity to block MAPK pathway activity. As SHP2 inhibitors alone have already proven not to hamper MAPK pathway activation in *KRAS*-mutant tumors under standard *in vitro* culture conditions,[23] we decided to treat murine and human *KRAS*-mutant PDAC cell lines with either LY3214996 alone or LY3214996 + RMC-4550 for 6, 72, and 144 h. Western blot analysis was performed to examine protein expression levels of phosphorylated ribosomal S6 kinase 1 (pRSK-1), a direct downstream target of ERK.[39] Compared with LY3214996 monotherapy, the combined RMC-4550 treatment inhibited MAPK pathway activity more effectively at all time points analyzed (Figure 1A), and, importantly, it was able to prevent the feedback reactivation of the route, which occurs at late time points when inhibiting ERK alone. After 6 days (144 h), a 100%, 80%, and 70% reduction in pRSK-1 levels compared with the control could still be observed for LY3214996 + RMC-4550-treated murine *Kras;Trp53*$^{-/-}$ (KCP) K2101 as well as human MiaPaCa-2 and Panc10.05 cells, respectively, compared with only 20%, 40%, and 30% reduction in the same cells with LY3214996 monotherapy. Of note, and as expected, the combined LY3214996 + RMC-4550 treatment also proved superior to the RMC-4550 monotherapy by preventing reactivation of the pathway in MiaPaCa-2 cells, as shown by pRSK-1 levels in Figure S1A.

To better understand the potential clinical benefit of the combination therapy, we further tested the effect of LY3214996 + RMC-4550 treatment on cell proliferation (Figures 1B and S1B) and on the induction of cell death (Figure 1C). For the former, we performed 6-day colony-formation assays using two murine KCP and 5 different human PDAC cell lines, harboring $KRAS^{G12C}$, $KRAS^{G12V}$, or $KRAS^{G12D}$ mutations (Figures 1B and S1B). The 96-well format allowed us to test a range of inhibitor concentrations both as monotherapy as well as in combination. Synergism (i.e., a combination index [CI] score below 0.75, indicated in shades of green in Figures 1B and S1B) was observed in at least 70% of all inhibitor combinations tested in all 7 cell lines, regardless of the type of KRAS mutation present. These data indicate that LY3214996 and RMC-4550 can synergistically inhibit PDAC cell growth *in vitro* at micromolar concentrations.

To study the effect of the drug combination on apoptosis, KCP_K2101, MiaPaCa-2, and Panc10.05 cells were treated with either LY3214996 or RMC-4550 alone at roughly half-maximal inhibitory concentration (IC50) concentrations or with the combination of the two inhibitors for up to 76 h, and the rate of apoptosis was measured by tracking GFP-labeled cleaved caspase 3 over time (Figure 1C, top panels). In murine KCP_K2101 cells,

CellPress
OPEN ACCESS

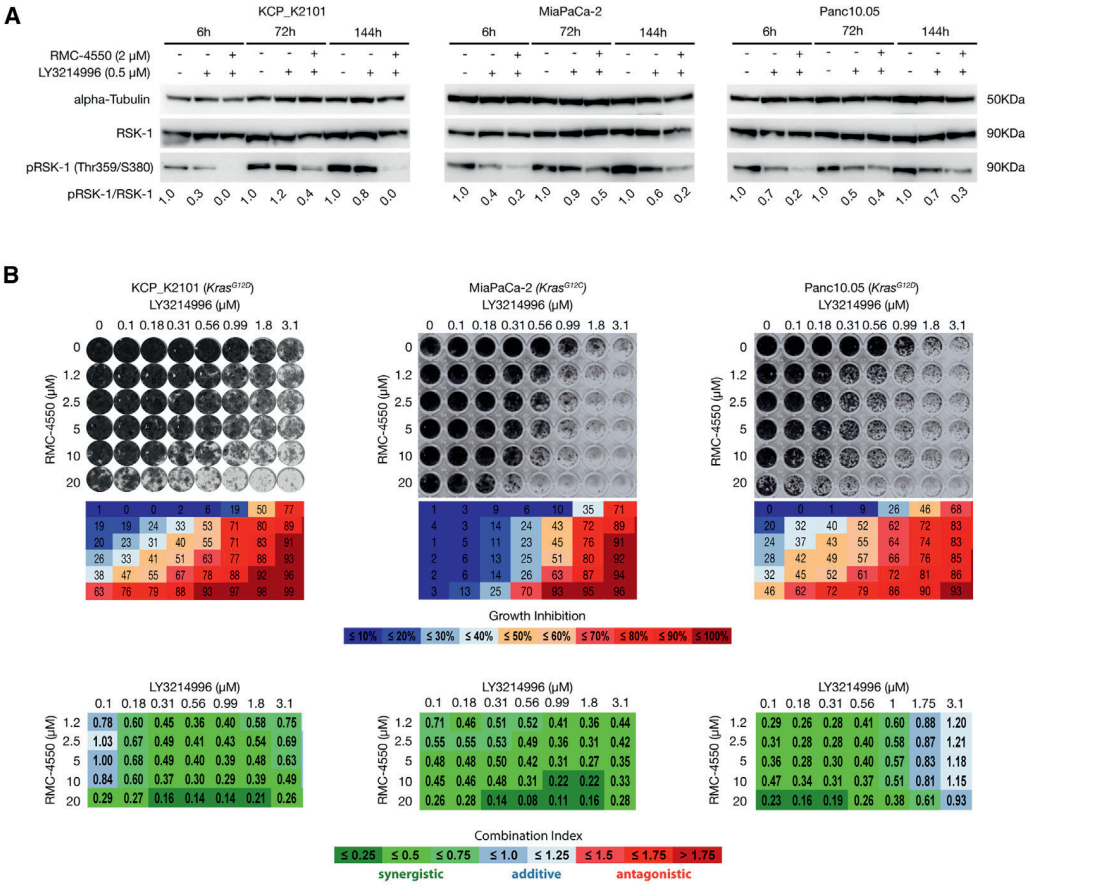

(legend on next page)

GFP-positive cleaved caspase 3 levels peaked after 48 h, and the fraction of caspase 3-positive cells was significantly higher in the combination-treated group compared with vehicle or LY3214996 and RMC-4550 monotherapy. Similarly, human cell lines MiaPaCa-2 and Panc10.05 showed a peak of GFP coupled to a cleaved caspase 3/7-specific recognition motif after 76 h, with a significant increase in combination-treated cells compared with either vehicle or monotherapies, indicating that apoptosis was triggered significantly with the combination. Based on the kinetics of the different cell lines, we identified the time point where apoptosis was maximally triggered to calculate the fold change in apoptosis for the monotherapies and combination treatment compared with vehicle (Figure 1C, bottom panels).

Taken together, our data show that LY3214996 and RMC-4550 act synergistically to both inhibit PDAC cell proliferation and MAPK signaling as well as induce significant levels of apoptosis *in vitro,* which prompted us to test the combination treatment *in vivo*.

In vivo tolerability

Due to the only recent development of both LY3214996 and RMC-4550, the scarcity of available *in vivo* data, as well as the non-existent data on combined toxicity, we performed a tolerability study in non-tumor-bearing wild-type (*Kras*^{LSLG12D}; *Trp53*$^{flox/flox}$ - no Cre) and NOD-scid gamma (NSG) mice to determine the maximum tolerated dose (MTD) of combined LY3214996 and RMC-4550. The inhibitors were administered once per day via oral gavage for 14 consecutive days (Figure 2A). Following dosing recommendations by Eli Lilly and Revolution Medicines, we determined 9 different doses of inhibitor combinations labeled d1 (lowest) through d9 (highest), as illustrated in Figure 2B. We applied a modified "3 + 3" study design[40,41] using cohorts of three animals per dose. As shown in Figure 2C, the first cohort was treated at a starting dose, and the subsequent cohorts were treated with ascending or descending doses according to the observed response. Dosing was increased until one or more mice per cohort experienced dose-limiting toxicities (DLTs). In case two or more mice experienced DLTs, the dose escalation was stopped, and the next lower dose, with no more than 1 in 6 mice showing signs of DLTs, was determined as the MTD. If only one in three mice experienced DLTs, the cohort was expanded to 6 mice, and the dose escalation continued if none of the additional three mice showed signs of DLTs; otherwise, the previous dose was determined as the MTD. Endpoints used as signs of DLT were weight loss of more than 20%, clinical score (abnormal behavior, signs of physical discomfort), and death. These parameters were evaluated daily, and animals were euthanized if either of these endpoints were met. Due to ethical and practical considerations, and to minimize the number of mice in the experiment, dose d5 was chosen as the starting dose. Figure 2 shows the body weight profile of both wild-type (Figure 2D) and NSG (Figure 2E) mice over the course of 14 days of treatment. All doses were well tolerated in wild-type mice (Figure 2D), while dose d9 (i.e., 100 mg/kg LY3214996 + 30 mg/kg RMC-4550) caused dose-limiting weight loss in NSG mice (Figure 2E).

Thus, dose d8, i.e., 100 mg/kg LY3214996 + 10 mg/kg RMC-4550, was the highest dose that was well tolerated in both wild-type and NSG mice and was therefore used to assess anti-tumor efficacy.

In vivo efficacy

Once we found a well-tolerated dose for the combination therapy of LY3214996 + RMC-4550, we investigated its potential anti-tumor efficacy *in vivo*. First, we used a xenograft model of subcutaneously transplanted human PDAC cell lines (Figures 3A and 3B). Mice bearing tumors with a volume of approximately 200 mm^3 were randomly assigned into either the vehicle, RMC-4550 (A), LY3214996 (B), or combination (C) cohort and were treated daily for 21 days via oral gavage (Figure 3A). While RMC-4550 alone was already partially effective at reducing MiaPaCa-2 xenograft tumor growth compared with vehicle, tumor volume reduction of more than 30% in 12 out of 16 mice was only achieved upon continuous combination treatment. We were able to confirm these results in a model of orthotopically transplanted *Kras*$^{G12D/+}$; *Trp53*$^{R172H/+}$; *Pdx-1Cre* tumors in immunocompetent C57BL/6J mice (KCP^{mut}). Specifically, following post-surgical tumor expansion over 2 weeks, mice were randomized into either the baseline, vehicle, RMC-4550 (A), LY3214996 (B), or combination (C) cohort. Baseline

Figure 1. Evaluation of the combined effects of RMC-4550 (SHP2i) and LY3214996 (ERKi) administration in murine and human *KRAS*-mutant pancreatic cancer cell lines

(A) Western blot analysis with murine cancer cell line KCP_K2101 derived from KCP mouse model (KRAS^{G12D}) of spontaneous tumor formation and in human cancer cell lines: MiaPaCa-2 (KRAS^{G12C}) and Panc10.05 (KRAS^{G12D}). Cells were treated as depicted and collected for lysis at the indicated time points. Protein extracts were probed with specific antibodies against total RSK-1, phosphorylated RSK-1 (pRSK-1), and alpha-tubulin (as loading control). Numerical values indicate the pRSK-1/RSK-1 ratio quantified by densitometry. The blots are representative of at least three independent experiments. RSK-1, ribosomal S6 kinase 1.

(B) Synergistic effects of SHP2i and ERKi administration were evaluated by colony-formation assay in the *KRAS*-mutant cell lines used in (A). SHP2i and ERKi were combined at the indicated concentrations. Representative crystal violet staining of cells is shown (top panel). Box matrices below the plate scans depict quantification of growth inhibition in relation to control wells (middle panel). Bottom panel: calculation of the combination index (CI) scores from the growth inhibition values (shown above) via CompuSyn software demonstrating strong synergism between SHP2i and ERKi across a wide range of combinatorial concentrations. CI <0.75 (shades of green) indicates synergism, CI = 0.75–1.25 (shades of blue) indicates additive effects, and CI >1.25 (shades of red) indicates antagonism. Experiments were repeated independently at least three times each, with similar results.

(C) Apoptosis was analyzed in cell lines treated with either DMSO, SHP2i alone, ERKi alone, or a combination of SHP2i and ERKi at the indicated concentration in real time (top panel). GFP signal coupled to cleaved caspase 3 was quantified as readout. Bar plots for selected time points (48 h for KCP_K2101 and 76 h for MiaPaCa-2 and Panc10.05) show the fraction of GFP-positive cells (AU) (top panel) and the fold change GFP signal (bottom panel). AU, arbitrary units; GFP, green fluorescent protein. Experiments were repeated independently at least three times each. Results represent mean ± SD. *$p < 0.05$, ****$p < 0.0001$, as determined by ordinary one-way ANOVA test.

See also Figure S1.

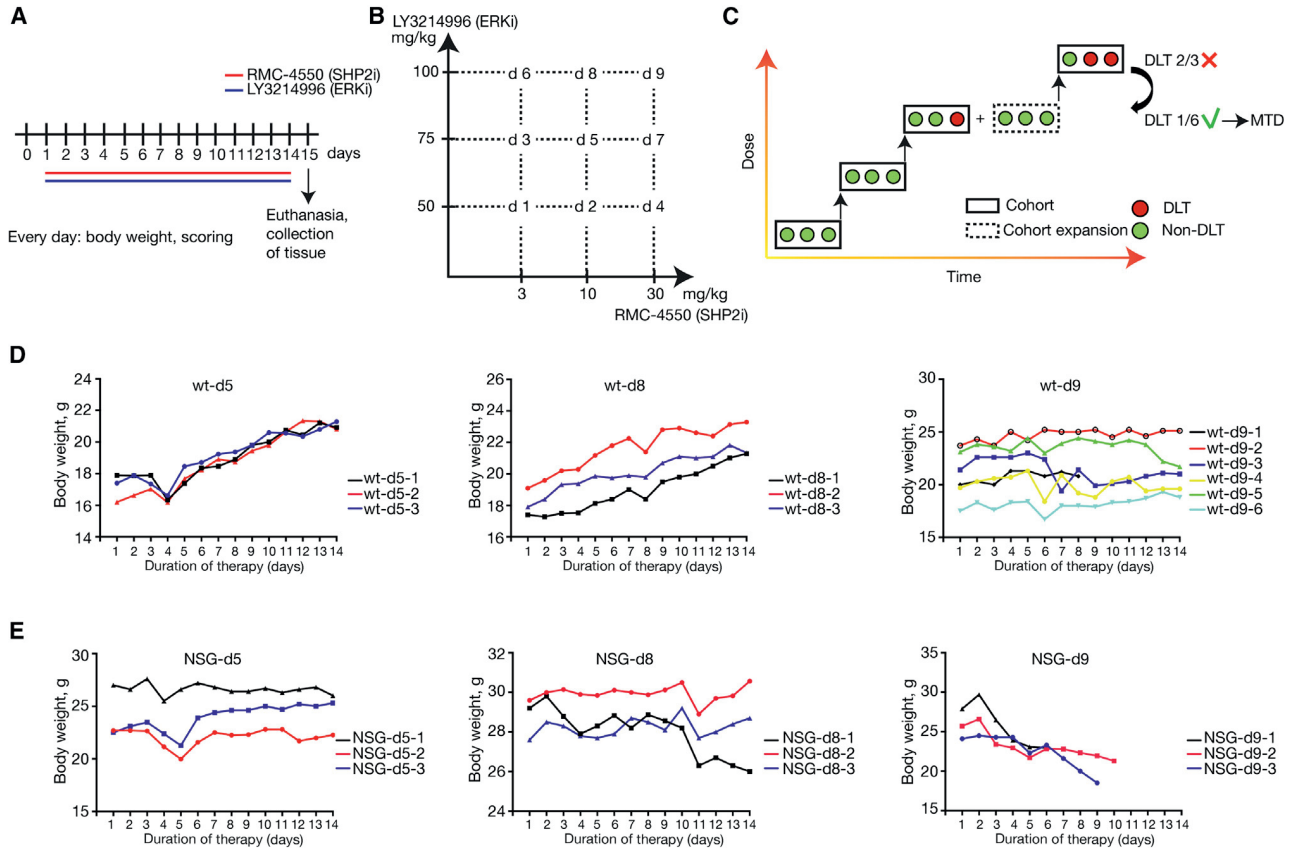

Figure 2. MTD study design

(A) Treatment schedule. Non-tumor-bearing wild-type and NOD scid gamma (NSG) mice were treated with the combination of RMC-4550 (SHP2i) and LY3214996 (ERKi) once per day via oral gavage for 14 consecutive days.

(B) Graphical representation of dose combinations. SHP2i and ERKi were combined in different concentrations to make up 9 combined doses.

(C) An illustration of the modified "3 + 3" study design. Each box represents a cohort comprising the indicated number of mice treated at a given dose level. DLT, dose-limiting toxicity; MTD, maximum tolerated dose.

(D) Individual body weight-time profile of the treatment groups in male wild-type (WT) mice: d5 (n = 3), d8 (n = 3), and d9 (n = 6).

(E) Individual body weight-time profile of the treatment groups in male NSG mice: d5 (n = 3), d8 (n = 3), and d9 (n = 3).

mice were sacrificed to confirm the presence of well-integrated and uniform orthotopic tumors. All other mice were treated for 14 days via oral gavage as shown in Figure 3A. As Figures 3C and 3D show, significant inhibition in tumor growth, seen macroscopically and indicated by decreased tumor weight, was observed in both monotherapy groups as well as in the combination treatment group compared with the vehicle cohort. No difference in treatment efficacy was observed between weight-matched male and female mice (Figure 3D). Notably, and in agreement with the synergy described *in vitro*, the combination therapy (cohort C) was the most effective and induced a significantly stronger tumor volume reduction compared to LY3214996 or RMC-4550 monotherapies (Figures 3C and 3D). To confirm the on-target activity of the combination therapy, we show substantial reduction in transcriptional-based MAPK pathway activity score[42] *in vivo* in both the orthotopic KCP^{mut} tumors as well as the subcutaneous MiaPaCa-2 xenografts (Figure 3E) treated with continuous LY3214996 + RMC-4550 compared with vehicle-treated controls.

While the lack of effectiveness of LY3214996 single treatment *in vivo* was congruent with the negligible effects we observed *in vitro* in terms of cell proliferation and pathway inhibition, the same was not true for RMC-4550, which also showed very little effect *in vitro* but induced a substantial impairment of tumor growth, in multiple *in vivo* models. Differences in response to SHP2 inhibitors in *in vivo* versus *in vitro* models have been previously attributed, in the context of KRAS mutant tumors, to either the serum concentration (accounting for growth factor availability)[23] or to the tridimensional versus bidimensional growth.[43] In order to better understand which factors played a role in our context, we grew MiaPaCa-2 and Panc10.05 cells in the presence of 10% or 3% serum, both in normal and ultra-low attachment 96-well plates. We then analyzed the response to RMC-4550 treatment using the CellTiter-Glo 3D assay as a readout for cell viability. As shown in Figure S2A, tridimensional growth seems to be the main factor influencing the response to the SHP2 inhibitor in the PDAC cell lines. In particular, MiaPaCa-2 and Panc10.05 were equally unresponsive to SHP2 inhibition in

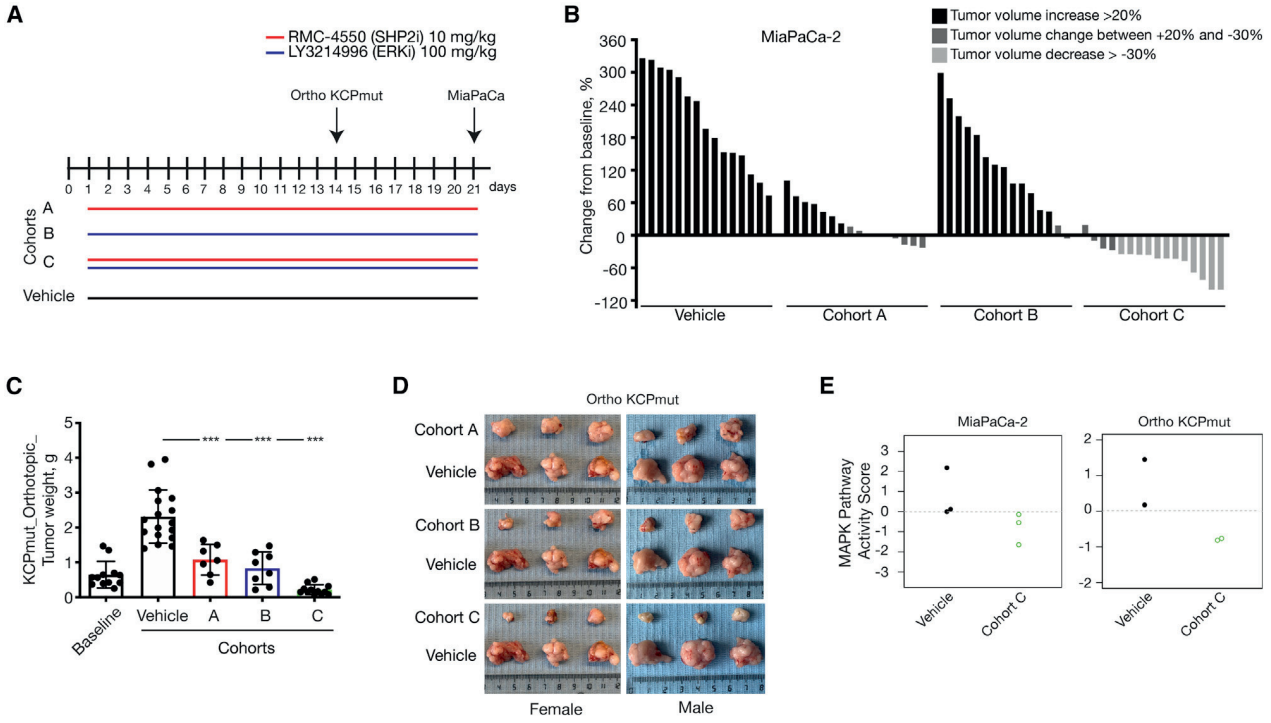

Figure 3. *In vivo* assessment of treatment response in a xenograft and in an orthotopic PDAC model

(A) Schematic representation of the treatment schedule applied in a xenograft model of subcutaneously transplanted MiaPaCa-2 cell line and in a model of orthotopically transplanted KCP^{mut} tumors. Cohort A: continuous treatment with RMC-4550 (SHP2i) alone daily (n = 15); cohort B: continuous treatment with LY3214996 (ERKi) alone daily (n = 15); and cohort C: continuous treatment with the combination of SHP2i and ERKi daily (n = 16). Control mice were continuously treated with vehicle (n = 15).

(B) Evaluation of ERKi and SHP2i monotherapy treatments and combined administration of SHP2i and ERKi. For all the xenograft experiments, 5 × 10^6 MiaPaCa-2 cells were subcutaneously injected into the right flank of NSG mice. When tumors reached 200–250 mm^3, mice were randomly assigned into cohorts and treated by oral gavage with inhibitors or vehicle according to treatment schedule for 21 days, after which tumors were resected. The y axis shows tumor volume change in percentage from baseline. Each bar represents the difference in pancreatic volume in an individual animal. According to the RECIST criteria, black indicates progressive disease, dark gray indicates stable disease, and light gray indicates partial response. Significance was determined by one-way ANOVA with Bonferroni's multiple comparison test.

(C and D) *In vivo* assessment of treatment response of orthotopically implanted tumors. ~40 mm^3 tumor pieces (KCP^{mut}) were orthotopically implanted into the pancreata of 8-week-old male and female C57BL/6 mice. After 2 weeks, mice were either sacrificed as baseline (n = 12) or randomly assigned into cohorts and treated with inhibitors or vehicle according to the treatment schedule (A).

(C) Tumor weight (mean ± SD) was determined after 14 days of therapy as indicated: baseline (n = 12), vehicle (n = 17), cohort A (n = 7), cohort B (n = 8), cohort C (n = 12). ****p < 0.0001, as determined by one-way ANOVA with Bonferroni's multiple comparison test.

(D) Representative macroscopic photographs of tumors in (C).

(E) MAPK pathway activity scores in MiaPaCa-2 xenograft and in KCP^{mut} orthotopic mouse models.

See also Figures S2 and S6.

the presence of high or low serum concentrations in two-dimensional (2D) culture conditions. Nevertheless, cell viability was strongly impaired when both cell lines were treated with RMC-4550 in 3D conditions. Additionally, for Panc10.05, a significant difference in sensitivity to RMC-4550 was also observed in 3% versus 10% serum but only in the context of 3D growth.

Overall, despite RMC-4550 showing a stronger anti-tumor effect *in vivo* compared with *in vitro*, we could still observe a synergistic effect when used in combination with LY3214996 in multiple mouse models.

Optimal treatment regimen

Having shown a potent anti-tumor benefit of the LY3214996 + RMC-4550 combination treatment, compared with the monotherapies in MiaPaCa-2 xenografts and orthotopic KCP^{mut} tumors, we decided to further expand our validation in additional PDAC models of murine and human origin and, at the same time, compare intermittent treatment schedules. With regards to future clinical application and the possibility of adverse effects in patients, we wanted to determine the optimal treatment regimen, defined as maximum anti-tumor effect with minimum toxicity. For the LY3214996 + RMC-4550 combination, these schedules included continuous administration (daily) of both drugs in combination (cohort C), as well as three different non-continuous (intermittent) schedules (cohorts D, E, and F). Control cohorts included daily vehicle treatment, as well as intermittent LY3214996 or RMC-4550 monotherapy (cohorts G, H, and I) (Figure 4A).

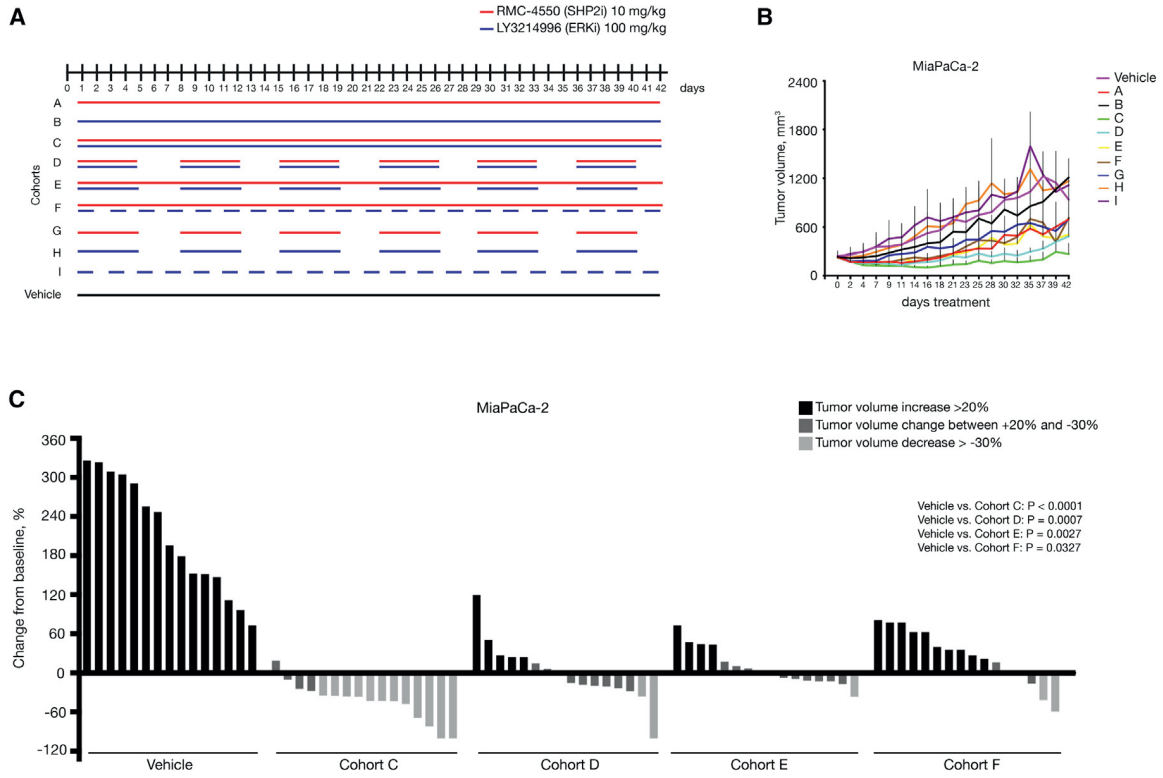

Figure 4. *In vivo* assessment of optimal treatment regimen in a xenograft model

(A) Schematic representation of the treatment schedule applied in MiaPaCa-2 xenograft model. Cohort A: continuous treatment with SHP2i alone daily; cohort B: continuous treatment with ERKi alone daily; cohort C: continuous treatment with the combination of SHP2i and ERKi daily; cohort D: intermittent treatment with the combination of SHP2i and ERKi 5 days on/2 days off; cohort E: semi-continuous treatment schedule with daily dosing of SHP2i and intermittent dosing with ERKi 5 days on/2 days off; cohort F: continuous treatment with SHP2i and on alternate days with ERKi; cohort G: intermittent dosing with SHP2i alone 5 days on/2 days off; cohort H: intermittent dosing with ERKi alone 5 days on/2 days off; and cohort I: treatment with ERKi alone on alternate days. Control mice were continuously treated with vehicle. For all the xenograft experiments, 5×10^6 cells were subcutaneously injected into the right flank of NSG mice. When tumors reached 200–250 mm^3, mice were randomly assigned into cohorts and treated by oral gavage with inhibitors or vehicle according to treatment schedule.

(B) Treatment response was assessed through tumor volume change using caliper measurements 3 times/week in MiaPaCa-2 ($KRAS^{G12C}$) xenograft model. Results represent mean ± SD.

(C) Tumor volume change at time point day 21(n = 15 for vehicle cohort, n = 16 for all other cohorts). The y axis shows tumor volume change in percentage from baseline. Each bar represents the difference in tumor volume in an individual animal. According to the RECIST criteria, black indicates progressive disease, dark gray indicates stable disease, and light gray indicates partial response. Vehicle and cohort C data from Figure 3 B are reported again for comparison. Significance was determined by one-way ANOVA with Bonferroni's multiple comparison test.

See also Figure S2.

We tested these regimens in three different tumor models: the subcutaneous xenograft model with transplanted human PDAC cell lines (Figures 4 and S2B–S2E), the endogenous *Kras; Trp53*$^{-/-}$ (KCP) model of spontaneous PDAC formation (Figures 5, S3, and S4), and the subcutaneous model of transplanted patient-derived PDAC tissue xenografts (PDX) (Figures 6 and S5; Table S1) None of the tested schedules were associated with dose- or schedule-limiting toxicities (Figure S6) in any of the three tumor models.

The potent tumor-inhibitory effect of the continuous combination treatment (cohort C) shown in MiaPaCa-2 xenografts (Figure 4C) was also observed in Panc10.05, ASPC1, and YAPC xenografts (Figures S2B–S2E). While we observed varying degrees of sensitivity among the 4 PDAC cell lines, the common findings were that all combination schedules showed stronger anti-tumor efficacy compared with all monotherapies or vehicle controls and that the continuous schedule had the strongest inhibitory effect of all the combination regimens (Figures 4C and S2B–S2E). However, complete tumor elimination was not achieved, even with the continuous treatment schedule.

In agreement with these findings, our endogenous KCP model showed that the combination treatment was able to significantly inhibit tumor growth (Figures 5B–5D) or even induce pancreatic volume reduction. Of note, the continuous treatment was able to induce more than 30% pancreatic volume reduction (Figures 5B and S3C) and prevent tumor outgrowth from the microscopic to macroscopic scale if the mouse was treated early enough. This was indicated by morphological analysis, the relative pancreatic weight, and the considerable number of intact acini, as well as the significant reduction in proliferating, i.e., Ki67-positive, cells

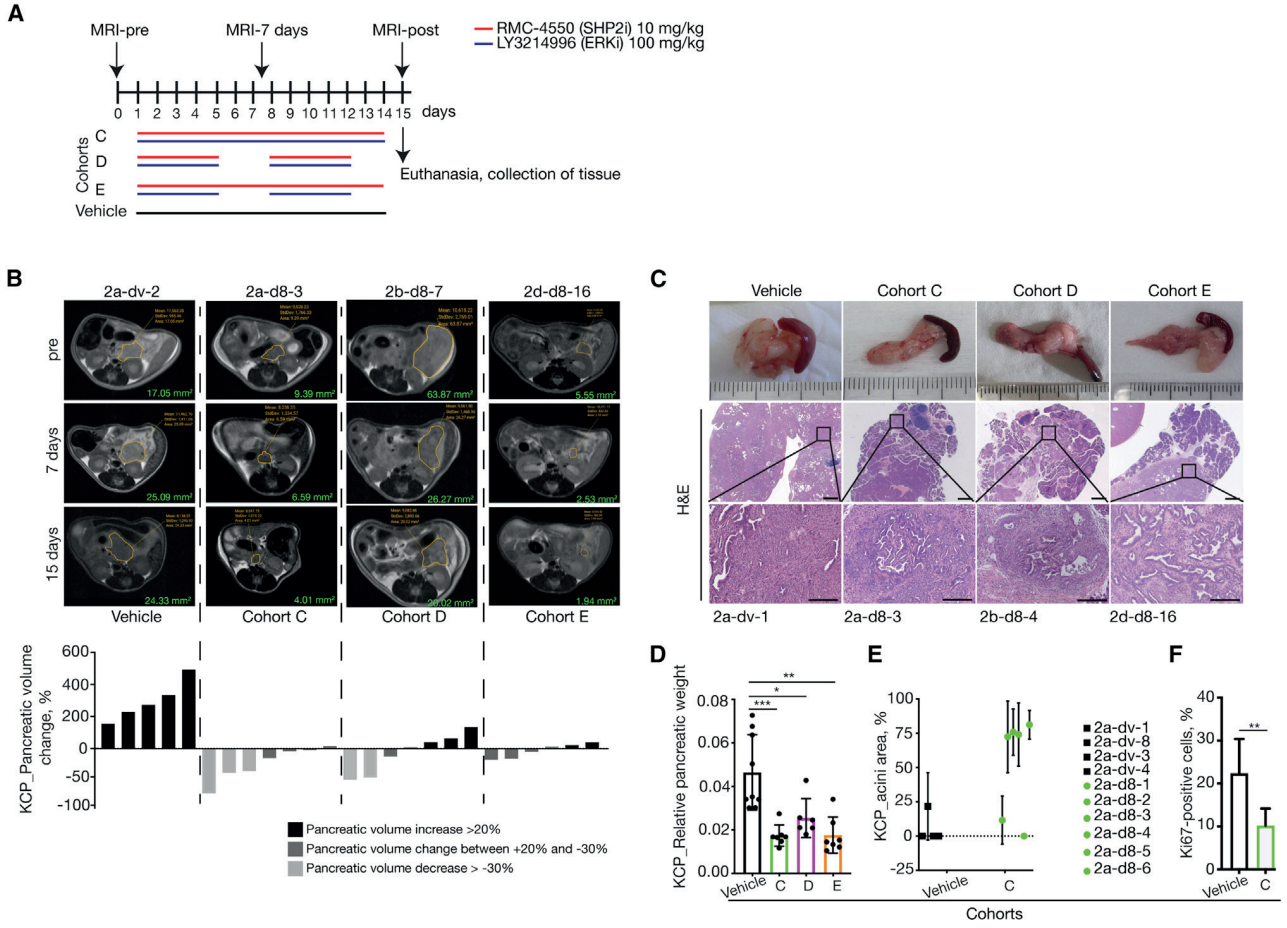

Figure 5. *In vivo* assessment of optimal treatment regimen in an endogenous murine PDAC model

(A) Schematic representation of the treatment schedule applied in the endogenous (KPC) murine model of spontaneous tumor formation as well as the magnetic resonance imaging (MRI) time points applied. Cohort C: continuous treatment with the combination of SHP2i and ERKi daily; cohort D: intermittent treatment with the combination of SHP2i and ERKi 5 days on/2 days off; and cohort E: semi-continuous treatment schedule with daily dosing of SHP2i and intermittent dosing with ERKi 5 days on/2 days off. Control mice were treated with vehicle for 14 consecutive days. All treated mice were sacrificed on day 15, and tumors were resected for histological analysis.

(B) Representative MRI scan slices depicting PDAC tumor sections of KCP mice treated with vehicle (n = 5), cohort C (n = 7), cohort D (n = 7), or cohort E (n = 6) at the indicated time points (days) following the start of therapy (pre), with similar results among the groups. Volumetric measurements indicate a decrease in pancreatic volume in mice treated with the combination of SHP2i and ERKi for 2 weeks compared with vehicle-treated mice. The y axis shows pancreatic volume change in percentage quantified by measurements of MRI scans. Each bar represents the difference in pancreatic volume in an individual animal from days 0 to 15. According to the RECIST criteria, black indicates progressive disease, dark gray indicates stable disease, and light gray indicates partial response. Significance was determined by one-way ANOVA with Bonferroni's multiple comparison test. Volume-tracking curves for individual mice over the whole course of therapy are available in Figures S3B–S3E.

(C) Macroscopic images of pancreas and spleen (top row). Representative H&E-stained sections of pancreata from mice, treated as indicated. Scale bars represent 1,000 (middle) and 200 μm (bottom). Mice numbers are indicated below.

(D) Relative pancreatic weight was significantly lower in all groups treated with the combination of SHP2i and ERKi: cohort C (n = 7), cohort D (n = 6), and cohort E (n = 7) compared with vehicle-treated control mice (n = 9). Results represent mean ± SD. *$p < 0.05$, ***$p < 0.001$, significance was determined by one-way ANOVA with Bonferroni's multiple comparison test.

(E) Quantification of relative intact acinar area as ratio of whole pancreatic area. Analysis performed on n = 4 individual mice in vehicle group and on n = 6 individual mice in cohort C. Results represent mean ± SD.

(F) Ki67-positive cells in percentage quantified in pancreata of mice treated with vehicle (n = 6) or with the combination of SHP2i and ERKi daily (n = 7). Results represent mean ± SD. **p = 0.0044, significance was determined by unpaired t test.

See also Figures S3, S4, and S6.

compared with the control (Figures 5C–5F and S4A). PDAC is associated with significant formation of desmoplastic stroma, which is recapitulated very well in the murine KCP model. This stroma compartment has been shown to be an obstacle for the tumor penetration of chemotherapeutic drugs.[44,45] Here (Figures S4B and S4C), we show that RMC-4550 indeed

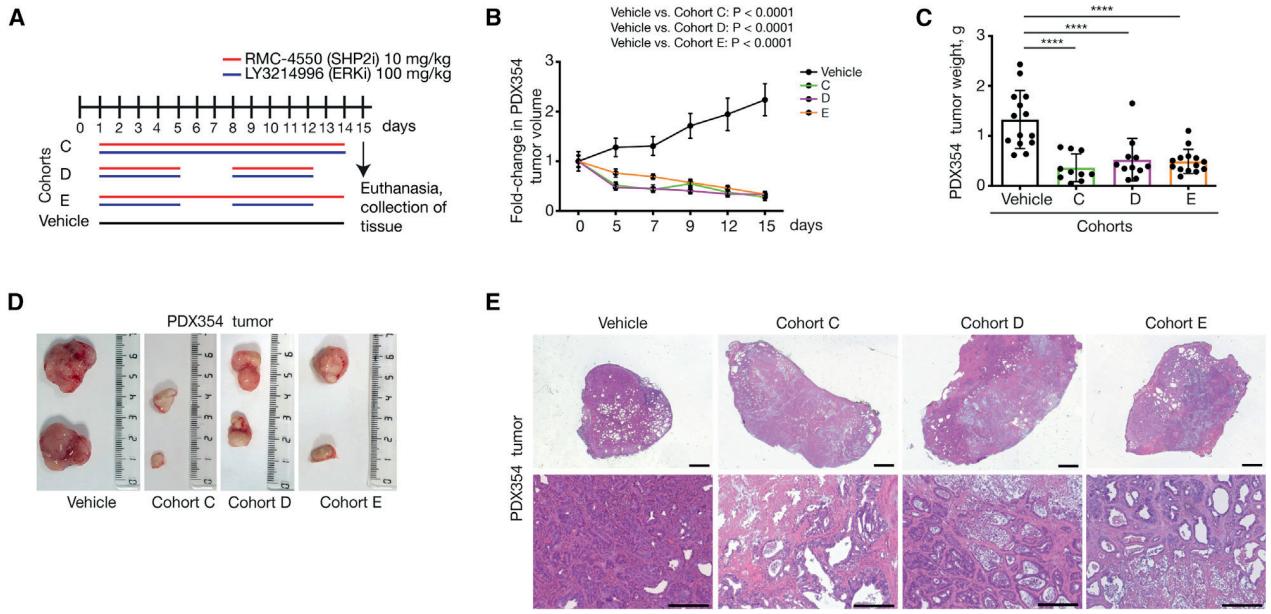

Figure 6. Evaluation of treatment response by the combined administration of RMC-4550 (SHP2i) and LY3214996 (ERKi) in patient-derived xenograft (PDX) models

(A) Treatment schedule. Mice were treated with the combination of RMC-4550 (SHP2i) and LY3214996 (ERKi) once per day via oral gavage for 14 consecutive days (cohort C) or 5 days on/2 days off (cohort D) or SHP2i continuously and ERKi5 days on/2 days off (cohort E). For PDX354 model, tumor pieces of 50 mm^3 were subcutaneously implanted into both flanks of NSG mice (n = 7 mice per cohort). When tumors reached 200–250 mm^3 (approximately 6–8 weeks after subcutaneous transplantation), mice were randomly assigned into cohorts and treated by oral gavage with inhibitors or vehicle according to treatment schedule for the indicated time, after which tumors were resected.

(B and C) Treatment response was assessed through tumor volume changes using daily caliper measurements (B) and tumor weight at endpoint (C) in PDX354 model. Results represent mean ± SD. ****$p < 0.0001$, as determined by one-way ANOVA with Bonferroni's multiple comparison test.

(D) Representative macroscopic images of resected tumors.

(E) Representative H&E-stained sections of vehicle- and combination-therapy-treated PDX354 tumors. Scale bars represent 1,000 (top) and 200 μm (bottom). See also Figure S5.

takes longer to reach the fibrotic/cancerous pancreas tissue compared with healthy pancreas tissue. However, after 8 h, the levels of RMC-4550 recovered from both tissues are very similar. Interestingly, we see that the RMC-4550 levels decline more rapidly in cancerous pancreas tissue. LY3214996 penetration of the pancreas tissue seems less affected by the tumor stroma since the amount of recovered drug from cancerous and healthy pancreas tissue is very similar. We further found that LY3214996 does not persist in the pancreas like RMC-4550 does. Twenty h after treatment, we still recovered 1/6th of the maximal RMC-4550 amount, while LY3214996 levels were virtually undetectable.

Additionally, three different PDX models, each representing a different patient harboring $KRAS^{G12D}$ mutations, corroborated the observation that all tested combination therapy regimens were able to significantly reduce tumor growth and even induce tumor volume reduction (Figures 6 and S5). While there was no statistically significant difference between the three treatment arms, the data seem to indicate a slight benefit of the continuous treatment compared with the intermittent schedules (Figures 6C, 6D, S5C, and S5G). Interestingly, all tumors from mice receiving the combination treatments contained lytic necrotic cores, suggesting tumor cell elimination in addition to the cytostatic affects observed (Figures 6E, S5D, and S5H).

Assessment of treatment response

Having shown efficacy data in multiple different *KRAS*-mutant PDAC mouse models, our aim is to bring this therapy to the clinic. While we have tried to diversify our models and thus account for inter-patient heterogeneity, it is still essential to distinguish responders from non-responders in a clinical setting, preferably using minimally invasive methods. Using a small cohort of tumor-bearing KCP mice (Figure S7), we were able to show that congruent with the *in vitro* setting (Figure 1), pRSK levels are also a good marker to show MAPK pathway inhibition *in vivo*. However, as the level of pRSK is highly dependent on the time elapsed between treatment and sample collection, pRSK is not a useful marker for the evaluation of treatment response in a clinical setting. Indeed, 1 or 2 h after the treatment, pRSK levels have not been decreased to the fullest extent, while this is only achieved after 4 h. However, 16 or 20 h after the treatment, pRSK levels are increasing again. We thus conclude that sample collection either too soon or too late after the last treatment could lead to detection of misleading pRSK levels.

Interestingly, Ying et al.[10] described that oncogenic $KRAS^{G12D}$ is required for PDAC tumor maintenance and reprograms PDAC metabolism by stimulating glucose uptake and glycolysis, while Bryant et al.[46] found that both KRAS suppression and ERK inhibition decreased glucose uptake in PDAC. Based on those

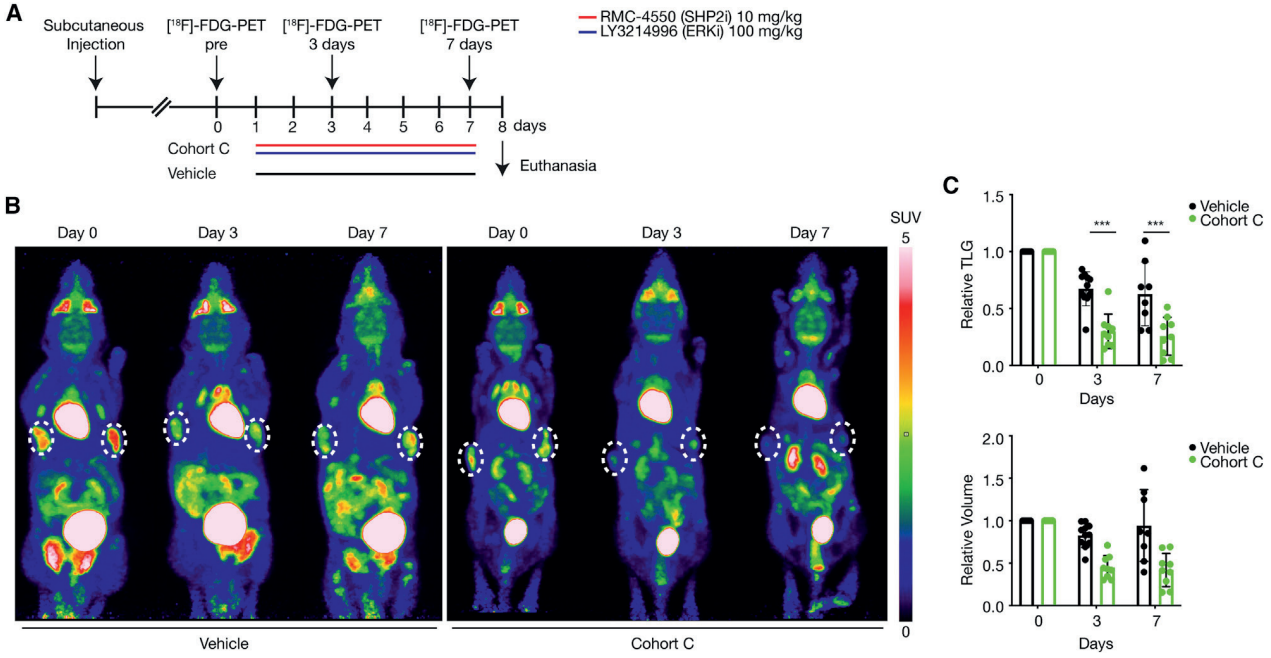

Figure 7. Early non-invasive assessment of the treatment response in a subcutaneous tumor mouse model

(A) Schematic representation of the treatment schedule applied in the subcutaneous tumor mouse model as well as the [^{18}F]-FDG-PET imaging time points applied. 2.5 × 10^6–3 × 10^6 cells were injected subcutaneously into the left and right flank of 10- to 15-week-old non-tumor-bearing littermates. Two to three weeks after subcutaneous injection, mice were randomly assigned into cohorts and treated by oral gavage with inhibitors or vehicle for 7 consecutive days. [^{18}F]-FDG-PET scans were obtained at baseline before commencement of therapy (day 0) and at days 3 and 7 during treatment.

(B) Representative [^{18}F]-FDG-PET images of tumor-bearing mice treated with vehicle or undergoing treatment with the combination of RMC-4550 (SHP2i) and LY3214996 (ERKi) once per day for 7 consecutive days (cohort C). Subcutaneous tumor areas are shown in dashed circles, and SUV of FDG uptake is indicated by color. White color indicates highest uptake, red color high uptake, yellow and green intermediate, and blue low uptake. [^{18}F]-FDG-PET, 18-fluordesoxyglucose positron emission tomography; PET, positron emission tomography; SUV, standardized uptake value; FDG, fluorodeoxyglucose.

(C) Upper panel: relative total lesion glycolysis (TLG) on days 0, 3, and 7 in vehicle versus cohort C (n = 8–9 animals/group). Lower panel: relative tumor volume on days 0, 3, and 7 in vehicle versus cohort C. Results represent mean ± SD. ***$p < 0.001$, significance was determined by unpaired, two-tailed t test.

See also Figure S7.

reports, we explored the possibility of using ^{18}F-fluorodeoxyglucose (FDG) uptake, as measured by positron emission tomography (PET) scan, as an early response marker and a surrogate readout of MAPK activity.

To this aim, we treated mice bearing subcutaneous KCP tumors with either vehicle or the combination of RMC-4550 + LY3214996 daily for 7 days. PET scans were performed at days 0 (pretreatment), 3, and 7. Our results show that ^{18}F-FDG uptake is readily detected by PET-CT scan of subcutaneously implanted KCP tumors and that a significant decrease in PET signal is already observable at a time when reduction in tumor volume is not yet significant (Figure 7). This finding raises the possibility of using FDG uptake in the clinic to monitor early response to this combinatorial therapy for patients with PDAC.

DISCUSSION

Pancreatic cancer has one of the highest mortality rates among all tumor types, and innovative treatment options against this devastating cancer are urgently needed.[2] Since targeted therapies are lacking and PDAC seems to be refractory to immunotherapy,[47] classic chemotherapy is still the treatment of choice for the management of PDAC at all stages of the disease.[48]

We recently identified a strategy for targeting *KRAS*-mutant tumors, irrespective of the specific mutation, which consists of the concomitant blockade of the RAS downstream effector MEK and the upstream activator SHP2.[23,24] Similarly, the combination of SOS1 and MEK inhibition has been proven effective in *KRAS*-mutant preclinical tumor models.[49] In the present work, we validate this "up plus down" double blockade strategy in multiple *in vivo* models of PDAC by combining inhibition of the MEK downstream effector ERK (by using LY3214996) with upstream inhibition of SHP2 (with RMC-4550).

In agreement with our earlier findings, we show that ERK inhibitor monotherapy is insufficient to induce a durable suppression of the MAPK pathway, as demonstrated by a rebound in phosphorylated RSK1 levels and failure to induce apoptosis. We have previously demonstrated that the rebound in MAPK signaling following RAS downstream inhibition can be attributed to the feedback overexpression and activation of multiple RTKs. Therefore, the most effective way to short circuit this resistance-inducing loop is to disrupt the signal transmission from activated RTKs to RAS. The protein phosphatase SHP2

has been found to be recruited by virtually all phosphorylated growth factor receptors, as well as other cell-surface receptors like cytokine or hormone receptors, where it mediates the signal transmission to downstream protein effectors, making it the ideal target to prevent ERK inhibitor resistance.[50] Indeed, we show that co-treatment with LY3214996 and RMC-4550 promptly induces apoptosis in cell cultures and tumor regression in several mouse models of PDAC, especially when administered continuously.

The previous failure of MEKis like selumetinib against *KRAS*-mutant tumors during clinical trials[51] has been attributed not only to the above-mentioned resistance mechanisms[22] but also to the highly toxic profile of such drugs. On the other hand, ERK inhibitors are compounds that only recently have entered the earliest phases of clinical testing, holding promise for improved tolerability and efficacy in the treatment of tumors with a MAPK pathway dependency. In the present study, we extensively evaluated the toxicity of the LY3214996 + RMC-4550 combination in multiple murine backgrounds and identified for each compound a dose that, in combination, is well tolerated as well as efficacious against PDAC tumor growth.

Apart from its role in the MAPK pathway, the SHP2 phosphatase is also recruited by the immune checkpoint receptor PD1, which is expressed on T and pro-B lymphocytes.[52] PD1 activity is known to suppress T cell activation and therefore mediate cancer immune evasion.[53,54] It has been reported that inhibition of SHP2 can stimulate an anti-tumor immune response by both promoting T cell function and depleting pro-tumorigenic M2 macrophages.[55,56] Therefore, the use of SHP2 inhibitors could have a double beneficial effect: in the tumor cells, it would act synergistically with ERK inhibitors to suppress MAPK-induced proliferation, and in the tumor microenvironment, it could promote the anti-tumor immune response. Further investigation, for example using a pancreatic cancer model that can be transplanted both in immuno-competent and immuno-compromised hosts, will be needed in order to elucidate the non-tumor-intrinsic benefits of using SHP2 inhibitors.

As a translational approach to monitor the early response of patients, we searched for dynamic biomarkers that could be used in a clinical setting. So far, computed tomography (CT) is the method of choice to determine therapy response; however, this is usually done retrospectively. Thus, the idea of non-invasive but quick methods to evaluate an early drug response is gaining increasing attention in modern oncology as it allows monitoring of therapy failure, sparing the patient unnecessary toxicity. In 2006, Su et al.[57] showed that inhibition of the MAPK pathway by treatment with anti-EGFR therapy in colorectal cancer models induced a rapid downregulation of glucose receptors, which was reflected by decreased FDG glucose uptake in PET scans. Recently, Bryant et al.[46] reported that small interfering RNA (siRNA)-mediated silencing of KRAS or pharmacological ERK inhibition decreased glucose uptake and resulted in a clear reduction of key glycolytic intermediates in KRAS-driven PDAC. Furthermore, a pilot study by Wang et al.[58] showed that ^{18}F-FDG-PET and diffusion-weighted magnetic resonance imaging (DW-MRI) can be used as early treatment response assessment in patients with advanced PDAC. Based on these data, we suggest ^{18}F-FDG imaging via PET scans as a tool to sensitively monitor tumor shrinkage shortly after therapy initiation to evaluate the early drug response. Indeed, we confirmed that co-inhibition of ERK and SHP2 in subcutaneous *KRAS*-mutant PDAC tumors induces a rapid and significant decrease in FDG uptake, which precedes the decrease in tumor volume.

In conclusion, LY3214996 + RMC-4550 combination has shown a positive tolerability profile as well as the capacity to synergistically induce a high percentage of partial response in several preclinical models of PDAC. In addition, the preliminary data of the PET scans to monitor early drug response warrants the ERK + SHP2 inhibitor combination to be explored at a clinical level. To this end, we started the phase 1a/1b SHERPA trial (ClinicalTrials.gov: NCT04916236) with the objective of testing the tolerability and early evidence of efficacy of the combination of RMC-4630 (the clinical equivalent of RMC-4550) and LY3214996, which may represent a promising targeted therapeutic option for the majority of patients with *KRAS*-mutant pancreatic cancer.

Limitations of the study

Although we have extensively validated the tolerability and efficacy of the RMC4550 plus LY3214996 combination in preclinical models, the results may vary when testing the combination in patients (where RMC4630 is used). In particular, pharmacokinetics and toxicity may be different in human subjects and may lead to a different dosing and schedule of the treatment.

STAR★METHODS

Detailed methods are provided in the online version of this paper and include the following:

- KEY RESOURCES TABLE
- RESOURCE AVAILABILITY
  - Lead contact
  - Materials availability
  - Data availability
- EXPERIMENTAL MODEL AND SUBJECT DETAILS
  - Mouse strains
  - Cell culture and cell lines
  - Human pancreatic cancer cell line xenografts
  - Orthotopic PDAC mouse models
  - Subcutaneous cancer cell line mouse models
- METHOD DETAILS
  - Drugs and inhibitors
  - *In vitro* drug synergy and quantitative analysis
  - Cell viability assay
  - Incucyte cell-proliferation assay and apoptosis assay
  - *In vivo* drug combination dose finding escalation
  - *In vivo* therapy treatment schedules
  - Drug distribution of RMC-4550 and LY3214996 in tumor mice and non-tumor bearing controls
  - PET imaging and ^{18}F-FDG *in vivo*
  - Magnetic resonance imaging (MRI)
  - Histology
  - Sequencing and MAPK pathway activity score
  - Protein lysate preparation and immunoblotting
- QUANTIFICATION AND STATISTICAL ANALYSIS

- ADDITIONAL RESOURCES
  - Clinical trial

SUPPLEMENTAL INFORMATION

Supplemental information can be found online at https://doi.org/10.1016/j.xcrm.2022.100815.

ACKNOWLEDGMENTS

We thank the Preclinical Imaging Core at TranslaTUM (PICTUM) at Klinikum rechts der Isar der Technischen Universität München for its support, specifically Markus Mittelhäuser and Hannes Rolbieski. We thank the NKI Intervention Unit for technical assistance with the human cell lines xenograft experiment, as well as Arthur Burylo from the NKI Pharmacology Department for helping with the pharmacokinetic studies. The graphical abstract was created with BioRender.com (agreement number TK24HPDSXK). This work was funded by the American Association for Cancer Research, Lustgarten Foundation, and Stand Up to Cancer as a Pancreatic Cancer Collective New Therapies Challenge grant (grant no. SU2C-AACR-PCC-01-18).

AUTHOR CONTRIBUTIONS

The authors confirm contribution to the paper as follows: R.B., H.A., S.M., M.L., B.S., K.J.F., A. Berninger, and A.M.-S. designed the study. *In vitro* cell culture and colony-formation assays were performed by A.M.-S., S.M., and A. Bosma. Apoptosis assay and immunoblotting were done by A.M.-S. *In vitro* data was analyzed by K.J.F. and A.M.-S. K.J.F., A. Berninger, M.L., K.G., N.W., K.N.D., E.K.-A., F.S., and L.K. conducted the KCP mouse model experiment. K.J.F. and A. Berninger performed the subcutaneous mouse model experiment. S.M., M.v.d.V., and N.P. designed and performed the human xenograft mouse model experiment. L.R.C. conducted the orthotopic mouse model experiment. The human PDX mouse model experiment was done by L.R.C. Imaging (MRI and PET) was performed by K.J.F., A. Berninger, K.N.D., N.W., and K.G. with the help of PICTUM. K.J.F. analyzed the MRI data. S.K. analyzed the PET data. RNA isolation and MAPK activity scoring were done by A Berninger, S.M., and B.T. O.v.T. performed the drug measurements for the pharmacokinetic studies. Histology was performed by A. Berninger. Image acquisition and quantification was performed by M.L. and A. Berninger. Maintenance of mouse strains and genotyping were done by A. Berninger, K.J.F., N.W., K.G., E.K.-A., D.K., K.N.D., F.S., L.K., M.v.d.V., and N.P. K.J.F., A. Berninger, A.M.-S., B.S., M.L., and S.M. selected and analyzed the data shown in this manuscript. M.L. generated the figures with the help of A. Berninger and K.J.F. K.J.F., A. Berninger, A.M.-S., M.L., and S.M. wrote the manuscript. The manuscript was edited by D.A.R., B.S., S.K., H.A., and R.B. Supervision was provided by R.B. and H.A. The shared first authors K.J.F., A.M.-S., and A. Berninger contributed equally to the experimental work, and their order was assigned considering that K.J.F. and A.M.-S. also produced preliminary data and K.J.F. coordinated inter-lab meetings.

DECLARATION OF INTERESTS

The authors declare no competing interests.

INCLUSION AND DIVERSITY

We support inclusive, diverse, and equitable conduct of research.

Received: January 24, 2022
Revised: August 5, 2022
Accepted: October 14, 2022
Published: November 15, 2022

REFERENCES

1. Carioli, G., Bertuccio, P., Boffetta, P., Levi, F., La Vecchia, C., Negri, E., and Malvezzi, M. (2020). European cancer mortality predictions for the year 2020 with a focus on prostate cancer. Ann. Oncol. *31*, 650–658.
2. Mizrahi, J.D., Surana, R., Valle, J.W., and Shroff, R.T. (2020). Pancreatic cancer. Lancet *395*, 2008–2020.
3. Siegel, R.L., Miller, K.D., and Jemal, A. (2020). Cancer statistics, 2020. CA. Cancer J. Clin. *70*, 7–30. 2020.
4. Pishvaian, M.J., Bender, R.J., Halverson, D., Rahib, L., Hendifar, A.E., Mikhail, S., Chung, V., Picozzi, V.J., Sohal, D., Blais, E.M., et al. (2018). Molecular profiling of patients with pancreatic cancer: initial results from the know your tumor initiative. Clin. Cancer Res. *24*, 5018–5027.
5. Pishvaian, M.J., Blais, E.M., Brody, J.R., Lyons, E., DeArbeloa, P., Hendifar, A., Mikhail, S., Chung, V., Sahai, V., Sohal, D.P.S., et al. (2020). Overall survival in patients with pancreatic cancer receiving matched therapies following molecular profiling: a retrospective analysis of the Know Your Tumor registry trial. Lancet Oncol. *21*, 508–518.
6. Golan, T., Hammel, P., Reni, M., Van Cutsem, E., Macarulla, T., Hall, M.J., Park, J.O., Hochhauser, D., Arnold, D., Oh, D.Y., et al. (2019). Maintenance olaparib for germline BRCA-mutated metastatic pancreatic cancer. N. Engl. J. Med. *381*, 317–327.
7. Waddell, N., Pajic, M., Patch, A.M., Chang, D.K., Kassahn, K.S., Bailey, P., Johns, A.L., Miller, D., Nones, K., Quek, K., et al. (2015). Whole genomes redefine the mutational landscape of pancreatic cancer. Nature *518*, 495–501.
8. Iacobuzio-Donahue, C.A., Velculescu, V.E., Wolfgang, C.L., and Hruban, R.H. (2012). Genetic basis of pancreas cancer development and progression: insights from whole-exome and whole-genome sequencing. Clin. Cancer Res. *18*, 4257–4265.
9. Collins, M.A., Bednar, F., Zhang, Y., Brisset, J.C., Galbán, S., Galbán, C.J., Rakshit, S., Flannagan, K.S., Adsay, N.V., and Pasca di Magliano, M. (2012). Oncogenic Kras is required for both the initiation and maintenance of pancreatic cancer in mice. J. Clin. Invest. *122*, 639–653.
10. Ying, H., Kimmelman, A.C., Lyssiotis, C.A., Hua, S., Chu, G.C., Fletcher-Sananikone, E., Locasale, J.W., Son, J., Zhang, H., Coloff, J.L., et al. (2012). Oncogenic Kras maintains pancreatic tumors through regulation of anabolic glucose metabolism. Cell *149*, 656–670.
11. Bar-Sagi, D., Knelson, E.H., and Sequist, L.V. (2020). A bright future for KRAS inhibitors. Nat. Can. *1*, 25–27.
12. Hallin, J., Engstrom, L.D., Hargis, L., Calinisan, A., Aranda, R., Briere, D.M., Sudhakar, N., Bowcut, V., Baer, B.R., Ballard, J.A., et al. (2020). The KRAS(G12C) inhibitor MRTX849 provides insight toward therapeutic susceptibility of KRAS-mutant cancers in mouse models and patients. Cancer Discov. *10*, 54–71.
13. Ostrem, J.M.L., and Shokat, K.M. (2016). Direct small-molecule inhibitors of KRAS: from structural insights to mechanism-based design. Nat. Rev. Drug Discov. *15*, 771–785.
14. Hong, D.S., Fakih, M.G., Strickler, J.H., Desai, J., Durm, G.A., Shapiro, G.I., Falchook, G.S., Price, T.J., Sacher, A., Denlinger, C.S., et al. (2020). KRAS(G12C) inhibition with sotorasib in advanced solid tumors. N. Engl. J. Med. *383*, 1207–1217.
15. Jänne, P., Rybkin, I., Spira, A., Riely, G., Papadopoulos, K., Sabari, J., Johnson, M., Heist, R., Bazhenova, L., Barve, M., et al. (2020). 3LBA late breaking - KRYSTAL-1: activity and safety of adagrasib (MRTX849) in advanced/metastatic non–small-cell lung cancer (NSCLC) harboring KRAS G12C mutation. Eur. J. Cancer *138*, S1–S2.
16. Johnson, M.L., Ou, S., Barve, M., Rybkin, I., Papadopoulos, K., Leal, T., Velastegui, K., Christensen, J., Kheoh, T., Chao, R., and Weiss, J. (2020). 4LBA late breaking - KRYSTAL-1: activity and safety of adagrasib (MRTX849) in patients with colorectal cancer (CRC) and other solid tumors harboring a KRAS G12C mutation. Eur. J. Cancer *138*, S2.

17. Witkiewicz, A.K., McMillan, E.A., Balaji, U., Baek, G., Lin, W.C., Mansour, J., Mollaee, M., Wagner, K.U., Koduru, P., Yopp, A., et al. (2015). Whole-exome sequencing of pancreatic cancer defines genetic diversity and therapeutic targets. Nat. Commun. *6*, 6744.

18. Castellano, E., and Downward, J. (2011). RAS interaction with PI3K: more than just another effector pathway. Genes Cancer *2*, 261–274.

19. Engelman, J.A., Chen, L., Tan, X., Crosby, K., Guimaraes, A.R., Upadhyay, R., Maira, M., McNamara, K., Perera, S.A., Song, Y., et al. (2008). Effective use of PI3K and MEK inhibitors to treat mutant Kras G12D and PIK3CA H1047R murine lung cancers. Nat. Med. *14*, 1351–1356.

20. Hatzivassiliou, G., Haling, J.R., Chen, H., Song, K., Price, S., Heald, R., Hewitt, J.F.M., Zak, M., Peck, A., Orr, C., et al. (2013). Mechanism of MEK inhibition determines efficacy in mutant KRAS- versus BRAF-driven cancers. Nature *501*, 232–236.

21. Waters, A.M., and Der, C.J. (2018). The critical driver and therapeutic target for pancreatic cancer. Cold Spring Harb. Perspect. Med. *8*, a031435.

22. Sun, C., Hobor, S., Bertotti, A., Zecchin, D., Huang, S., Galimi, F., Cottino, F., Prahallad, A., Grernrum, W., Tzani, A., et al. (2014). Intrinsic resistance to MEK inhibition in KRAS mutant lung and colon cancer through transcriptional induction of ERBB3. Cell Rep. *7*, 86–93.

23. Mainardi, S., Mulero-Sánchez, A., Prahallad, A., Germano, G., Bosma, A., Krimpenfort, P., Lieftink, C., Steinberg, J.D., de Wit, N., Gonçalves-Ribeiro, S., et al. (2018). SHP2 is required for growth of KRAS-mutant non-small-cell lung cancer in vivo. Nat. Med. *24*, 961–967.

24. Ruess, D.A., Heynen, G.J., Ciecielski, K.J., Ai, J., Berninger, A., Kabacaoglu, D., Görgülü, K., Dantes, Z., Wörmann, S.M., Diakopoulos, K.N., et al. (2018). Mutant KRAS-driven cancers depend on PTPN11/SHP2 phosphatase. Nat. Med. *24*, 954–960.

25. Wong, G.S., Zhou, J., Liu, J.B., Wu, Z., Xu, X., Li, T., Xu, D., Schumacher, S.E., Puschhof, J., McFarland, J., et al. (2018). Targeting wild-type KRAS-amplified gastroesophageal cancer through combined MEK and SHP2 inhibition. Nat. Med. *24*, 968–977.

26. Neel, B.G., Gu, H., and Pao, L. (2003). The 'Shp'ing news: SH2 domain-containing tyrosine phosphatases in cell signaling. Trends Biochem. Sci. *28*, 284–293.

27. Garcia Fortanet, J., Chen, C.H.T., Chen, Y.N.P., Chen, Z., Deng, Z., Firestone, B., Fekkes, P., Fodor, M., Fortin, P.D., Fridrich, C., et al. (2016). Allosteric inhibition of SHP2: identification of a potent, selective, and orally efficacious phosphatase inhibitor. J. Med. Chem. *59*, 7773–7782.

28. Infante, J.R., Somer, B.G., Park, J.O., Li, C.P., Scheulen, M.E., Kasubhai, S.M., Oh, D.Y., Liu, Y., Redhu, S., Steplewski, K., and Le, N. (2014). A randomised, double-blind, placebo-controlled trial of trametinib, an oral MEK inhibitor, in combination with gemcitabine for patients with untreated metastatic adenocarcinoma of the pancreas. Eur. J. Cancer *50*, 2072–2081.

29. Kasuga, A., Nakagawa, K., Nagashima, F., Shimizu, T., Naruge, D., Nishina, S., Kitamura, H., Kurata, T., Takasu, A., Fujisaka, Y., et al. (2015). A phase I/Ib study of trametinib (GSK1120212) alone and in combination with gemcitabine in Japanese patients with advanced solid tumors. Invest. N. Drugs *33*, 1058–1067.

30. Tolcher, A.W., Bendell, J.C., Papadopoulos, K.P., Burris, H.A., 3rd, Patnaik, A., Jones, S.F., Rasco, D., Cox, D.S., Durante, M., Bellew, K.M., et al. (2015). A phase IB trial of the oral MEK inhibitor trametinib (GSK1120212) in combination with everolimus in patients with advanced solid tumors. Ann. Oncol. *26*, 58–64.

31. Welsh, S.J., and Corrie, P.G. (2015). Management of BRAF and MEK inhibitor toxicities in patients with metastatic melanoma. Ther. Adv. Med. Oncol. *7*, 122–136.

32. Pathania, S., and Rawal, R.K. (2020). An update on chemical classes targeting ERK1/2 for the management of cancer. Future Med. Chem. *12*, 593–611.

33. Hayes, T.K., Neel, N.F., Hu, C., Gautam, P., Chenard, M., Long, B., Aziz, M., Kassner, M., Bryant, K.L., Pierobon, M., et al. (2016). Long-term ERK inhibition in KRAS-mutant pancreatic cancer is associated with MYC degradation and senescence-like growth suppression. Cancer Cell *29*, 75–89.

34. Yang, J.C.-H., Lin, C.-C., and Chu, C.-Y. (2018). 49 - management of toxicities of targeted therapies. In IASLC Thoracic Oncology, Second Edition, H.I. Pass, D. Ball, and G.V. Scagliotti, eds. (Elsevier, Philadelphia), pp. 490–500.e493.

35. Drosten, M., and Barbacid, M. (2020). Targeting the MAPK pathway in KRAS-driven tumors. Cancer Cell *37*, 543–550.

36. Ryan, M.B., Der, C.J., Wang-Gillam, A., and Cox, A.D. (2015). Targeting RAS-mutant cancers: is ERK the key? Trends Cancer *1*, 183–198.

37. Bhagwat, S.V., McMillen, W.T., Cai, S., Zhao, B., Whitesell, M., Shen, W., Kindler, L., Flack, R.S., Wu, W., Anderson, B., et al. (2020). ERK inhibitor LY3214996 targets ERK pathway-driven cancers: a therapeutic approach toward precision medicine. Mol. Cancer Therapeut. *19*, 325–336.

38. Nichols, R.J., Haderk, F., Stahlhut, C., Schulze, C.J., Hemmati, G., Wildes, D., Tzitzilonis, C., Mordec, K., Marquez, A., Romero, J., et al. (2018). RAS nucleotide cycling underlies the SHP2 phosphatase dependence of mutant BRAF-NF1- and RAS-driven cancers. Nat. Cell Biol. *20*, 1064–1073.

39. Doehn, U., Hauge, C., Frank, S.R., Jensen, C.J., Duda, K., Nielsen, J.V., Cohen, M.S., Johansen, J.V., Winther, B.R., Lund, L.R., et al. (2009). RSK is a principal effector of the RAS-ERK pathway for eliciting a coordinate promotile/invasive gene program and phenotype in epithelial cells. Mol. Cell *35*, 511–522.

40. Huang, X., Biswas, S., Oki, Y., Issa, J.P., and Berry, D.A. (2007). A parallel phase I/II clinical trial design for combination therapies. Biometrics *63*, 429–436.

41. Le Tourneau, C., Lee, J.J., and Siu, L.L. (2009). Dose escalation methods in phase I cancer clinical trials. J. Natl. Cancer Inst. *101*, 708–720.

42. Wagle, M.C., Kirouac, D., Klijn, C., Liu, B., Mahajan, S., Junttila, M., Moffat, J., Merchant, M., Huw, L., Wongchenko, M., et al. (2018). A transcriptional MAPK Pathway Activity Score (MPAS) is a clinically relevant biomarker in multiple cancer types. NPJ Precis. Oncol. *2*, 7.

43. Hao, H.X., Wang, H., Liu, C., Kovats, S., Velazquez, R., Lu, H., Pant, B., Shirley, M., Meyer, M.J., Pu, M., et al. (2019). Tumor intrinsic efficacy by SHP2 and RTK inhibitors in KRAS-mutant cancers. Mol. Cancer Therapeut. *18*, 2368–2380.

44. Jiang, B., Zhou, L., Lu, J., Wang, Y., Liu, C., You, L., and Guo, J. (2020). Stroma-targeting therapy in pancreatic cancer: one coin with two sides? Front. Oncol. *10*, 576399.

45. Neesse, A., Algül, H., Tuveson, D.A., and Gress, T.M. (2015). Stromal biology and therapy in pancreatic cancer: a changing paradigm. Gut *64*, 1476–1484.

46. Bryant, K.L., Stalnecker, C.A., Zeitouni, D., Klomp, J.E., Peng, S., Tikunov, A.P., Gunda, V., Pierobon, M., Waters, A.M., George, S.D., et al. (2019). Combination of ERK and autophagy inhibition as a treatment approach for pancreatic cancer. Nat. Med. *25*, 628–640.

47. Balachandran, V.P., Beatty, G.L., and Dougan, S.K. (2019). Broadening the impact of immunotherapy to pancreatic cancer: challenges and opportunities. Gastroenterology *156*, 2056–2072.

48. Nevala-Plagemann, C., Hidalgo, M., and Garrido-Laguna, I. (2020). From state-of-the-art treatments to novel therapies for advanced-stage pancreatic cancer. Nat. Rev. Clin. Oncol. *17*, 108–123.

49. Hofmann, M.H., Gmachl, M., Ramharter, J., Savarese, F., Gerlach, D., Marszalek, J.R., Sanderson, M.P., Kessler, D., Trapani, F., Arnhof, H., et al. (2021). BI-3406, a potent and selective SOS1-KRAS interaction inhibitor, is effective in KRAS-driven cancers through combined MEK inhibition. Cancer Discov. *11*, 142–157.

50. Dance, M., Montagner, A., Salles, J.P., Yart, A., and Raynal, P. (2008). The molecular functions of Shp2 in the Ras/Mitogen-activated protein kinase (ERK1/2) pathway. Cell. Signal. *20*, 453–459.

51. Jänne, P.A., van den Heuvel, M.M., Barlesi, F., Cobo, M., Mazieres, J., Crinò, L., Orlov, S., Blackhall, F., Wolf, J., Garrido, P., et al. (2017). Selumetinib plus docetaxel compared with docetaxel alone and progression-free survival in patients with KRAS-mutant advanced non-small cell lung cancer: the SELECT-1 randomized clinical trial. JAMA *317*, 1844–1853.

52. Liu, Z., Zhao, Y., Fang, J., Cui, R., Xiao, Y., and Xu, Q. (2017). SHP2 negatively regulates HLA-ABC and PD-L1 expression via STAT1 phosphorylation in prostate cancer cells. Oncotarget *8*, 53518–53530.

53. Juneja, V.R., McGuire, K.A., Manguso, R.T., LaFleur, M.W., Collins, N., Haining, W.N., Freeman, G.J., and Sharpe, A.H. (2017). PD-L1 on tumor cells is sufficient for immune evasion in immunogenic tumors and inhibits CD8 T cell cytotoxicity. J. Exp. Med. *214*, 895–904.

54. Schoenfeld, A.J., and Hellmann, M.D. (2020). Acquired resistance to immune checkpoint inhibitors. Cancer Cell *37*, 443–455.

55. Quintana, E., Schulze, C.J., Myers, D.R., Choy, T.J., Mordec, K., Wildes, D., Shifrin, N.T., Belwafa, A., Koltun, E.S., Gill, A.L., et al. (2020). Allosteric inhibition of SHP2 stimulates antitumor immunity by transforming the immunosuppressive environment. Cancer Res. *80*, 2889–2902.

56. Zhao, M., Guo, W., Wu, Y., Yang, C., Zhong, L., Deng, G., Zhu, Y., Liu, W., Gu, Y., Lu, Y., et al. (2019). SHP2 inhibition triggers anti-tumor immunity and synergizes with PD-1 blockade. Acta Pharm. Sin. B *9*, 304–315.

57. Su, H., Bodenstein, C., Dumont, R.A., Seimbille, Y., Dubinett, S., Phelps, M.E., Herschman, H., Czernin, J., and Weber, W. (2006). Monitoring tumor glucose utilization by positron emission tomography for the prediction of treatment response to epidermal growth factor receptor kinase inhibitors. Clin. Cancer Res. *12*, 5659–5667.

58. Wang, Z.J., Behr, S., Consunji, M.V., Yeh, B.M., Ohliger, M.A., Gao, K., Ko, A.H., Cinar, P., Tempero, M.A., and Collisson, E.A. (2018). Early response assessment in pancreatic ductal adenocarcinoma through integrated PET/MRI. AJR Am. J. Roentgenol. *211*, 1010–1019.

59. Jackson, E.L., Willis, N., Mercer, K., Bronson, R.T., Crowley, D., Montoya, R., Jacks, T., and Tuveson, D.A. (2001). Analysis of lung tumor initiation and progression using conditional expression of oncogenic K-ras. Genes Dev. *15*, 3243–3248.

60. Nakhai, H., Sel, S., Favor, J., Mendoza-Torres, L., Paulsen, F., Duncker, G.I.W., and Schmid, R.M. (2007). Ptf1a is essential for the differentiation of GABAergic and glycinergic amacrine cells and horizontal cells in the mouse retina. Development *134*, 1151–1160.

61. Marino, S., Vooijs, M., van Der Gulden, H., Jonkers, J., and Berns, A. (2000). Induction of medulloblastomas in p53-null mutant mice by somatic inactivation of Rb in the external granular layer cells of the cerebellum. Genes Dev. *14*, 994–1004.

62. Hingorani, S.R., Wang, L., Multani, A.S., Combs, C., Deramaudt, T.B., Hruban, R.H., Rustgi, A.K., Chang, S., and Tuveson, D.A. (2005). Trp53R172H and KrasG12D cooperate to promote chromosomal instability and widely metastatic pancreatic ductal adenocarcinoma in mice. Cancer Cell *7*, 469–483.

63. D'Errico, G., Alonso-Nocelo, M., Vallespinos, M., Hermann, P.C., Alcalá, S., García, C.P., Martin-Hijano, L., Valle, S., Earl, J., Cassiano, C., et al. (2019). Tumor-associated macrophage-secreted 14-3-3zeta signals via AXL to promote pancreatic cancer chemoresistance. Oncogene *38*, 5469–5485.

64. Chou, T.C. (2010). Drug combination studies and their synergy quantification using the Chou-Talalay method. Cancer Res. *70*, 440–446.

65. Manchado, E., Weissmueller, S., Morris, J.P., 4th, Chen, C.C., Wullenkord, R., Lujambio, A., de Stanchina, E., Poirier, J.T., Gainor, J.F., Corcoran, R.B., et al. (2016). A combinatorial strategy for treating KRAS-mutant lung cancer. Nature *534*, 647–651.

66. Lesina, M., Kurkowski, M.U., Ludes, K., Rose-John, S., Treiber, M., Klöppel, G., Yoshimura, A., Reindl, W., Sipos, B., Akira, S., et al. (2011). Stat3/Socs3 activation by IL-6 transsignaling promotes progression of pancreatic intraepithelial neoplasia and development of pancreatic cancer. Cancer Cell *19*, 456–469.

STAR★METHODS

KEY RESOURCES TABLE

REAGENT or RESOURCE	SOURCE	IDENTIFIER
Antibodies		
Anti-Ki67 antibody	Abcam	Cat# ab15580; RRID:AB_443209
Alpha-Tubulin antibody	Sigma-Aldrich	T9026; RRID:AB_477593
RSK-1 antibody	CST	#8408; RRID:AB_10828594
P-RSK antibody	CST	#8753; RRID:AB_2783561
P-RSK antibody	CST	#9344; RRID:AB_331650
GAPDH antibody	CST	#5174; RRID:AB_10622025
Vinculin antibody	Sigma-Aldrich	V9131; RRID:AB_477629
Biological samples		
Patient Derived Xenografts	Dr. Manuel Hidalgo, Spanish National Cancer Research Center (CNIO), Madrid, Spain	(Reference no. I409181220BSMH)
Chemicals, peptides, and recombinant proteins		
LY3214996 (Temuterkib)	Lilly	Available at https://www.selleckchem.com/ Catalog No.S8534
RMC-4550	Revolution Medicines	Available at https://www.selleckchem.com/ Catalog No.S8718
37% Formaldehyde solution	Merck	104,003
Crystal Violet	Sigma-Aldrich	HT90132-1 L
Matrigel	Corning	REF 354230 LOT 9364004
Critical commercial assays		
CellTiter-Glo 3D	Promega	REF G9682 LOT 0000496328
Caspase 3/7 reagent	Sartorius	#4440
Deposited data		
Uncropped Western Blots	Mendeley	Mendeley Data: https://doi.org/10.17632/cz4vfsk28h.1
RNAseq Data	GEO	GEO: GSE213706
Experimental models: Cell lines		
Murine KCP cell lines derived from KCP mice in house	This paper	N/A
MiaPaCa-2	ATCC	CRL-1420; RRID: CVCL_0428
ASPC1	ATCC	CRL-1682; RRID: CVCL_0152
Panc10.05	ATCC	CRL-2547; RRID: CVCL_1639
Panc-1	ATCC	CRL-1469; RRID: CVCL_1794
YAPC	DSMZ	REF 15070; RRID: CVCL_0480
Experimental models: Organisms/strains		
B6 (C57BL/6J) mice	Jackson Laboratory	RRID:IMSR_JAX:000,664
NSG (*NOD.Cg-Prkdc^{scid} Il2rg^{tm1Wjl}/SzJ*) mice	Jackson Laboratory	RRID:IMSR_JAX:005,557

(*Continued on next page*)

Continued		
REAGENT or RESOURCE	SOURCE	IDENTIFIER
KCP mice (Krastm4Tyj); (Ptf1atm1(Cre) Hnak); (Trp53tm1Brn) (KCP)	See References[59,60,61]	N/A
KCP^{mut} mice (Kras^{tm4Tyj}); (Tg(Pdx1-cre)6Tuv); Trp53tm1Tyj)	See Reference[62]	N/A
NU-Foxn1nu nude mice (*Hsd:Athymic Nude-Foxn1^{nu}/Foxn1^{+}*)	Envigo https://www.envigo.com/model/hsd-athymic-nude-foxn1nu-foxn1?selctry=France&ctry=	N/A
Software and algorithms		
ImageJ	https://imagej.nih.gov/ij/	RRID:SCR_003070
CompuSyn	https://www.combosyn.com/ See Reference[63]	N/A
Adobe Illustrator®	Adobe https://www.adobe.com/de/	RRID:SCR_010279
GraphPad Prism 8	GraphStats Technologies https://www.graphstats.net/	RRID:SCR_002798
Nucline™ NanoScan Software	Mediso	N/A
Flywheel DICOM viewer	Flywheel https://docs.flywheel.io/hc/en-us	N/A
Incucyte ZOOM	Essen Bioscience	N/A
Aperio ImageScope	Leica Biosystems https://www2.leicabiosystems.com/	
Axiovision	Zeiss https://www.micro-shop.zeiss.com/de/de/system/software-axiovision+software-produkte/1007/	
BioRender	https://biorender.com/	

RESOURCE AVAILABILITY

Lead contact

Further information and requests for resources and reagents should be directed to and will be fulfilled by the lead contact, Dr. Sara Mainardi (s.mainardi@nki.nl).

Materials availability

This study did not generate new unique reagents.

Data availability

- Uncropped Western Blot images have been uploaded to Mendeley and can be accessed via Mendeley Data: https://doi.org/10.17632/cz4vfsk28h.1
- RNAseq data was uploaded to GEO under the reference Series GSE213706 and can be accessed via GEO: GSE213706
- This paper does not report original code
- Any additional information required to reanalyze the data reported in this work paper is available from the lead contact upon request.

EXPERIMENTAL MODEL AND SUBJECT DETAILS

Mouse strains

Kras^{G12D} (*Kras^{tm4Tyj}*)[59]; *p48-Cre* (*Ptf1a$^{tm1(Cre)Hnak}$*)[60]; *p53$^{flox/flox}$*(*Trp53^{tm1Brn}*)[61] (KCP) have been described previously and were bred in a mixed genetic background in our animal facility. Non-tumor-bearing littermates without mutational *Kras^{G12D}* (*Kras^{tm4Tyj}*) and *p48-Cre* (*Ptf1a$^{tm1(Cre)Hnak}$*) were used in the dose finding study and for subcutaneous tumor transplantation. *Kras^{G12D}* (*Kras^{tm4Tyj}*);

Pdx1-Cre (*Tg(Pdx1-cre)6Tuv*); *Trp53*$^{mut/+}$(*Trp53*^{tm1Tyj})[62] (KCP^{mut}) mouse strain with C57BL/6J background served as tumor donor for orthotopic transplantation experiments.

At the age of weaning and after death, genotypes were determined by PCR and gel electrophoresis. B6 (C57BL/6J) mice and NSG (*NOD.Cg-Prkdc*^{scid} *Il2rg*^{tm1Wjl}/*SzJ*) mice were obtained from Jackson Laboratory. NU-Foxn1nu nude mice (*Hsd:Athymic Nude-Foxn1*^{nu}/*Foxn1*$^{+}$) were obtained from Envigo.

All mice were kept in an animal room (room temperature range between 20 and 22°C) with light-dark cycle of 12:12 h in groups of 2–4 animals in type III cages (Tecniplast) or in groups of 5 animals in IVC cages from (Innovive) with bedding and nesting material. All animals were provided with the standard maintenance food for mice (No. 1324–10 mm pellets, Altromin, or SDS diets Technilab BMI) and water *ad libitum* and housed under specific pathogen-free conditions in accordance with the European Directive 2012/63/EU.

All animal experiments and care were performed in accordance with the guidelines of institutional committees and European regulations (Directive 2012/63/UE) and approved by the local authorities, Regierung von Oberbayern (ROB-55.2-2532.Vet_02-15-143), the animal experiment committee at the Netherlands Cancer Institute (IVD 1.1.9082), the Dutch Central Authority for Scientific Procedures on Animals (AVD30100202010644), the Universidad Autónoma de Madrid Ethics Committee (CEI 60-1057-A068) and the Comunidad de Madrid (PROEX 335/14).

Cell culture and cell lines

Primary murine tumor cell lines were obtained from chopped pieces of explanted tumors without enzymatic digestion. All murine cell lines were routinely cultured in DMEM supplemented with 10% FBS and penicillin–streptomycin (100 U/mL, 100 μg/mL) (all Life Technologies). Human PDAC cell lines: YAPC (*KRAS*$^{p.G12V}$; *p53*$^{p.H179R}$; *SMAD4*$^{p.R515fs*22}$) was purchased from DSMZ. ASPC1 (*KRAS*$^{p.G12D}$; *p53*$^{p.C135fs*35}$; *SMAD4*$^{p.R100T}$; *CDKN2A*$^{p.L78fs*41}$), Panc10.05 (*KRAS*$^{p.G12D}$; *p53*$^{p.I255N}$), Panc1 (*KRAS*$^{p.G12D}$; *p53*$^{p.R273H}$) and MiaPaCa-2 (*KRAS*$^{p.G12C}$; *p53*$^{p.R248W}$; Homozygous for *CDKN2A* deletion) were purchased from the American Type Culture Collection (ATCC). Mutational status of the cell lines was compiled from the ATCC, Catalog of Somatic Mutations in Cancer (COSMIC; Wellcome Trust Sanger Institute) and Cancer Cell Line Encyclopedia (CCLE, Broad Institute) databases. Human cell lines were cultured in RPMI1640 (Life Technologies), supplemented with 10% FBS, penicillin/streptomycin (100 U/mL, 100 μg/mL, Life Technologies), and 2 mM L-glutamine (Thermo Fisher Scientific). All cells were kept at 37°C in a humidified incubator with 5% CO_2.

Human pancreatic cancer cell line xenografts

MiaPaCa-2, Panc10.05, ASPC1, and YAPC cells were resuspended (5 × 10^6 cells per mouse) in a 1:1 mixture of RPMI and Matrigel (Corning) and injected subcutaneously into the right flanks of 8-week-old NSG mice. Tumor volume was monitored three times a week as described for the patient-derived tissue xenografts. Mice were randomized when the tumor reached a volume of approximately 200 mm^3 and treated for a maximum period of 30 days (YAPC) or 42 days (MiaPaCa-2, Panc10.05, ASPC1). Mice were sacrificed after 1, 3 or 6 weeks of treatment (8 mice per time point and per cohort) or at humane end point. In this experimental set up, RMC-4550 (10 mg/kg) and LY3214996 (100 mg/kg) were dissolved in 2% HPMC E-50, 0.5% Tween-80 in 50 mM Sodium Citrate Buffer, pH 4.0, and administered according to the different schedules (cohorts A, B, C, D, E, F, G, H, I). Control groups were treated daily with the vehicle alone. End-of-treatment tumor material was partly snap frozen in liquid nitrogen and stored at −80°C.

Orthotopic PDAC mouse models

30 mm^3 KCP^{mut} tumor pieces were obtained from endogenous mouse models and subcutaneously transplanted into the flanks of female B6 host mice for expansion. Tumor growth was monitored as indicated for the patient-derived tissue xenografts by caliper analysis. After 4 weeks, subcutaneous KCP^{mut} tumors from donor mice were harvested and chopped into ∼40 mm^3 pieces and orthotopically transplanted into pancreata of 8-week-old female and weight matched 18–20 g male B6 mice, as previously described.[63] Briefly: Mice were anesthetized via isoflurane inhalation, shaved and skin wiped with ethanol-containing skin antiseptic. A small cutaneous midline incision was performed (0.8 cm) and a small subcutaneous pocket was prepared. An equally small incision (0.8 cm) was made into the peritoneum, the pancreas was mobilized and exposed. Tumor pieces were orthotopically implanted into the pancreas. Then the pancreas and spleen were carefully repositioned in the abdomen and the peritoneum was closed with a single stitch suture using 6–0 Prolene sutures. The skin was then closed with surgical staples. Tumor growth was monitored by palpation. After 2 weeks, a representative number of mice were sacrificed to determine pre-treatment baseline pancreas/tumor weights, and the remaining mice were randomly grouped into cohort A, B, C, and vehicle and treated with inhibitors as described in the following. End-of-treatment tumor material was partly snap frozen in liquid nitrogen and stored at −80°C.

Subcutaneous cancer cell line mouse models

Pancreatic cancer cells from KCP endogenous donor mouse model were obtained and cultured as described above. 2.5 × 10^6–3 × 10^6 cells were suspended in 100 μL of a 1:1 mixture of DMEM and Matrigel (Corning) and injected subcutaneously into the left and right flank of 10–15-week-old non-tumor-bearing female and male littermates from mixed background mouse strain *Kras*^{G12D} (*Kras*^{tm4Tyj}), *p53*$^{flox/flox}$ (*Trp53*^{tm1Brn}). Tumor volume was monitored as indicated for the patient-derived tissue xenografts. Randomized therapy was initiated after tumors had reached a palpable volume of <300 mm^3. Therefore, female, and male mice were treated

continuously with inhibitors (cohort C) or vehicle alone. On day 0, 3 and 7 of treatment, mice were scanned by animal PET (Mediso), imaging radioactive labeled glucose (^{18}F-FDG) uptake. Mice were sacrificed after different time points, with a minimum treatment time of 3 days.

METHOD DETAILS

Drugs and inhibitors

SHP2 inhibitor RMC-4550 was kindly provided by Revolution Medicines, Redwood City, California U.S.A. RMC-4550 was diluted in 50 mM Sodium Citrate Buffer pH = 4 with 1% Hydroxyethylcellulose (Sigma-Aldrich), 0.25% Tween (Sigma-Aldrich) and 0.05% Antifoam A concentrate (Sigma-Aldrich). Erk1/2 inhibitor LY3214996 was kindly provided by Eli Lilly and Company, Indianapolis IN 46285 U.S.A. LY3214996 powder was dissolved in dH_2O (Braun) with 1% Hydroxyethylcellulose (Sigma-Aldrich), 0.25% Tween (Sigma-Aldrich) and 0.05% Antifoam A concentrate (Sigma-Aldrich). Inhibitor combinations were used according to company's recommendation.

In vitro drug synergy and quantitative analysis

Indicated cells were cultured and seeded into 96-well plates at a density of 300–2,000 cells per well, depending on growth rate. Twenty-four hours later, drugs were added at the indicated concentrations using the HP D300 Digital Dispenser (HP). After 72 h, medium and drugs were refreshed. The total duration of the experiment was 6 days (two treatments) for KCP_K2101, KCP_P0012, MiaPaCa-2 and Panc10.05, and 10 days (three treatments) for Panc1, ASPC1 and YAPC. Cells were fixed with 4% PFA diluted in PBS (37% Formaldehyde solution, Merck) and stained with 2% crystal violet solution (HT90132-1 L, Sigma-Aldrich). Drug synergy was calculated using CompuSyn software (version 1.0), which is based on the median-effect principle and the combination index–isobologram theorem.[64] CompuSyn software generates combination index values, where combination index 0–0.75 indicates synergy, 0.75–1.25 indicates an additive effect and CI > 1.25 indicates antagonism.[65] Following the instructions of the software, drug combinations at non-constant ratios were used to calculate the combination index in our study.

Cell viability assay

1000 cells were seeded in 96 Well-plates for adherent growth (Cellstar®, 655,180) and for growth in suspension 96 well-plate F-Bottom (Cellstar®, 655,970). After approximately 6 h 2 μM RMC-4550 was added using an HP D300 Digital Dispenser. PAO and DMSO were used as a positive and negative control, respectively. After 96 h measurement was conducted with EnVision plate reader (PerkinElmer) by adding CellTiter-Glo® 3D cell viability assay reagent. The data was corrected for PAO treated cells and normalized to DMSO treated cells. Statistical analyses compared the effect of SHP2 inhibition between 2D/3D growth both in 10% serum and 3% serum using ordinary one-way ANOVA test.

Incucyte cell-proliferation assay and apoptosis assay

Indicated cell lines were seeded into 96-well plates at a density of 200–2,000 cells per well, depending on growth rate and the design of the experiment. Approximately 24 h later, drugs were added at the indicated concentrations using the HP D300 Digital Dispenser (HP). Cells were imaged every 4 h using the Incucyte ZOOM (Essen Bioscience). Phase-contrast images were analyzed to detect cell proliferation on the basis of cell confluence. For cell apoptosis, caspase-3/caspase-7 green apoptosis-assay reagent (Essen Bioscience) was added to the culture medium (1:1000), and cell apoptosis was analyzed on the basis of green-fluorescent staining of apoptotic cells.

In vivo drug combination dose finding escalation

Dose finding was established according to modified "3 + 3" scheme. Non-tumor-bearing mice were put on continuous oral administration of both drugs over 14 days (NSG mice, *Kras^{G12D}; p53$^{flox/flox}$*, *p53$^{flox/flox}$*, *p53$^{flox/wt}$* or wildtype mice from *Kras^{G12D}; p48-Cre; p53$^{flox/flox}$* litter). Toxicity was evaluated daily by measuring mice body weight (endpoint at body weight loss >20%), general clinical signs (abnormal behavior, signs of physical discomfort). According to modified "3 + 3" design, mouse cohorts consisting of 3 animals were given an initial combination dose (d5), followed by increased dose d7 as no side effects were observed in all 3 mice. Up to six mice were assigned to one dose. If the combination dose showed side effects in 1/6 mice, the dose was designated as an admissible dose, opening next dose level for testing. If dose-limiting toxicity was observed in 2/6 mice, the combination was accepted as a maximum tolerated dose, closing higher doses for testing. If more than two of the six mice experienced dose-limiting toxicity, the dose was down staged. The following dose combinations were administered: dose d5 (10 mg/kg RMC-4550 + 75 mg/kg LY3214996), dose d7 (30 mg/kg RMC-4550 + 75 mg/kg LY3214996), dose d8 (10 mg/kg RMC-4550 + 100 mg/kg LY3214996) and dose d9 (30 mg/kg RMC-4550 + 100 mg/kg LY3214996). One cohort was administered vehicle (50 mM Sodium Citrate Buffer pH = 4 with 1% Hydroxyethylcellulose, 0.25% Tween and 0.05% Antifoam A concentrate) to monitor gavage-mediated side effects.

In vivo therapy treatment schedules

For *in vivo* application in KCP mice, human cell line xenografts, PDX xenografts, orthotopically transplanted KCP^{mut} mice, and subcutaneously transplanted KCP mice, dose d8 (10 mg/kg RMC-4550 + 100 mg/kg LY3214996) was administered by oral gavage.

Depending on the mouse model, the drug administration followed different schedules: continuous administration (daily) of both drugs (cohort C), administration of both drugs 5 days on/2 days off (cohort D), or continuous administration of RMC-4550 plus LY3214996 every other day (cohort E), or continuous administration of RMC-4550 plus LY3214996 5 days on/2 days off (cohort F). As controls, mice were treated daily with vehicle or with monotherapy. Monotherapy was scheduled either RMC-4550 continuous (cohort A) or 5 days on/2 days off (cohort G). Monotherapy with LY3214996 was accomplished continuously (cohort B), 5 days on/2 days off (cohort H) or every other day (cohort I).

Drug distribution of RMC-4550 and LY3214996 in tumor mice and non-tumor bearing controls

Tumors of female and male KCP mice were detected by palpation. Endogenous KCP tumor bearing mice and non-tumor-bearing control littermates without mutational *Kras*^{G12D} (*Kras*^{tm4Tyj}) and p48-Cre (*Ptf1a*$^{tm1(Cre)Hnak}$) were administered a single dose d8 of the drug combination (10 mg/kg RMC-4550 + 100 mg/kg LY3214996) and sacrificed after 1, 2, 4, 8, 16, and 20 h, respectively. The control mice cohort includes two mice, the tumor mice cohort four mice for each time point. After sacrifice, half of the tumor was used for pharmacokinetics studies and the rest for protein analysis. After weighing, samples were homogenized using a FastPrep®-24 (MP-Biomedicals, NY) in 1% (w/v) bovine serum albumin in water. The biological samples were assayed by liquid chromatography triple quadrupole mass spectrometry (LC-MS/MS) using an API4000 detector (Sciex) for determination of LY3214996 and RMC-4550 using ion pairs 453.5/367.0 and 437.0/279.9, respectively. LC separation was achieved using a Zorbax Extend C18 column (100 × 2.0 mm: ID). Mobile phase A and B comprised 0.1% formic acid in water and methanol, respectively. The flow rate was 0.4 mL/min and a linear gradient from 20% B to 95% B in 2.5 min, followed by 95% B for 2 min, followed by re-equilibration at 20% B for 10 min was used for elution. Sample pre-treatment was accomplished by mixing 5 μL biological matrix with 30 μL of formic acid in acetonitrile (1 + 99). After centrifugation, the clear supernatant was diluted 1 + 8 with water and 2 μL was injected into the LC-MS/MS system.

PET imaging and ^{18}F-FDG *in vivo*

Two-to-six hours fasted female and male mice bearing subcutaneous KCP tumors were randomly divided into two groups (vehicle versus cohort C). For PET imaging, mice received 12–14 MBq of the radiotracer ^{18}F-Fluordeoxyglucose (^{18}F-FDG) via injection through the lateral tail vein. PET images were acquired on a nanoScan PET system (Mediso, Budapest, Hungary) from 45–60 min post injection under isoflurane anesthesia (1–2% in medical air by precision vaporizer (Baxter Healthcare, Deerfield, IL, USA). During the imaging procedure, mice were placed on a heated bed and their heart rate was constantly monitored. For 3D whole body image reconstruction with a 0.4 mm^3 voxel size, the Tera-Tomo 3D image reconstruction algorithm (integrated into Nucline NanoScan Software, Mediso) was applied (4 iterations, 6 subsets), without AC and scatter corrections. Image counts per voxel per second were converted into standardized uptake values (SUV) using the activity concentrations computed the Nucline NanoScan software normalized to the animal's body weight. Quantification of tumor uptake was carried out using the Nucline NanoScan software, by drawing spherical regions of interest (ROIs), creating a volume that represented the entire tumor lesion. We recorded the volume, SUVmean, SUVmax and total lesion glycolysis (TLG) of each tumor.

Magnetic resonance imaging (MRI)

MR imaging for KCP male and female mice was started at an age of 24–37 days and repeated after 7 and 14 days of treatment (cohort C, D, E versus vehicle). Sedation was achieved via continuous inhalation of 2% isoflurane (Abbott) in 1.6% O_2 using a veterinary anesthesia system (Vetland Medical). Body temperature was maintained and monitored, and eyes were protected by eye ointment. Image acquisition was achieved using a mouse 3T coil inside a preclinical 3T nano scan PET/MR (Mediso) and a T2 weighted fast spin echo sequence (resolution: 192 × 128–25 slices, echo time 55,52 ms; repetition time 3000 ms). Analysis, visualization, and calculation was done by Flywheel DICOM viewer. Solid tumor volumes were calculated by summating truncated pyramid volumes between tumor areas on vicinal slices. As drug treatment prevented tumor development in some of the endogenous KCP mice, pancreatic areas including tumor and non-neoplastic tissue were defined as regions of interest and summarized in the scanned slices to calculate pancreatic volume.

Histology

Tissue specimens were fixed in 4%-buffered paraformaldehyde for 48 h at 4°C, dehydrated and embedded in paraffin. H&E was performed as described previously on 2.5 μm cut sections.[66] In brief, the paraffin-embedded tissue sections were deparaffinized in Roti®Histol (Roth) for 2 × 5 min followed by rehydration in ethanol of descending concentration (100%, 96%, 70%; 3–5 min each) and deionized water (3–5 min). Slides were then incubated in hematoxylin solution (Merck Millipore) for 5 min, washed with running tap water for 10 min and incubated in eosin solution (Merck) for 3.5 min. Subsequently, the stained tissue sections were dehydrated in 96% Ethanol and Isopropanol for 25 s each followed by Roti®Histol for 2 × 3 min. They were then covered with Pertex mounting medium (Medite GmbH) and coverslips (Merck). For immunohistochemistry, sections were probed with the antibody for Ki67 (ab15580, 1:2,500, abcam). Immunohistochemistry was performed using avidin-biotin-enhancement (Vector Laboratories). Slides were developed with DAB (3,3′ apos; -diaminobenzidine, Vector Laboratories) and counterstained with hematoxylin. Image acquisition was performed on a Zeiss AxioImager.A1 microscope. Quantitative interpretation of nuclear Ki67 staining was done with Aperio ImageScope (Leica). Quantitative analyses of tumor and acini areas were performed with Axiovision (Zeiss).

Sequencing and MAPK pathway activity score

For preparation of the MiaPaCa-2 and the Panc10.05 xenograft tumors, snap frozen material (3 mice from cohort C and vehicle, treated for 3 weeks), was cut at the cryostate (30 cryosections of 30 μm thickness per sample) and RNA was extracted using the RNeasy Mini Kit from Qiagen and analyzed using an Agilent 2100 Bioanalyzer system. For the orthotopically transplanted KCP^{mut} tumors, snap frozen tissue (cohort C versus vehicle) was homogenized, and RNA was isolated with Maxwell® 16 LEV simplyRNA Purification Kit from Promega. Sample purity was evaluated by nanoDrop, and RNA quality validated by agarose gel electrophoresis. Transcript levels were quantified with Kallisto (v0.46), using the GENCODE reference transcriptome (mouse version m25 and human version h34). For the human cell line xenograft samples, the human and mouse reference transcriptome were combined, and only human transcripts were kept for downstream analysis. The transcript levels were summed to gene levels and the gene expression levels were normalized between samples with EdgeR (v3.26.8) using trimmed mean of M-values. MAPK activity scores were calculated as described,[42] using the normalized log2 counts per million values for the following genes: SPRY2, SPRY4, ETV4, ETV5, DUSP4, DUSP6, CCND1, EPHA2, and EPHA4.

The AmpliSeq Cancer HotSpot Panel v2 for Illumina, which includes 50 oncogenes and tumor suppressor genes was used to prepare the sequencing library to analyze the Panc185 and Panc354 cells derived from PDX tumors. Sequencing was performed using the MiSeq instrument from Illumina with V2 MiSeq 2 × 150 (300-cycle) cartridges. Downstream analysis was performed using the Varsome Clinical software. The reads were aligned to the hg19 version of the genome and the Sentieon's Tnhaplotyper2 algorithm was used to call the variants, which were filtered based on call quality using the standard parameters designed for the AmpliSeq Cancer HotSpot Panel.

Protein lysate preparation and immunoblotting

To prepare analysis of cell lysates, cells were plated in complete medium. The morning after, cells were refreshed with medium and drugs of interest. At the desired time points, the cells were washed with cold-PBS and lysed in RIPA buffer supplemented with Halt™ Protease & Phosphatase single-use inhibitors cocktail (100 X) (78,442) and Halt™ Protease single-use inhibitors cocktail (100 X) (78,430). For preparation of tissue lysates, PDAC tissue from mice was homogenized in MLB Buffer containing protease inhibitor (Serva) and phosphatase inhibitor cocktails (Serva). Protein quantification was performed with the BCA Protein Assay Kit (Pierce). The lysates were then resolved by electrophoresis in Bolt 4–12% Bis-Tris Plus Gels (Thermo Fisher Scientific) followed by western blotting as described previously.[23] The following antibodies were used: Antibodies against RSK-1 (8408), phosphorylated RSK-1 (9344 and 8753) and GAPDH (5174) were purchased from Cell Signaling Technology (CST). Antibodies against alpha Tubulin (T9026) and Vinculin (V9131) were purchased from Sigma-Aldrich. Relative pRSK1 levels were quantified by densitometry using ImageJ.

QUANTIFICATION AND STATISTICAL ANALYSIS

All *in vitro* data are expressed as averages from at least two technical replicates ± SD, unless differently stated, and they have been independently reproduced at least twice with similar results. Significance was determined by ordinary one-way ANOVA test or by one-way ANOVA with Bonferroni's multiple comparison test or by unpaired, two-tailed t test. Statistical analysis was performed with GraphPad PRISM 8.0 software.

ADDITIONAL RESOURCES

Clinical trial

The clinical trial entitled Combination Therapy of RMC-4630 and LY3214996 in Metastatic KRAS Mutant Cancers (SHERPA), which arose from the results reported in this article, is registered under the ClinicalTrials.gov Identifier: NCT04916236. No data from this clinical trial are reported in this study.